Planetary migration in Solar System formation

Aurélien Crida

Ecole Doctorale Sciences Fondamentales et Appliquées
Université de Nice Sophia-Antipolis — Observatoire de la Côte d'Azur

PhD THESIS

THÈSE de DOCTORAT

Aurélien CRIDA

PLANETARY MIGRATION IN SOLAR SYSTEM FORMATION

MIGRATION PLANÉTAIRE AU COURS DE LA FORMATION DU SYSTÈME SOLAIRE

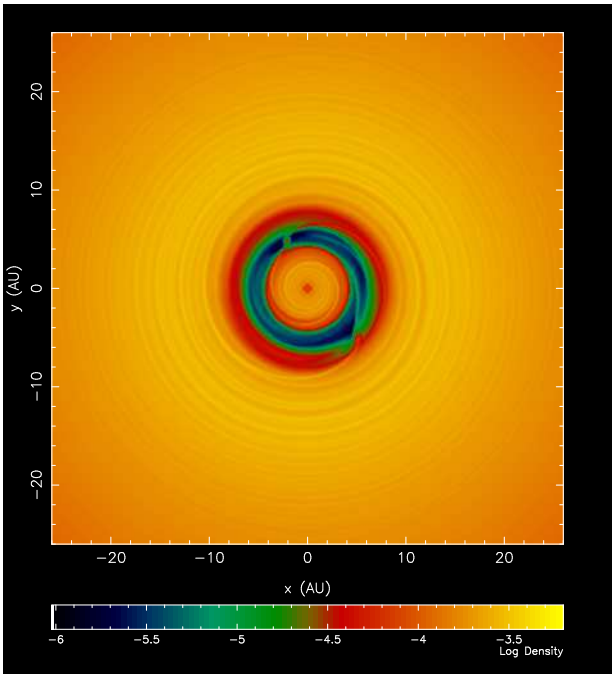

soutenue à l'Observatoire de la Côte d'Azur le 15 décembre 2006 à 14h devant le jury composé de :

defended at Observatoire de la Côte d'Azur at 2PM on December, 15, 2006 in front of the committee :

Pr. W. Kley	Universität Tübingen	Rapporteur / Reviewer
Pr. R. P. Nelson	Queen Mary, University of London	Rapporteur / Reviewer
Pr. M. Faurobert	Université de Nice Sophia-Antipolis	Examinatrice / Committe member
Pr. J-M. Huré	Université de Bordeaux	Examinateur / Committe member
Pr. B. Sicardy	Observatoire de Paris-Meudon	Examinateur / Committe member
Dr. A. Morbidelli	Observatoire de la Côte d'Azur	Directeur de thèse / PhD advisor

Couverture : La thèse résumée en une image : cette carte de densité montre Jupiter et Saturne dans un disque de gaz dans une configuration telle qu'elles ne migrent pas vers le Soleil (voir Chapitre 7). Les deux planètes ont ouvert un sillon dans le disque (l'anneau vert et bleu, voir Chapitre 4) et lancé un sillage (spirale jaune). La simulation a été obtenue avec un nouveau code qui utilise un système de grilles 2D et 1D emboitées. La grille 2D couvre la région où les planètes orbitent, de 1.5 à 25 Unités Astronomiques du Soleil. Une grille 1D s'étend du bord interne physique du disque (à 0.08 UA ici) jusqu'au bord interne de la grille 2D, et une seconde grille 1D s'étend du bord externe de la grille 2D jusqu'au bord physique du disque (à 200 UA). Ainsi, l'évolution des planètes est calculée conjointement avec l'évolution globale du disque (voir Chapitre 5). Noter la continuité aux transitions entre les domaines couverts par les grilles 2D et 1D, et que le sillage n'y est pas réfléchi. Noter enfin qu'il n'y a pas disparition du disque interne ni ouverture d'une cavité, ce qui est typique des cas sans migration (indépendamment du fait qu'il y ait une plusieurs planètes, voir Chapitre 6). L'extension de la grille 1D jusqu'à très petit rayon permet, pour la première fois, une représentation réaliste de l'état du disque interne.

Cover picture : The thesis summarized in an image. The plot shows Jupiter and Saturn in a gas disk configuration such that they avoid radial migration (see Chapter 7). The two planets have opened a gap in the disk (green-blue annulus, see Chapter 4) and launched a wake (yellow spiral). The simulation has been obtained with a new code that uses a system of nested 1D and 2D grids. The 2D grid covers the region in which the planets evolve, from 1.5 to 25 Astronomical Units in radius. A 1D grid extends from the inner physical radius of the disk (here 0.08 AU) to the inner boundary of the 2D grid, and a second 1D grid extends from the outer boundary of the 2D grid up to outer physical radius of the disk (here 200 AU). The grids communicate information in a way that conserves mass and angular momentum. In this way, the planet evolution is computed together with the correct global evolution of the disk (see Chapter 5). Notice that the transitions between the domains covered by the 2D and 1D grids are smooth, and no reflection of the wakes occurs at the boundaries among these grids. Notice finally that a cavity is not opened in the inner part of the disk. This is typical in all non-migrating cases (independently of the fact that there is one planet or multiple planets) (see Chapter 6). The extension of the inner 1D grid down to a very small physical radius allows, for the first time, a realistic representation of the state of the inner part of the disk.

Contents

1 Introduction **7**
1.1 The Solar System . . . 7
1.1.1 Antiquity . . . 7
1.1.2 Modern ages . . . 8
1.2 Planetary formation . . . 10
1.2.1 Star formation . . . 10
1.2.2 Planet formation . . . 12
1.2.3 Solar System formation . . . 15
1.2.4 Surprising Exoplanets . . . 16
1.3 Planet-disk interactions . . . 17
1.4 Problems and thesis plan . . . 20
1.4.1 Planetary migration and formation, general issues . . . 20
1.4.2 Solar System structure and constraints . . . 21

2 Torques calculation **23**
2.1 Fluid mechanics . . . 23
2.1.1 Notations and prerequisite in fluid mechanics . . . 23
2.1.2 Polar coordinates . . . 25
2.1.3 Viscous torque in a Keplerian disk . . . 25
2.2 Planetary torque . . . 26
2.2.1 Impulse approximation . . . 26
2.2.2 Lindblad Resonances . . . 29
2.3 Type I migration and differential Lindblad torque . . . 34
2.4 Type III migration and Corotation torque . . . 35
2.4.1 Case of a planet on a fixed circular orbit . . . 36
2.4.2 Corotation torque on a migrating planet . . . 39
2.5 Gap opening : a simple approach . . . 41
2.6 Type II migration . . . 43
2.6.1 A first approach . . . 43
2.6.2 Viscous disk evolution . . . 44
2.6.3 Application to type II migration . . . 48

3 Disk surface density transitions as protoplanet traps **49**
3.1 Introduction . . . 49
3.2 A simple analytic estimate . . . 50
3.3 Numerical set up . . . 52

3.4 Results of numerical simulations . . . 52
3.4.1 Torque sampling on a cavity edge . . . 52
3.4.2 Halting migration at a cavity edge . . . 54
3.4.3 Torque sampling at a shallow surface density jump . . . 56
3.4.4 Driving of trapped planets . . . 56
3.4.5 Dissipation and corotation torque saturation . . . 56
3.5 Discussion . . . 61
3.6 Conclusions . . . 65

4 On the width and shape of gaps **67**
4.1 Introduction . . . 67
4.2 First determination of the gap profile . . . 68
4.3 Pressure torque . . . 71
4.3.1 Computation of the torques along the trajectories . . . 71
4.3.2 Torque balance at equilibrium . . . 75
4.4 Gap profiles . . . 78
4.4.1 An explicit equation for the gap profile . . . 79
4.4.2 Note on disk evolution during gap opening . . . 82
4.5 Dependence of gap profiles on viscosity and aspect ratio . . . 82
4.6 A new generalized criterion for gap opening . . . 86
4.7 Discussion . . . 88
4.8 Appendix . . . 89

5 Simulating planet migration in globally evolving disks **95**
5.1 Introduction . . . 95
5.2 Angular momentum conservation in 2D hydrodynamical algorithms . . . 98
5.2.1 Choice of reference frame . . . 99
5.2.2 Sub-steps sequence . . . 101
5.2.3 Action-reaction symmetry . . . 102
5.2.4 Results and discussion . . . 102
5.3 Coupling of the 2D grid with a 1D grid . . . 103
5.3.1 1D equations . . . 104
5.3.2 Ghost rings . . . 105
5.3.3 Fluxes at the interface . . . 107
5.3.4 Results and discussion . . . 110
5.4 Performance of the code . . . 113
5.4.1 Position of the interfaces with respect to the planet. . . . 113
5.4.2 Computational cost . . . 116
5.5 An astrophysical application : Outwards type II migration . . . 118
5.6 Discussion and perspectives . . . 119

6 Type II migration and cavity opening **121**
6.1 Introduction . . . 121
6.2 Evidences for cavities in protoplanetary disks. . . . 122
6.3 Numerical simulations . . . 123
6.3.1 Density profile and cavity opening . . . 123
6.3.2 Migration rate . . . 124

6.4 Interpretation of the density profile . . . 127
6.4.1 Gap opening in an evolving disk . . . 128
6.4.2 Cavity opening . . . 129
6.5 Interpretation of the migration rate: a simple model . . . 133
6.5.1 Classical type II torque . . . 133
6.5.2 Torque exerted on the outer disk by the gas in the gap . . . 134
6.5.3 Corotation torque . . . 135
6.5.4 Total torque exerted on the planet . . . 136
6.5.5 Dependence of the migration rate on inner disk radii . . . 136
6.6 Effect of planet migration on the inner disk depletion . . . 140
6.7 Discussion . . . 141

7 Dynamics of Jupiter and Saturn in the protoplanetary disk 145
7.1 Introduction . . . 145
7.2 The Masset–Snellgrove mechanism . . . 146
7.3 Influence of the disk properties and simulation parameters . . . 149
7.3.1 Dependence on the disk aspect ratio . . . 149
7.3.2 Dependence on the technical parameters of the simulations . . . 153
7.3.3 Dependence on the disk viscosity . . . 154
7.4 The effect of mass accretion onto the planets . . . 156
7.5 Generic two-planet dynamics: dependence on the masses and mass ratio . . . 158
7.6 Possible ratios of orbital periods of Jupiter and Saturn . . . 159
7.7 Summary . . . 163

8 Conclusion 165
8.1 Preventing planetary migration . . . 165
8.2 Placing our work in the general context . . . 166
8.3 Outlining a scheme of Solar System formation . . . 167
8.4 Perspectives . . . 170
8.5 Summary . . . 171

A Papers from the thesis at day of thesis defense 173

B Notations index – Index des notations 175
B.1 Notations index (in english) . . . 175
B.2 Index des notations (en français) . . . 176

C Ackowledgments – Remerciements 177

D Introduction en français 183
D.1 Le Système Solaire . . . 183
D.1.1 Antiquité . . . 183
D.1.2 Les temps modernes . . . 184
D.2 Formation planétaire . . . 186
D.2.1 Formation des étoiles . . . 186
D.2.2 Formation des planètes . . . 188
D.2.3 Formation du système solaire . . . 191
D.2.4 Surprenantes exoplanètes . . . 192

D.3 Interactions planète-disque. 193
D.4 Problématique et plan de la thèse 196
D.4.1 Migration et formation planétaire, problèmes généraux 196
D.4.2 Structure du système solaire et contraintes 197

Bibliography **199**

Chapter 1

Introduction

1.1 The Solar System

1.1.1 Antiquity

The 5 planets of the Solar System visible with the naked eyes (Mercury, Venus, Mars, Jupiter and Saturn) were identified very early in the story of Mankind. They are named "planets" after the Ancient Greek word for "moving celestial body". The ancient Greeks studied their motion in the sky. It appeared that they all moved close to a plane containing the Sun and the Earth : the ecliptic. This is the first notion of the Solar System.

Aristarchus of Samos ($\sim$ 310 BC, figure 1.1), used a very clever reasoning to deduce that the planets, including the Earth, orbit in this plane around the Sun. He had noticed that the Moon shifts with respect to the background stars by a Moon diameter in one hour. As Moon eclipses last at the longest 3 hours, he concluded that the Earth shadow cylinder was three times larger than the Moon, and thus that the Moon was about 3 times smaller than the Earth (in fact, the Moon is about 4 times smaller than the Earth because the shadow of the Earth is not a cylinder but a cone). From geometrical considerations on the lunar phases, he found that the Sun was about 20 times further from the Earth than the Moon (the exact value is 390 times further). Given that the Sun and the Moon have the same apparent angular sizes, the Sun has to be 20 times bigger than the Moon, and thus clearly larger than the Earth. It seemed more logical to him that the smallest object moves around the biggest. However, there is no visible parallax among the stars, which should be the case if the Earth moves. Aristarchus assumed that the stars were infinitely far. This is about right : stars do have an apparent motion due to parallax, but they are too far for this motion to be observable with the naked eye ; the closest star is about 250 000 times further from the Sun than the Earth, so that it is apparently displaced with respect to the other stars by less than an arc-second within a year.

Nevertheless, the most simple explanation for the absence of parallax was that the Earth does not move. The geocentric model proposed by Claudius Ptolemaeus (second century, see figure 1.1) was made of circular coplanar orbits centered on the Earth for the 5 planets, the Moon, and the Sun. However, the planets have a motion in the sky that cannot be explained in this way. They periodically go through apparent retrogradation. Ptolemaeus explained this by the use of epicycles : in his model, a planet rotates on a circle around a point that is itself rotating on a circle around the Earth. The former circle is called an *epicycle* and the latter is named *deferant*. The use of epicycles refines the motions of the planets, and the Ptolemaic system provided reliable ephemerids. In addition, it was supported by theological arguments. In the

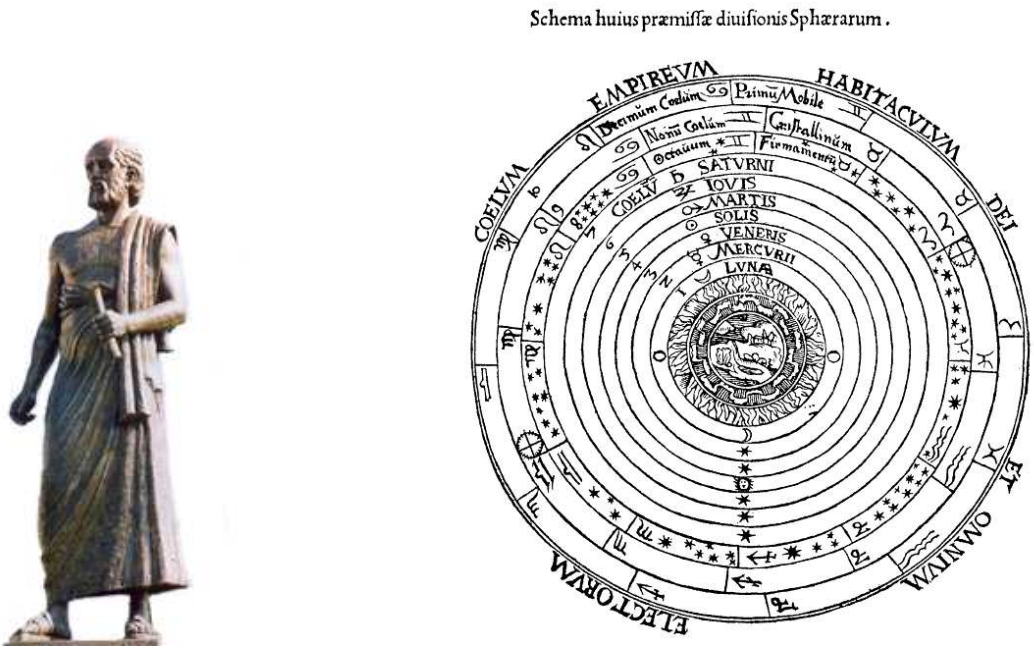

Figure 1.1: Left : Arisartchus of Samos ; Statue at Aristoteles University in Thessaloniki, Greece. Right : The Ptolemaic system ; the Earth is at the center of the Universe.

Aristotelian conception of the world, all should be perfect in the heavens, so that only circles can be used to explain the motion of the celestial bodies. In the Christian religion, God created the Earth and Man on Earth, so they should be at the center of the Universe. For these reasons, the Ptolemaic system became the official theory in Western and Arabic civilizations for more than thirteen centuries.

1.1.2 Modern ages

Copernicus was the first in Europe to suggest that the Earth was not the center of the universe and that the planets (including the Earth) orbit around the Sun (*De Revolutionibus Orbium Cœlestium*, 1543). This finally became an evidence (at least for scientists) in the following decades ; in particular the remarkably precise observations of the motion of Mars by Tycho Brahe (who died in 1601) showed unambiguously that this planet was orbiting following an ellipse (and not a circle) with the Sun at one focus. However, the Danish astronomer was convinced that the Earth was fixed because no parallax was observable among the stars[1]. He imagined a model in which the planets rotate around the Sun, and the Sun rotates around the Earth. Studying Tycho Brahe's observations, Kepler (left portrait in figure 1.3) was finally convinced by heliocentrism. He synthesized his work on the planetary motions into his famous three laws in 1609 and 1618 :

Law on the orbits : The orbit of a planet about the Sun is an ellipse with the star at one focus,

[1]The parallax of the stars has been observed at last in 1838 by Friedrich Wilhelm Bessel. He was the first to use this technique to determine the distance of the binary star 61 Cygni. The position of this star in the sky varies by $0''31$ within a year, which gives a distance of 10.5 light-years. This definitely confirms that the Earth rotates around the Sun.

Figure 1.2: Copernicus, Conversation with God, Painting by Jan Matejko, the greatest historic painter of Poland (1872). One can see the heliocentric system behind the astronomer.

Law of equal areas : A line joining a planet and the Sun sweeps out equal areas during equal intervals of time,

Kepler's third law : The squares of the orbital periods of planets are directly proportional to the cubes of the semi-major axis of the orbits.

The theory of heliocentrism showed that scientific facts could refute the Bible and the religious dogmas, and that a clever reasoning is more powerful than *a priori* intuitions. This contributed to a revolution in philosophy : the age of Enlightenment. Modern science developed, with the aim of finding universal laws to model the mechanics of the world, such as the gravitation law (expressed by Newton in 1687). Once the structure of the Solar System understood, the question of its origin became opportune. This fundamental question was addressed from a philosophical and scientific point of view instead of a religious one. Among various theories that appeared in the eighteenth century, the philosopher Kant in 1755 and the scientist Laplace in 1796 independently proposed that the Solar System could have formed out of a cold disk of gas and dust rotating around the Sun in the ecliptic plane. This hypothesis explained why all the planets have quasi-coplanar, prograde orbits. The discoveries of Uranus by Herschel in 1781 and of Neptune by Le Verrier, Adams, and Galle in 1846 were consistent with this theory, as they also orbit close to the ecliptic plane in the prograde direction. Pluto, with an inclination of 17 degrees, would be a strange planet in this frame of thought ; however, it is simply one of the hundreds of the Kuiper Belt Trans Neptunian Objects and belongs to the category of "dwarfs planets" since I.A.U. meeting in Prague in August 2006.

Kant and Laplace's model for the formation of the Solar System is still the most popular scenario among astronomers. This model has been observationally confirmed and theoretically refined for two centuries. In the following section, we detail the formation of stars with disks around them, and we show how planets are supposed to form in these disks.

Figure 1.3: Kepler, Kant, and Laplace.

1.2 Planetary formation

1.2.1 Star formation

Stellar formation occurs in gas nebulae in the inter-stellar medium. Because of its self-gravitation, a gas cloud of mass above a critical value (the Jeans mass, which is a few solar masses ($M_\odot$) in nebulae) collapses, so that the initial nebula fragments in isolated systems. The collapse lasts about a million years. The pressure and temperature at the center of the cloud increase dramatically, so that the first nuclear fusion reactions begin. This produces a protostar, emitting mostly Infra-Red light, called a *class 0* object. During the cloud collapse, the angular momentum conservation limits the contraction in the plane perpendicular to the rotation axis of the cloud, while nothing prevents gravitational fall in the "vertical" direction. This leads to the formation of a torus around the protostar in about ten thousand years. These Infra-Red source young objects are called *class I* objects. In a hundred thousand years, the torus becomes a disk: its height H is a few percent of the distance to central star r. The *aspect ratio* H/r is between 0.03 and 0.1.

About a million years after its birth, the young star, now called a Classical T-Tauri Star (CTTS), is surrounded by the disk. The latter is heated by the star, and emits an Infra-Red flux. Such an object has the Spectral Energy Distribution [2] of a classical star, with a strong Infra-Red excess. It is called a *class II* object.

Within ten million years, the disk dissipates. Objects with low Infra-Red excess are called *class III* objects, or Evolved T-Tauri Stars, or Weak-line T-Tauri Stars (WTTS).

This chronology comes from observations of the Spectral Energy Distributions of very young stars. They have been classified with regards to their Infra-Red excess. Recently, disks have been imaged by the space telescope (see figure 1.4). These observations confirm that planetary systems form in disks. This imposes a strong constraint on the formation of planets: it has to occur within a period of ten million years at most. The disks surrounding young stars, where planetary formation is supposed to occur, are called *protoplanetary disks*.

[2] The Spectral Energy Distribution is the distribution of the flux radiated by the star as a function of the wavelength of the radiation; for instance, yellow is the dominant wavelength in the Spectral Energy Distribution of the Sun.

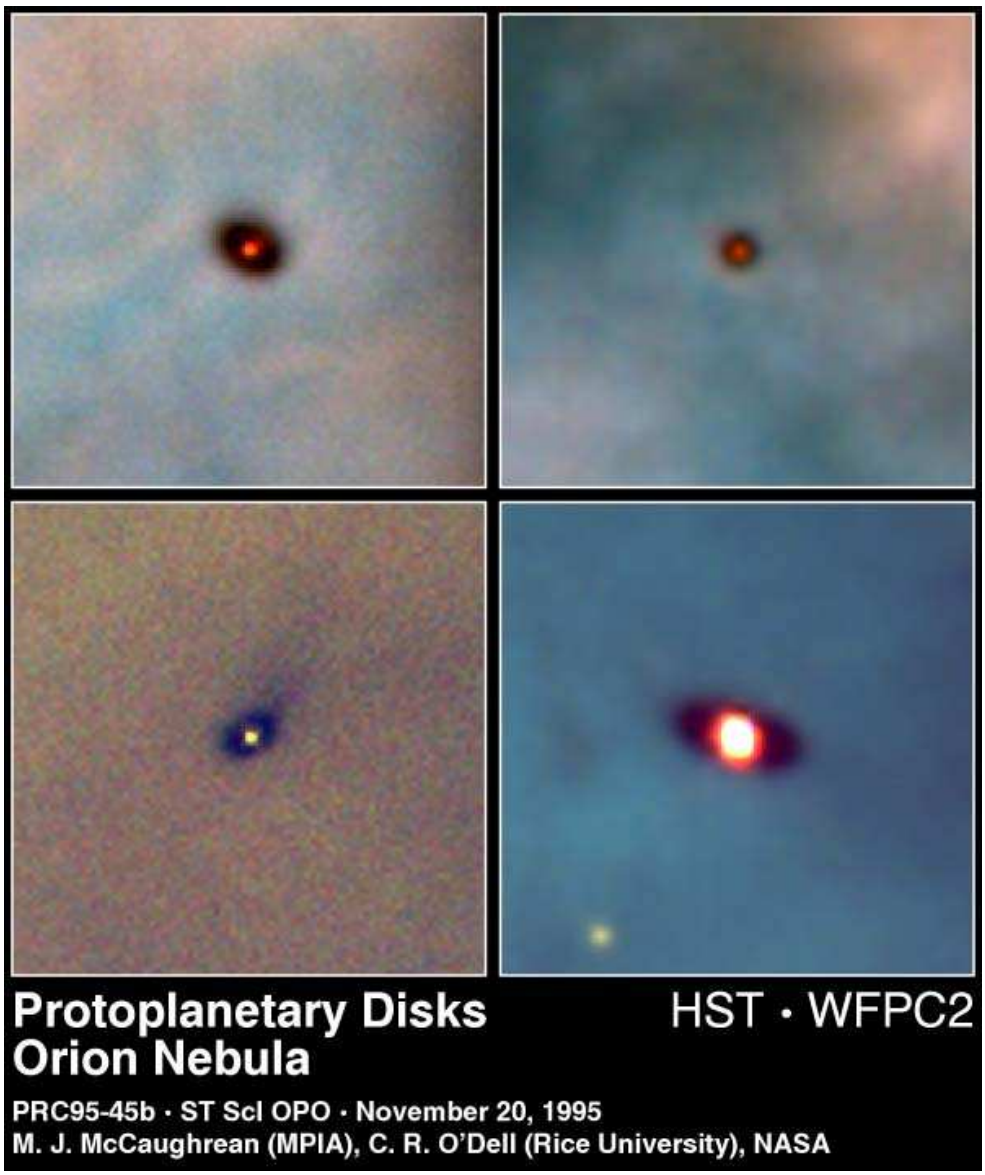

Figure 1.4: Protoplanetary disks in the Orion Nebula, imaged by the Hubble Space Telescope, NASA. The young star is shining at the center, while the disk is dark in visible light.

1.2.2 Planet formation

Let us focus on the protoplanetary disk. If the disk mass $M_{\rm disk}$ is similar to the mass of the central star (noted M_*) or more, instabilities develop, that drive rapid accretion onto the star. The Toomre stability condition reads $Q = \Omega c_s/\pi G\Sigma > 1$, where c_s is the sound speed, G the gravitational constant, and Σ is the surface density of the disk. Making the three assumptions that $c_s = H\Omega$ (which is the classical disk structure), that Σ is constant, and that the angular velocity obeys to Eq. (1.1) below, the Toomre stability parameter reduces to $Q = (H/r)(M_*/M_{\rm disk})$. Then the stability condition is $M_{\rm disk}/M_* < (H/r)$. As H/r is typically a few percents, a massive disk decays in a very short time until its mass is small with respect to the central star mass. Therefore, we consider disks with a mass of less than a tenth of M_*. In such disks, the motion of the gas in the disk is determined by the gravity of the star, and is about Keplerian, with angular velocity Ω given by the third Kepler's law :

$$\Omega = \sqrt{\frac{GM_*}{r^3}} \ . \tag{1.1}$$

From the total mass of the disk and the rotation law, the total angular momentum can be calculated :

$$J = \int_0^{R_{\rm disk}} \Sigma r^2 \Omega \, 2\pi r {\rm d}r = 3 M_{\rm disk} R_{\rm disk}^2 \sqrt{GM_*} \ ,$$

Because the cloud is an isolated system, its angular momentum is conserved during the collapse. From typical estimates of the angular momentum of a cloud and of the mass of the disk, one can estimate that the disk size $R_{\rm disk}$ is about 500 Astronomical Units (AU). We recall that the Astronomical Unit is the radius of the Earth's orbit around the Sun : 1 AU = 150 000 000 kms.

In this disk, one finds mostly Hydrogen and Helium, but also heavy elements (Carbon, Nitrogen, Oxygen, Neon, Magnesium, Silicium, Sulfur, Iron ...), which represent about one percent of the total mass for stars with solar composition. The formation of the planets decomposes in 5 phases, illustrated in figure 1.5 :

(a) Formation of the disk.

(b) Sedimentation : the grains settle down to the equatorial plane of the disk.

(c) Coagulation of the first solids ; growth of planetesimals (kilometer-sized bodies).

(d) Formation of embryos (Moon-sized bodies) by a process named *runaway growth*.

(e) Formation of a planetary system, and gas disappearance.

The transition from molecular grains to planetesimals is not fully understood and we will not detail this. After their formation by runaway growth from planetesimals, embryos collide and merge. They form planetary cores and terrestrial planets on orbits sufficiently separated for the system to be stable (Kokubo and Ida, 2000).

Some of these planetary cores may be massive enough (about 10 terrestrial masses) to accrete a gaseous atmosphere, and become giant gaseous planets like Jupiter and Saturn. The Pollack et al. (1996) model for the formation of giant planets takes place in 3 phases : (i) formation of a massive core (about five hundred thousand years), (ii) slow accretion of gas by the core (several millions of years), (iii) exponential accretion of gas and collapse (about a hundred thousand years) (see figure 1.6). Another model by Boss (1997, 2000) proposes that giant gaseous planets form

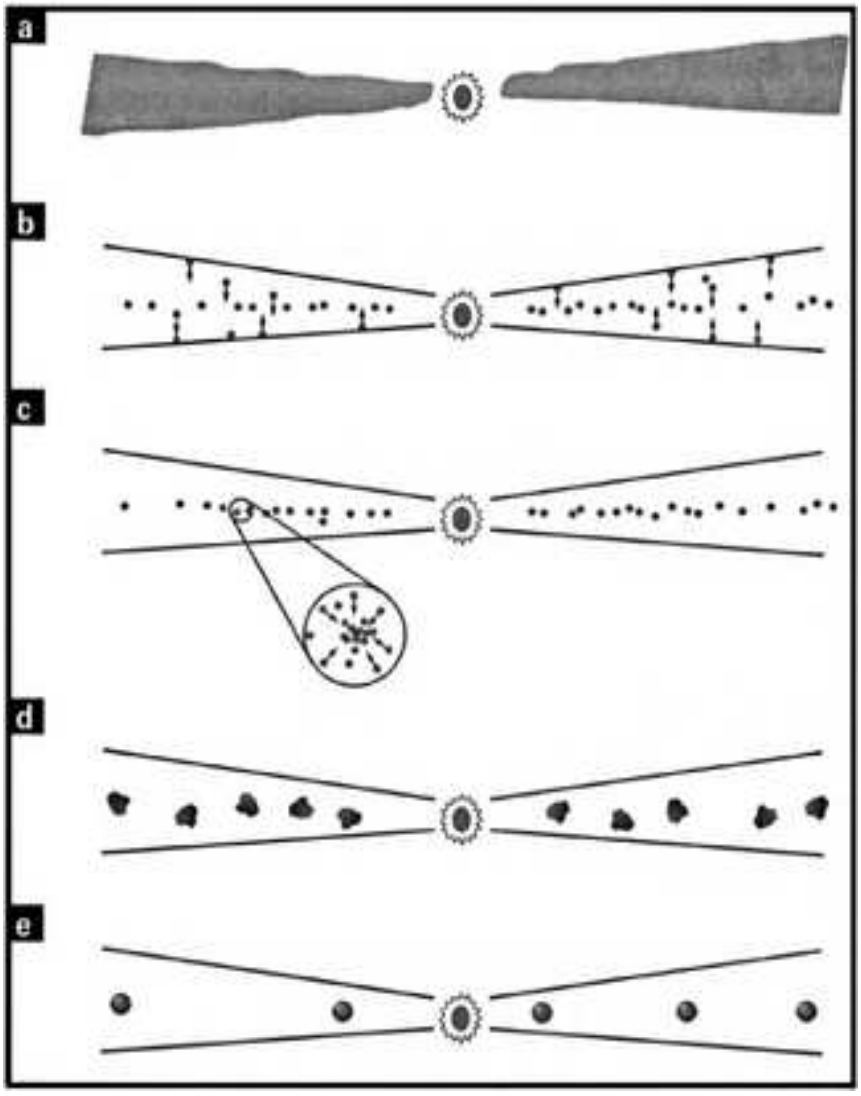

Figure 1.5: Sketch on the five steps of planetary formation inside protoplanetary disks. Drawing from S. Charnoz.

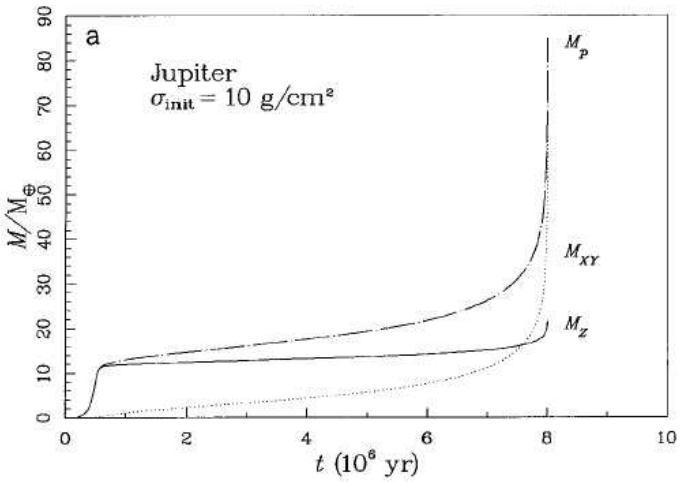

Figure 1.6: Formation of a giant gaseous planet with the core accretion model (from Pollack et al., 1996). The planet mass in Earth masses is plotted with time in million years as the top dot-dashed line labeled M_p; the plain line M_Z corresponds to the mass of solids, while the dotted line M_{XY} represents the mass of gas. After the rapid formation of a $12M_\oplus$ solid core (phase (i)) the slow accretion of gas begins (phase (ii)). Eventually, when the planet reaches $20-30M_\oplus$, a runaway accretion occurs (phase (iii)).

by gravitational instabilities in the protoplanetary gas disk; this has the advantage of forming a planet on a short timescale, without the (too) long second phase of the core accretion model; however, this model hardly explains the observed masses, obliquity, and composition of the giant planets. On the contrary, the core accretion model is supported by the presence of a $10-25$ Earth masses ($M_\oplus$) dense core in Saturn and a $10-15\,M_\oplus$ solid core in Uranus and Neptune. The case of Jupiter is more complex, as it may or may not have a small core of less than about $10\,M_\oplus$ but it may have been eroded away into the envelope (Guillot, 2005). In parallel, Alibert et al. (2005, two papers) propose an accretion model in which the formation timescale is reduced (bringing it in good agreement with typical observed disk lifetimes) and the global compositions of Jupiter and Saturn are reproduced within the uncertainties.

The formation of a massive core requires a great quantity of solids. Thus, it is favored if water, which is an abundant molecule, is under the form of ice instead of vapor. The temperature in the disk is a decreasing function of the distance to the star. Thus, there exists a radius in the disk beyond which water condensates and within which water sublimates. This limit is called the *snow line*; it slowly moves inward as time passes. Around a star like the Sun, the snow line is located at about 3 to 5 AU. This implies that it is easier to form a giant planet just beyond the snow line than close to the parent star. This is consistent with the structure of the Solar System. Another consequence is that planetesimals formed beyond the snow-line are ice-rich, while those formed closer to the Sun are ice-poor. This corresponds to the difference between a comet and an asteroid of the Main Asteroid Belt, once again consistent with the architecture of the Solar System.

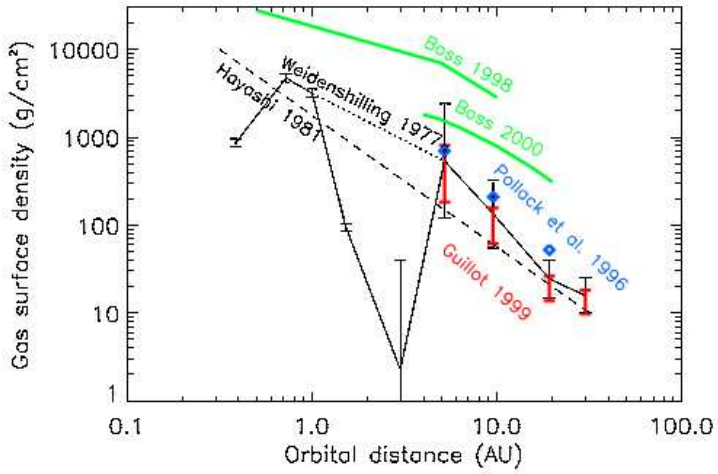

Figure 1.7: The Minimal Mass Solar Nebula density profile (dashed line labeled "Hayashi 1981"). The points represent the constrains given by the masses of the planets. For comparison, the required density for planetary formation with the gravitational instability model is represented as the two upper curves labeled "Boss".

1.2.3 Solar System formation

From the masses and positions of the planets, Hayashi (1981) proposed the concept of a Minimal Mass Solar Nebula (MMSN). The material constituting a planet is spread on an annulus between the orbits of the two neighboring planets, restoring the solar composition. This protoplanetary disk has a density proportional to $r^{-3/2}$ and the same composition as the Sun. Figure 1.7 shows (in logarithmic scale) the density profile of the MMSN (dashed line). The points with the error bars correspond to the density required to form each planet of the Solar System (estimated by different authors). In the MMSN, all the planets of the Solar System are assumed to have formed where they actually orbit.

This theory was extremely satisfactory. It is summed up by four cartoons in figure 1.8. All the mechanisms involved are general enough for planetary systems like ours to be expected around other stars.

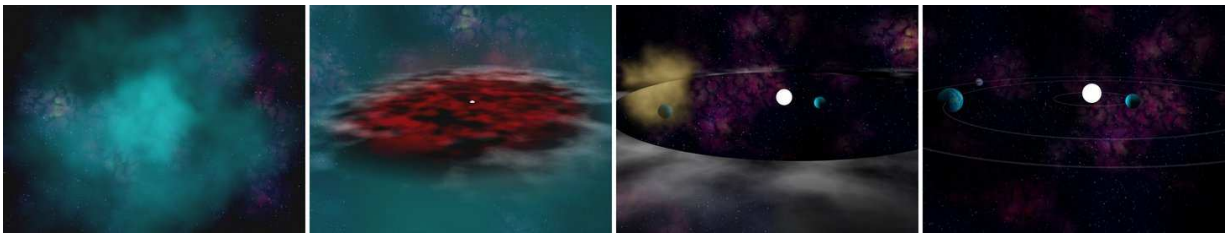

Figure 1.8: Imaged summary of planetary formation. From left to right : a molecular cloud, that collapses into a protostar surrounded by a disk, in which planets form, before the disk dissipates.

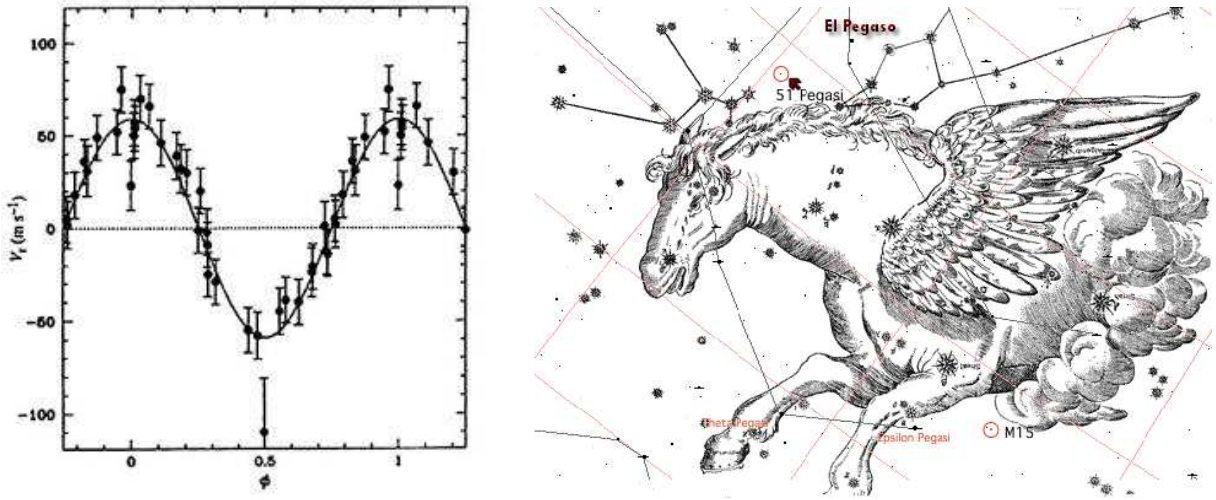

Figure 1.9: Left : Radial velocity variation of the star 51 Pegasi in meters per second, as a function of time in planetary orbits.
Right : Location of 51 Pegasi in the sky, in the constellation of Pegasus.

1.2.4 Surprising Exoplanets

In 1995, the first planet located around another star (*exoplanet*) was detected by Michel Mayor and Didier Queloz at the Haute-Provence Observatory around the star 51 Pegasi. Its detection had been performed using the radial velocity technique. This consists in tracking variations in the velocity of the star in the direction of the line of sight (which can be determined by Doppler effect). If the star has a planetary companion, both the planet and the star rotate around the center of mass of the system. Thus, the planet makes the star approach and move away from the observer. The variations of the radial velocity of 51 Pegasi are shown in figure 1.9 as a function of time in a normalized unit ; there is unambiguously an oscillation of period 1 in this diagram, showing the presence of a planet orbiting around the star with the same period. Given the mass of the star (which can be estimated from its luminosity and color), the orbital period gives the radius of the orbit (third Kepler's law). The amplitude of the star's motion gives the mass of the planet – or more exactly, its mass multiplied by the sine of the inclination angle of its orbital plane with respect to the line of sight.

This first planet to be ever discovered outside the Solar System has a mass of about one half of Jupiter (about 5/3 of Saturn) : it is a giant (gaseous ?) planet. Its orbital period is 4.23 days, so that its orbital radius is only 0.056 AU, about seven times smaller than Mercury's semi-major axis ! This is extremely surprising, and this discovery has been a real thunder clap for most astronomers. Since this date, more than two hundred exoplanets have been discovered. Most of them are *hot* or *warm Jupiters* : giant planets orbiting very close to their parent star. When an exoplanet transits in front of its host star (like Venus did in front of the Sun on June, the 8th, 2004), the diminution of luminosity of the star can be detected and quantified. This can be another way of detecting exoplanets, and it provides the radius of the transiting planet. In addition, in the case of a transiting planet, the orbital plane contains the line of sight, so that the exact mass can be measured with the radial velocity technique. From the radius and mass, the density is easily derived. The thirteen known transiting exoplanets have low density : smaller

than 1 for nine of them, smaller than 1.5 for the other four[3]. Thus, they are gaseous giants; it can be suspected that the other ones are no different.

Ultimately, the Solar System seems to be an exception. However, one should be aware that hot Jupiters are the easiest kind of planets to detect. In truth, present observation techniques allow neither the detection of terrestrial planets, nor of long-period giants. There may be analogs of the Solar System around other stars which are not yet detected. In any case, the Solar System is not a general model for planetary systems.

According to the theory seen above, hot Jupiters could not have formed where they currently orbit. Something must be added to this theory. Actually, the theoretical stage was already set well before the discovery of the first exoplanet (Lin and Papaloizou, 1979, 1986b; Goldreich and Tremaine, 1980). Planets form in the protoplanetary gas disk. They acquire their final mass while they are embedded in this disk. Thus, during planetary formations, there are some planet-disk interactions. In fact, through these interactions, planets typically lose angular momentum and migrate inward. Although models for the local formation of hot Jupiters have been developed (Bodenheimer et al., 2000), radial migration is the generally accepted explanation for the presence of hot Jupiters: they formed beyond the snow line in the disk, and then migrated to their current orbit. The migration processes are presented in the next section.

1.3 Planet-disk interactions

In this section, the nature of the planet-disk interactions and the theory of planetary migration are presented at a descriptive level. A more detailed presentation is done in Chapter 2.

In the frame centered on the central star, with axis pointing at fixed distant stars, the planets and the disk fluid elements rotate around the star, with an angular velocity Ω defined by the third Kepler's law (Eq. (1.1)). This frame is called the *heliocentric frame*. Consider a regular right-hand-side orthogonal coordinate frame centered on the central star, with the x axis always pointing at the planet, and the z axis in the direction of the angular momentum vector of the planet. This frame rotates around the star at the same speed as the planet in the heliocentric frame. It is called the *corotating frame*. In the corotating frame, the planet is motionless; the angular velocity of a fluid element is: $\Omega - \Omega_p$, where the subscript p refers to the planet. In this frame, a period corresponds to the time between two conjunctions with the planet: this is called a *synodic period*. A synodic period is equal to $2\pi/|\Omega - \Omega_p|$. Notice that fluid elements on orbits larger than the planetary orbit have an angular velocity in the heliocentric frame Ω smaller than the one of the planet Ω_p; consequently, they have a negative angular velocity in the corotating frame: they seem to orbit backwards. This is the reason for the absolute value symbol in the expression of the synodic period.

Angular momentum exchanges

The planet perturbs the motion of the fluid elements. At conjunction, a fluid element is deflected by the gravity of planet. This makes it oscillate around its circular, unperturbed orbit. The interferences of these oscillations lead to the formation of a one-armed spiral wave, called the *wake* (see figure 1.10). The wake is a pressure-supported density wave. It is fixed in the corotating frame. It is directed backwards in the outer disk and forwards in the inner disk. The wake overdensity and the planet gravitationally attract each other. Thus, the planet exerts a force on

[3]For comparison, the density of Jupiter is 1.4, the one of Saturn is 0.7, and the one of the Earth is 5.5 .

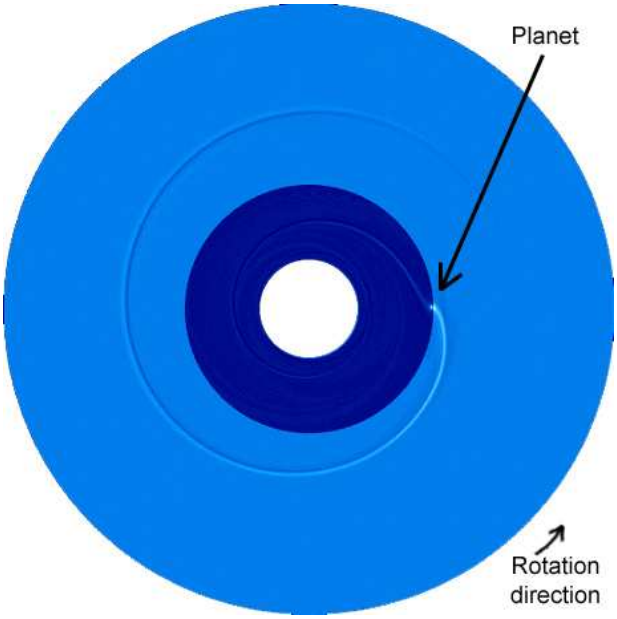

Figure 1.10: A planet on a fixed circular orbit launches a wake in the gas disk. The light blue corresponds to over density. The inner disk has been artificially darkened for distinction between the outer and inner disk.

the outer disk in the direction of the Keplerian rotation, which gives a positive torque. This tends to accelerate the outer disk in the heliocentric frame, and pushes it away from the star. Reciprocally, this slows down the planet in the heliocentric frame, and pushes it toward the star. Symmetrically, the planet exerts a negative torque on the inner disk that tends to slow it down, and pushes it towards the star; reciprocally, the inner disk exerts a positive torque on the planet, and pushes it away from the star. These angular momentum exchanges can be symbolized as below:

$$\text{Inner disk} \xrightarrow[\text{a.m.}]{} \text{Planet} \xrightarrow[\text{a.m.}]{} \text{Outer disk} . \tag{1.2}$$

The torques are proportional to the mass of the planet and to the amplitude of the wake because they are due to the mutual gravitational attraction of the planet and the wake. The wake amplitude is proportional to the planet's mass because it is created by the planet gravity field. Thus, these torques are proportional to the square of the planet's mass.

Type I migration

The effect of the outer disk on the planet is always bigger than the effect of the inner disk by a factor independent of the planet mass, for reasons we will develop in section 2.3. Consequently, the result for the planet is a net negative torque which is proportional to the planet mass squared. Thus, it leads to a decay of specific angular momentum for the planet at a rate proportional to its mass M_p. The specific angular momentum is $j = r^2\Omega = \sqrt{GM_* r}$. Thus, the derivative of j with respect to time is $(\mathrm{d}j/\mathrm{d}t) = \frac{1}{2}\sqrt{GM_*/r}(\mathrm{d}r/\mathrm{d}t) = \frac{1}{2}r\Omega(\mathrm{d}r/\mathrm{d}t)$. As j decreases at a rate proportional to the planet mass, so does r_p. This is called *type I migration.*

Gap opening

The planetary torques push the outer disk outward and the inner disk inward, *id est* away from the planetary orbit. This tends to split the disk into its inner and outer part. However, the gas tends to spread into the void regions and internal stress into the disk naturally makes the profile smooth. These two effects are competing. As the planetary torques are proportional to the square of the planetary mass, it seems logical that if the planet is massive enough, it effectively repels the disk and opens a gap around its orbit. In typical protoplanetary disks, this is the case for giant gaseous planets. The gap opening conditions will be addressed in section 2.5 and Chapter 4.

Type II migration

A planet orbiting inside a clear gap is locked into it. In fact, if the planet approaches the outer disk, it feels a stronger negative torque from it, which repels the planet inward. Symmetrically, if the planet moves inward with respect to the gap, it feels a stronger positive torque from the inner disk, which pushes the planet outward. Contrarily to type I migration, the planet cannot move with respect to the gap and to the disk. Nonetheless, an accretion disk evolves under its own viscosity. Typically, its innermost part tends to accrete onto the central star, while the outermost part spreads outward for angular momentum conservation (see section 2.6.2). Locked into its gap, the planet has to follow this evolution. Most often, the planets location is in the accreting part of the disk (Lin and Papaloizou, 1986b). This leads the planet to migrate inwards. Here, the migration is governed by the viscous evolution of the disk. Thus, the migration rate is proportional to the viscosity (Ward, 1997). This is called *type II migration*.

Type III migration

If the planet opens only a partial gap, the inner and the outer disk are separated by a dip, which is not gas proof. In this regime, the planet can move with respect to the disk. If the planet migrates inward with respect to the dip, it enters into a region which is not depleted. To maintain the dip, the planet takes the gas on the inner edge of the dip and sends it outward. In doing so, the planet transfers angular momentum to the gas. This accelerates its loss of angular momentum, that is its inward migration. Under some conditions, this process leads to an exponential growth of the migration rate. This runaway migration is called *type III migration*.

Type III migration can be inward or outward, depending on the initial conditions. It does not lead to infinitely rapid migration and saturates at some point. However, this can completely change the orbital radius of a planet in a few orbital times.

Stochastic migration

Lastly, in turbulent disks where the density has strong fluctuations, the torque felt by a planet also fluctuates. The result for low planets that do not open gaps is a stochastic migration. One could believe that the stochastic torque only adds to the classical torque. In that case, the fluctuations would only be a noise on the underlying classical type I migration. However, this seems not to be the case in numerical simulations (Nelson, 2005) although the reason is not fully understood. Is type I migration deleted and replaced by a stochastic migration in turbulent disks? This remains an open issue. However, in this work, we are concerned with laminar disks in which the flow is not turbulent. Therefore, we will not expand on this regime.

1.4 Problems and thesis plan

The aforementioned planet-disk interactions show that planets do not necessarily form directly on their final orbit. In fact, they most likely migrate during their growth until the disk dissipates. In this section, we discuss the influence of planetary migration on the planetary formation, with particular attention paid to the Solar System.

1.4.1 Planetary migration and formation, general issues

In type I migration, the more massive the planet, the more rapidly it migrates. The timescale for migration all the way to the central star is shorter than the disk life time for planets more massive than Mars (see Chapter 2 for detailed calculation). This actually constitutes a bottleneck for the theory of planet formation. If it is possible that terrestrial planets formed after the disappearance of the gas, the cores of the giant planets must have accreted in presence of a massive gas disk, given that they captured massive hydrogen atmospheres. The phase (ii) of the core accretion model is very critical: in this phase, the giant planet embryo has a mass of about $20M_\oplus$ and slowly accretes a gaseous atmosphere for several million years. The core is not massive enough to open a gap, but massive enough for type I migration to drive it toward the central star in about a hundred thousand years, that is well before it can accretes its atmosphere (figure 1.6).

Thus, this theory cannot afford for the existence of giant gaseous planets. A possible solution to this problem is discussed in Chapter 3, where we present the idea of a planet trap in the disk. We show that a jump in the gas density on a small distance constitutes a barrier for migrating embryos. Trapped there, embryos could merge and accrete a gaseous atmosphere without suffering type I migration.

Once it has accreted a massive gaseous atmosphere, the planet opens a gap in the disk (which destroys the trap). The gap opening process was not precisely described in literature, and the commonly admitted theory (see section 2.5) was not consistent with numerical simulations. With a novel approach, we found a gap opening criterion that involves at the same time the three parameters of the problem: the planet mass, the disk aspect ratio, and the gas viscosity. This work is the subject of Chapter 4.

If for some reason (the existence of a planet-trap, or other mechanism presented in the literature, or yet to be discovered) a massive core avoids type I migration until it accretes a massive gaseous atmosphere and opens a gap, it should be subject to type II migration. This drives the planet to the star on the timescale of the disk evolution. This explains satisfactorily the presence of hot Jupiters. But this is a new bottleneck for the formation of 'normal' giant planets, including Jupiter, Saturn, and some of the newly discovered exoplanets, at distances of 3-5 AUs from their central star. How can the giant planets avoid type II migration? This question will be addressed in Chapters 6 and 7. We show that under some conditions, the giant planet may decouple from the gas disk evolution. Gas accretion onto the central star may occur through the planetary orbit without pushing the planet inward substantially.

However, before looking for a way of stopping type II migration, a performing tool for reliable numerical simulations of this type of migration had to be elaborated. In classical hydrodynamical codes, only a limited part of the disk is considered, for evident reasons of computing cost. Thus, the global evolution of the disk, that governs type II migration, cannot be taken into account. To solve this problem, we have improved the classical scheme, by surrounding the studied annulus with a simplified mesh in which the disk evolution can be computed all over the disk extent, for almost no additional computing cost. This algorithm is presented in Chapter 5.

1.4.2 Solar System structure and constraints

The complex structure of the Solar System imposes strong constraints on the possible migration of Jupiter and Saturn. The properties of the Main Asteroid Belt between Jupiter and Mars, in particular its quite tight zoning of taxonomic types, show that Jupiter never orbited in this region. Otherwise, the giant planet would have depleted the belt and mixed the surviving asteroids much more than observations show. Another belt in the Solar System, called the *Kuiper Belt*, is located around 40 AUs from the Sun, beyond the orbit of Neptune. The Kuiper Belt has even a richer orbital structure than the Asteroid Belt ; in particular, the existence of a 'cold' population excludes the passage of a massive planet through that zone. Thus, the 4 giant planets, presently orbiting at 5.2, 9.6, 19 and 30 AUs, must have formed between 4 and 35 AUs. There is almost no room for type II migration in the Solar System.

To be more precise, a recent model elaborated in Nice in 2004 and published in 3 articles in Nature (Tsiganis et al., 2005; Gomes et al., 2005; Morbidelli et al., 2005) imposes even stronger constraints. This model assumes an initial compact configuration of the outer Solar System. After the gas disk disappearance, the 4 giants should be on circular coplanar orbits of radii about 5.45, 8.2, $11-13$, and $14-17$ AUs. In particular, Saturn is assumed to be closer to Jupiter than their mutual 1:2 Mean Motion Resonance (where Saturn's period is exactly twice of Jupiter's one, and thus its orbital radius is 1.6 Jupiter's one). A disk of planetesimals is assumed to exist from about 1.5 AU beyond the location of the outermost planet, up to $\sim$ 35 AU, with a total mass of $\sim 35 M_\oplus$. With this setting, the planetesimals at the inner edge of the disk acquire Neptune scattered orbits on a timescale of a few million years. Consequently, they encounter the giant planets and are scattered, which on average makes Saturn, Uranus, and Neptune migrate outwards while Jupiter migrates inwards. This proceeds at very slow rate, governed by the slow escape rate of planetesimals from the disk. This slow migration continues for hundreds of millions of years, until Jupiter and Saturn cross their mutual 1:2 resonance. This resonance crossing excites their eccentricities, which destabilizes the planetary system as a whole. The planetary orbits become chaotic and start to approach each other. Both Uranus and Neptune are scattered outward, onto large eccentricity orbits ($e \sim 0.3$–0.4) that penetrate deeply into the disk. This destabilizes the full planetesimal disk and triggers the Late Heavy Bombardment (LHB). The LHB is a cataclysmic period characterized by huge impact rates on all planets which is supposed to explain the lunar basins ; it occurred between 4.0 and 3.8 billion years ago (namely about 600 million years after planet formation). The interactions with the planetesimals damp the planetary eccentricities, stabilizing the planetary system once again, and forcing a residual short radial migration of the planets. The planets eventually reach their final orbits when most of the disk has been eliminated. Simulations show that this model may explain the current orbital architecture of the giant planets of the Solar System, in particular their eccentricity and radial spacing.

If this model is right, it is clear that during their formation inside the disk, Jupiter, Saturn, Uranus and Neptune hardly suffered any type II migration. In addition, Jupiter and Saturn most likely orbited inside the 2:1 MMR on circular orbits after the disk disappearance. In Chapter 7, we explore in detail a mechanism, first presented by Masset and Snellgrove (2001), that may stop or reverse type II migration provided the two planets are close enough and the outer one is lighter than the inner one. In the particular case of Jupiter and Saturn, we obtain a stationary solution for some reasonable disk parameters, with Saturn inside the 2:1 Mean Motion Resonance with Jupiter.

Finally, in the concluding remarks of this thesis, we speculate on a scenario of formation of

the outer Solar System that seems consistent from the point of view of dynamics, at the light of what we have learned.

Chapter 2

Torques calculation

In this chapter, we summarize previous work on planet-disk interactions to provide the fundamental information that will be useful for the remainder of this thesis. The planet is considered on a circular orbit.

In section 2.1, we review the basic equations of the fluid mechanics, and the viscous torque in a Keplerian disk is derived. The torques exerted by a planet on the protoplanetary disk are quantified in section 2.2, using two different methods. In section 2.3, we show why the inner torque is smaller than the outer torques, which leads to type I migration. Then, the corotation torque is computed and the influence of the horseshoe drag on planetary migration is discussed in section 2.4; the runaway type III migration regime is explained. From the viscous and planetary torques expressions, the opening of a gap is discussed, and an elementary gap opening condition is derived in section 2.5. The type II migration time scale is evaluated in section 2.6, and the global viscous disk evolution is computed.

2.1 Fluid mechanics

2.1.1 Notations and prerequisite in fluid mechanics

Consider a continuous medium in which all quantities depend on time t and position $\vec{r}$. The sum of the forces exerted on the medium from external agents (like gravity) per mass unit is denoted $\vec{F}$. The symbol ∇ is the divergence operator. The gradient operator is denoted $\vec{\nabla}$. The partial derivative is noted $\frac{\partial}{\partial i}$ or ∂_i, where i is a coordinate or time. The total derivative with respect to time is denoted $\frac{\mathrm{D}}{\mathrm{D}t}$. The velocity is denoted $\vec{v} = \frac{\mathrm{D}}{\mathrm{D}t}\vec{r}$. The link between the partial and the total derivations reads:

$$\frac{\mathrm{D}}{\mathrm{D}t} \equiv \frac{\partial}{\partial t} + \vec{v}.\vec{\nabla} \ ,$$

where $\vec{v}.\vec{\nabla}$ is the operator: scalar product of the velocity and the gradient. For instance in two dimensional Cartesian coordinates, with A a scalar field, $\vec{v}.\vec{\nabla}A = \vec{v}.(\vec{\nabla}A) = v_x\,\partial_x A + v_y\,\partial_y A$.

The *strain tensor* is the matrix defined in Cartesian coordinates by $\bar{\bar{D}}_{ik} = \frac{1}{2}(\partial_i v_k + \partial_k v_i)$, where the indexes i and k go through the coordinates. It is a sort of measure of the shear. The general definition of $\bar{\bar{D}}$ is: the symmetrical part of the gradient of the velocity (the velocity being a vector, its gradient is a matrix whose columns are the gradients of the components of the velocity):

$$\bar{\bar{D}} = \frac{1}{2}\left(\vec{\nabla}\vec{v} + {}^t\vec{\nabla}\vec{v}\right) \ . \tag{2.1}$$

From the strain tensor, denoting $\bar{\bar{I}}$ the identity matrix, the *viscous stress tensor* reads:

$$\bar{\bar{d}} = 2\Sigma\nu\left(\bar{\bar{D}} - \frac{1}{3}(\nabla\vec{v})\bar{\bar{I}}\right) + \Sigma\zeta(\nabla\vec{v})\bar{\bar{I}}\ , \tag{2.2}$$

with Σ the density (surface density in 2D), ν the shear viscosity, and ζ the bulk viscosity (most often considered null in the context of interest here).

The *stress tensor* is denoted $\bar{\bar{\sigma}}$ and describes the physical stress exerted on the medium. The definition of a *fluid* is that its stress tensor is a function of its strain tensor. For instance, it can be the viscous stress tensor. More generally, denoting by P the pressure, the stress tensor reads:

$$\bar{\bar{\sigma}} = \bar{\bar{d}} - P\bar{\bar{I}}\ . \tag{2.3}$$

The two fundamental equations of fluid mechanics are:

Continuity equation (mass conservation):

$$\frac{\partial}{\partial t}\Sigma + \nabla.(\Sigma\vec{v}) = 0 \tag{2.4}$$

Momentum equation (momentum conservation):

$$\Sigma\frac{\mathrm{D}\vec{v}}{\mathrm{D}t} = \Sigma\vec{F} + \nabla\bar{\bar{\sigma}} \tag{2.5}$$

The stress tensor being a matrix, its divergence is a vector defined by: $(\nabla\bar{\bar{\sigma}})_i = \sum_k \partial_k\bar{\bar{\sigma}}_{ik}$. The divergence of the stress tensor corresponds to a force per unit volume. It describes the internal stress in the medium. For instance, $\nabla\left(-P\bar{\bar{I}}\right) = -\vec{\nabla}P$, which is the pressure force per unit volume. The divergence of the strain tensor reads, with ∇^2 the Laplacian operator:

$$\nabla\bar{\bar{D}} = \frac{1}{2}\left(\nabla^2\vec{v} + \vec{\nabla}(\nabla\vec{v})\right) \tag{2.6}$$

Proof in Cartesian coordinates:

$$\begin{aligned}
(\nabla\bar{\bar{D}})_i &= \sum_k \partial_k\bar{\bar{D}}_{ik} \\
&= \sum_k \partial_k\left(\frac{1}{2}(\partial_i v_k + \partial_k v_i)\right) \\
&= \frac{1}{2}\sum_k\left(\partial_k\partial_i v_k + \partial_k{}^2 v_i\right) \\
&= \frac{1}{2}\left(\partial_i\left(\sum_k \partial_k v_k\right) + \sum_k \partial_k{}^2 v_i\right) \\
&= \frac{1}{2}\left(\partial_i\left(\nabla\vec{v}\right) + \nabla^2 v_i\right) \\
&= \frac{1}{2}\left(\vec{\nabla}\left(\nabla\vec{v}\right) + \nabla^2\vec{v}\right)_i
\end{aligned}$$ □

From Eq. (2.5), using Eqs. (2.2), (2.3), and (2.6), we come to the vectorial form of the **Navier-Stokes equation:**

$$\frac{\mathrm{D}\vec{v}}{\mathrm{D}t} = \nu\nabla^2\vec{v} + (\zeta + \frac{1}{3}\nu)\vec{\nabla}(\nabla\vec{v}) - \frac{1}{\Sigma}\vec{\nabla}P + \vec{F} \tag{2.7}$$

2.1.2 Polar coordinates

In polar coordinates and in 2 dimensions (r, θ), the expression for the divergence of a vector field $\vec{A}$ is:

$$\nabla \vec{A} = \frac{1}{r}\frac{\partial}{\partial r}(rA_r) + \frac{1}{r}\frac{\partial}{\partial \theta}A_\theta \ .$$

Denoting by $\vec{e_r}$ and $\vec{e_\theta}$ the unitary vectors in the polar base, the gradient of a scalar field A reads:

$$\vec{\nabla} A = (\partial_r A)\, \vec{e_r} + \left(\frac{1}{r}\partial_\theta A\right) \vec{e_\theta} \ .$$

The strain tensor expression is:

$$\begin{aligned} \bar{\bar{D}}_{rr} &= \frac{\partial v_r}{\partial r} \\ \bar{\bar{D}}_{r\theta} = \bar{\bar{D}}_{\theta r} &= \frac{1}{2}\left(\frac{1}{r}\frac{\partial v_r}{\partial \theta} + r\frac{\partial (v_\theta / r)}{\partial r}\right) \\ \bar{\bar{D}}_{\theta\theta} &= \frac{1}{r}\frac{\partial v_\theta}{\partial \theta} + \frac{v_r}{r} \ . \end{aligned} \tag{2.8}$$

Last, the total derivative of the velocity with respect to time is:

$$\begin{aligned} \frac{\mathrm{D}\vec{v}}{\mathrm{D}t} &= \frac{\mathrm{D}}{\mathrm{D}t}\left(v_r \vec{e_r} + v_\theta \vec{e_\theta}\right) \\ &= \frac{\mathrm{D}\, v_r}{\mathrm{D}t}\vec{e_r} + v_r \frac{\mathrm{D}\vec{e_r}}{\mathrm{D}t} + \frac{\mathrm{D}\, v_\theta}{\mathrm{D}t}\vec{e_\theta} + v_\theta \frac{\mathrm{D}\vec{e_\theta}}{\mathrm{D}t} \\ \frac{\mathrm{D}\vec{v}}{\mathrm{D}t} &= \left(\partial_t v_r + v_r \partial_r v_r + \frac{v_\theta}{r}\partial_\theta v_r\right)\vec{e_r} + v_r \frac{v_\theta}{r}\vec{e_\theta} + \left(\partial_t v_\theta + v_r \partial_r v_\theta + \frac{v_\theta}{r}\partial_\theta v_\theta\right)\vec{e_\theta} + v_\theta \frac{-v_\theta}{r}\vec{e_r} \end{aligned}$$

$$\frac{\mathrm{D}\vec{v}}{\mathrm{D}t} = \begin{pmatrix} \partial_t v_r + v_r \partial_r v_r + \dfrac{v_\theta}{r}\partial_\theta v_r - \dfrac{{v_\theta}^2}{r} \\ \\ \partial_t v_\theta + v_r \partial_r v_\theta + \dfrac{v_\theta}{r}\partial_\theta v_\theta + \dfrac{v_r v_\theta}{r} \end{pmatrix} \ . \tag{2.9}$$

2.1.3 Viscous torque in a Keplerian disk

In a disk in Keplerian rotation, $v_r = 0$ and $v_\theta = r\Omega(r)$. Thus, $\nabla \vec{v} = 0$. Therefore, from Eqs. (2.2), (2.3) and (2.8), the stress tensor reads:

$$\bar{\bar{\sigma}} = 2\Sigma\nu\bar{\bar{D}} = \Sigma\nu \begin{pmatrix} 0 & -\Omega + \partial_r(r\Omega) \\ -\Omega + \partial_r(r\Omega) & 0 \end{pmatrix} = \Sigma\nu \begin{pmatrix} 0 & -\frac{3}{2}\Omega \\ -\frac{3}{2}\Omega & 0 \end{pmatrix}$$

The torque exerted by a given domain S of fluid on its complementary part S^c through its border $\mathcal{S}$ reads:

$$T = \int\int_{S^c} (\vec{r} \wedge (\nabla \bar{\bar{\sigma}}))\, \mathrm{d}s = \int_{\mathcal{S}} \vec{r} \wedge (\bar{\bar{\sigma}}\, \mathrm{d}l\, \vec{n})$$

where $\mathrm{d}s$ is an elementary surface, while $\mathrm{d}l$ is an elementary length and $\vec{n}$ is the unitary vector normal to $\mathcal{S}$ directed inside S. In the case where S is the centered disk of radius r_0, this gives:

$$T_\nu = 3\pi {r_0}^2 \Omega_0 \Sigma\nu \tag{2.10}$$

2.2 Planetary torque

In this section, the torque exerted by the planet on the outer disk (or the inner disk) is evaluated. This quantifies the arrows in the sketch (1.2). Two different methods are mentioned, which lead to the same result.

2.2.1 Impulse approximation

This approach has been performed by Lin and Papaloizou (1979). At conjunction with the planet, a fluid element trajectory is deflected by the gravity of the planet. Assuming the encounter is brief enough for the rotation around the Sun to be neglected, the planet and the fluid element are considered on a uniform straight motion. We switch to the frame centered on the planet, like in figure 2.1. The deflection angle of the fluid element β is given by :

$$\beta = 2 \arctan\left(\frac{GM_p}{b{v_0}^2}\right) , \tag{2.11}$$

where v_0 is the relative velocity between the planet and the fluid element, and b is the impact parameter, as shown in figure 2.1.

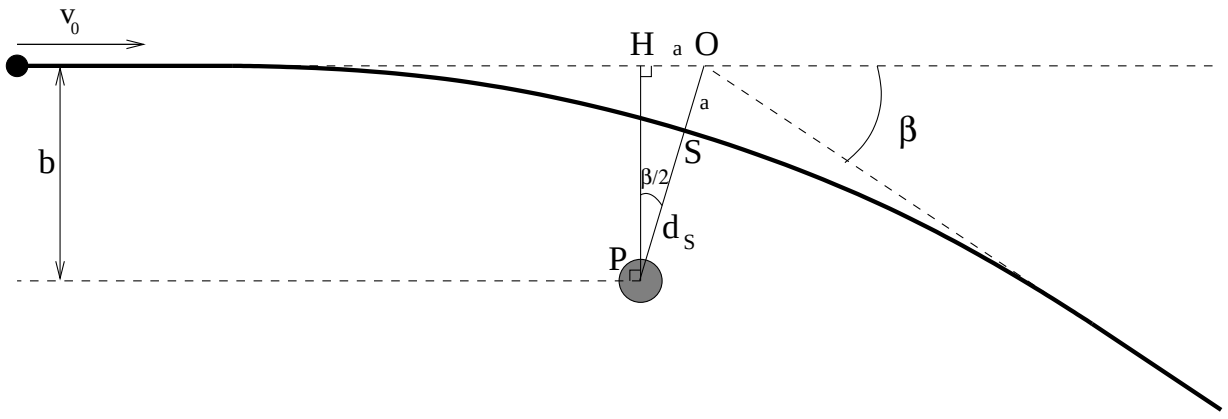

Figure 2.1: Scheme of an encounter with the planet (grey circle centered on P). A test particle incoming from infinity with a velocity v_0 and an impact parameter b follows the hyperbolic trajectory plotted as a bold line. It is deflected by an angle β.

Proof : Consider the planet as fixed, and a test particle of mass m incoming from infinity with an impact parameter b and a velocity v_0. The only force exerted on the particle is directed toward the planet, thus the particle trajectory is a conic. The total energy of the particle E is the sum of its kinetic energy ($E_k = \frac{1}{2}mv^2$) and of its potential energy in the gravity field of the planet ($E_p = -\frac{GM_pm}{d}$, where d is the distance between the planet and the particle). The total energy is conserved. Its initial value is $E = \frac{1}{2}m{v_0}^2$. It is positive, thus the trajectory is an hyperbola, with the planet at a focus.

In figure 2.1, the point S is the summit of the hyperbola. For symmetry reasons, the velocity of the particle in S is perpendicular to the direction of the planet. The angular

momentum with respect to the planet is conserved through out the trajectory, because the force exerted on the particle is directed to the planet and exerts no torque. This gives:

$$d_s v_s = b v_0 \ .$$

Energy conservation along the trajectory gives:

$$\frac{1}{2} m {v_0}^2 = \frac{1}{2} m {v_S}^2 - \frac{G M_p m}{d_S}$$

With $X = \dfrac{G M_p}{b {v_0}^2}$, these two equations lead to:

$$ {d_S}^2 + 2bX\, d_S - b^2 = 0 \ . \tag{2.12}$$

Denoting a the parameter of the hyperbola such that $P'M - PM = 2a$ for any point M on the hyperbola where P' is the second focus (which is the symmetric of P with respect to O), one has $OS = a = OH$. Then, from the Pythagorean Theorem in the triangle OHP, $b^2 + a^2 = (d_S + a)^2$, which, using Eq. (2.12) gives $a = bX$.

The geometrical angle $\widehat{OPH}$ is equal to the angle between the initial direction of the particle trajectory and its direction at S. It is half of the deviation: $\widehat{OPH} = \beta/2$.

Thus, $\tan(\dfrac{\beta}{2}) = \dfrac{a}{b} = X$. □

After deflection, the fluid element in the disk has no longer a circular trajectory around the central star, but it has acquired some eccentricity. The combination of the perturbed trajectories of the fluid elements leads to the formation of a one armed spiral density wave, the *wake* (see figure 1.10). The interactions between the fluid elements in the disk also circularize the trajectories. After the deflection, a fluid element recovers slowly its initial circular motion. It is assumed that this occurs within a synodic period (*id est* before the next conjunction with the planet).

The exchange of angular momentum with respect to the central star between the planet and the outer disk can be calculated using Eq. (2.11). During the encounter with the planet, the direction of the velocity of the fluid element relative to the planet is changed, but not its value. Thus, in the frame centered on the planet, the change of specific angular momentum with respect to the star (j) for a fluid element is: $\delta j = r v(\cos\beta - 1)$, where r is the radius of its orbit around the star ($r = r_p + b$). Under our assumption that the planet has a uniform straight motion, δj is also the change of angular momentum in the frame centered on the star. We have $v = r(\Omega - \Omega_p)$. The deflection angle is small, so that $\cos\beta - 1 = -\beta^2/2 = -2\frac{G^2 M_p^2}{b^2 v^4}$. Finally, one gets:

$$\delta j = -2r\frac{G^2 M_p^2}{b^2 v^3} = -\frac{2G^2 M_p^2}{r^2 b^2 (\Omega - \Omega_p)^3} \ .$$

This is the expression of the loss of specific angular momentum during one encounter with the planet. Such an encounter occurs every synodic period. Thus, the rate of loss of specific angular momentum reads:

$$\frac{\delta j}{\delta t} = \frac{\delta j}{2\pi/|\Omega - \Omega_p|} = \frac{G^2 M_p^2}{\pi r^2 b^2 (\Omega - \Omega_p)^2}.$$

To derive the total torque exerted on the outer disk, Lin and Papaloizou (1993) make a Taylor expansion of Ω :

$$\Omega - \Omega_p \approx \frac{\mathrm{d}\Omega}{\mathrm{d}r} b \approx -\frac{3}{2}\frac{\Omega_p}{r} b$$

From this approximation, and considering $r = r_p$, they derive the total torque exerted by the gravity of the planet on the outer disk extending from $r = r_p + \Delta$ to infinity, for any $\Delta > 0$. An integration in polar coordinates over this domain gives :

$$\begin{aligned}
T_g &= \int_{r_p+\Delta}^{\infty} \int_0^{2\pi} \frac{\delta j}{\delta t} \Sigma \, r \mathrm{d}\theta \, \mathrm{d}r \\
&= \int_{\Delta}^{\infty} 2\pi r \frac{\delta j}{\delta t} \Sigma \, \mathrm{d}b \\
&= \int_{\Delta}^{\infty} \frac{2\pi \Sigma r G^2 M_p^2}{\pi r^2 b^4 \left(\frac{3}{2}\frac{\Omega_p}{r}\right)^2} \mathrm{d}b \\
&= \frac{8}{9} \Sigma r_p \frac{G^2 M_p^2}{{\Omega_p}^2} \int_{\Delta}^{\infty} \frac{\mathrm{d}b}{b^4} \\
&= \frac{8}{9} \Sigma {r_p}^4 \frac{G^2 M_p^2}{G M_*} \frac{1}{3\Delta^3} \\
T_g &= \frac{8}{27} \Sigma {r_p}^4 \left(\frac{M_p}{M_*}\right)^2 \frac{G M_*}{{r_p}^3} \frac{{r_p}^3}{\Delta^3}
\end{aligned}$$

$$T_g = \frac{8}{27} q^2 \, \Sigma \, {r_p}^4 \, {\Omega_p}^2 \, \frac{{r_p}^3}{\Delta^3} \, , \tag{2.13}$$

where $q = M_p/M_*$ is the planet to primary mass ratio. This estimate is not exact because of the two approximations mentioned, which are obviously not valid when r tends to infinity. However, when r tends to infinity, the term b^{-4} tends to zero, so that the errors made using these approximations vanish. Based on simple considerations, this calculation provides a correct result. It corresponds to the total torque exerted by the planet on the part of the disk extending from $r_p + \Delta$ to infinity. For the torque exerted on the part of the disk extending from 0 to $r_p - \Delta$ (in the inner disk), just reverse the sign.

This calculation relies on the impulse approximation. Thus, Eq. (2.13) is not valid for too small Δ otherwise the encounter is too slow for the impulse approximation to be justified. In a gaseous disk, if the relative velocity is smaller than the sound speed, the gas particle is aware of the presence of the planet before the encounter, because of pressure effects. Thus, the minimal Δ is the distance to planetary orbit at which the relative velocity is equal to the sound speed c_s. This makes $\Delta_{\min} = c_s |\mathrm{d}\Omega/\mathrm{d}r|^{-1}$. With $c_s = H\Omega$, which is the usual relation in astrophysical disks, it makes $\Delta_{\min} = \frac{2}{3}H$. Refining the model, and using this values of $\Delta_{\min}$ Papaloizou and Lin (1984) find that the total torque exerted by the planet on the outer disk reads (their Eq. (4.21)) :

$$T_g \approx 0.23 \, q^2 \, \Sigma \, {r_p}^4 \, {\Omega_p}^2 \, \frac{{r_p}^3}{H^3} \, , \tag{2.14}$$

2.2.2 Lindblad Resonances

Definition of a Lindblad Resonance

A Lindblad Resonance with a perturbing potential occurs when the pattern speed of the perturbation is equal or opposite to the epicyclic speed κ. The epicyclic frequency is the rotation frequency around the epicycle, that is the frequency of the periastron passages on an eccentric orbit (the *periastron* is the closest point to the central object). This resonance increases the eccentricity and enables angular momentum exchange. In Keplerian motion, the epicyclic frequency is equal to the orbital frequency: $\kappa = \Omega$.

In the case of a planet in a gas disk, the perturbation is the gravitational potential of the planet $\Phi_p = -\frac{GM_p}{d}$ where d is again the distance from the planet. In polar coordinates centered on the star, $\Phi_p(r,\theta)$ is a 2π-periodic function of θ. Thus, it can be decomposed into Fourier series of the variable $(\theta - \theta_p)$, where θ_p is the azimuth of the planet. Assuming that the planet is on a circular orbit, $\theta_p = \Omega_p t$, and the Fourier series of Φ_p reads:

$$\Phi_p(r,\theta,t) = \Re\left(\sum_{m\in\mathbb{N}} \hat{\Phi}_p^m\right) \tag{2.15}$$

where $\Re$ denotes the real part of a complex number and:

$$\hat{\Phi}_p^m = \Phi_p^m(r)\exp\left(im(\theta-\theta_p)\right) = \Phi_p^m(r)\exp\left(im(\Omega-\Omega_p)t\right) \ . \tag{2.16}$$

As $\Phi_p(r,\theta,t)$ is an even function of $(\theta - \theta_p)$, $\Phi_p^m(r)$ is real. The expression of $\Phi_p^m(r)$ is (Goldreich and Tremaine, 1980):

$$\Phi_p^m(r) = -\frac{GM_p}{2r_p}\, b_{1/2}^{(m)}\left(\frac{r}{r_p}\right) \ , \tag{2.17}$$

where $b_{1/2}^{(m)}(x)$ is the Laplace coefficient defined by: $b_\gamma^{(m)}(x) = \dfrac{2}{\pi}\displaystyle\int_0^\pi \cos(m\phi)(1+x^2-2x\cos\phi)^{-\gamma}\,\mathrm{d}\phi$.
It appears that each of these components has a pattern speed $\tilde{\omega} = m(\Omega - \Omega_p)$. Thus, Lindblad resonances correspond to:

$$m(\Omega-\Omega_p) = \pm\Omega$$

$$\Leftrightarrow \Omega = \frac{m}{m\pm 1}\Omega_p \ . \tag{2.18}$$

For all $m > 2$, there are two Lindblad resonances of order m. The inner one corresponds to $\Omega(r) = \frac{m}{m-1}\Omega_p > \Omega_p$, and the outer one corresponds to $\Omega(r) = \frac{m}{m+1}\Omega_p < \Omega_p$. For $m = 1$, there is only an outer Lindblad resonance. Note that at a Lindblad resonance, the fluid elements are in Mean Motion Resonance with the planet: while they describe m orbits around the central star, the planet describes $m \pm 1$ orbits.

In a gas disk, the effect of a m-order Lindblad resonance is the launching of an m-fold pressure-supported wave, which obeys the dispersion relation:

$$\tilde{\omega}^2 = \kappa^2 + {c_s}^2 k^2 \ , \tag{2.19}$$

where again c_s is the sound speed and k is the wave number. The wave number decomposes into a radial and an azimuthal part: $k^2 = {k_r}^2 + {k_\theta}^2$; the latter is 2π over the wavelength in the

azimuthal direction, which is $2\pi r/m$. Thus, using $c_s = H\Omega$, one gets ${c_s}^2 k^2 \geq m^2\Omega^2(H/r)^2$. This means that the waves do not reach the nominal resonance location given by Eq. (2.18), but are launched at the effective radius r_m such that:

$$\tilde{\omega} = m(\Omega(r_m) - \Omega_p) = \mp\Omega(r_m)\left[1 + m^2(H/r)^2\right]^{1/2} \quad . \tag{2.20}$$

When m tends to infinity, this makes $m(1-(H/r))\Omega = m\Omega_p$ and thus:

$$\lim_{m\to\infty} r_m = r_p \pm \frac{2}{3}H \ , \tag{2.21}$$

where the upper sign corresponds to outer resonances, while the lower sign is for inner resonances. This convention is adopted from now on.

Application to the planetary torque

The expression of the torque exerted by the planet potential can be decomposed in the torques exerted at each Lindblad Resonance.

Proof: The surface density Σ can also be decomposed in Fourier series of $(\theta - \theta_p)$; however, its coefficients $\Sigma^m(r)$ are not necessarily real. In the following calculation, $\Im(z)$ and $\bar{z}$ denote respectively the imaginary part and the complex conjugate of any complex number z. The torque exerted on the disk by the perturbing potential Φ_p given by Eqs. (2.15) and (2.16) is naturally:

$$\begin{aligned}
T &= \left(\int_0^\infty\int_0^{2\pi} (\vec{r}\wedge\vec{\nabla}\Phi_p)\Sigma\, r\mathrm{d}\theta\,\mathrm{d}r\right).\vec{e_z} \\
&= \int_0^\infty\int_0^{2\pi} r\left(\frac{1}{r}\partial_\theta\Phi_p\right)\Sigma\, r\mathrm{d}\theta\,\mathrm{d}r \\
&= \int_0^\infty\int_0^{2\pi} \Re\left(\sum_{m\in\mathbb{N}} im\hat{\Phi}_p^m\right)\Re\left(\sum_{m\in\mathbb{N}}\hat{\Sigma}^m\right) r\mathrm{d}\theta\,\mathrm{d}r \\
&= \frac{1}{4}\int_0^\infty\int_0^{2\pi}\left(\sum_{m\in\mathbb{N}}\left(im\Phi_p^m(r)e^{im(\theta-\theta_p)} - im\Phi_p^m(r)e^{-im(\theta-\theta_p)}\right)\right) \\
&\qquad\qquad \left(\sum_{m\in\mathbb{N}}\left(\Sigma^m(r)e^{im(\theta-\theta_p)} + \bar{\Sigma}^m(r)e^{-im(\theta-\theta_p)}\right)\right) r\mathrm{d}\theta\,\mathrm{d}r \\
&= \frac{1}{4}\int_0^\infty 2\pi r\sum_{m\in\mathbb{N}} im\Phi_p^m(r)(\bar{\Sigma}^m(r) - \Sigma^m(r))\,\mathrm{d}r \\
&= \sum_{m\in\mathbb{N}*}\pi m\int_0^\infty \Phi_p^m(r)\Im(\Sigma^m(r))\, r\,\mathrm{d}r
\end{aligned}$$

Finally, denoting by T_{LR}^m:

$$T_{LR}^m = \pi m\Im\left(\int_0^\infty \Phi_p^m(r)\Sigma^m(r)\, r\,\mathrm{d}r\right) \ , \tag{2.22}$$

the total torque reads:

$$T = \sum_{m\in\mathbb{N}*} T_{LR}^m \tag{2.23}$$

□

Torque at a Lindblad Resonance

The torque T_{LR}^m can be derived with some algebra (Goldreich and Tremaine, 1979; Meyer-Vernet and Sicardy, 1987). The calculations of Meyer-Vernet and Sicardy is here reproduced.

Effect of a perturbation on the velocity in the disk: Consider the case of an infinitesimally thin, pressure-less and inviscid disk rotating in the gravity field of the central star Φ_*. The velocity $\vec{v_0}$ is purely azimuthal, with a magnitude given by the Kepler's third law (Eq. (1.1)). The Navier-Stokes equation reads:

$$\frac{\mathrm{D}\vec{v_0}}{\mathrm{D}t} = -\nabla\Phi_* \tag{2.24}$$

Under effect of a perturbing potential Φ', the velocity is perturbed. The perturbed quantity is denoted with a prime: $\vec{v} = \vec{v_0} + \vec{v'}$. This gives: $\frac{\mathrm{D}}{\mathrm{D}t}(\vec{v_0} + \vec{v'}) = -\nabla(\Phi^* + \Phi')$. In polar coordinates, using Eqs. (2.9) and (2.24), expanding to first order in $\vec{v'}$ yields:

$$\left\{\begin{array}{rcl} \partial_t v'_r + [\Omega\partial_\theta]v'_r + 0 - \dfrac{2v'_\theta v_{0\theta}}{r} & = & -\partial_r\Phi' \\ \partial_t v'_\theta + [\Omega\partial_\theta]v'_\theta + \left[v'_r\partial_r + \dfrac{v'_\theta}{r}\partial_\theta\right] r\Omega + \dfrac{v_r v_\theta}{r} & = & -\dfrac{1}{r}\partial_\theta\Phi' \end{array}\right.$$

$$\Leftrightarrow \left\{\begin{array}{rcl} \left[\partial_t + \Omega\partial_\theta\right] v'_r - 2\Omega v'_\theta & = & -\partial_r\Phi' \\ \left[\partial_t + \Omega\partial_\theta\right] v'_\theta + \dfrac{\Omega}{2}v'_r & = & -\dfrac{1}{r}\partial_\theta\Phi' \end{array}\right.$$

Assuming, again, that the planet is on a circular orbit, we consider that every quantity X writes $X = X(r)\exp\left(im(\theta - \Omega_p t)\right)$. For instance, the perturbation reads $\Phi' = \Phi_p^m(r)\exp\left(im(\theta - \Omega_p t)\right)$. Then, $\partial_t \equiv -im\Omega_p$ and $\partial_\theta \equiv -im$. This gives:

$$\left\{\begin{array}{rcl} im(\Omega - \Omega_p)v'_r(r) - 2\Omega v'\theta(r) & = & -\dfrac{\mathrm{d}}{\mathrm{d}r}\Phi_p^m(r) \\ im(\Omega - \Omega_p)v'_\theta(r) + \dfrac{\Omega}{2}v'_r(r) & = & -\dfrac{im}{r}\Phi_p^m(r) \end{array}\right.$$

The solution of this system is:

$$\left\{\begin{array}{rcl} v'_r(r) & = & -\dfrac{im}{rD}\left[(\Omega - \Omega_p)r\dfrac{\mathrm{d}}{\mathrm{d}r} + 2\Omega\right]\Phi_p^m(r) \\ v'_\theta(r) & = & -\dfrac{1}{2rD}\left[\Omega r\dfrac{\mathrm{d}}{\mathrm{d}r} + 2m^2(\Omega - \Omega_p)\right]\Phi_p^m(r) \end{array}\right. \tag{2.25}$$

where

$$D(r) = \Omega^2 - m^2(\Omega - \Omega_p)^2 \tag{2.26}$$

is the distance to the resonance.

Perturbation on the density: Similarly, the continuity equation (2.4) can be linearized by expansion to first order in perturbed quantities:

$$\begin{array}{rcl} \partial_t\Sigma' + \nabla(\Sigma'\vec{v_0}) + \nabla(\Sigma_0\vec{v'}) & = & 0 \\ \left(\partial_t + \Omega\partial_\theta\right)\Sigma' & = & -\Sigma_0\left(\dfrac{1}{r}\partial_r(rv'_r) + \dfrac{1}{r}\partial_\theta v'_\theta\right) \end{array}$$

With the same consideration, it leads to:

$$\Sigma'(r) = \frac{-\Sigma_0}{imr(\Omega-\Omega_p)}\left(\frac{\mathrm{d}}{\mathrm{d}r}(rv'_r) + imv'_\theta\right) \ . \tag{2.27}$$

Calculation of T^m_{LR}: At a Lindblad resonance of order m, the angular velocity is $\Omega_m = \frac{m}{m\pm1}\Omega_p$. Thus, near the resonance, $\Omega - \Omega_p \approx \mp\Omega_m/m$. Then, the system (2.25) degenerates and transforms into:

$$\left\{\begin{array}{rcl} v'_r(r) & = & -\dfrac{i\Omega_m}{r_m D}\overbrace{\left(\mp r_m\dfrac{\mathrm{d}}{\mathrm{d}r} + 2m\right)\Phi^m_p(r)}^{A(r)} \\ v'_\theta(r) & = & \mp\dfrac{\Omega_m}{2mD}A(r) = \mp\dfrac{i}{2}v'_r(r) \end{array}\right. \tag{2.28}$$

Using Eqs. (2.27) and (2.28), the expression of T^m_{LR} given by Eq. (2.22) becomes:

$$\begin{aligned} T^m_{LR} &= -\pi m\,\Im\left(\int_0^\infty \Phi^m_p(r)\frac{-\Sigma_0}{imr(\Omega-\Omega_p)}\left[\frac{\mathrm{d}}{\mathrm{d}r}(rv'_r) \mp \frac{m}{2}v'_r\right] r\,\mathrm{d}r\right) \\ &= -\pi\Sigma_0\,\Re\left(\int_0^\infty \frac{\Phi^m_p(r)}{\Omega-\Omega_p}\frac{\mathrm{d}}{\mathrm{d}r}(rv'_r) \mp \frac{\Phi^m_p(r)}{\Omega-\Omega_p}\frac{m}{2}v'_r\,\mathrm{d}r\right) \end{aligned}$$

Integration by part of the first term of the integrand yields:

$$\begin{aligned} T^m_{LR} &= -\pi\Sigma_0\,\Re\left(\left[rv'_r\frac{\Phi^m_p(r)}{(\Omega-\Omega_p)}\right]_0^\infty - \int_0^\infty v'_r\frac{\mathrm{d}}{\mathrm{d}r}\left(\frac{\Phi^m_p(r)}{\Omega-\Omega_p}\right) r\,\mathrm{d}r \mp \int_0^\infty \frac{m}{2}v'_r\frac{\Phi^m_p(r)}{\Omega-\Omega_p}\,\mathrm{d}r\right) \\ &= -\pi\Sigma_0\,\Re\left(\int_0^\infty \left[r\frac{\mathrm{d}}{\mathrm{d}r}\left(\frac{\Phi^m_p(r)}{\Omega-\Omega_p}\right) \mp \frac{m}{2}\frac{\Phi^m_p(r)}{\Omega-\Omega_p}\right] v'_r\,\mathrm{d}r\right) \end{aligned}$$

Assuming that v'_r varies sufficiently rapidly near the resonance so that the term in brackets can be taken out of the integral and evaluated at $r = r_m$ (so that $\Omega \approx \Omega_m$ and $\Omega - \Omega_p = \mp\Omega_m/m$), this yields:

$$T^m_{LR} = \frac{\pi m\Sigma_0 A(r_m)}{\Omega_m}\,\Re\left(\int_0^\infty v'_r\,\mathrm{d}r\right) \ . \tag{2.29}$$

Denote $\mathcal{D}$ the derivative of D with respect to r at $r = r_m$, and $x = (r - r_m)/r_m$; so, $\mathrm{d}r = r_m\mathrm{d}x$ and $D = r_m\mathcal{D}x$. Using Eq. (2.28) in Eq. (2.29) yields:

$$T^m_{LR} = \frac{\pi m\Sigma_0 A(r_m)^2}{r_m\mathcal{D}}\,\Im\left(\int_{-1}^\infty \frac{\mathrm{d}x}{x}\right) \ . \tag{2.30}$$

The integral in Eq. (2.30) is not defined. To eliminate the singularity, let us consider a slowly increasing perturbation, *id est* take Ω_p to have a small positive imaginary part: $\Omega^c_p = \Omega_p(1 + i\alpha')$. Then, r_m should be replaced by $r_m + \delta r$ such that $\Omega_p + i\alpha'\Omega_p = \Omega_p + \delta r(\mathrm{d}\Omega/\mathrm{d}r)$. Thus, $\delta r = -\frac{2}{3}i\alpha' r_m$. Consequently, to first order in $\alpha = \frac{2}{3}\alpha'$, x should be replaced by $x^c = x + i\alpha$, leading to

$$\Im\left(\int_{-1}^\infty \frac{\mathrm{d}x}{x^c}\right) = -\int_{-1}^\infty \frac{\alpha\,\mathrm{d}x}{x^2+\alpha^2} = -\frac{\pi}{2} + \arctan\left(-\alpha^{-1}\right) = -\pi$$

where we have assumed $\alpha \ll 1$ to find the final result. Eventually, the introduction of a small imaginary part allows one to avoid the singularity at resonance ($x = 0$), and the total area under the bell-shaped curve $\Im(1/x^c)$ is independent of α. This yields to the expression of T_{LR}:

$$T_{LR}^m = -\frac{\pi^2 m \Sigma_0 A(r_m)^2}{r_m \mathcal{D}}$$

For Keplerian disks $\Omega \propto r^{-3/2}$; therefore, from the definition of D (Eq. (2.26)):

$$\begin{aligned}
\frac{\mathrm{d}D}{\mathrm{d}r} &= -\frac{3}{r}\Omega^2(1-m^2) - \frac{3}{r}m^2\Omega\Omega_p \ . \\
\text{Thus, } \mathcal{D} &= -\frac{3}{r_m}\Omega_m(\Omega_m(1-m^2) + m^2\Omega_p) \\
&= -\frac{3}{r_m}\Omega_m\left(\frac{m}{m\pm 1}\Omega_p(1-m^2) + m^2\Omega_p\right) \\
&= -\frac{3m}{r_m}\Omega_m\Omega_p\left(\frac{-(m-1)(m+1)}{(m\pm 1)} + m\right) \\
&= -\frac{3m}{r_m}\Omega_m\Omega_p\left(-(m\mp 1) + m\right) \\
\mathcal{D} &= \mp\frac{3m}{r_m}\Omega_m\Omega_p
\end{aligned}$$

Finally:

$$T_{LR}^m = \pm\frac{\pi^2\Sigma_0 A(r_m)^2}{3\Omega_m\Omega_p} \tag{2.31}$$

This gives a positive torque exerted at Outer Lindblad Resonances and a negative torque exerted at Inner Lindblad Resonances.

The final result Eq. (2.31) is Eq. (16) of Meyer-Vernet and Sicardy (1987) (which is also Eq. (46) of Goldreich and Tremaine, 1979), modulo a multiplicative factor 4. This difference with the papers is only apparent: this factor is located in $A(r)^2$ because our $\Phi_p^m(r)$ corresponds to twice the $\Phi_p^m(r)$ considered by Meyer-Vernet and Sicardy who expanded the Fourier series of Φ_p over $\mathbb{Z}$ and not over $\mathbb{N}$.

The magnitude of T_{LR}^m is shown for different m in figure 2.2. Notice that T_{LR}^m initially increases for increasing m, but eventually declines. This is called the *torque cutoff*. The reason for this decline is precisely that r_m does not tend to r_p for $m \to \infty$, but tends to $r_p + 2/3H$ as explained above, while $\Phi_p^m(r)$ peaks more and more narrowly at r_p (Eq. (2.17)).

Total torque

Assuming that the torque associated to a m-order Lindblad resonance given by Eq. (2.31) applies in a local neighborhood of $r = r_m$, the sum of these torques can be considered as a smooth function of r, whose density is (Goldreich and Tremaine, 1980, Eq. (18)):

$$\frac{\mathrm{d}}{\mathrm{d}r}\left(\sum_m T_{LR}^m\right) = \frac{32}{81}\tilde{K}\,\mathrm{sgn}(r-r_p)\,q^2\Sigma r^3\Omega^2\left(\frac{r}{\Delta}\right)^4 \tag{2.32}$$

with $\tilde{K} = [2K_0(2/3) + K_1(2/3)]^2 \approx 6.35$ (K_0 and K_1 being modified Bessel functions). This is the same result as the derivative of Eq. (2.13) with respect to Δ (if one keeps in mind that the

approximation $r = r_p$ has been done), except for a numerical factor of the order of 2.83 (see Papaloizou and Lin, 1984).

Then, the total torque is the integral of the torque density over all the outer or inner disk. Given that the torque of each resonance is null in the range between r_p and r_m and that r_m accumulates at $r = r_p + 2/3H$ for $m \to \infty$, Eq. (2.32) should be integrated from $\Delta = 2/3H$ to ∞. This leads to:

$$T_{LR} = \frac{4\tilde{K}}{27} \mathrm{sgn}(r - r_p)\, q^2 \Sigma r^4 \Omega^2 \left(\frac{r}{H}\right)^3 . \tag{2.33}$$

Because it comes from Lindblad resonances, the torque exerted by the planet on the outer (resp. inner) disk is called the *outer (resp. inner) Lindblad Torque*. In general, the expressions Eq. (2.14) and (2.33) are called the *one-sided Lindblad Torque*.

2.3 Type I migration and differential Lindblad torque

It has been shown by Ward (1986) that the inner and the outer Lindblad torques are not exactly opposite. For every m, the torque exerted at the inner mth order Lindblad resonance is smaller in absolute value than the outer one, for three reasons (Ward, 1997) :

1. From the definition of r_m in (2.20), it appears that the outer resonances are located closer to the planetary orbit than the inner ones. Because the potential Φ_p^m declines symmetrically away from the planet, this enhances the coefficient $A(r_m)$ in (2.31).

2. Even if the inner and outer resonances of the same order were located symmetrically with respect to the planet, the $\pm$ sign in the definition of $A(r)$ (see (2.28)) makes $A(r)$ larger for outer resonances.

3. The angular velocity at the location of the resonance (Ω_m) appears at the denominator of the expression of T_{LR}^m Eq. (2.31). Obviously, Ω_m is larger for inner resonances than for outer ones, which favors the latter.

This result is robust. If one increases the density slope in the disk in order to have the density Σ significantly larger in the inner disk than in the outer disk, then the radial pressure gradient increases (the pressure is proportional to the density). This partially counterbalances the gravity of the central star and makes the angular velocity in the disk decrease, so that the resonances are shifted inward, which increases the strength the outer resonances with respect to the inner ones. This effect is called the *pressure buffer*.

Figure 2.2 illustrates the difference between $|T_{LR}^m|$ at the inner (triangles) and outer resonances (diamonds), for m from 2 to 60, for two values of the aspect ratio. The difference appears to increase with (H/r). The torque cutoff mentioned in previous section also appears ; it corresponds to the decrease of $|T_{LR}^m|$ as m increases for large m. The thicker the disk, the smaller is the value of m beyond which T_{LR}^m starts to decrease (about 9 for $(H/r) = 0.07$, about 21 for $(H/r) = 0.03$).

Consequently, the sum of the torques exerted on the planet by the inner and outer disk is a negative fraction of the absolute one sided Lindblad torque. It is called the *differential Lindblad torque*, and this fraction scales with the aspect ratio H/r. As the one-sided Lindblad torque scales with $(H/r)^{-3}$, the differential Lindblad torque is proportional to $(H/r)^{-2}$.

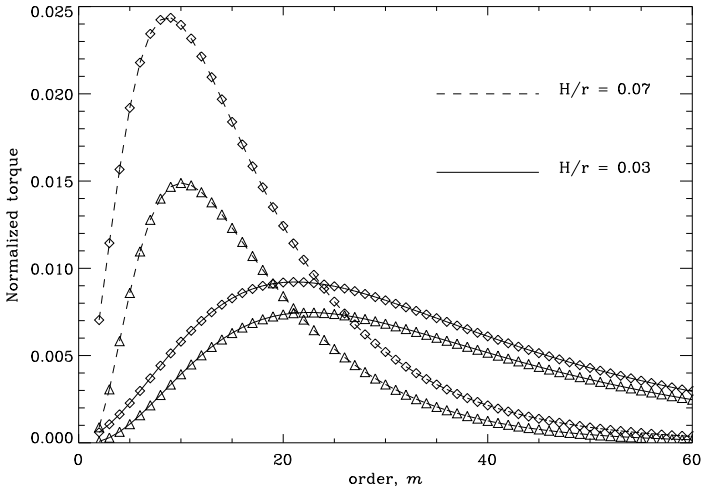

Figure 2.2: Inner (triangles) and outer (diamonds) torques $|T^m_{LR}|$, normalized to $T^0 = \pi q^2 \Sigma {r_p}^4 {\Omega_p}^2 (H/r)^{-3}$, for two different aspect ratios (figure from Masset (2006), inspired from Ward (1997)).

Tanaka et al. (2002) provide the most up to date estimate of the differential Lindblad Torque in a two dimensional infinitely thin isothermal disk:

$$T_{dLR} = -Cq^2 \Sigma {r_p}^4 {\Omega_p}^2 \left(\frac{H}{r}\right)^{-2} , \tag{2.34}$$

where $C = (3.200 + 0.468\xi)$, and ξ is the slope of the density power law: $\Sigma \propto r^{-\xi}$. In the case of a vertically resolved, three dimensional isothermal disk, they find $C = (2.340 - 0.099\xi)$.

This negative torque exerted on the planet leads to inward migration. As this torque is proportional to the square of the planet mass, it leads to a migration rate proportional to the planet mass. This is type I migration. The angular momentum of the planet is given by $J_p = {r_p}^2 \Omega_p M_p$, which is proportional to ${r_p}^{1/2}$. Its derivative with respect to time is $\frac{1}{2}\dot{r_p} r_p \Omega_p M_p$. Thus, denoting $\mu(r) = \Sigma \pi r^2 / M_*$ the reduced disk mass, an estimate of the migration time scale is:

$$\tau_{\text{migr I}} = \frac{r_p}{|\dot{r_p}|} = \frac{\dot{J}_p}{T_{dLR}} = \frac{{r_p}^2 \Omega_p M_p}{2\,|T_{dLR}|} \tag{2.35}$$

$$\tau_{\text{migr I}} = \frac{(H/r)^2}{4Cq\mu(r_p)} \frac{2\pi}{\Omega_p} . \tag{2.36}$$

Let us give an approximate migration time scale for a 10 $M_\oplus$ planet embedded at $r_p = 5$ A.U. in a Minimum Mass Solar Nebula, with $H/r = 0.07$. The disk reduced mass is $\mu = 1.4\ 10^{-3}$. This gives $\tau_{\text{migr I}} = \frac{3}{C} 10^4$ orbits, that is a few hundred thousand years. This is much shorter than the disk life time (a few million years).

2.4 Type III migration and Corotation torque

A corotation resonance occurs when the perturbing potential corotates with the fluid. Assuming the planet on a circular orbit, the corotation with the mth Fourier component of the planetary

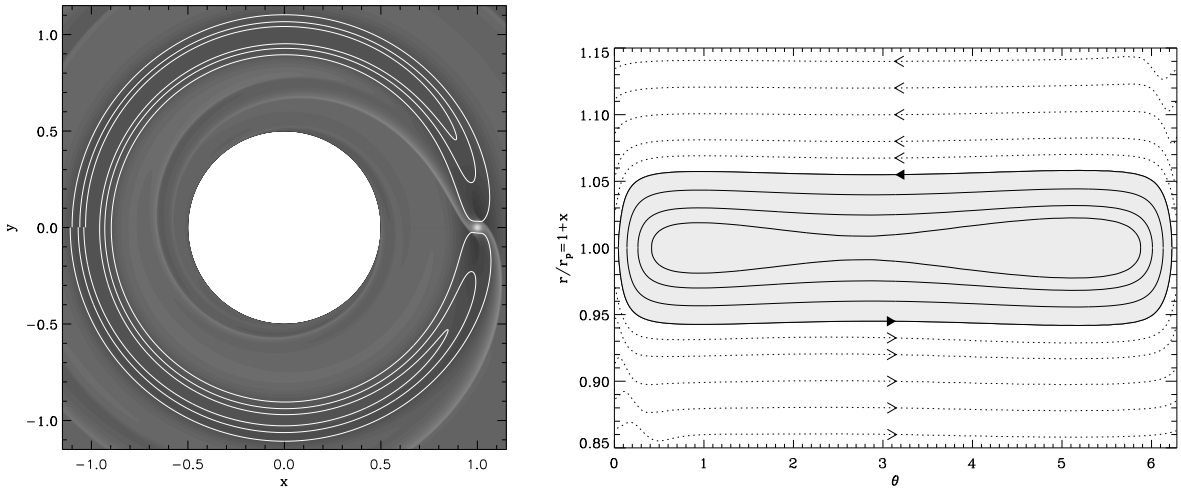

Figure 2.3: Horseshoe trajectories of fluid elements perturbed by a large mass planet held on a fixed circular orbit, in the corotating frame. The left plot displays trajectories as white lines over a density map in Cartesian (x, y) coordinates. Polar (θ, r) coordinates are used in the right plot. The shaded area in the right plot is the whole set of horseshoe streamlines, *i.e.* the horseshoe region. Figures from Masset (2006).

potential (given by Eq. (2.16)) corresponds to: $m(\Omega - \Omega_p) = 0$. Therefore, under the circular planet assumption, all the corotation resonances are located at corotation with the planet, where $\Omega = \Omega_p$.

In this section, the torque exerted on the planet by the gas in the region around its orbit is discussed. This corresponds to the region between the inner and the outer disk, for which the calculations of section 2.2 do not hold.

2.4.1 Case of a planet on a fixed circular orbit

Stationary disk

In the corotating frame, a fluid element on a circular orbit of radius $r = r_p + b$ is deflected at each encounter with the planet. However, if b is small enough, the dynamics of the encounter is not as simple as described in figure 2.1. In figure 2.1, the gravity of the Sun is neglected. Thus, it holds for fast encounters during which the motion of the planet around the Sun can be neglected. If b is small, the encounter is slow: the relative velocity is $r(\Omega - \Omega_p)$, which tends to zero when b tends to zero. Thus, we enter the realm of the restricted 3-bodies problem. In that case, for small impact parameter b, a fluid element initially on an orbit of radius $r = r_p + b$ around the Sun is sent by the planet on an orbit of radius $r = r_p - b$. On this new orbit, the angular velocity in the corotating frame is of opposite sign with respect to the former orbit. Thus, the fluid element moves away from the planet in the direction it came from. After a revolution on this new orbit, the fluid element encounters the planet again, from the opposite direction, and is sent back on the orbit of radius $r_p + b$ where it moves away from the planet. After a revolution on this orbit, the initial condition is recovered. This describes a trajectory that has the shape of a horseshoe in Cartesian coordinates in the corotating frame, illustrated in figure 2.3 (white lines in the left

hand plot). The right hand plot of figure 2.3 shows trajectories in the corotating frame in polar coordinates : the abscissa is the azimuth θ, ranging from 0 to 2π, and the ordinate is the distance to the Sun r. In this representation, the horseshoe trajectories have an about rectangular shape. There is a threshold limit for b for a U-turn to take place ; it is denoted x_s, the half width of the *horseshoe region*. Fluid elements with $b > x_s$ are in *circulation* with respect to the planet, while those with $b < x_s$ *librate* in the horseshoe region. The critical curve separating the region of libration from the regions of circulation is called *separatrix* (therefore the subscript s in x_s). The value of x_s is about 0.06 in figure 2.3. It scales with the square-root of the planet mass for low mass planets ($q \lesssim 10^{-4.5}$), and with the *Hill Radius* of the planet $R_H = r_p(q/3)^{1/3}$ for massive planets ($q \gtrsim 10^{-4}$) (Masset et al., 2006; Masset, 2006).

A fluid element on the upper part of the horseshoe region, when it experiences the first U-turn decreases its orbital radius, losing angular momentum, and therefore exerts a positive torque on the planet. Conversely, a fluid element on the lower part of the horseshoe region exerts a negative torque on the planet during its first U-turn.

The torque exerted simultaneously by all fluid elements in the horseshoe region is called the corotation torque, and its expression has been evaluated in Goldreich and Tremaine (1979) and Ward (1991, 1992), and can be written more generally as:

$$T_C = \frac{3}{4} {x_s}^4 {\Omega_p}^2 \Sigma \frac{\mathrm{d}\log(\Sigma/B)}{\mathrm{d}\log r} \ , \tag{2.37}$$

where $B = \Omega(r) + (r/2)(\mathrm{d}\Omega/\mathrm{d}r)$ is *the second Oort Constant*. In Keplerian rotation, $B = \Omega/4$, so that if $\Sigma \propto r^{-\beta}$ one has $\mathrm{d}\log(\Sigma/B)/\mathrm{d}\log r = 3/2 - \beta$ (this expression, plugged in Eq. (2.37) gives exactly the formula for the corotation torque in Ward (1992)). The coefficient B is also $(1/2r)\,\mathrm{d}(r^2\Omega)/\mathrm{d}r$, which is half the vertical component of the flow *vorticity*. Thus, B/Σ scales with the flow *vortensity*.

However, as the fluid elements librate, they periodically give and take back angular momentum from the planet at the U-turns. As librating fluid elements remain in a radially bounded interval, the angular momentum they exchange with the planet averages out to zero over a timescale that is long compared to their libration timescale. Furthermore, the libration period depends on the horseshoe libration amplitude. This implies that phase mixing makes the corotation torque tend to zero after a few libration timescales, not only on average, but in instantaneous value as well. This is known as the *saturation of the corotation torque*. It corresponds to the flattening of the vortensity profile (that is : $\Sigma \propto r^{-3/2}$) that makes T_C vanish as can be seen in Eq. (2.37). It can be avoided if fluid elements have the possibility to exchange angular momentum not only with the planet, but also with the rest of the disk. Viscous stress can act to extract angular momentum from the libration region and prevent saturation.

Accounting for the role of viscosity to prevent full saturation, the steady state value of the corotation torque is derived by Masset (2001) :

$$T_C = \frac{3}{4} {x_s}^4 {\Omega_p}^2 \Sigma \frac{\mathrm{d}\log(\Sigma/B)}{\mathrm{d}\log r} \mathcal{F}(z_s) \ , \tag{2.38}$$

where

$$z_s = \frac{x_s}{r_p} \left(\frac{{r_p}^2 \Omega_p}{2\pi\nu} \right)^{\frac{1}{3}}$$

and $\mathcal{F}(z) = z^{-3} - z^{-4}g(z)/g'(z)$, with $g(z) = \left(\mathrm{Bi}(z) - \sqrt{3}\mathrm{Ai}(z)\right)/2\mathrm{Bi}'(0)$ a linear combination of the Airy functions Ai and Bi. This expression of the corotation torque coincides with Eq. (2.37) if $\mathcal{F}(z_s) = 1$, namely if there is no saturation.

It has been estimated that the corotation torque amounts to a few tens of percent (Korycansky and Pollack, 1993) of the differential Lindblad torque for a disk with a power-law surface density profile. Tanaka et al. (2002) give the following estimate for a three dimensional disk with flat surface density and temperature profiles:

$$T_C \approx -(1/2)T_{dLR} \ . \tag{2.39}$$

Accretion disk

Consider a planet on a fixed circular orbit, embedded in a disk in which the radial velocity of the fluid elements is constant and equal to $v_r < 0$ (because of viscous accretion for instance). In that case, the dynamics is different from that considered above. A fluid element circulating in the outer disk spirals inward and approaches the planetary orbit. Let $b_0 = r - r_p$ the distance to planetary orbit of a fluid element at conjunction with the planet and τ the unperturbed synodic period at $r = r_p \pm x_s$:

$$\tau \approx 2\pi/|x_s(\mathrm{d}\Omega/\mathrm{d}r)| = 4\pi r_p/3x_s\Omega_p \ . \tag{2.40}$$

If $x_s < b_0$, the considered fluid element is circulating in the outer disk, but if $x_s < b_0 < x_s - \tau v_r$, it will have $r - r_p = b_1 < x_s$ at next conjunction. Then, the fluid element will execute an inward U-turn and will be placed on an orbit of radius $r = r_p - b_1$. As $|r - r_p| = r_p - r$ now increases at a rate $(-v_r)$, at the next conjunction $r_p - r = b_1 - \tau v_r = b_0 > x_s$. Thus, no outward U-turn is possible anymore, the fluid element is left in the inner disk where it goes on spiraling inward. In conclusion, there is a net flow of gas through the planetary orbit via the inward U-turn. This is illustrated in figure 2.4, which is the same as the right panel of figure 2.3 in the case of an accretion disk. The solid line in the white region is a single trajectory of a fluid element that spirals inward in the outer disk, crosses the planetary orbit, and then spirals inward in the inner disk.

At the inward U-turn, the specific variation of angular momentum for a fluid element that encounters the planet with $b \approx x_s$ is $\delta j = -2x_s(\mathrm{d}j/\mathrm{d}r) = -x_s r_p \Omega_p$. Thus, denoting Σ_s the density on the separatrix, the torque felt by the planet from the flow reads:

$$T_2 = (-2\pi r_p \Sigma_s v_r)(x_s r_p \Omega_p) \ . \tag{2.41}$$

Yet, there is still a closed horseshoe region. If $|r - r_p|$ is smaller than $x_s + \tau v_r$ at the inward U-turn, $r_p - r$ is still smaller than x_s at the next encounter with the planet. Then, an outward U-turn is performed; its amplitude $r_p - r$ is larger than the amplitude of the previous inward U-turn because r has decreased since this time. As the fluid element goes on spiraling inward, $r - r_p$ decreases and the next inward U-turn has a smaller amplitude than the previous outward U-turn, and so on. This kind of trajectory can be seen in the shaded area of figure 2.4. Fluid elements on such orbits are trapped at corotation with the planet. However, the viscous stress in the disk makes them spiral inward and gives them a radial velocity v_r. Denoting M_{HS} the mass contained in the horseshoe region, the viscous stress exerted on the horseshoe region is equivalent to a torque $T_s = v_r(\mathrm{d}j/\mathrm{d}r)M_{HS} = \frac{1}{2}v_r r_p \Omega_p M_{HS}$. As the corotation region is trapped by the planet, the planet has to exert on it a torque opposite to T_s. In fact, the planet gives angular momentum to the trapped material via wider outward U-turns than inward U-turns.

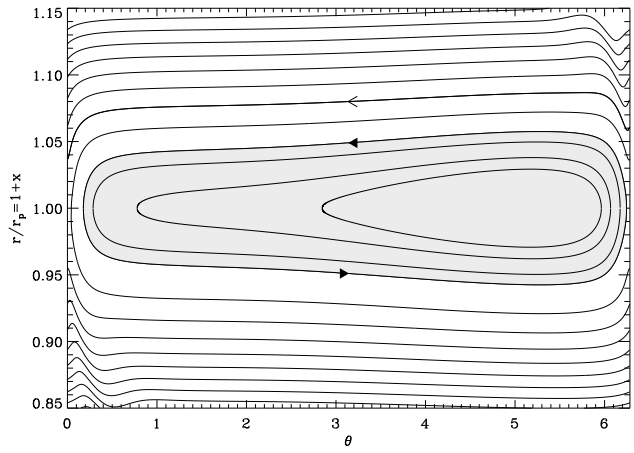

Figure 2.4: Horseshoe trajectories in the corotating frame in polar (θ, r) coordinates, in a viscous accretion disk. The horseshoe region has a trapezoidal shape. Outside the horseshoe region is plotted one trajectory of a fluid element that spirals inward. Figures from Masset (2006).

Reciprocally, the torque felt by the planet from the trapped material in the horseshoe region reads:

$$T_3 = T_s = \frac{1}{2} v_r r_p \Omega_p M_{HS} \ .$$

Denote $4\pi x_s r_p \Sigma_s = \mathcal{M}_{HS}$. This quantity is approximately the surface of the horseshoe region, multiplied by the density on the separatrix. Thus $\mathcal{M}_{HS}$ is the mass that the horseshoe region would have if its density were uniformly equal to Σ_s, while M_{HS} is the actual mass in the horseshoe region. The difference $\delta m = \mathcal{M}_{HS} - M_{HS}$ is called the *coorbital mass deficit* (Masset and Papaloizou, 2003). It is null if the planet does not perturb the disk density profile, but it is positive (and it can be comparable to the planet mass) if the planet opens a non-negligible dip in a massive disk.

Finally, the total torque felt by the planet from horseshoe effect reads:

$$T_{HS} = T_2 + T_3 = -\frac{1}{2} v_r r_p \Omega_p \, \delta m \ . \tag{2.42}$$

It is proportional to $(-v_r)$; thus it is positive in accretion disks.

2.4.2 Corotation torque on a migrating planet

In this subsection, we consider a planet migrating in a non evolving, Keplerian disk.

Constant migration rate

Notice that the cause of the torque T_{HS} on the planet is the relative motion of the gas with respect to the planet. If the planet is migrating with respect to the stationary disk at a constant rate $\dot{r_p} > 0$, the dynamics is the same. Fluid elements circulating on circular orbits in the outer disk may be caught in libration by the outward move of the planet. In fact, the distance to the planetary orbit $r - r_p$ is decreasing as r_p increases. If a fluid element at conjunction with the planet has $b_0 = r - r_p$ such that $x_s < b_0 < x_s + \tau \dot{r_p}$, it is circulating in the outer disk

but at next conjunction it will have $r - r_p = b_1 < x_s$. Then, the fluid element will execute an inward U-turn and will be placed on an orbit of radius $r = r_p - b_1$. At the next conjunction, $r_p - r = b_1 + \tau \dot{r_p} = b_0 > x_s$. Thus, no outward U-turn is possible anymore because the planet has migrated too far, and the fluid element is left circulating in the inner disk. Once again, there is a net flow of gas through the planetary orbit via the inward U-turn.

Adapting Eq. (2.41), the torque felt by the migrating planet from the flow reads:

$$T_2 = (2\pi r_p \Sigma_s \dot{r_p})(x_s r_p \Omega_p) \ . \tag{2.43}$$

Yet, there is still trapped material that follows the planet. If $r - r_p$ is sufficiently small at the inward U-turn, $r_p - r$ is still smaller than x_s at the next encounter with the planet. Then, an outward U-turn is performed; its amplitude $r_p - r$ is larger than the amplitude of the previous inward U-turn because r_p has increased since this time. As the planet goes on migrating outward, $r - r_p$ decreases and the next inward U-turn has a smaller amplitude than the previous outward U-turn, and so on. Fluid elements in this regime are trapped in the planet migration; their orbital radii increases on average at a rate $\dot{r_p}$. They gain angular momentum. Their angular momentum is taken from the planet through outward U-turns wider than inward U-turns. Thus, the rate of variation of angular momentum for the planet from the trapped material reads:

$$T_3 = -\frac{1}{2} \dot{r_p} r_p \Omega_p M_{HS} \ . \tag{2.44}$$

Finally, the total torque felt by the migrating planet from horseshoe effect reads:

$$T_{HS} = T_2 + T_3 = \frac{1}{2} \dot{r_p} r_p \Omega_p \, \delta m \ ,$$

which is the same as Eq. (2.42) with $\dot{r_p}$ instead of $(-v_r)$. It is proportional to $\dot{r_p}$. There is a positive feedback on the migration when $\delta m > 0$: in that case, if the planet migrates outward, $\dot{r_p} > 0$, and thus the planet receives from the horseshoe effect a positive torque, which pushes the planet outward even more. If the planet migrates inward, the horseshoe effect is a negative torque, that helps inward migration.

Varying migration rate

The positive feedback on migration is delayed with respect to the planetary motion. In fact, if the planet orbital radius suddenly increases by δr_p, the material of the outer disk caught in the horseshoe region will experience an inward U-turn only when it arrives at conjunction with the planet. The positive feedback is thus delayed by a duration $\tau/2$, where τ is still the unperturbed synodic period at the location of the edge of the horseshoe orbit. This gives:

$$T_{HS}(t) = \frac{1}{2} \dot{r_p}(t - \frac{\tau}{2}) r_p \Omega_p \, \delta m$$

A first order Taylor expansion gives $\dot{r_p}(t - \frac{\tau}{2}) = \dot{r_p}(t) - \frac{\tau}{2} \ddot{r_p}$.

The migration rate of the planet $\dot{r_p}$ is determined by the total torque T_p that it feels via: $T_p = \frac{1}{2} \dot{r_p} r_p \Omega_p M_p$. The total torque felt by the planet decomposes into the horseshoe effect and the differential Lindblad torque. The latter does not depend on $\dot{r_p}$. Finally, the migration rate of the planet is ruled by the following differential equation:

$$\begin{aligned} T_p &= T_{HS} + T_{dLR} \\ \frac{1}{2} \dot{r_p}(t) r_p \Omega_p M_p &= \frac{1}{2} r_p \Omega_p \, \delta m \left(\dot{r_p}(t) - \frac{\tau}{2} \ddot{r_p} \right) + T_{dLR} \end{aligned}$$

$$\frac{\tau}{2}\frac{\delta m}{M_p}\ddot{r_p} + \left(1 - \frac{\delta m}{M_p}\right)\dot{r_p} = \frac{2T_{dLR}}{r_p\Omega_p} \tag{2.45}$$

A particular solution of this differential equation in $\dot{r_p}$ is a constant migration rate determined by T_{dLR}; this is type I migration. If $\delta m = 0$, this is the only solution. If $\delta m > 0$, the general solution is the sum of the particular solution and of solutions of the homogeneous equation obtained by the suppression of the right hand side of Eq. (2.45). The homogeneous equation is a classical first order differential equation. Its solution is an exponential function $a \exp\left(-2\frac{t}{\tau}\left(\frac{M_p}{\delta m} - 1\right)\right)$, where a is an arbitrary multiplicative constant. It appears that if $0 < \delta m < M_p$, this exponential function decreases with time, and the classical type I regime is reached. But if $\delta m > M_p$, this is an exponentially increasing function of time. In that case, the migration regime is very different from the classical ones. It can be inward or outward, depending on the sign of a, that is of the initial conditions. This runaway regime has been identified by Masset and Papaloizou (2003) and is called *type III migration* (because it has been identified after types I and II –sections 2.3 and 2.6 respectively).

The migration rate $\dot{r_p}$ can increase to the limit where the dynamics of the horseshoe region is so perturbed that the above reasoning is no more valid. The expression of T_2 given by Eq. (2.43) is wrong if gas flows through the planetary orbit without experiencing an encounter with the planet (a U-turn). This happens if the planet migrates by more than the horseshoe width in less than an unperturbed synodic period on the edge of the horseshoe region: $|\dot{r_p}|_{\max} > x_s/\tau$. In that case, a test particle in the outer disk may cross the planetary orbit before reaching conjunction with the planet; it orbits then in the inner disk, but there has been no exchange of angular momentum with the planet during that process. Using Eq (2.40), it gives a migration speed limit:

$$|\dot{r_p}|_{\max} = \frac{3{x_s}^2\Omega_p}{4\pi r_p} \ .$$

Planets that do open partial gaps in reasonable protoplanetary disks have typically masses of the order of Saturn's one. Thus, it can be considered that $x_s \approx R_H$, and consequently $|\dot{r_p}|_{\max} \approx q^{2/3} r_p\Omega_p/2\pi$. This corresponds to a migration timescale $r_p/\dot{r_p}$ of the order of $q^{-2/3}2\pi/\Omega_p$, which is about two hundreds of orbits for a planet of the mass of Saturn. This shows that type III migration can be, in principle, a spectacularly rapid phenomenon.

2.5 Gap opening: a simple approach

In previous sections, we have considered a planet embedded inside a gas disk of fixed density. In this section, we address the question whether the planet can modify the gas disk density, and in particular at which condition it can open a gap around its orbit. In section 2.2, we have seen how the planet exerts torques on the gas. It appears that the planet gives angular momentum to the disk exterior to its orbit, while it takes some to the inner disk. This tends to repel the outer disk outward and the inner disk inward, that is away from the planetary orbit. Internal stress inside the disk tends to smooth the density profile and to refill any possible depletion. These two opposite effects compete. In a first approximation, consider the outer disk as a whole. It receives from the planet the torque T_{LR}; never mind whether this torques is carried far away by waves or if it is locally deposited, this does not change the total amount of angular momentum received by the outer disk. The viscous stress in the outer disk causes dissipation, and loss of angular

momentum; the integral of all the viscous stress in the outer disk gives the viscous torque T_ν expressed by Eq. (2.10). In this model, the outer disk is effectively repelled outward by the planet if the one-sided gravity torque is larger in absolute value than the viscous torque.

In that case, the gap is considered to have a step function profile, with the edges placed at a distance Δ from the planet orbit such that the gravity torque T_g exerted on the outer disk is exactly opposite to the viscous torque T_ν. In fact, Δ is determined as the solution of the equation $T_g(\Delta) + T_\nu(r_p + \Delta) = 0$. The viscous torque $T_\nu(r)$ is given by and Eq. (2.10), and $T_g(\Delta)$ is given by Eq. (2.13) or can be computed by integration of the torque density given by the Lindblad resonance analysis and expressed in Eq. (2.32).

However, Δ cannot be taken a small as one would like. We already mentioned that Δ should be taken larger than $\frac{2}{3}H$ and that the maximal Lindblad torque is given by Eq. (2.33). Thus, making the approximation $H/r_p \ll 1$ a gap can be opened only if (Papaloizou and Lin, 1984):

$$\frac{\nu}{{r_p}^2\Omega_p} < 0.0887 q^2 \left(\frac{r_p}{H}\right)^3 \ , \tag{2.46}$$

otherwise T_ν is larger than T_g in absolute value and the gas overruns the planet.

In addition, simple 3D considerations lead to think unreasonable that a planet opens a gap if its Roche lobe is smaller than the disk height: in this case, gas in the upper layer would hardly feel the planet and would not be repelled. Furthermore, in that case, the planetary torque is totally evacuated away by the wake and not deposited locally, so that the local opening the gap is not possible (Lin and Papaloizou, 1986b). Hence, it is considered as a necessary condition for gap opening that:

$$R_H > H \ . \tag{2.47}$$

Note that this criterion is verified by a Jupiter mass planet ($q = 10^{-3}$) in a 5% aspect ratio disk, because then $R_H/r_p = (q/3)^{1/3} = 0.069 > 0.05$.

So, the smallest possible planet mass to open a gap is such that $H = R_H$. Thus, replacing H by R_H in Eq. (2.46) gives a second criterion for gap opening, based on the consideration that the viscous torque has to be smaller than the gravitational torque (see section 3 of Bryden et al., 1999, and references therein):

$$q > \frac{40\,\nu}{{r_p}^2\Omega_p} \ . \tag{2.48}$$

Note that this criterion is verified by a Jupiter mass planet in a disk with Reynolds number $\mathcal{R} = {r_p}^2\Omega_p/\nu = 10^5$, which is a quite standard value in astrophysical disks.

Finally, we find two criteria for gap opening, the first one, Eq. (2.47), compares –indirectly– the planet mass and the pressure, and the second one, Eq. (2.48), compares the planet mass and the viscosity, in dimensionless expressions. However, this scheme is obviously an over simplification. In particular, the gap profile is not a step. In Chapter 4, we present a refined method by Varnière et al. (2004). They consider the differential viscous and planetary torque on every elementary ring in the disk (*id est* the torque density) and obtain a differential equation in the gas density that gives the gap profile. However, this method assumes total local deposition of the gravity torque. With a novel approach, which consists of following the fluid elements along their trajectories, we show that the flux of angular momentum carried by the waves corresponds to a pressure torque. The equilibrium profile of the disk is then set by the balance between gravity, viscous and pressure torques. This enables us to obtain correct gap profiles and a unified criterion for gap opening.

2.6 Type II migration

In previous section, we have derived two criteria on the planet mass for a planet to open a gap in a protoplanetary disk. In particular, we have seen that a Jupiter mass planet opens a gap in a classical disk. If the planet opens a gap, it can no longer exchange angular momentum with the gas and drift with respect to the disk like in sections 2.3 and 2.4. There is necessarily a change of regime. In this section, we study the behavior of a planet locked into its gap in a viscous disk.

2.6.1 A first approach

In the classical conception of gap opening presented in previous section, the planet orbits in vacuum between the inner and the outer disk. If the distance between the planet and the edge of the gap, Δ, decreases, the torque exerted by the disk on the planet given by Eq. (2.13) increases (it is proportional to Δ^{-3}). This repels the planet away from the disk. Thus, the planet is locked in the middle of the gap.

Moreover, the equilibrium is such that the planetary torque is exactly opposite to the viscous torque in the disk. Thus, the torque exerted by the disk on the planet is equal to the viscous torque. The planet drift is thus linked to the viscous evolution of the disk. This is the definition of type II migration. The migration timescale, given by Eq. (2.35) with $-T_\nu$ for T_{dLR}, reads :

$$\tau_{\text{migr II}} = \tau_\nu \frac{q}{6\mu} ,$$

where μ is the reduced mass of the disk ($\mu = \pi {r_p}^2 \Sigma / M_*$), and τ_ν is the *viscous time* at the planetary location defined by :

$$\tau_\nu = \frac{{r_p}^2}{\nu} . \tag{2.49}$$

Thus, the migration time scale in type II migration is about the viscous time. It cannot be smaller, even if $q < \mu$ because if the planet moves inward faster than the disk, it is repelled by the inner disk toward the center of the gap, as discussed above. If the planet is sensibly more massive than the disk, the migration is effectively slowed down because of the inertia of the planet. The migration speed becomes inversely proportional to the planet mass. However, a giant planet forms by accretion of gas from its neighborhood. Thus, its mass is linked to the gas density, and the ratio q/μ is unlikely larger than 1 ; this would require that the planet accretes gas from all the disk (which is actually possible in the case of a migrating planet or an evolving disk if the accretion efficiency is good). Therefore, in general giant planets should suffer type II migration with viscous timescale. When the disk dissipates, there is a phase during which $q \gg \mu$. Then, the planet migrates much more slowly than the gas would do, and it perturbs the disk viscous evolution. From these considerations, we can write a more appropriate timescale for type II migration :

$$\tau_{\text{migr II}} = \tau_\nu . \max\left(1, \frac{q}{6\mu}\right) . \tag{2.50}$$

In the case where the planet migrates more slowly than the disk would do, the inner disk still accretes onto the central star on a viscous time scale. Thus, the density in the inner disk decreases. In extreme cases, the inner disk may fully deplete, leading to the formation of an inner cavity in the disk. This has been noticed by Quillen et al. (2004). We will come back to cavity opening more generally in Chapter 6.

2.6.2 Viscous disk evolution

In the above description of type II migration, the evolution of a viscous disk is assumed to be inwards accretion onto the central star, with a viscous torque equal, for any r, to $T_\nu(r)$ given by Eq. (2.10). The viscous torque T_ν is the torque exerted on the part of the disk outside the centered circle of radius r by the part of the disk inside the circle. It is positive. Thus, through every centered circle, there is an outward flow of angular momentum. Because the disk is in Keplerian rotation, the specific angular momentum $j = r^2\Omega$ is an increasing function of r ($j \propto \sqrt{r}$). Therefore, a loss of angular momentum leads to an inwards flux of the gas. However, angular momentum should be conserved. Consequently, the inward flux cannot concern the full disk. The outermost part of the disk has to receive angular momentum and spread outwards. The minimal energy configuration consists in an infinitely small mass particle orbiting infinitely far from the central star carrying all the angular momentum, while all the mass is concentrated on the central point. Due to viscous dissipation, the disk naturally tends to this configuration. Therefore, there is no stationary state and the density, as well as the viscous torque, depend on time. In this subsection, we review the work by Lynden-Bell and Pringle (1974 ; LP74 hereafter) on the global evolution of viscous disks.

Denote $F = 2\pi r\Sigma v_r$ the outward flux of material through radius r. The disk evolving under its own viscosity is assumed to be axisymmetric. We consider that Σ, v_r, F and T_ν depend on r and on the time t, while j only depends on r because the rotation is assumed Keplerian at all time. Because j is univoquely linked to r, functions of r may be expressed and treated as functions of j via :

$$\frac{\partial}{\partial r} \equiv \frac{\mathrm{d}j}{\mathrm{d}r}\frac{\partial}{\partial j} \tag{2.51}$$

Consider an elementary ring between r and $r + \delta r$, of mass $m = 2\pi r\Sigma\delta r$. Its variation of angular momentum comes from the differential viscous torque it receives and reads :

$$\frac{\mathrm{D}}{\mathrm{D}t}(jm) = -\delta r\frac{\partial T_\nu}{\partial r} \ .$$

The mass m is constant, and $\mathrm{D}j/\mathrm{D}t = (\mathrm{d}j/\mathrm{d}r)v_r$. This leads to : $(\mathrm{d}j/\mathrm{d}r)F = -\partial T_\nu/\partial r$. Using Eq. 2.51, it can be rewritten as :

$$F = -\frac{\partial T_\nu}{\partial j} \ . \tag{2.52}$$

In the continuity equation (2.4), the term $\nabla(\Sigma\vec{v})$ can be expressed as $(2\pi r)^{-1}\partial F/\partial r$. Therefore, using Eqs. (2.10) and (2.52) the continuity equation reads :

$$\frac{\partial}{\partial t}\left(\frac{T_\nu}{3\pi\nu r^2\Omega}\right) + \frac{1}{2\pi r}\frac{\partial}{\partial r}\left(\frac{\partial T_\nu}{\partial j}\right) = 0$$

Multiplying by $(2\pi r)$ and using Eq. (2.51) leads to Eq. (12) of LP74 :

$$\frac{\partial^2 T_\nu}{\partial j^2} = -\frac{\partial}{\partial t}\left[\frac{T_\nu}{\frac{3}{2}r\Omega\nu(\mathrm{d}j/\mathrm{d}r)}\right] \ . \tag{2.53}$$

Denoting $\tilde{k}^{-2} = 3(GM_*)^2\nu$ and using the third Kepler's law Eq. (1.1) leads to a simplified expression of Eq. (2.53), which is Eq. (14) of LP74 :

$$\frac{\partial^2 T_\nu}{\partial j^2} = 4\tilde{k}^2 j^2\frac{\partial T_\nu}{\partial t} \ . \tag{2.54}$$

Particular solutions Let us assume $T_\nu(j,t) = \tilde{T}_\nu(j)e^{-st}$, where s is an arbitrary constant with the dimension of a frequency. Then, denoting $k^2 = \tilde{k}^2 s$, Eq. (2.54) gives:

$$\frac{\mathrm{d}^2}{\mathrm{d}j^2}\tilde{T}_\nu + 4k^2 j^2 \tilde{T}_\nu = 0 \tag{2.55}$$

We now set $x = j^2 = GM_* r$ and $\tilde{T}^1_\nu = x^{-1/4}\tilde{T}_\nu = j^{-1/2}\tilde{T}_\nu$. Then, $\mathrm{d}j = \mathrm{d}x/(2x^{1/2})$, and Eq. (2.55) transforms into:

$$\begin{aligned}
2x^{1/2}\frac{\mathrm{d}}{\mathrm{d}x}\left(2x^{1/2}\frac{\mathrm{d}}{\mathrm{d}x}\left(x^{1/4}\tilde{T}^1_\nu\right)\right) + 4k^2x^{5/4}\tilde{T}^1_\nu &= 0 \\
2x^{1/2}\frac{\mathrm{d}}{\mathrm{d}x}\left(2x^{3/4}\frac{\mathrm{d}}{\mathrm{d}x}\tilde{T}^1_\nu + \frac{1}{2}x^{-1/4}\tilde{T}^1_\nu\right) + 4k^2x^{5/4}\tilde{T}^1_\nu &= 0 \\
4x^{5/4}\frac{\mathrm{d}^2}{\mathrm{d}x^2}\tilde{T}^1_\nu + 4x^{1/4}\frac{\mathrm{d}}{\mathrm{d}x}\tilde{T}^1_\nu - \frac{1}{4}x^{-3/4}\tilde{T}^1_\nu + 4k^2x^{5/4}\tilde{T}^1_\nu &= 0 \\
x^2\frac{\mathrm{d}^2}{\mathrm{d}x^2}\tilde{T}^1_\nu + x\frac{\mathrm{d}}{\mathrm{d}x}\tilde{T}^1_\nu + \left(k^2x^2 - \frac{1}{16}\right)\tilde{T}^1_\nu &= 0
\end{aligned}$$

Denoting $X = kx$, this makes:

$$X^2\frac{\mathrm{d}^2}{\mathrm{d}X^2}\tilde{T}^1_\nu + X\frac{\mathrm{d}}{\mathrm{d}X}\tilde{T}^1_\nu + \left(X^2 - \left(\frac{1}{4}\right)^2\right)\tilde{T}^1_\nu = 0\ ,$$

which is Bessel's equation. Thus, $\tilde{T}^1_\nu = \tilde{A}(k)J_{1/4}(X) + \tilde{B}(k)J_{-1/4}(X)$, where $\tilde{A}(k)$ and $\tilde{B}(k)$ are arbitrary constants, corresponding to the k mode in study. We define $\mathcal{A}(k) = k^{-1/4}\tilde{A}(k)$ and $\mathcal{B}(k) = k^{-1/4}\tilde{B}(k)$ This makes:

$$\begin{aligned}
\tilde{T}^1_\nu &= k^{1/4}\left[\mathcal{A}(k)J_{1/4}(kx) + \mathcal{B}(k)J_{-1/4}(kx)\right] \\
\tilde{T}_\nu &= (kx)^{1/4}\left[\mathcal{A}(k)J_{1/4}(kx) + \mathcal{B}(k)J_{-1/4}(kx)\right] \\
T_\nu &= e^{-st}(kx)^{1/4}\left[\mathcal{A}(k)J_{1/4}(kx) + \mathcal{B}(k)J_{-1/4}(kx)\right]\ .
\end{aligned}$$

For all $s > 0$, and associated k, there is a mode like this. The general solution of Eq. (2.55) is a superposition of such modes, so:

$$T_\nu = \int_0^\infty e^{-k^2t/\tilde{k}^2}(kx)^{1/4}\left[\mathcal{A}(k)J_{1/4}(kx) + \mathcal{B}(k)J_{-1/4}(kx)\right]\mathrm{d}k\ . \tag{2.56}$$

This solution simply has to be fitted to the boundary conditions.

For instance, the elementary solutions under the boundary solution that $T_\nu = 0$ at $x = x_*$ are:

$$T_\nu = e^{-st}(kx)^{1/4}\left[J_{1/4}(kx) - \frac{J_{1/4}(kx_*)}{J_{-1/4}(kx*)}J_{-1/4}(kx)\right]\ .$$

The solutions for which $x_* = 0$ (no central torque) have $B(k) = 0$. The Fourier-Bessel Theorem states that:

$$\int_0^\infty\int_0^\infty \mathcal{A}(k)J_n(kx)(kx)^{1/2}\,\mathrm{d}k\,J_n(k'x)(k'x)^{1/2}\,\mathrm{d}x = \mathcal{A}(k')\ .$$

Applying this to Eq. (2.56) with $t = \mathcal{B}(k) = 0$ provides a way of fitting $\mathcal{A}(k)$ to the initial conditions. It gives:

$$\int_0^\infty T_\nu(j,0)J_{1/4}(k'x)(k'x)^{1/2}\,\mathrm{d}x = \mathcal{A}(k')\ . \tag{2.57}$$

Gaussian density profile Consider the particular case $T_\nu(j,0) = Cj\exp(-aj^4)$, with a and C arbitrary constants. This corresponds to an initial density distribution with a Gaussian shape:

$$\Sigma = \frac{T_\nu}{3\pi\nu j} = \frac{C}{3\pi\nu}\exp(-a(GM_*r)^2) \ .$$

For this special initial condition, another theorem is very convenient. It states that:

$$\int_0^\infty \exp(-ax^2)J_l(kx)k^{1-l}x^{1+l}\,\mathrm{d}x = k(2a)^{-(l+1)}\exp(-k^2/4a) \ . \tag{2.58}$$

Applied with $l = 1/4$ to Eq. (2.57) with our Gaussian initial condition, it gives:

$$\mathcal{A}(k) = Ck(2a)^{-3/2}\exp(-k^2/4a) \ ,$$

and thus:

$$T_\nu(j,t) = \int_0^\infty \exp\left[-k^2(t\tilde{k}^{-2} + \frac{1}{4a})\right] k^{5/4}x^{1/4}J_{1/4}(kx)\,\mathrm{d}k\ C(2a)^{-5/4} \ .$$

The integral is in essence the same as the preceding one, so that applying Eq. (2.58) we obtain: $T_\nu(j,t) = C\mathcal{T}^{-5/4}j\exp-(ax^2/\mathcal{T})$, where

$$\mathcal{T} = 4a\tilde{k}^{-2}t + 1 = 12a(GM_*)^2\nu t + 1$$

is a dimensionless time.

From now on in this thesis, we set as unit the mass of the central star M_* and the gravitational constant G; consequently, $\Omega = r^{-3/2}$ and $j = \sqrt{r}$. Finally, in terms of the physical variables, this solution is:

$$T_\nu = C\mathcal{T}^{-5/4}\sqrt{r}\exp\left(-\frac{ar^2}{\mathcal{T}}\right) \tag{2.59}$$

$$F = C\mathcal{T}^{-5/4}\exp\left(-\frac{ar^2}{\mathcal{T}}\right)\left[1 - \frac{4ar^2}{T}\right] \tag{2.60}$$

$$\Sigma = \frac{C\mathcal{T}^{-5/4}}{3\pi\nu}\exp\left(-a\frac{r^2}{\mathcal{T}}\right) \tag{2.61}$$

$$v_r = -\frac{3}{2}\frac{\nu}{r}\left[1 - \frac{4ar^2}{\mathcal{T}}\right] \tag{2.62}$$

This solution (which is Eq. (18') of LP74, except that they have (GM_*r) where we have r) is illustrated on figure 2.5. The density profile keeps a Gaussian shape, the height of which decreases while the width increases (bottom panel of the figure). This corresponds to a loss of material by accretion onto the central object and spreading outward for angular momentum conservation. The radial velocity (top panel) is an increasing function of r and a decreasing function of time. It is negative close to the star and positive as $r \to \infty$. The radius separating inflow and outflow is given by:

$$r_o(t) = \frac{1}{2}\left(\frac{\mathcal{T}}{a}\right)^{\frac{1}{2}} \propto \sqrt{\mathcal{T}} \ . \tag{2.63}$$

We note in passing that the particular case $a = 0$ in Eqs. (2.59)-(2.62) corresponds to the regime where the density is constant in space and time ($\Sigma = C/3\pi\nu$). This gives $T_\nu = 3\pi\nu\Sigma\sqrt{r}$ – which is Eq. (2.10) – and a simple constant expression for v_r that we will use further:

$$v_r = -\frac{3}{2}\frac{\nu}{r} \ . \tag{2.64}$$

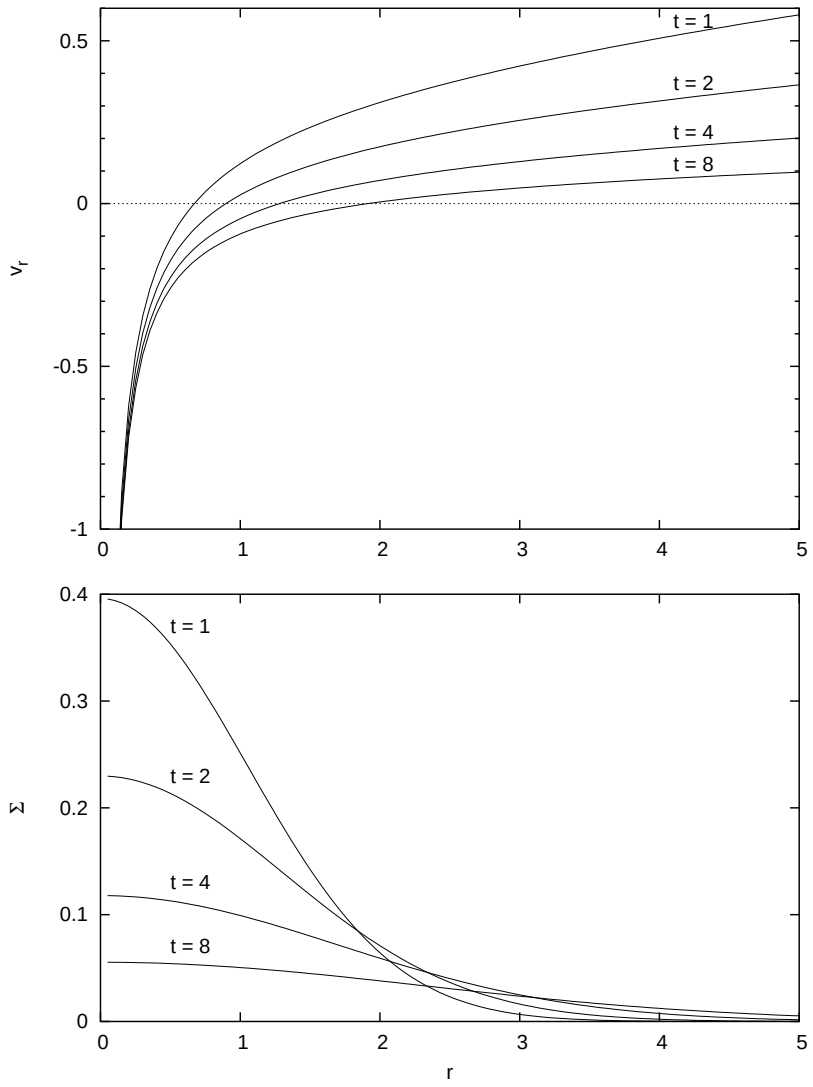

Figure 2.5: Evolution of the radial velocity and the density with time as described by Eqs. (2.62) and (2.61). The parameters are $a = C = G = M_* = 1$, $\nu = 0.1$, so that $\mathcal{T} = 1.2\,t + 1$. The abscissa is the radius from central star, r.

Elementary solution With initial condition a Dirac distribution $\delta(r - r_1)$, for $T \gg 1$ and $T \gg r/r_1$, the solution of Eq. (2.54) has the form :

$$T_\nu = 2{-}1/4\tilde{k}^{-2}\frac{1}{r_1}\sqrt{\frac{r}{r_1}}\mathcal{T}^{-5/4}\exp\left(-\frac{r^2}{2\mathcal{T}r_12}\right)$$

which has precisely the form of the special solution above. As Eq. (2.54) is linear, the disk configuration converges to the one described by Eqs. (2.59)-(2.62) for any initial distribution (which is a linear combination of Diracs).

2.6.3 Application to type II migration

In type II migration, the planet follows the viscous evolution of the disk. Thus, if $r_p < r_o(t)$, it migrates inwards. But if the planet orbits beyond the radius separating inflow and outflow, it should be pushed outward by the spreading of the disk. This idea has been promoted by Ward (2003) and Veras and Armitage (2004).

This shows that the global evolution of the disk has to be taken into account to model properly type II migration. The simple consideration of section 2.6.1, based on expression Eq. (2.10) for the viscous torque only provides a qualitative idea of the migration timescale. We will come back to this issue at the end of Chapter 5 and in Chapter 6.

Chapter 3

Disk surface density transitions as protoplanet traps

3.1 Introduction

As we discussed in Chapters 1 and 2, type I migration is a serious bottle-neck for the formation of planets because the timescale for drifting into the Sun is shorter than the growth timescale. Recent work by Alibert et al. (2005) has shown that the core build up time scale can be lowered by taking migration into account, which prevents the depletion of the core feeding zone. However, these authors find that the most up to date type I migration timescale estimate, which includes three dimensional effects and the co-rotation torque (Tanaka et al., 2002), still needs to be lowered by a factor $10 - 100$ in order to allow for the solid core survival.

Some mechanisms have been proposed to reduce or prevent type I migration. As mentioned in Chapter 1, the turbulence can exert strong stochastic torques on the proto-planets, leading to a random walk of semi major axis, rather than a monotonic decay (Nelson, 2005). Menou and Goodman (2004) have found that a realistic temperature profile may induce a significant reduction of the differential Lindblad torque. More recently, Paardekooper and Mellema (2006) have shown that in non-isothermal disks, when one takes into account the radiative transfer of energy in a self consistent manner, in some cases the torque felt by the planet can change of sign, leading to an outward migration.

In this chapter we show that even in a laminar, iso-thermal disk, type I migration into the Sun can be prevented, provided that the surface density has a steep positive radial gradient at some location. This location acts as a planet trap for type I drifting bodies.

The idea, originally proposed by Masset (2002), is that the total torque exerted by the disk onto the planet can be split into two parts: the differential Lindblad torque, that corresponds to the torque of the spiral wake that the planet excites in the disk, and the corotation torque, exerted by the material located in the planet coorbital region (see Chapter 2). The corotation torque scales with the radial gradient of Σ/B (see Eq. (2.38)), where Σ is the disk surface density and B is the second Oort's constant. This scaling makes the corotation torque a quantity very sensitive to local variations of the disk surface density or rotation profile.

In the following, we assume that the surface density transition occurs on a length scale Λ of a few pressure scale heights H. We consider the case in which the surface density is larger on the outside of the transition, but we do not limit ourselves to the case where the surface density on the inside is negligible compared to its value on the outer side.

In section 3.2 we provide simple analytical estimates of the Lindblad and corotation torques at a surface density transition. We show that the corotation torque, which is a positive quantity there, is likely to overcome the Lindblad torque if the transition is localized enough, *i.e.* Λ smaller than a few H. In section 3.3 we describe the numerical setup that we used to check this prediction with a numerical hydro-code. In section 3.4, we present the results of our numerical simulations which indeed exhibit for a wide range of parameters a fixed point at the transition, *i.e.* a point where the corotation and Lindblad torques cancel each other and where planetary migration stops. We also discuss in this section the issue of the saturation of the corotation torque and the need of turbulence to prevent it, and the conditions under which turbulence is able or not to unlock a planet from the transition. We then discuss in section 3.5 where in protoplanetary disks such surface density transitions can be found, and what are the consequences of these planet traps on giant planet formation. This work has been done in collaboration with F. Masset and J. Ferreira and led to the publication of an article (Masset et al., 2006). This Chapter is based on the paper.

3.2 A simple analytic estimate

As shown in Chapter 2, a protoplanet embedded in a gaseous protoplanetary disk excites in the latter a one-armed spiral wake (Ogilvie and Lubow, 2002). This wake exerts a torque on the planet, which can be decomposed into the outer Lindblad torque (T_{Lo}), which is negative and that is exerted by the outer arm, and the inner Lindblad torque (T_{Li}), which is positive and that is exerted by the inner arm. These two torques do not cancel out. The residue $T_{dLR} = T_{Lo} + T_{Li}$, called the differential Lindblad torque, is negative (Ward, 1986; Tanaka et al., 2002), thereby leading to inward migration. In particular, for a disk with uniform surface density and aspect ratio (Ward, 1997) :

$$T_{dLR} \approx -8\frac{H}{r}\left(\frac{T_{Li}+|T_{Lo}|}{2}\right).$$

As noted by Ward (1997), in a nebula with $h = O(10^{-1})$, the differential Lindblad torque is a sizable fraction of the one-sided Lindblad torque. This is of some importance for our concern : denoting T'_{dLR} the Lindblad torque on an empty cavity edge (it then amounts to the outer Lindblad torque, i.e. $T'_{dLR} = T_{Lo}$) and T_{dLR} the Lindblad torque further out in the disk where we assume the surface density and aspect ratio profiles to be flat, we have :

$$T'_{dLR} \approx \frac{T_{dLR}}{8H/r}, \tag{3.1}$$

which means that the Lindblad torque on a cavity edge is at most $2-3$ times larger than further out in the disk, for $0.04 < H/r < 0.06$.

In addition to the wake torque, the material in the orbit vicinity exerts on the planet the so-called corotation torque. This torque scales with the gradient of the specific vorticity (or vortensity) (Goldreich and Tremaine, 1979; Ward, 1991, 1992) :

$$T_C \propto \Sigma\frac{d\log(\Sigma/B)}{d\log r}. \tag{3.2}$$

We now estimate the ratio of the corotation torque at a cavity edge and further out in the disk (assuming a flat surface density profile). We assume that the surface density inside of the transition is Σ_i, while it is $\Sigma_o > \Sigma_i$ on the outside. We do not need to assume that $\Sigma_i \sim 0$.

However, we require that the transition from Σ_i to Σ_o occurs on a length scale $\Lambda \ll r$. In the outer disk where $\Sigma \equiv \Sigma_o$, we have :

$$\frac{d\log(\Sigma/B)}{d\log r} = 3/2, \tag{3.3}$$

while at the transition, $d\log\Sigma/d\log r$ is a sharply peaked function with a maximum that scales as :

$$\left.\frac{d\log\Sigma}{d\log r}\right|_{\max} \sim \frac{r}{\Lambda}\log\left(\frac{\Sigma_o}{\Sigma_i}\right). \tag{3.4}$$

Similarly, retaining only the terms that vary most rapidly with r at the transition :

$$\frac{d\log B}{d\log r} \simeq \frac{2r^2}{\Omega}\frac{d^2\Omega}{dr^2}, \tag{3.5}$$

where Ω is the angular velocity. The last factor of the above equation can also be expressed, using the disk rotational equilibrium and again keeping only the terms that vary most rapidly with r, as :

$$\frac{d^2\Omega}{dr^2} \simeq -\frac{\Omega h^2 r}{2}\frac{d^3\log\Sigma}{dr^3}. \tag{3.6}$$

The last factor of the right hand side is a function of r that scales as $(H^2 r/\Lambda^3)\log(\Sigma_o/\Sigma_i)$, and that has, for a sufficiently smooth, monotonic transition from Σ_i to Σ_o, two minima and one maximum, the exact locations and amplitudes of which depend on the surface density profile. The (inverse of) the specific vorticity logarithmic gradient is therefore :

$$\frac{d\log(\Sigma/B)}{d\log r} = \frac{r}{\Lambda}\log\left(\frac{\Sigma_o}{\Sigma_i}\right)\left(a + b\frac{H^2}{\Lambda^2}\right), \tag{3.7}$$

where a and b are numerical functions of r of order unity that depend on the exact shape of the surface density profile. In particular, one sees immediately that if $\Lambda \sim H$, the contributions of both terms (the surface density gradient and the vorticity gradient) to the corotation torque are of similar magnitude.

The corotation torque at the transition T_C' can therefore be larger than the corotation torque T_C further out in the disk by a factor :

$$\frac{T_C'}{T_C} \approx \frac{2r}{3\Lambda}C, \tag{3.8}$$

where C is a numerical factor of order unity that depends on the surface density profile.

Using Eqs. (3.1), (2.39) and (3.8), we find that :

$$\frac{T_C'}{T_{dLR}'} \approx -\frac{8H}{3\Lambda}C, \tag{3.9}$$

which means that the (positive) corotation torque can counteract the (negative) Lindblad torque at a cavity, provided that the edge of the latter be narrow enough ($\Lambda < 8HC/3$). We check by means of numerical simulations that it is indeed possible to halt type I migration on the edge of a surface density transition.

3.3 Numerical set up

We performed a large number of two-dimensional hydrodynamical simulations that we detail below. The code used was FARGO (see introduction of Chapter 5).

The surface density transition was set in the following manner. We call R the target surface density ratio between the inside and the outside of the cavity : $R = \Sigma_o/\Sigma_i$. In order to realize this ratio, we adopt a fixed profile of kinematic viscosity with an inverse ratio : $\nu_o/\nu_i = R^{-1}$. If we call r_t the mean radius of the transition, then for $r > r_t + \Lambda/2$, $\nu \equiv \nu_o$, for $r < r_t - \Lambda/2$, $\nu \equiv \nu_i$, and for $r_t - \Lambda/2 < r < r_t + \Lambda/2$, ν is an affine function of r. We then relax the surface density profile during a preliminary 1D calculation over $\sim 10^5$ orbits, so that the profile can safely be considered as steady state in the 2D calculations. In our calculations we use non-reflecting inner and outer boundary conditions, while we impose the disk surface density at the inner and outer boundary.

In all our calculations the disk aspect ratio is $H/r = 0.05$, the disk is not self-gravitating and it has a locally isothermal equation of state. The length unit is r_t. The mesh inner and outer boundaries are respectively at $r = 0.42$ and $r = 2.1$.

The mesh size in all our runs is $N_r = 168$ and $N_\phi = 450$, hence the radial resolution is 10^{-2}. The horseshoe zone width for a 15 $M_\oplus$ planet is $\sim 7.8\ 10^{-2}$, so it is ~ 8 zones wide. The error on the corotation torque due to this finite width therefore amounts to at most ~ 10 % (see Masset, 2002, figure A.3). We also made calculations with a 4 $M_\oplus$ mass planet for which the horseshoe zone is only 4 zones wide. This resolution may seem low but the corotation torque is very well captured at low resolution for small mass planets which hardly perturb the surface density profile (see discussion in Masset, 2002, Appendix A).

We contemplated the issue of whether the Roche lobe content must be included or not when integrating the torque over the disk material (D'Angelo et al., 2005; Masset and Papaloizou, 2003). We found that taking that material into account or not makes essentially no difference in our case because we consider low mass planets for which the mass of the envelope in a small fraction of the planet mass. In addition, for low-mass planets in the linear limit, the gas flow does not exhibit any Roche lobe around the planet, while the two ends of the horseshoe region reconnect through a single stagnation point located on the orbit (Masset et al., 2006, ; Tanaka, private communication).

In 2D simulations one has to introduce a potential smoothing length ϵ meant to mimic the disk vertical extent. The planet potential expression is then $-GM_p/(d^2+\epsilon^2)^{1/2}$, where d is again the distance to the planet. In our calculations we use a potential smoothing length $\epsilon = 0.7H$. This is quite a large value, which leads to underestimate the corotation torque (Masset, 2002), as it lowers the horseshoe zone width, while the corotation torque is proportional to the fourth power of this width. Our calculations are therefore conservative, and it is likely that 3D calculations would yield a torque cancellation for an even wider set of disk parameters than what we found.

3.4 Results of numerical simulations

3.4.1 Torque sampling on a cavity edge

We consider in this section a disk with a target surface density ratio between the inside and the outside of the transition set to $R = 7$. As this value is large compared to one, we call the inside part of the transition a cavity. We performed two sequences of 75 calculations in which a planet was set on a fixed circular orbit with radius $a_i = 0.65 + 10^{-2} i$ ($i = 0 \ldots 74$). For these calculations

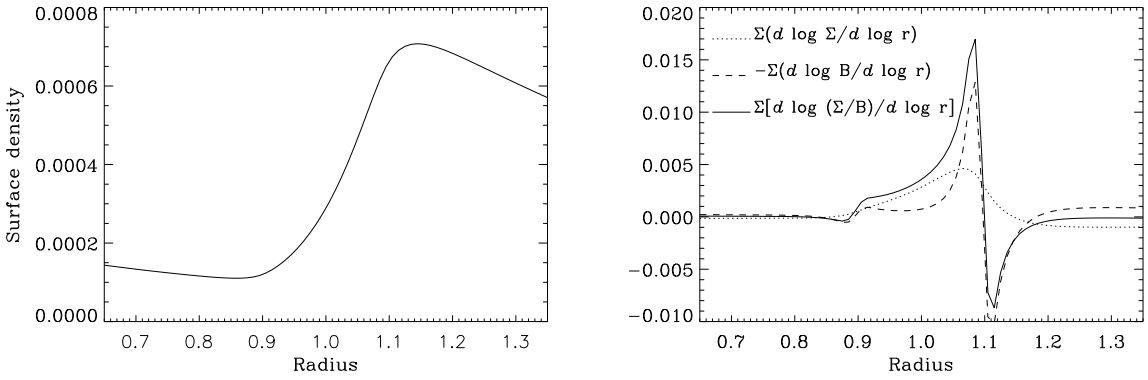

Figure 3.1: Left : surface density profile for the runs of section 3.4.1. The surface density transition occurs over $\sim 4H$, between $r \approx 0.9$ and $r \approx 1.1$.
Right : Corresponding profiles of the different logarithmic derivatives involved in the expression of the corotation torque, weighted by the surface density. The dotted line shows the logarithmic derivative of the surface density, the dashed line shows the opposite of the logarithmic derivative of the flow vorticity, and the solid line shows the sum of these two quantities. It corresponds to the R.H.S. of Eq. (3.2).

we report as a function of a_i the total torque exerted on the planet (averaged over 100 orbits, in order for the libration flow inside the co-orbital region to reach a steady state (Masset, 2002)).

The left plot of figure 3.1 shows the relaxed surface density profile after 10^5 orbits of the preliminary 1D calculation, and the right plot shows the quantities involved in the corotation torque scaling. The right panel of figure 3.1 shows that the vortensity gradient peak is only partially due to the surface density gradient, since the gradient of the flow vorticity plays a role of comparable importance, as suggested in section 3.2.

The total torque measured from numerical simulations is presented in figure 3.2. Both plots, which correspond to two different planet masses, exhibit similar features :

- On the left side (for $r < 0.8$) and on the right side (for $r > 1.2$), the torque profile is flat and negative. This corresponds to the total negative torque acting on a planet embedded in a flat surface density disk (T_{dLR}). Since the surface density is $R = 7$ times lower on the inside, the torque value is much smaller on that side.

- In the range $0.8 < r < 1.2$, the torque as a function of radius exhibits a shape very similar to the vortensity gradient shown in figure 3.1. In particular the torque has a maximum value near $r = 1.08 - 1.10$ and a minimum value near $r = 1.12 - 1.13$.

This last observation unambiguously indicates that the corotation torque largely dominates the total torque at the surface density transition, as expected from the analytic estimate. In particular, there are two positions in the disk where the total torque cancels out (and therefore where the migration is halted) : one at $r \approx 0.92$ and the other one at $r \approx 1.11 - 1.12$. The first of these fixed points is unstable : moving the planet away from it yields a torque that moves it further away, while the second one (*i.e.* the outermost one) is stable : moving the planet to a higher radius yields a negative torque that tends to bring the planet back to its former position, and vice-versa for a motion towards smaller radii. The fixed point at $r = 1.12$ should therefore trap

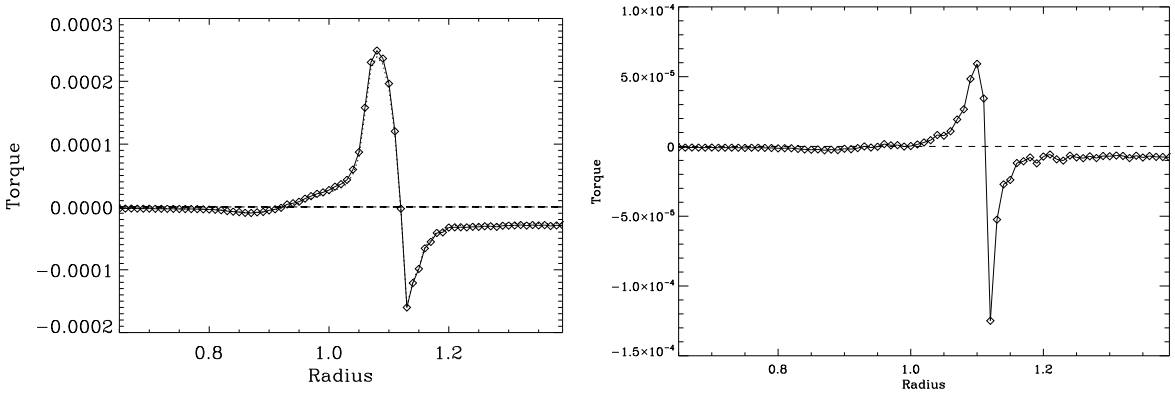

Figure 3.2: Left: Specific torque acting upon a 15 $M_\oplus$ planet on a fixed circular orbit, as a function of its orbital radius. Right: Same thing for a 4 $M_\oplus$ planet.

all type I migrating embryos. We note in passing that the torque as a function of radius does not have exactly the same shape between a 15 $M_\oplus$ and a 4 $M_\oplus$ planet. There are two reasons for this: the onset of non-linear effects between 4 $M_\oplus$ and 15 $M_\oplus$, and the inaccuracy of the corotation torque estimate for the 4 $M_\oplus$ case, for the resolution that we have adopted. However, we see that even in the 4 $M_\oplus$ case, the value of the torque maximum ($\sim$ 6. 10^{-5}) is much larger than the torque absolute value away from the cavity (for $r > 1.2$, this value is $\sim 10^{-5}$). Therefore, even if the error on the corotation torque amounts to 50 % (see Masset, 2002), one still gets a torque cancellation and a stable fixed point.

3.4.2 Halting migration at a cavity edge

We have performed a series of ten calculations with planets of masses 1.3 $M_\oplus$ to 15 $M_\oplus$ in geometric sequence, with the same disk cavity as in the previous section ($R = 7$). In these calculations the planets were released at $r = 1.35$, i.e. beyond the cavity edge, and then allowed to freely migrate under the action of the disk torque. The results are presented in figure 3.3. We see how the transition efficiently traps all these objects at the fixed point at $r = 1.12$ identified at the previous section. We note in passing that on the lower side of the mass range considered, the small width of the horseshoe region may lead to large uncertainties on the corotation torque. Nevertheless, the migration of all objects stops at locations which are all very close to 1.12. This indicates that the corotation torque at the edge, even misrepresented by a too low resolution, still strongly dominates the differential Lindblad torque. For masses lower than a few earth masses, the Hill radius is much smaller than the disk thickness and the disk response is linear. In the linear regime, the corotation to Lindblad torque ratio is independent of the planet mass. As we have stressed already, our potential smoothing length is large and our corotation torque estimate is conservative. This indicates that any small mass infalling embryo will be trapped at the cavity edge that we modeled.

Disk profiles with an extremum of the specific vorticity are prone to a linear Rossby wave instability that eventually leads to the formation of vortices (Li et al., 2000, 2001). This is the case of the transitions that we have simulated. The arc-shaped over-dense region located near $x = -0.8, y = +0.6$ in the right plot of figure 3.3 corresponds to such a vortex. It leads to a torque modulation over the synodic period between the planet and the vortex, that is seen on the

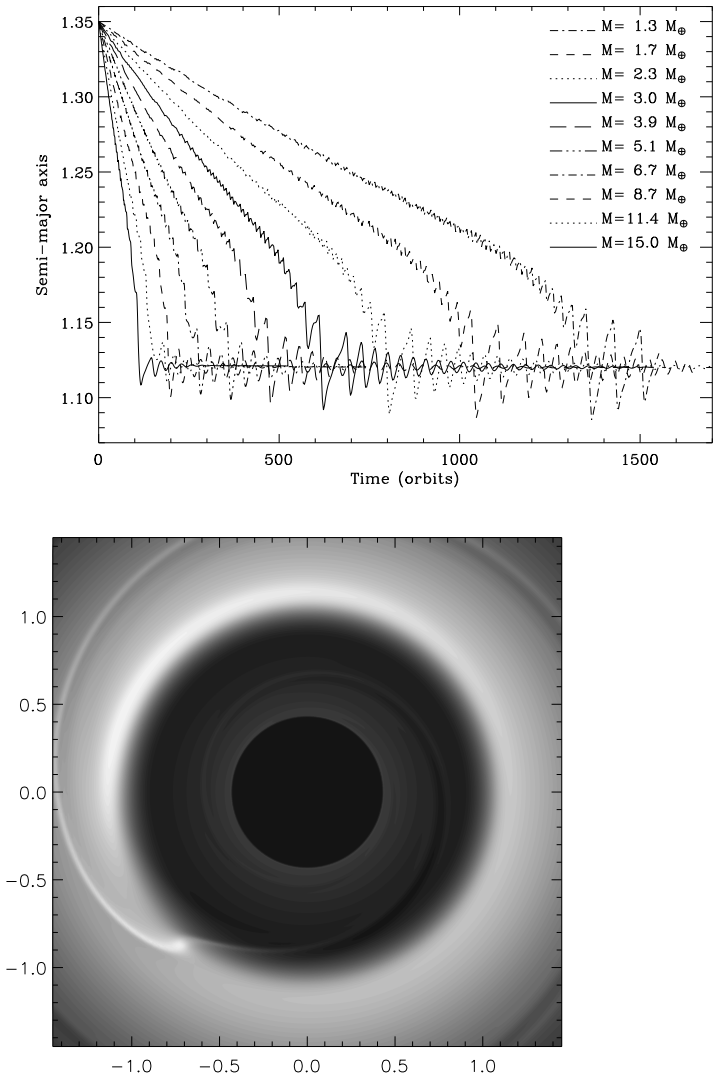

Figure 3.3: Top : Semi major axis of planet as a function of time, for the 10 different planet masses.
Bottom : Snapshot of the surface density map with a 15 $M_\oplus$ planet embedded at $t = 480$ orbits.

migration curves of the left plot of figure 3.3. As a planet approaches the transition, the synodic period increases, and so does the period of the semi-major axis modulations.

3.4.3 Torque sampling at a shallow surface density jump

We have performed a series of calculations similar to those of section 3.4.1, except that we adopted a much smaller target outer to inner surface density ratio: $R = 1.4$ instead of 7. The surface density jump is therefore a very shallow one. The results are presented in figure 3.4. They show that again there is a fixed point at which migration is halted, at $r \approx 1.09$. We have not searched further the limit inner to outer surface density ratio that leads to migration reversal, as this quantity depends on the jump radial size, on the profile adopted for the kinematic viscosity and on the potential smoothing length. We just stress that a factor $R = 1 + O(1)$ and a jump size of $\sim 4H$ suffices to halt migrating bodies.

3.4.4 Driving of trapped planets

As can be seen in figure 3.2 or 3.4, the torque maximum value is positive and large. This implies that, if the cavity radius evolves with time, either inwards or outwards, it drives any planet trapped on its edge so that its migration follows the edge evolution. More precisely, a planet will be held at a location where the specific torque acting upon it endows it with a drift rate equal to that of the cavity radius. As the torque maximum in absolute value is at least of the order of the total torque in the outer disk, this means that the edge expansion or contraction can be as fast as the type I drift rate of its trapped objects and still keep these objects trapped. We illustrate this shepherding on figure 3.5. We performed a calculation in which an initially fixed cavity such as the one considered at the previous sections (here with $R = 10$ and a transition over $4 - 5H$) traps a 15 $M_\oplus$ in-falling planet and then is endowed with an expansion rate $\dot{r}_t = 8.\ 10^{-5}$. This is achieved by imposing a kinematic viscosity profile as described in section 3.3 with a radius r_t that varies linearly with time. One can see that the planet semi-major axis follows the cavity radius evolution, so that the planet remains trapped on the cavity edge.

3.4.5 Dissipation and corotation torque saturation

Corotation torque saturation

The corotation torque, in the absence of any angular momentum exchange between the horseshoe region and the rest of the disk, is prone to saturation (see section 2.4). Here we estimate the amount of viscosity required to prevent saturation, as a function of the planet mass. The maximal amount of saturation for which one still has a torque cancellation depends on the planet mass and on the detailed disk profiles. Here we just give an order of magnitude of the viscosity needed to prevent saturation by assuming a 50 % saturation. This amount of saturation is reached when the viscous timescale across the horseshoe region is equal to the horseshoe libration timescale (Masset, 2001) :

$$\frac{x_s^2}{3\nu} = \frac{4\pi r_p}{(3/2)\Omega_p x_s}, \tag{3.10}$$

where again x_s is the horseshoe zone half width, ν is the disk effective kinematic viscosity, Ω_p is the planet orbital frequency and r_p the radius of its orbit. In order to express x_s as a function of

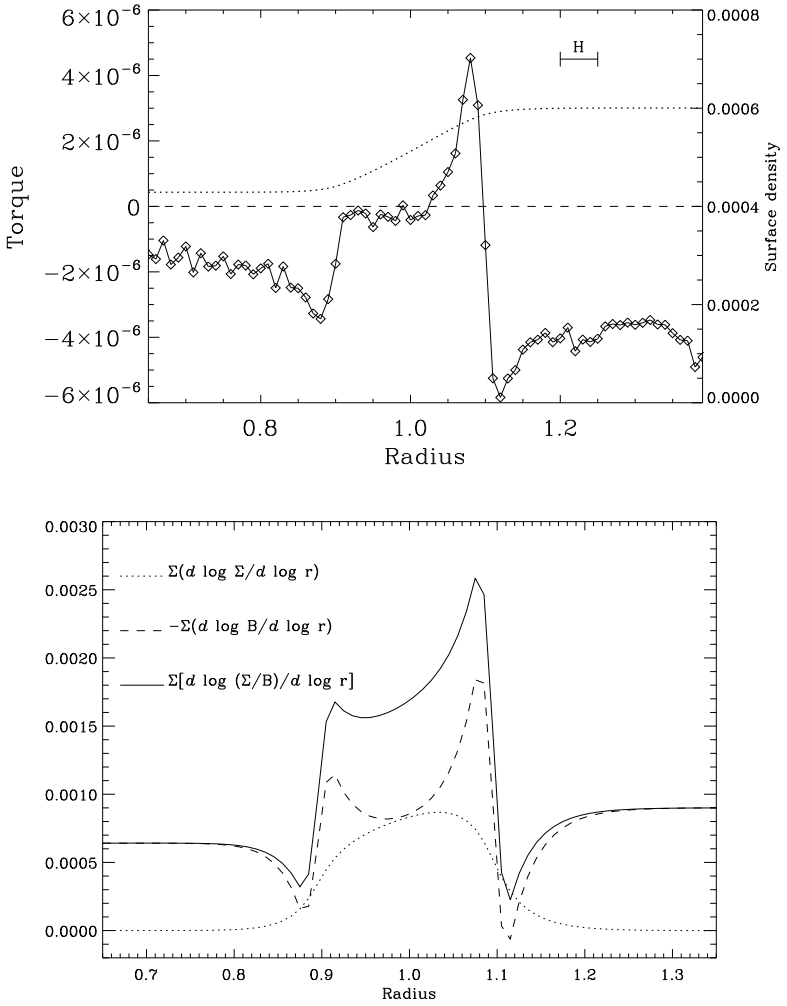

Figure 3.4: Top : surface density profile for the runs of section 3.4.3 (dotted line and right axis) and total torque exerted by the disk on the planet as a function of its semi-major axis (diamonds and left axis), for a 4 $M_\oplus$ planet.
Bottom : Corresponding profiles of the different logarithmic derivatives involved in the expression of the corotation torque, weighted by the surface density, as in figure 3.1.

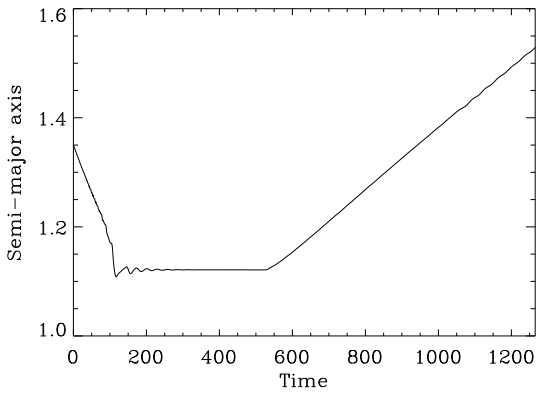

Figure 3.5: Semi-major axis as a function of time for a planet trapped in an expanding cavity. The cavity is fixed for the first 520 orbits, then is linearly expanding with time. The planet semi-major axis follows the cavity evolution so that the planet remains trapped at the cavity edge. At $t = 0$ the planet is released beyond the cavity, at $r = 1.35$. During the first 100 orbits it migrates towards the cavity where it gets trapped.

the planet mass[1], we note that in the linear (hence fully unsaturated) limit the corotation torque can be expressed as (Ward, 1991; Masset, 2001) :

$$T_C = \frac{9}{8} x_s^4 \Omega_p^2 \Sigma \ , \tag{3.11}$$

which is Eq. (2.37) with a flat density profile. From Tanaka et al. (2002) we have :

$$T_C = 0.939 (H/r)^{-2} q^2 {r_p}^4 \Omega_p^2 \Sigma \ , \tag{3.12}$$

where q is, as usual, the planet mass normalized to the stellar mass. Equations. (3.11)) and (3.12) yield :

$$x_s = 0.96 \, r_p \sqrt{\frac{q}{H/r}} \ . \tag{3.13}$$

Equations. (3.10) and (3.13) give the minimum effective viscosity to prevent the corotation torque saturation :

$$\nu = 0.035 \left(\frac{q}{H/r} \right)^{3/2} {r_p}^2 \Omega_p \ .$$

The value of ν required to prevent the corotation torque saturation of an Earth mass planet is therefore much smaller than the one inferred from disk lifetimes of T-Tauri stars, namely $\nu = 10^{-3} - 10^{-2} \ H^2 \Omega_p$ (Hartmann, 2001). Note that this also holds for large mass solid cores ($M_p = 10 - 15 \ M_\oplus$). The corotation torque acting on these objects should therefore be a large fraction of the unsaturated estimate, so the analysis presented above for the torque cancellation is essentially valid. We also note that the planets of figures 3.3 and 3.5 remain trapped over a timescale much longer than the horseshoe libration timescale, so that their corotation torque

[1]The estimate provided here is given for a flat surface density profile, but the horseshoe region width should not or very weakly depend on this assumption.

partial saturation is weak enough. The disk effective viscosity at the trap location is in these calculations $5.\ 10^{-6}$.

We comment that the corotation torque saturation could be different in a laminar disk with kinematic viscosity ν and in a turbulent disk (we discuss more in detail this topic in the next section) with the same effective viscosity, when the horseshoe region width is smaller than the turbulence length scale. The saturation should be easier to remove in this last case, which suggests that our saturation estimates is a conservative one.

Dissipation and turbulence

Since the likely physical origin of the disk effective viscosity is turbulence, in particular the turbulence generated by the Magneto-Rotational Instability (MRI) (Balbus and Hawley, 1991), the torque acting upon the planet does not have a value constant in time as in a laminar disk, but rather displays large temporal fluctuations arising from the density perturbations in the planet vicinity. It is important to assess the impact of these fluctuations on the mechanism outlined here. In the bulk of a disk with a smooth surface density profile, these torque fluctuations can yield an erratic behavior of the planet semi-major axis referred to as *stochastic migration* (section 1.3 ; Nelson and Papaloizou, 2004; Nelson, 2005). In what follows we use the torque fluctuation estimates of Nelson and Papaloizou (2004) and Nelson (2005) in order to determine whether despite of its semi-major axis jitter the planet is confined to the trap vicinity, or whether it is unlocked the from the trap position. We use the following simple prescription to perform Monte-Carlo calculations of the planet semi-major axis over a period of time $t = 10^7\ \Omega^{-1}$.

The planet orbital radius is evolved in time using an Euler method :

$$r_p(t + \Delta t) = r_p(t) + \Delta t \frac{T_l + T_f}{2B[r_p(t)]r_p(t)}, \tag{3.14}$$

where $r_p(t)$ is the planet orbital radius at date t, T_l is the torque as measured in a laminar disk for a planet in circular orbit of radius r_p, linearly interpolated from the results displayed either in figure 3.2 (left) or 3.4 (top), T_f is the torque fluctuation due to turbulence, and where a Keplerian profile is assumed for B (this is grossly wrong as far as its radial derivative is concerned, as we saw in the main text, but this is largely sufficient for our purpose here). The torque fluctuation is evaluated as follows :

$$T_f = G\Sigma_{\max}[r_p(t)]r_p(t)[2V - 1], \tag{3.15}$$

where $\Sigma_{\max}[r] = \max\left\{\Sigma(r')\right\}_{r' \in [r-H, r+H]}$, and where V is a random variable uniformly distributed over $[0, 1]$. The value of T_f is kept constant over t_c. We use the above prescription for $\Sigma_{\max}[r_p]$ since the planet is located in a region where the surface density gradient is large. The largest torque fluctuations may arise from regions located within $r_p - H$ to $r_p + H$ from the central object, and where the surface density may be significantly different from the one at the planet location. Each realization of the random variable is independent of the previous ones. We anticipate that the results should not depend on the torque fluctuation law, since the Central Limit Theorem states that the cumulative torque law tends towards a normal law (Nelson, 2005).

We place initially the planet at the outer stable fixed point, and we declare it trapped if over that amount of time it never goes through the inner, unstable fixed point, while we declare it not trapped if it happens to go through the inner fixed point. We discuss below a number of issues relevant to these calculations.

- Can the torque acting upon the planet be considered as the sum of the torque in a laminar disk and the fluctuations arising from turbulence? Nelson (2005) finds that this might not be the case, at least as long as the differential Lindblad torque is concerned, since the corotation region is not sufficiently resolved in his calculations; as an alternative explanation to the lack of the torque convergence to the laminar value, Nelson (2005) suggests the existence of very low frequency components of the torque fluctuations. As this problem is essentially open (and totally unaddressed as far as the corotation torque is concerned), we chose to describe the torque acting upon the planet by the sum of the torque in the laminar case and of the torque fluctuations due to the turbulence.

- The amplitude of the torque fluctuations can be estimated by considering a density fluctuation of order unity with a length scale of order H, at a distance H from the planet (Nelson and Papaloizou, 2004; Nelson, 2005) and found to amount to $G\Sigma r$, where G is the gravity constant and r the distance to the central object. This is the value that we adopt for our calculations.

- The time scale of the fluctuations is of particular importance to assess the torque convergence towards its laminar value. Nelson (2005) finds in his calculations that the torque fluctuations due to turbulence contain significant power at very low frequency, and suggests that this could be linked to global communication across the disk on the viscous timescale. Here our situation is rather different, as the planet lies on a radially localized structure, with a radial extent Λ. Fluctuations with frequency lower than $\sim \Lambda/c_s$ would imply turbulent structures larger than the trap width, and therefore would imply a radial displacement of the trap itself along the lines of section 3.4.4. Here we choose a correlation timescale for the turbulence of $t_c = 8\Omega^{-1} \sim 2\Lambda/c_s$ for $\Lambda \sim 4H$.

- Both the tidal torque and the torque fluctuations scale with the disk surface density, so that the time needed for the time averaged torque to reach convergence does not depend on the latter. However, the spread of the probability density of the planet semi-major axis after that timescale does depend on the disk surface density. If the expectancy of the distance of the planet to its initial location is larger than the trap width, then the planet can certainly be lost, while if it is much smaller than the trap width, the planet is certainly trapped. Our study therefore amounts to a disk critical mass search. For a given trap profile, a given planet mass and given fluctuation characteristics (amplitude – proportional to the density – and correlation timescale), there exists a critical disk mass so that a lighter disk keeps the planet trapped, while a heavier disk is unable to lock it and the planet is likely to go through the inner unstable fixed point. We perform this search in a dichotomous manner until we reach a precision of 5 % on the disk mass, and we repeat the calculation with different random seeds, so as to get an idea of the precision on the disk critical mass estimate. Our results are displayed in figure 3.6. The *disk outer mass* is defined as $M_{\text{outer disk}} = \pi r_t^2 \Sigma_{\text{out}}$, where Σ_{out} is the disk surface density on the outside of the surface density transition. We see on this figure that the deep cavity with $R = 7$ unconditionally traps $M = 1$ to 15 $M_\oplus$ protoplanets in a disk with a density profile of the minimum mass solar nebula, at any distance up to ~ 5 AU, while the shallow surface density transition would be able to retain infalling bodies only in the very central regions ($r_t \simeq 0.01$ AU, if the nebula extends that far in) of such a nebula. Further out in the disk, at $r = 0.1$ AU, a shallow transition in the MMSN would only capture embryos with $M > 4\ M_\oplus$, etc.

It is not unreasonable to assume that these simple calculations are conservative, for the following reasons :

- We have assumed the torque fluctuations to scale only with the disk surface density, which implies that all the disk material in the trap vicinity is turbulent. There is at least one realization of the trap, which is the inner edge of a dead zone (detailed in the next section), for which this statement is wrong. In our example, the trap stable fixed point corresponds to a location with a large surface density, therefore located rather on the "dead" side of the transition, *i.e.* where turbulent transport of angular momentum is inefficient and hence where the turbulence should be much weaker than contemplated in our simple Monte Carlo calculations.

- We recall that our large potential smoothing length tends to significantly underestimate the corotation torque, while the trap ability to lock infilling bodies, for a given turbulence characteristics, strongly depends on the corotation torque peak value at the surface density transition.

We conclude this section with two remarks. Firstly, the numerical simulations undertaken by Nelson and Papaloizou (2004) and Nelson (2005) neglect, for reasons of computational speed, the gravitational potential z dependency, which means that their disks have no vertical stratification. Future numerical experiments with vertical stratification may lead to different characteristics of the torque fluctuations. Secondly, other sources of turbulence have been suggested in protoplanetary disks, such as the global baroclinic instability (Klahr, 2004), which may have different torque fluctuations statistics, and for which the trap efficiency may therefore be different. To date this is essentially an unaddressed issue.

3.5 Discussion

The mechanism exhibited here is generic, since it plays a role at any positive disk surface density transition, even shallow ones, with the cautionary remark that some turbulence is required to prevent the corotation torque saturation, and that a condition is required on the disk mass to prevent the stochastic migration induced by the turbulence to overcome the trap effect. Although our knowledge of the detailed properties of protoplanetary disks is still incipient, we already know a number of locations for transitions exhibiting the above properties, which constitute potential traps for infalling embryos :

- At the inner edge of a dead zone (Gammie, 1996; Fromang et al., 2002), the surface density is expected to be significantly larger in the dead zone than in the ionized inner disk, while the inner disk turbulence provides the dissipation required to maintain the corotation torque. If the dead zone inner radius changes with time (since layered accretion involving a dead zone is thought not to be a steady process) the objects trapped at the fixed point follow the transition radius, as shown in section 3.4.4.

- Sizable surface density transitions can also be found at the transition between an inner disk region where jets are launched and the outer viscous disk (Ferreira and Pelletier, 1995). Indeed, the accretion velocity in the jet emitting disk (hereafter JED) region is entirely due to the jet torque and becomes much larger than in a standard accretion disk (hereafter SAD). Mass flux conservation then leads to a surface density jump at the transition radius

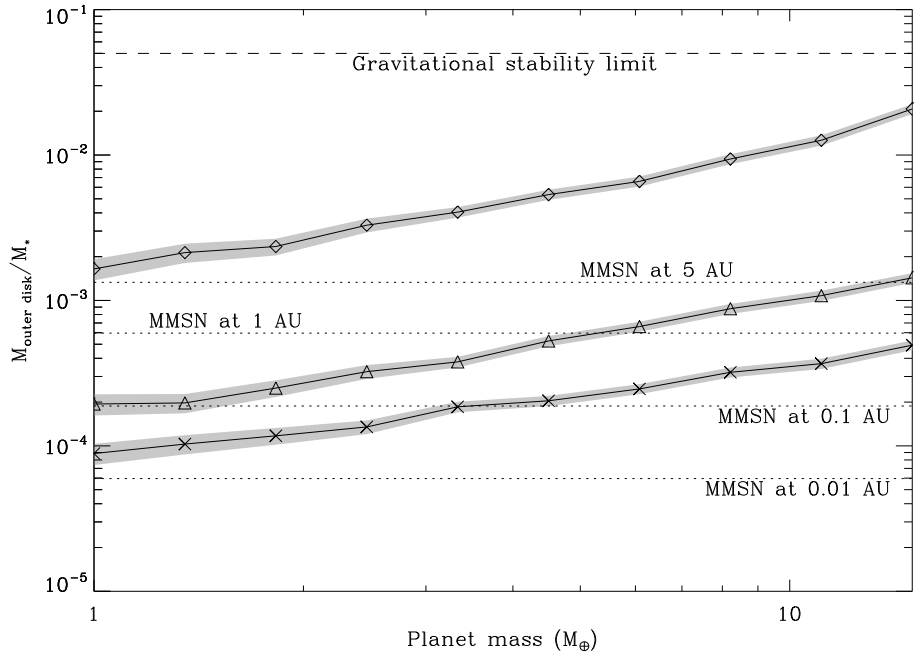

Figure 3.6: Critical disk mass as a function of the planet mass (from 1 $M_\oplus$ to 15 $M_\oplus$), for different transition profiles: the $R = 7$ cavity of section 3.4.1 (diamonds), the $R = 1.4$ shallow jump of section 3.4.3 (crosses). The triangles represent the trapping limit for a torque curve with a peak maximum which is the geometric mean of the peak values of the $R = 7$ and $R = 1.4$ transitions, which we assume to be representative of a transition with $R \simeq 1 + \sqrt{0.4 \times 6} = 2.5$. The dotted lines show the minimum mass solar nebula relative mass (as defined by its local surface density) at different radii. The thickness of the gray line indicates the results standard deviation found with different random seeds.

between the SAD and the JED. This radius has been inferred to vary from 0.3 to a few astronomical units in some T-Tauri stars[2] (Coffey et al., 2004; Pesenti et al., 2004). As all known embedded objects have jets, the existence of such a transition radius provides a natural trap for in-falling embryos over the jet lifetime.

- We finally mention the outer edge of a gap opened by a preexisting giant protoplanet. The latter can trap planetesimals at Mean Motion Resonances (Hahn and Ward, 1996), but also at the large positive surface density gradient found on its gap outer edge.

We note that the first two possibilities might not coexist in an accretion disk. Not all T-Tauri stars show indeed evidence of high velocity jets (Hartigan et al., 1995). For these jet-less stars, the whole disk is likely to resemble a SAD with a dead zone in its innermost region. The protoplanet trap would then be realized at the inner radius of the dead zone, namely only if there is a SAD settled at smaller radii. Objects with a dead zone extending down to the star would have no trap. On the contrary, young stars producing jets require the presence of a JED in the inner disk region. In that case, the trap is located at the outer JED radius (the JED itself may extend down to the star with no impact on the trap). Note also that since a JED is less dense than a SAD, it is unlikely that a dead zone would exist (Ferreira, private communication).

The likely existence of such planetary traps in protoplanetary disks has important implications for the formation of giant planets. It constitutes a workaround to the timescale conflict between a solid core build up (which is slow) and its migration to the central object (which would be fast, if the object was not stopped at a trap). Figure 3.5 may suggest that a large amount of solid embryos should accumulate at the trap location, speeding up the build up of a critical mass core ($M_p \simeq 15\ M_\oplus$) which could accrete the nebula gas and convert itself into a giant planet. This is actually misleading. We have done a series of simulations, where we placed one embryo at the trap location and a second embryo (of smaller or equal mass) further out in the disk. In all cases, we observe that the outermost embryo stops migrating before reaching the trap location, so that it has no chance to accrete with the first embryo. If the mass of the embryo at the trap is larger than 5 Earth masses, this happens because of the indirect perturbations that the embryos exert on each other through the disk. If the mass of the embryo at the trap is less than 5 Earth masses, direct effects dominate, and the outer embryo stops its inward migration when it is trapped in a Mean Motion Resonance with the inner body. The left and right panels of figure 3.7 show these situations, respectively. In the left case, the embryo in the trap (at $r \approx 1.13$) has a mass of 10 $M_\oplus$, and the incoming embryo is 5 $M_\oplus$. The outer embryo stops its inward migration far from the trap after $\sim$ 1000 orbits. The direct interactions between the two embryos are switched off at $t = 4900$ (vertical dashed line), and this does not affect the dynamics. Maybe the circumplanetary disks are massive enough to replace the switched off planet. In the right panel of figure 3.7, the masses of the embryos are five times smaller than in the preceding case. Then, when the direct interactions are switched off (at $t = 6800$, first vertical dashed line), the incoming embryo is released from the resonance in which it was trapped, and goes on migrating inwards. Then, switching on again the direct interactions (at $t = 7000$, right vertical dashed line) does not prevent this migration, but the incoming embryo is finally trapped in another resonance at $t \approx 7800$. In any case the smaller incoming embryo does not reach the trap and the bigger embryo.

[2]In fact, velocity shifts detected in jets are interpreted as being a rotation signature which then allows one to derive the outer jet launching radius in the underlying accretion disk. This radius corresponds to our transition radius.

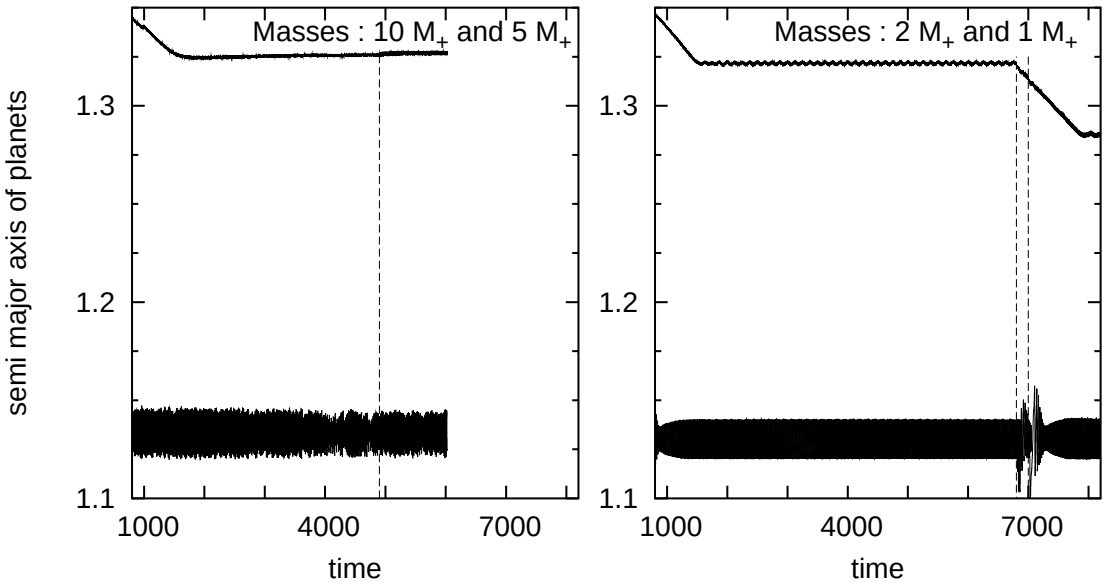

Figure 3.7: Evolutions of two embryos, the innermost one being placed at the location of the planet trap. The direct interaction between the two embryos is switched off after 4900 and 6800 orbits (vertical dashed lines) in the simulations illustrated in the left panel and in the right planet respectively. In the simulation corresponding to the right panel, the direct interaction is switched on again at time 7000 (second vertical dashed line). In the left case, the evolution is essentially unaffected, which shows the dominance of the indirect perturbations, unlike in the right case.

We have seen in section 3.2 that the corotation torque value is boosted not only by the large surface density gradient but also by the alteration of the rotation profile, which yields a large gradient of B, with both large minimal and maximal values since the gradient of B involves the second derivative of the angular velocity. One may wonder whether at a disk opacity transition, in which there is a disk temperature jump and hence a pressure gradient radial jump, the alteration of the rotation profile is sufficient to yield a peak value of the corotation torque that counteracts the Lindblad torque. We have undertaken subsidiary calculations in which we have a power law surface density profile and a sound speed profile with a localized radial jump. We found that we need a jump of the aspect ratio of ~ 1.5 over $4H$ in order to halt migration. This ratio is too large and is unrealistic in a SAD. Indeed, in a standard accretion disk in which energy is transported vertically by radiative diffusion, the central temperature scales as the optical depth to the power 1/8. As a consequence, even in the vicinity of an opacity transition, the temperature profile exhibits a smooth behavior and the corotation torque is not sufficiently strong to counterbalance the Lindblad torque. Nevertheless, Menou and Goodman (2004) have found that the opacity transitions may induce a significant reduction of the differential Lindblad torque, but they explicitly neglected the corotation torque in their study. It would be of interest to investigate whether the corotation torque boost at these locations can be sufficient to halt migration.

Remarkably, the scale height of a JED is always smaller than that of the SAD, so that the transition between these two flows naturally yields a jump in the disk aspect ratio. This is due to two effects. First, a JED feeds its jets with most of the released accretion power so that only a small fraction of it is radiated away at the disk surface: the disk is cooler. Second, in addition

to gravity, the large scale magnetic field vertically pinches the disk (Ferreira, 1997).

We also stress that at the inner dust puffed-up rims of protoplanetary disks (Isella and Natta, 2005), there can be a large radial gradient of the gas temperature, which may be sufficient to trap migrating planets.

We finally emphasize that the mechanism presented here does not allow low mass objects to proceed inside of a cavity, but rather traps them on the cavity edge. This is quite different from what has been studied in the context of gap opening planets, which migrate further inside until they reach the 2:1 resonance with the cavity edge (Kuchner and Lecar, 2002).

3.6 Conclusions

We have shown that the type I migration of $M_p < 15 M_\oplus$ planets can be halted at radially localized disk surface density jumps (the surface density being larger on the outside of the jump). Some viscosity is then required to prevent the corotation torque saturation. It is well known that turbulent viscosity tends to induce stochastic migration of the embryos, and therefore tends to act against the trap. The lighter the disk, the easier it is to keep an embryo trapped, since its radial jitter over the timescale needed to reach torque convergence is small and can be confined to the vicinity of the trap stable fixed point. Inversely, the lighter the embryo, the more difficult it is to trap it : in the zero mass limit, the embryo has no tidal torque and only feels the torque fluctuations arising from turbulence. We have shown that a jump with a large surface density ratio efficiently traps embryos above one Earth mass up even in relatively massive disks, such as the MMSN at $r = 5$ AU, while shallow jumps (a 40 % surface density increase over ~ 4 disk scale heights) will retain embryos of a few Earth masses and more only in light disks, such as the MMSN at $r = 0.1$ AU. We have illustrated by means of numerical simulations that a surface density jump traps in-falling embryos, and that it drives them along with it if it moves radially as the disk evolves. Such a jump can occur at different locations in a protoplanetary disk : it can be found at the transition between the standard accretion disk solution (SAD) and the jet emitting disk (JED), thought to be at a distance 0.3 to $1 - 2$ AU from the central object. It can also be found at the inner edge of a dead zone, where one expects a very large ratio of outer to inner surface densities. It may also be found at the outer edge of a protoplanetary gap if one giant planet already exists in the disk. We will come back to this in the final chapter of this thesis. Planetary traps can hold the type I migration of proto-giant cores over the timescale needed to overcome the critical mass ($\sim 15\ M_\oplus$) over which rapid gas accretion begins onto these cores, which are then quickly converted into giant planets that should enter the slow, type II migration regime. Finally, we mentioned that although temperature radial jumps in principle also yield large peaks of the corotation torque, they are unlikely to be able to counteract the Lindblad torque by themselves, as the temperature gradients required for that are unrealistically large in a standard accretion disk.

Chapter 4

On the width and shape of gaps

4.1 Introduction

Among all the features resulting from planet-disk interaction, the opening of a gap is one of the most spectacular, and one of those which play the most crucial role on planet migration. In fact, whether a gap is opened or not, the planet obeys the type I or type II migration regime. For type III migration, the shape and the depth of the gap is a critical parameter because it determines the coorbital mass deficit and the mass flow through the gap.

However, there is a lack of a quantitative analytical understanding of the gap profiles. Classically, the gap is considered to have a step function profile, with the edges located at the sites where the total gravity torque is equal to the total viscous torque, as described in section 2.5. A more sophisticated approach has been recently presented by Varnière et al. (2004). They provide an analytic expression that describes the gap profile, by equating the viscous and gravity torques on each elementary disk ring. We will give more details on this approach in section 4.2. The problem is that, when the viscosity is small, the viscous torque is small as well, and thus it cannot counterbalance the gravity torque. Consequently, in a low viscosity disk, a non-migrating planet should open a very wide gap, unlike what is observed in numerical simulations (see e.g. figure 4.1) : gaps do increase in width and depth as the viscosity decreases, but the dependence of the gap profile is less sensitive on viscosity in the numerical simulations than it is expected in theory.

The reason for this difference is that not all of the gravity torque is locally deposited in the disk. It is transported away by density waves (Goldreich and Nicholson, 1989; Papaloizou and Lin, 1984; Rafikov, 2002, see Appendix C). These waves are observed in simulations. In this situation, the viscous torque has to counterbalance only a *fraction* of the gravity torque, which yields narrower gaps than expected from the simple viscous/gravitational torque balance.

An evaluation of the fraction of the gravitational torque that is locally deposited at shock sites in the disk has been undertaken by Rafikov (2002). However he did not use his analysis to provide an analytic representation of the gap profile. Moreover, his calculation required several assumptions (the planet Hill radius had to be much smaller than the local disk height, the disk surface density was assumed to be uniform, etc.), which are not satisfied in the general giant planet case.

Here we introduce a novel approach. We follow a fluid element along its trajectory which, in the steady state, is periodic in the planet corotating frame. A flux of angular momentum carried by the density waves corresponds to a pressure torque acting on the fluid element, whose

average over a synodic period is non-zero. In this work, we evaluate this averaged pressure torque, together with the gravity and viscous torques. The fact that the fluid element path is closed implies that these time averaged torques balance.

In section 4.3 we introduce the pressure torque, and we use numerical simulations to check that the gap structure is set by the equilibrium between the gravity torque and the sum of the viscous and the pressure torques. In section 4.4 we construct a semi-analytic algorithm and we get an expression to compute that gap profile. We compare our results with the profiles obtained in numerical simulation, and we discuss the merits and limitations of our method. In section 4.5 we use our algorithm to explore the dependence of the gap structure on disk viscosity and aspect ratio. We recover the trends observed in numerical simulations, namely the limited gap width in low viscosity disks and the filling of the gap with increasing viscosity and/or aspect ratio. Finally in section 4.6, we provide a gap opening criterion that simultaneously involves the viscosity, the scale height and the planet mass. This work was published in Icarus (Crida et al., 2006) ; the following chapter is based on the article.

4.2 First determination of the gap profile

In this section we refine the simple model presented in Chapter 2 by differentiating the gravity and viscous torques which, in principle, allows to determine the gap profile. Nevertheless, we show that considering only these two torques, as usually done, is not sufficient to achieve a quantitatively correct description of the gap profiles.

Differential torques

Varnière et al. (2004) proposed a more refined approach than the one described in section 2.5 to model the surface density profile in the gap. Their approach is based on a simple consideration : in equilibrium, when a steady state is reached, the gravity torque and the viscous torque must be equal on every elementary ring of the disk. The torques acting on elementary rings can be computed by differentiation relative to r of the expressions of the total torques given by Eqs. (2.10) and (2.13) :

$$\delta T_\nu(r) = -\frac{3}{2}\nu\Omega\left[\frac{r}{\Sigma}\frac{\mathrm{d}\Sigma}{\mathrm{d}r} + \frac{1}{2}\right](2\pi r\Sigma) \tag{4.1}$$

$$\delta T_g(r) \approx 0.4\, q^2 {r_p}^3 {\Omega_p}^2 r^{-1}\left(\frac{r_p}{\Delta}\right)^4 (2\pi r\Sigma) \tag{4.2}$$

Matching δT_ν and δT_g gives a differential equation in Σ :

$$\frac{1}{\Sigma}\frac{\mathrm{d}\Sigma}{\mathrm{d}r} = \frac{\delta T_g(r)}{3\pi\nu r^2\Omega\Sigma} - \frac{1}{2r} \tag{4.3}$$

The integration of this equation gives the profile of the gap.

The top panel of figure 4.1 gives examples of the solution of Eq. (4.3) for several values of the viscosity, from strong ($\nu = 10^{-3.14}$) to weak ($\nu = 10^{-6.5}$). The viscosity is assumed to be independent of the radius. Assuming an α-model in which $\nu = \alpha c_s H$ (Shakura and Sunyaev, 1973), with again $c_s = H\Omega$ denoting the sound speed, would not change the results at a conceptual level. To compute the gap profile from Eq. (4.3), we have (i) assumed that the mass of the planet is 10^{-3} in our normalized units, (ii) imposed the boundary condition $\Sigma(r_0 = 3) = 1/\sqrt{3}$ and (iii) assumed that the gravity torque is null in the horseshoe region, here approximated by :

$r_p - 2\,R_H < r < r_p + 2\,R_H$. As a consequence of (iii) the surface density profile in the vicinity of the planet assumes an equilibrium slope proportional to $1/\sqrt{r}$, which makes δT_ν null. Notice that the slopes of the surface density at the edges of the gap do not depend on our assumptions (ii) and (iii), but are dictated solely by the differential equation (4.3). We remark that the profiles illustrated in the figure are the same as in Varnière et al. (2004), despite the fact that these authors consider the gravity torque as given by the sum of the individual Lindblad resonances. This again underlines the equivalence of the two approaches for the calculation of the gravity torque discussed in section 2.2.

Numerical simulations

We have tested the results of these analytic calculations using purely numerical simulations. For this purpose, we have used the 2D hydrodynamic code FARGO, described in section 5.1, and considered a Jupiter mass planet ($q = 10^{-3}$) in a disk, whose initial surface density profile decays as $1/\sqrt{r}$, and $\Sigma(r_p) = 6.10^{-4}$ (the value of the Minimal Mass Solar Nebula, assuming that our unitary radius corresponds to 5 AU (Hayashi, 1981)). The disk aspect ratio was fixed at 5%. The viscosity was chosen equal to the values used for the analytic computations, for direct comparison, and independent of radius. In these simulations, the planet was assumed not to feel the gravity of the disk, so that it did not migrate. It's orbit was circular. The grid used by the code for the hydrodynamical calculations extended from 0.5 to 3 (we recall that the planet location is $r_p = 1$). The boundary conditions in r are non-reflecting, which means that the waves behave as if they were propagating outside the boundaries of the grid. The angular momentum they carry is thus lost ; we have checked that the flux through the outer boundary represents only a negligible fraction of the total gravity torque (see Appendix C). The relative surface density amplitude perturbation at the outer boundary has been measured to be less than 5%. The size of the grid was 150 cells in radius and 325 cells in azimuth. The simulations were carried on for 1000 planetary orbits, for viscosity down to $10^{-5.0}$ and 5000 orbits for weaker viscosities. At these times, the profile of the gap does not seem to evolve significantly any more, as also found by Varnière et al. (2004).

Comparisons

The results are illustrated in the bottom panel of figure 4.1. We remark an evident difference with the analytic predictions. The simulated gap is much narrower than the one predicted by the analytic expression Eq. (4.3) for low viscosities ($\nu < 10^{-6}$). At first sight, one might think that the discrepancy between the analytical and numerical solutions is due to the numerical viscosity (dissipation due to numerical errors) of the computer code. However, this is unlikely for the following reasons: (i) different gap profiles are observed for different viscosities, which shows that the simulation is not dominated by the numerical viscosity, as the latter should be the same in all simulations; (ii) changing the resolution of the grid used in the numerical scheme, which changes the numerical viscosity, does not affect the gap profiles significantly; (iii) different numerical schemes give consistent results (De Valborro, private communication).

As anticipated in the introduction of this chapter, the problem with this analytical modeling is the assumption that the gravity torque is entirely deposited in each annulus of the disk. However, even if deposition occurs, a fraction of the gravity torque is still evacuated by the waves. The problem is to evaluate this fraction. Below we show that it can be computed from a mean pressure torque acting on the fluid elements over their periodic equilibrium trajectories.

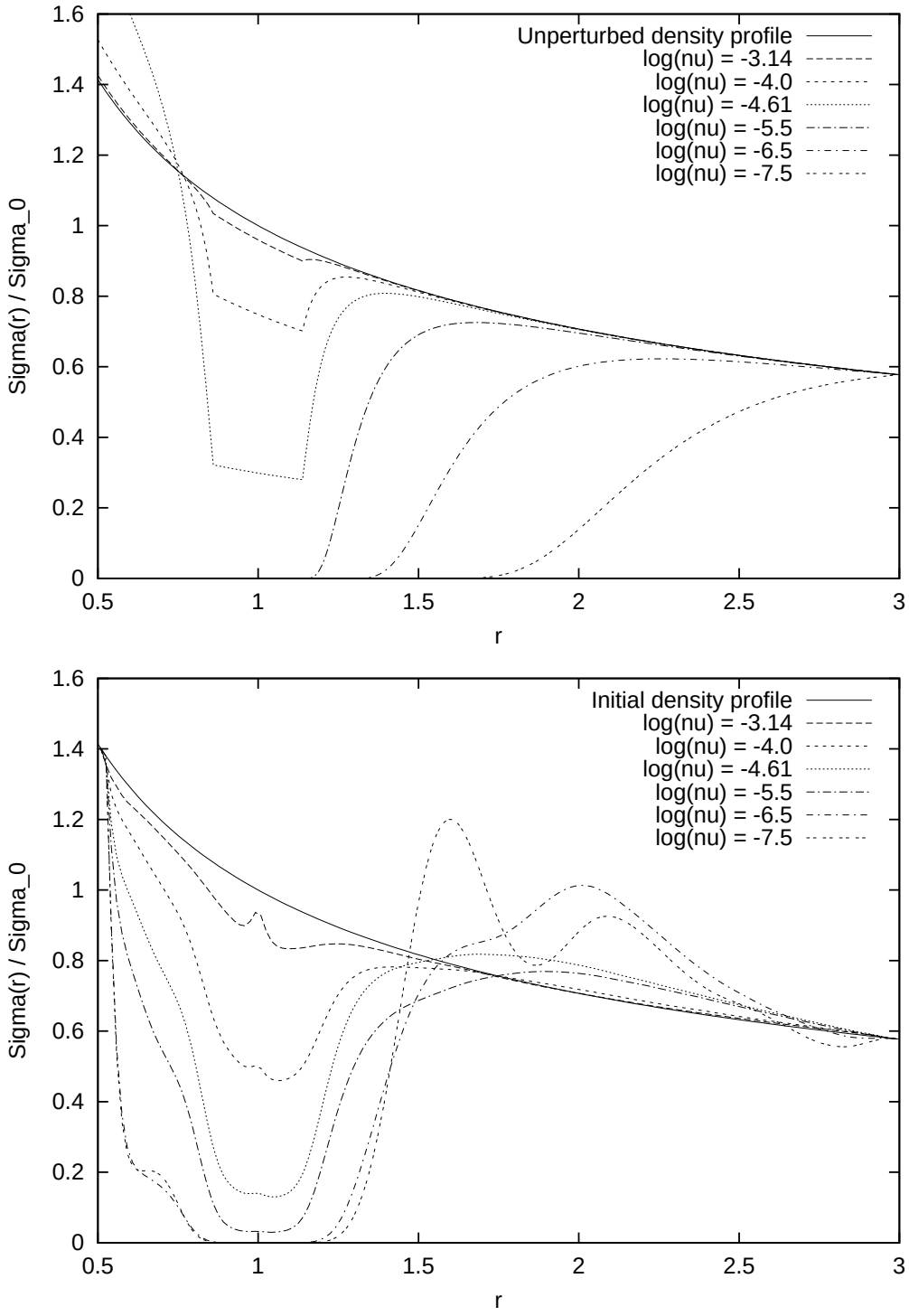

Figure 4.1: Gap profiles created by a Jupiter mass planet, for different viscosities. The vertical axis represents the normalized azimuth-averaged density. The horizontal axis represents the distance to the primary in normalized units. Top panel: analytic curves obtained by matching the differential torques due to gravity and viscosity on each elementary ring of the disk. Bottom panel: numerical profiles obtained in simulations, after 1000 planetary orbits for the three largest viscosities, and 5000 orbits for $\log(\nu) = -5.5$ and -6.5.

4.3 Pressure torque

Consider an arbitrary closed curve in the disk and a little tube around it. The rate of change of angular momentum of the matter in the tube is the sum of the differential flux of angular momentum through its boundaries (due to the advection of matter) and of the torques acting on it. From the Navier-Stokes equations, in addition to the gravity and viscous torques, there is a third torque due to pressure:

$$t_P = \oint {c_s}^2 \frac{\partial \Sigma}{\partial \theta} \mathrm{d}\theta \ , \tag{4.4}$$

where the integral is computed along the curve and we have assumed the usual state equation $P = {c_s}^2 \Sigma$. If the tube is a ring centered at the origin $r = 0$, the torque t_P is equal to zero (on the ring, r is constant and $\partial\Sigma/\partial\theta = \mathrm{d}\Sigma/\mathrm{d}\theta$), while the differential flux of angular momentum is generally not zero. The latter is the flux carried by the pressure supported wave (Goldreich and Nicholson, 1989, see Appendix C). Now, consider a streamline, which is a line always tangent to the local velocity vector. If one chooses a stream tube (*i.e.* a tube bounded by two neighboring streamlines), the differential flux is obviously zero (there is no flux of matter, by definition of stream tube), while t_P is non zero in general. The latter is true because the streamlines are strongly distorted by the planetary perturbation (see figure 4.2), and thus $\Sigma \equiv \Sigma(r(\theta), \theta)$ so that $\partial\Sigma/\partial\theta \neq \mathrm{d}\Sigma/\mathrm{d}\theta$. This shows that one can translate the angular momentum flux carried by the waves into a pressure torque, by a suitable partition of the disk in concentric tubes. Obviously the two approaches are equivalent as the physics is the same. However, working with stream tubes and pressure torques gives practical computational advantages. This is therefore the approach that we follow in this paper.

Below, we check that the gravity, pressure and viscous torques really cancel each other in the numerical simulations, once the steady state is reached.

4.3.1 Computation of the torques along the trajectories

The approach outlined above requires that the stream tubes are closed. In our simulations this is true at the steady state. Indeed, our boundary conditions preserve the initial radial velocity at the edges of the grid, which is null as a result of our choice for the initial disk density profile $\Sigma \propto 1/\sqrt{r}$. Consequently, the streamlines are bounded by the two circular streamlines at the edges of the grid ; hence, if a streamline were not a closed curve, it would present at least one accumulation point. At such a point, the density would perpetually increase, which is excluded at the steady state.

The calculation of the streamlines, which is done in Fourier space to ensure periodicity, is detailed in Appendix A. We remark that, in the steady state, the streamlines coincide with the fluid element trajectories.

Denoting the streamline by $r_i(\theta)$, we numerically compute the following expressions, which are the integrals of $(1/\Sigma)(r\vec{F}_\theta)$ with $\vec{F}_\theta$ the azimuthal component of the force due to gravity,

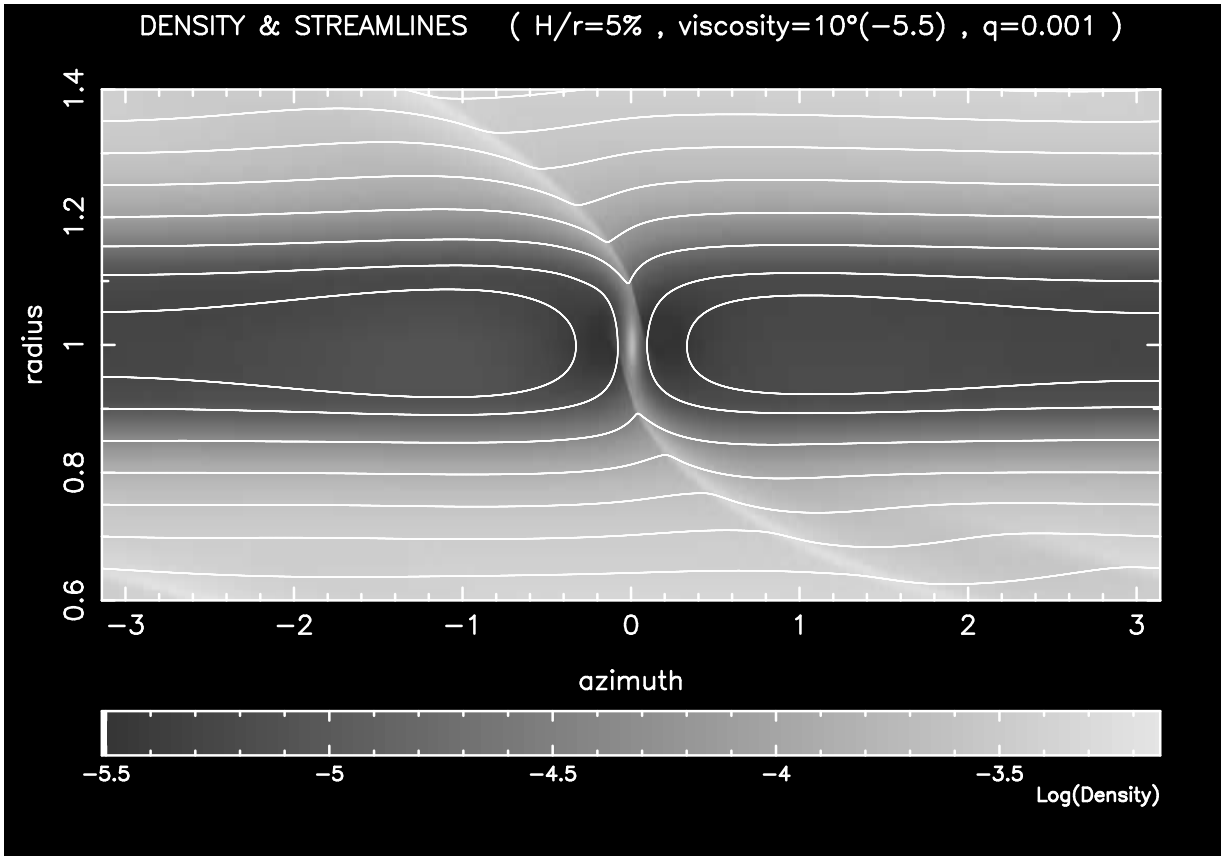

Figure 4.2: Disk surface density map in the vicinity of a gap opened by a Jupiter mass planet located at $(r_p = 1, \theta_p = 0)$. Light grey denotes high density and black low density, in a logarithmic scale. The white curves show some streamlines, in the corotating frame. They are followed from π to $-\pi$ for $r > 1$, and from $-\pi$ to π for $r < 1$, periodically. Two of them correspond to horseshoe orbits in the planet corotation region. Notice the strong distortion of the streamlines when they cross the over-density corresponding to the spiral wave (wake) launched by the planet.

viscosity, or pressure respectively:

$$t_g(\theta) = \frac{1}{\mathcal{T}_i(\theta)} \int_{\pi}^{\theta} r_i(\theta') \frac{\partial \Phi_p(r_i(\theta'), \theta')}{\partial \theta'} \left| \frac{d\theta'}{\dot{\theta}'} \right| \tag{4.5}$$

$$t_\nu(\theta) = \frac{1}{\mathcal{T}_i(\theta)} \int_{\pi}^{\theta} \frac{1}{\Sigma_{(r_i(\theta'),\theta')}} r_i(\theta') \vec{F}_\theta^{\nu}(r_i(\theta'), \theta') \left| \frac{d\theta'}{\dot{\theta}'} \right| \tag{4.6}$$

$$t_P(\theta) = \frac{1}{\mathcal{T}_i(\theta)} \int_{\pi}^{\theta} \frac{{c_s}^2}{\Sigma_{(r_i(\theta'),\theta')}} \frac{\partial \Sigma_{(r_i(\theta'),\theta')}}{\partial \theta'} \left| \frac{d\theta'}{\dot{\theta}'} \right| \tag{4.7}$$

Again, Φ_p denotes the gravitational potential of the planet, and $\vec{F}_\theta^{\nu} = \frac{1}{r}\left[\partial_r\left(r\bar{\bar{d}}_{r\theta}\right) + \partial_{\theta'}\bar{\bar{d}}_{\theta\theta} + \bar{\bar{d}}_{r\theta}\right]$, where $\bar{\bar{d}}$ is the local viscous stress tensor with no bulk viscosity: $\bar{\bar{d}} = 2\Sigma\nu\left(\bar{\bar{D}} - (\frac{1}{3}\nabla\vec{v})\bar{\bar{I}}\right)$ (see section 2.1). We integrate from π to θ, with $\pi > \theta \geqslant -\pi$, because we consider $r_0 > r_p$, so that the angular velocity is negative in the corotating frame. The time required to reach θ from π is denoted $\mathcal{T}_i(\theta)$. Thus, as the trajectories coincide with the streamlines in the steady state,

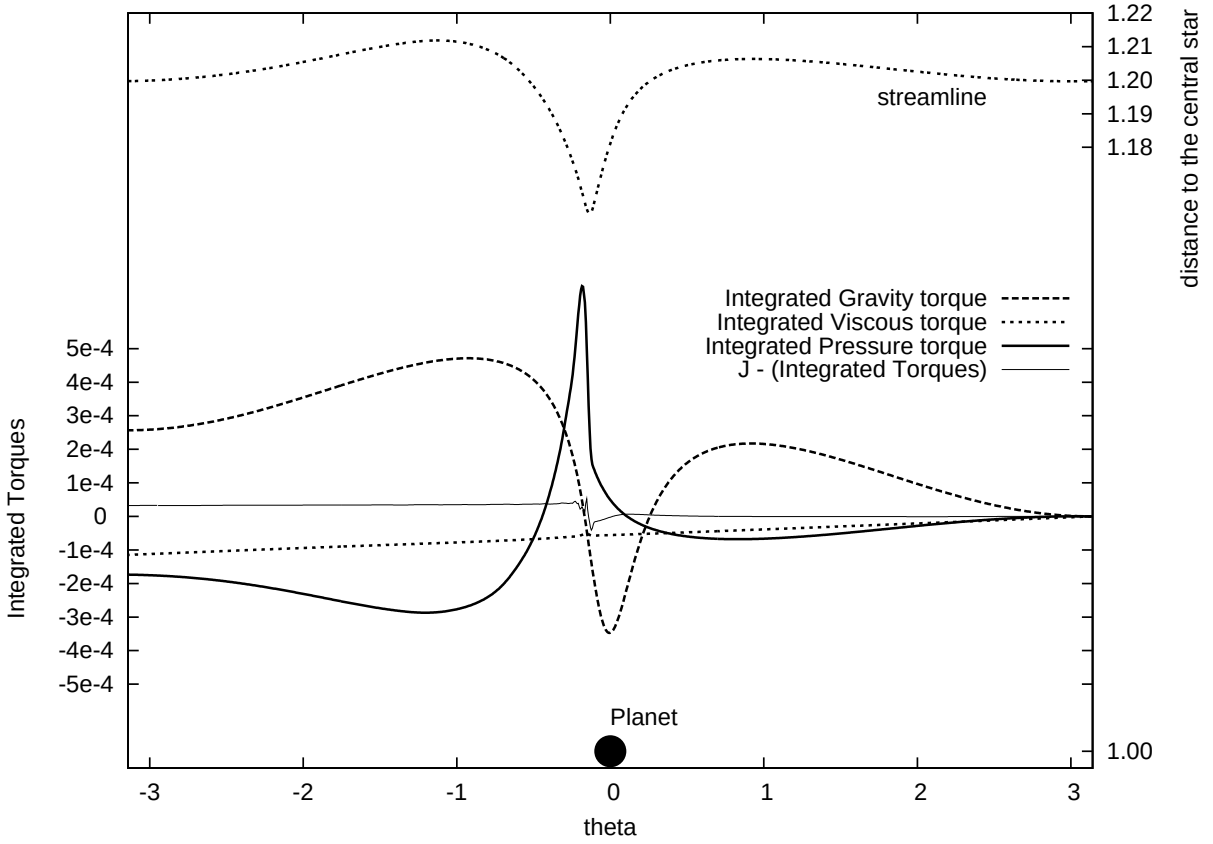

Figure 4.3: Graphical representation of the expressions given in Eq. (4.5) (integrated gravity torque, bold short-dash curve), Eq. (4.6) (integrated viscous torque, bold dotted curve) and Eq. (4.7) (integrated pressure torque, bold solid curve). Their reference scale is reported on the left vertical axis. The streamline followed for their calculation is plotted in the planet corotating frame as a dashed curve at the top of the figure and can also be seen in figure 4.2, while the position of the planet is shown by a filled dot at the bottom ; the corresponding scale is reported on the right vertical axis. The thin solid curve shows the difference between the angular momentum measured along the streamline ($J(\theta)$), and the sum of the three integrated torques and of the initial angular momentum ($\mathcal{J}(\theta)$). A small difference is almost impulsively acquired at the wake crossing, due to numerical approximations.

the expressions above describe the averaged torques felt by a fluid element that travels from the planet opposition to θ.

In the following, we denote for simplicity by t_g, t_ν, t_P the expressions (4.5)-(4.7) evaluated at $\theta = -\pi$. The total torques acting on the stream tube centered around the considered streamline are simply the product of these quantities times the mass carried by the tube.

We stress that $t_\nu \neq \delta T_\nu/(2\pi\Sigma r)$ and $t_g \neq \delta T_g/(2\pi\Sigma r)$, which are the torques exerted on an elementary ring of the disk per mass unit (see Eqs. (4.1) and (4.2)).

In the next paragraphs we give a brief description of the integrated torques given by Eqs. (4.5)-(4.7) as functions of θ, which are plotted in figure 4.3 for the streamline starting at $r = 1.2$ at opposition with the planet.

viscous torque : The growth of the integrated viscous torque appears to be nearly linear with respect to the azimuth, leading to a total negative torque. We verified that on this streamline $t_\nu \approx \delta T_\nu/(2\pi\Sigma r)$, with δT_ν from Eq. (4.1). Thus, the viscous torque depends only on the radial relative derivative of the azimuthally averaged density $\frac{1}{\Sigma}\frac{\mathrm{d}\Sigma}{\mathrm{d}r}$. However, on streamlines that pass closer to the planet, the difference between t_ν and $\delta T_\nu/(2\pi\Sigma r)$ becomes more significant (see figure 4.6).

gravity torque : The evolution of this integrated torque is not monotonic. The fluid element is first repelled by the planet, as a result of the indirect term in the gravitational potential. Then, when θ decreases below ~ 0.5, it starts to be attracted by the planet. The attraction becomes stronger and stronger as the fluid element approaches conjunction, namely as θ decreases to 0. The integrated torque becomes negative. After conjunction, the planet tends to pull the fluid element toward positive θ, giving a positive torque. As a result, the fluid element is rapidly repelled toward larger r, as one can see from the trajectory in figure 4.3. This is typical of the scattering of test particles in the restricted three body problem, which qualitatively justifies the impulse approach for the calculation of the gravitational torque, as in Lin and Papaloizou (1979) and section 2.2.1.

However, Lin and Papaloizou's calculation holds in the approximation $r \sim r_p$. By comparing the numerical estimate of $\delta T_g/(2\pi\Sigma r)$ with δT_g given by Eq. (4.2), we find that the following expression, which has the same dependence in Δ and nearly the same numerical coefficient, but which distinguishes r and r_p, provides a much more accurate representation of the gravity torque :

$$t_g = 0.35\ q^2 {r_p}^5\, {\Omega_p}^2\, r \left(\frac{1}{\Delta}\right)^4 \mathrm{sgn}(\Delta)\ , \tag{4.8}$$

In reality, t_g depends on the exact shape of the streamlines, which in turn depends on the scale height and the viscosity (see figures 4.4 and 4.6). However, the difference is moderate and limited to the vicinity of the planet, so that in the following we use Eq. (4.8) for all cases.

We stress that Eq. (4.8) gives the torque exerted on the fluid element, which is generally *not* the torque deposited in the disk. In fact, even in the absence of viscosity, it does not correspond to the change of angular momentum of the fluid element, because some of the angular momentum is carried away by the pressure torque.

pressure torque : The dependence of this torque on θ is simple to understand if one takes into account that : (i) the trajectories cross the wake immediately after the conjunction with the planet (figure 4.2) ; (ii) the wake is a strong over-density in the disk ; (iii) the pressure term $\partial\Sigma/\partial\theta$ makes over-densities repellent. Thus, as the fluid element approaches the wake, its azimuth θ decreasing in the corotating frame, the pressure rises and tends to push the fluid element back in the direction of increasing θ. This gives a positive local torque and it explains the peak in the integrated pressure torque in figure 4.3. Then, after that the fluid element has crossed the wake, the pressure decreases as θ decreases. This leads to a negative local pressure torque. It corresponds to the fall after the peak in figure 4.3. The negative contribution is bigger than the positive one because of the asymmetry of the trajectory relative to the wake position, which is clearly visible in figure 4.5.

Clearly, the pressure torque must depend on the shape of the streamlines and on the surface density relative radial gradient, which govern the shape of the wake and its density enhancement. We return to this in section 4.4.

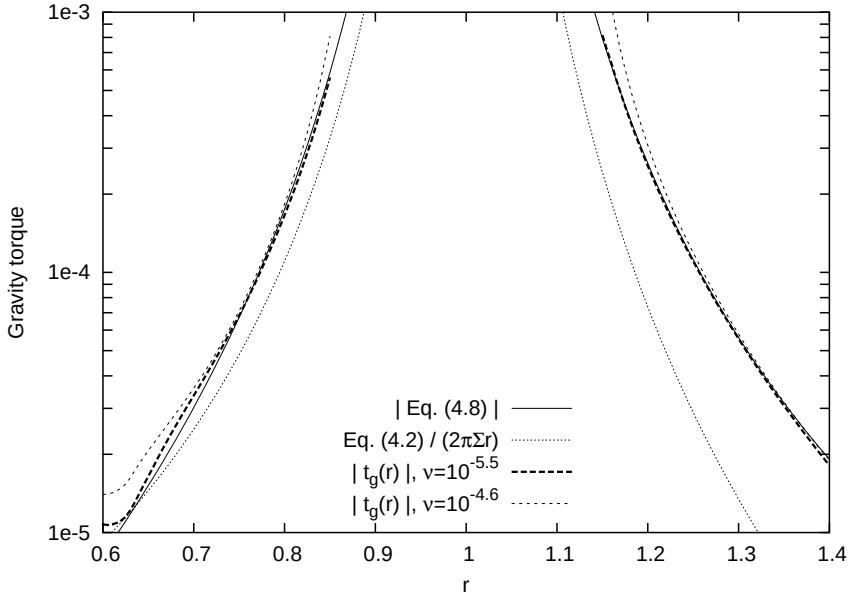

Figure 4.4: Absolute value of t_g as a function of r, where r is the distance to the central star at planet opposition of the streamline on which the gravity torque is integrated. The bold long-dashed curve is obtained from the simulation with $q = 10^{-3}$, $(H/r) = 5\%$, and $\nu = 10^{-5.5}$, while the bold short-dashed curve corresponds to a more viscous case ($\nu = 10^{-4.6}$). The solid line traces Eq. (4.8), which remarkably fits the results obtained in the less viscous case. The dashed-dotted curve traces Eq. (4.2), which shows that $\delta T_g \neq t_g$.

4.3.2 Torque balance at equilibrium

From figure 4.3 we remark that, at $\theta = -\pi$, the sum of the viscous and pressure torques is basically the opposite of the gravity torque. Therefore, the three torques approximately balance out.

Given the angular momentum J of a fluid element at $\theta = \pi$, one can compute the angular momentum $\mathcal{J}(\theta)$ that it would have if its trajectory were governed exclusively by the three torques mentioned above: $\mathcal{J}(\theta) = J(\pi) + t_g(\theta) + t_\nu(\theta) + t_P(\theta)$. This can be compared with the local angular momentum on the trajectory $J(\theta)$, measured directly from the numerical simulation. In figure 4.3 the thin line shows $J(\theta) - \mathcal{J}(\theta)$. This function is zero for θ evolving from π down to ~ 0, where the wake is crossed. At the wake crossing, a small kick is observed. Then, when θ evolves from the wake location to $-\pi$, the function $J(\theta) - \mathcal{J}(\theta)$ remains constant again. This confirms that the trajectory is essentially governed by the three torques mentioned above.

The small difference between J and $\mathcal{J}$ in figure 4.3 could in principle be due to the pseudo-viscous pressure introduced in the simulation to avoid numerical instabilities (Lin and Papaloizou, 1986a), but we have verified that the effect of the latter is negligible. Thus, we conclude that it is a consequence of numerical errors, introduced by the grid discretization at the shock site. This numerical issue evidently prevents the three cumulative torques from balancing out perfectly at $\theta = -\pi$: indeed, their sum is equal to $\mathcal{J}(-\pi) - J(-\pi) \neq 0$.

In order to explore the relative importance of viscosity and pressure in different situations, we show in figure 4.6 the three averaged torques as a function of r for two simulations, with $\nu = 10^{-4.6}$ (top panel) and $\nu = 10^{-5.5}$ (bottom panel). In the more viscous case, the pressure

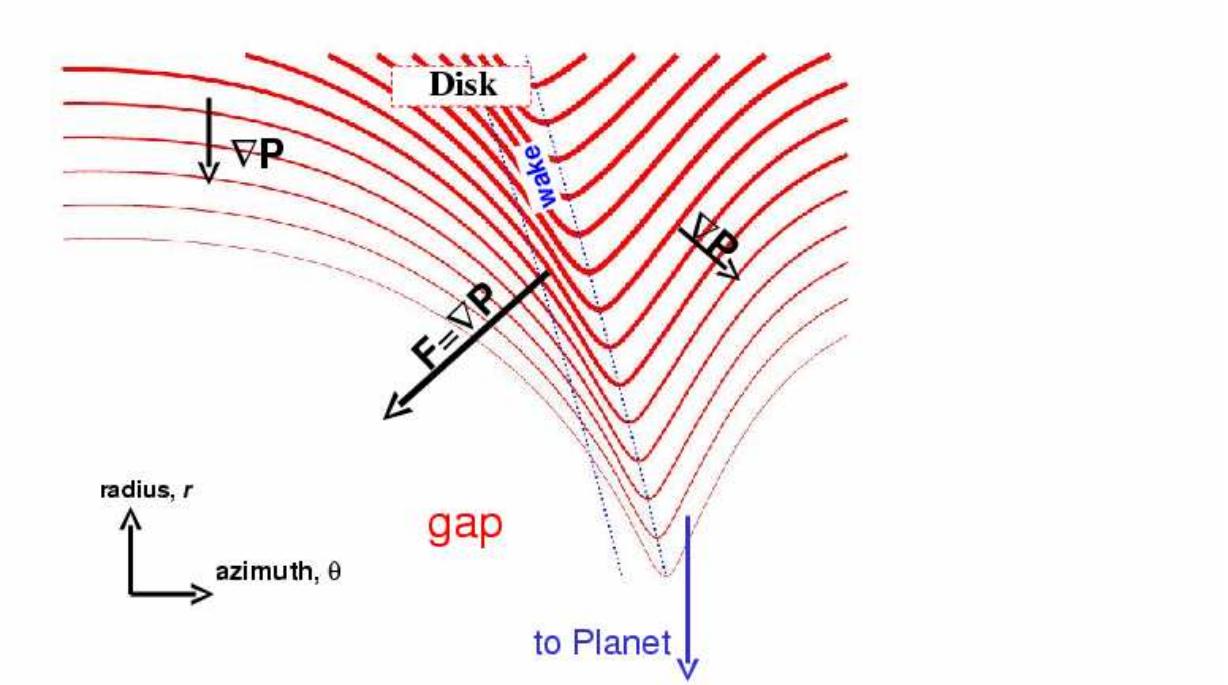

Figure 4.5: Sketch on the origin of the pressure torque. Here are drawn some streamlines, the width of which represents the mass carried by the corresponding streamtube. At the gap edge, the pressure gradient gives a force. The distortion of the streamlines at the wake leads to a large azimuthal component of this force, which gives a torque.

torque becomes relevant for $r < 1.2$, *i.e.* at the edge of the gap. There, it substantially helps the viscous torque in counterbalancing the gravity torque. This explains why the gap observed in the simulation is narrower than the one predicted by the theory considering only the gravity and the viscous torques alone (see figure 4.1). In fact, if the pressure torque were not present, all over the region $r < 1.2$ the relative radial gradient of the surface density of the disk would have needed to be much steeper, in order to enhance the viscous torque up to the value of the gravity torque (see Eq. (4.1)). This would have given a wider and deeper gap profile.

It is interesting to compare the top panel of figure 4.6 with the lower panel, which is plotted for a value of the viscosity that is almost an order of magnitude smaller. First, we remark that the gravity torque is somewhat smaller in the vicinity of the planet; this is due to a (moderate) change of the shape of the streamlines, as discussed in previous subsection. The viscous torque has decreased much more than the gravity torque, but not proportionally to the viscosity; this is because the profile of the gap has changed and the relative radial gradient of the surface density is now steeper. The pressure torque has *increased* relative to the gravity torque, and is now non-negligible in the full region $r < 1.3$. It is always larger in absolute value than the viscous torque. Its radial profile looks very similar to that of the gravity torque. In essence, it is the

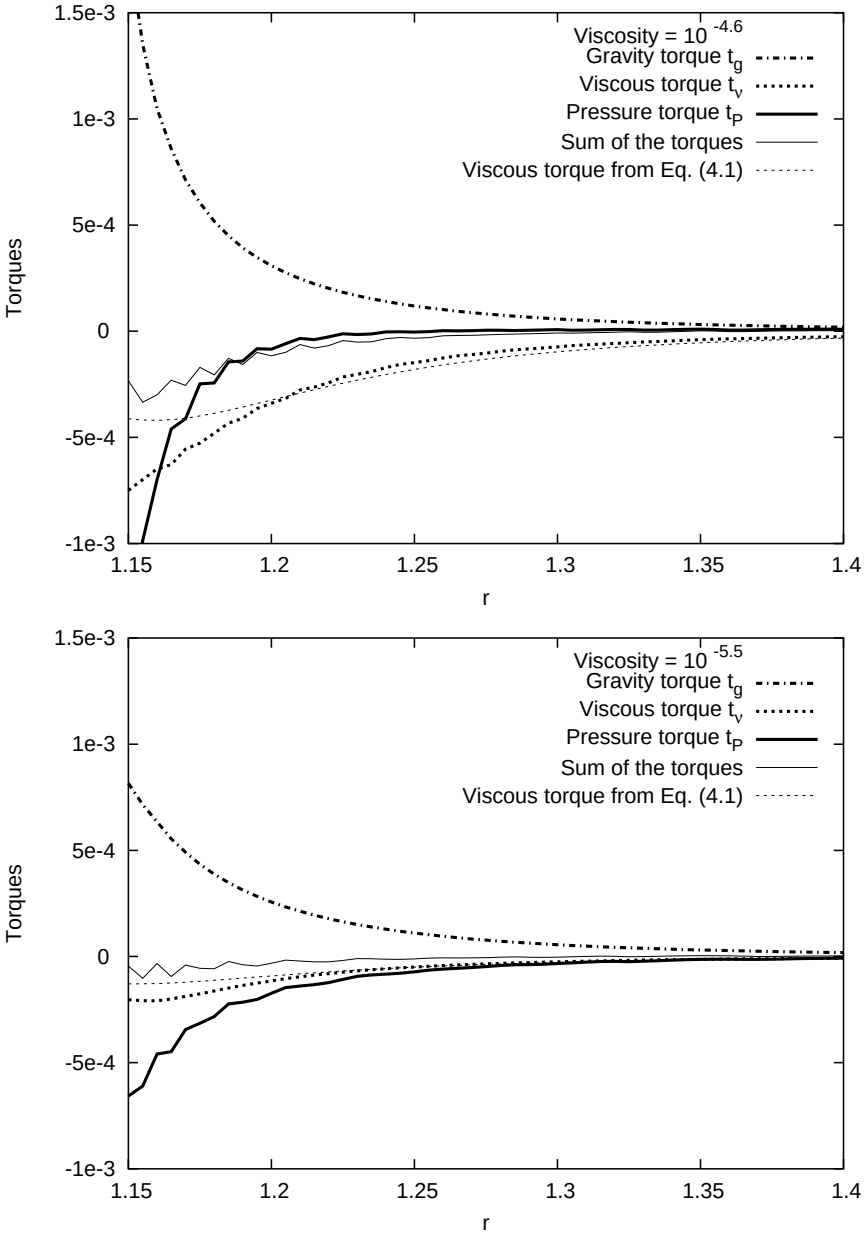

Figure 4.6: The torques t_g, t_ν, t_P are plotted in bold lines as a function of r, which denotes here and in the following plots the radius of the streamline at opposition with respect to the planet ($\theta = \pm\pi$); the horseshoe region $r \lesssim 1.15 \sim r_p + 2\,R_H$ (see figure 4.2) is excluded. The thin dotted line shows the value of the viscous torque given by $\delta T_\nu/(2\pi\Sigma r)$, with δT_ν from Eq. (4.1) (Keplerian circular approximation). The thin solid line is the sum of the three torques. It is not exactly zero, in particular in the vicinity of the planet, because of numerical approximations generated at the wake crossing. Top panel: large viscosity case; the pressure torque becomes relevant only close to the planet. Bottom panel: low viscosity case; the pressure torque appears further from planet, compensating for the smaller viscous torque.

pressure torque that counterbalances the action of the planet, with the viscosity only playing a minor role. Thus there is a dramatic qualitative change, with respect to the previous case, in how the torques balance out to settle the equilibrium configuration.

The two cases discussed above convincingly show that the disk equilibrium is set by the equation :

$$t_g + t_\nu + t_P = 0 \ . \tag{4.9}$$

When the viscosity fades, the role of pressure takes over in controlling the gap opening process, limiting the gap width. This means that, as viscosity decreases, a larger fraction of the gravity torque is transported away by the pressure supported waves. This phenomenon explains why the width of the gap increases with decreasing viscosity in a much less pronounced way than in Varnière et al.'s model, which does not include a pressure torque.

The role of pressure in limiting the gap width may still appear surprising, but it can be understood with some physical intuition. In an inertial environment, it is pressure – and not viscosity – which makes a gas fill the void space. In a rotating disk the situation is different, because a radial pressure gradient simply adds or subtracts a force to the gravitational force exerted by the central star. This changes the angular velocity of rotation of the gas, without causing any radial transport of matter. Thus if the edges of the gap were circular, the pressure could not play any role in limiting the gap opening. However, as the gap edges are not circular, as shown in figure 4.5, the pressure gradient is not entirely in the radial direction, and thus it exerts a force with a non-null azimuthal component. This gives a net torque, and tends to fill the gap.

4.4 Gap profiles

In the previous section, the pressure torque has been numerically computed in different cases. It has been shown that, when the disk is in equilibrium, the pressure, gravity and viscous torques cancel out. This suggests that it should be possible to compute a priori the shape of the gap by imposing that this equilibrium given by Eq. (4.9) is respected. Indeed, the viscous and pressure torques depend on the relative radial gradient of the azimuth-averaged density, whereas the gravity torque has no direct dependence on it. Therefore, on a given trajectory, there must be a value of this gradient that corresponds to the exact equilibrium between these three torques.

We compute the streamlines on the edge of the gap for a given numerical simulation. For each streamline, we derive the value of $(1/\Sigma)(\mathrm{d}\Sigma/\mathrm{d}r)$ that ensures the equilibrium. Our semi-numerical algorithm for the computation of this equilibrium value is described in appendix B. The results are shown in figure 4.7 as crosses and satisfactorily agree with the real value of the relative radial density gradient measured in the corresponding numerical simulation (solid curve).

The knowledge of the relative radial gradient of the azimuth-averaged density as a function of the radial distance enables us to construct a gap profile by simple numerical step by step integration, starting from a boundary condition. In the secondary panel of figure 4.7 this integrated profile (dashed curve) is plotted against the real one from the considered simulation. The match between the two profiles is almost perfect, which again proves that the gap profile is set by the balance between the three torques due to gravity, viscosity, and pressure.

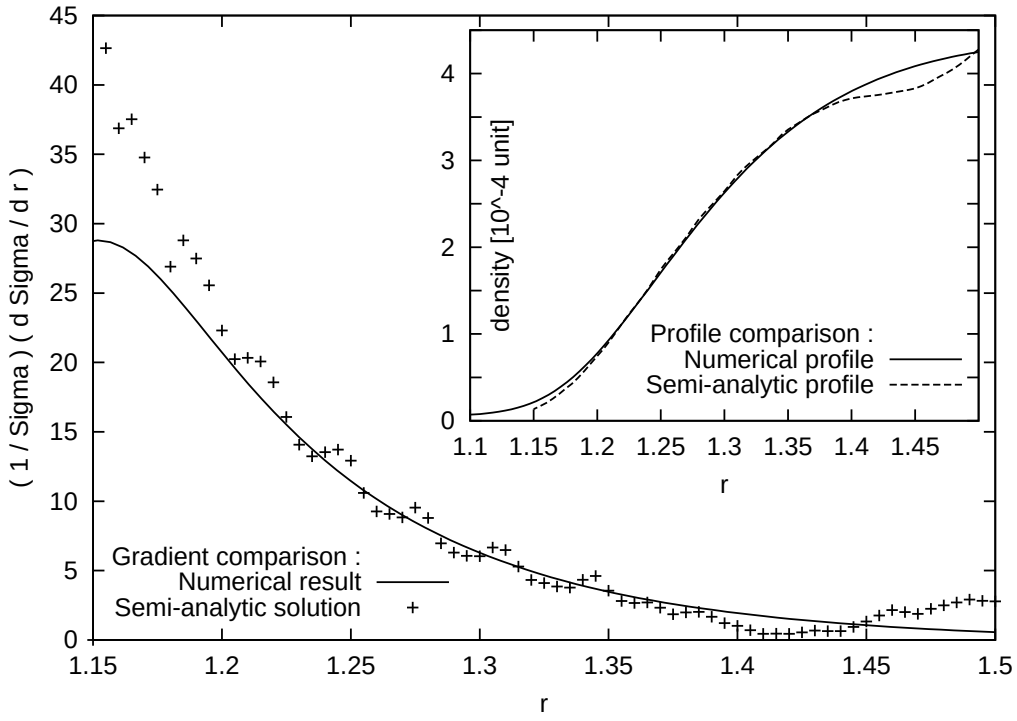

Figure 4.7: The crosses show the relative radial gradient of the surface density as computed by the algorithm described in Appendix B. The solid curve shows the same quantity, measured from the numerical simulation from which the streamlines used in the algorithm have been taken (aspect ratio = 0.05, viscosity = $10^{-5.5}$, planet mass = 10^{-3}). From the algorithm, the gap profile is computed (dashed curve in the little box), and compared to that obtained in the numerical simulation (solid curve).

4.4.1 An explicit equation for the gap profile

We now wish to go beyond the semi-numerical algorithm of Appendix B and obtain an approximate analytic expression for the pressure torque, to be used in an explicit differential equation for the gap profile.

As we have seen above, for a given streamline, the absolute value of the pressure torque is an increasing function of the relative radial gradient of the azimuthally averaged surface density. Furthermore, in a disk with no density gradient, the pressure torque must be zero. Thus, we approximate the dependence of the pressure torque on the relative radial density gradient with a linear function :

$$t_P = -a(r) \left(\frac{\mathrm{d}\Sigma}{\Sigma \, \mathrm{d}r} \right) \ .$$

Before looking for a numerical approximation of the function $a(r)$, we make two considerations on its functional dependence on the scale height of the disk and on the mass of the planet.

First, because of Eq. (4.4), $a(r)$ is necessarily proportional to ${c_s}^2$. As c_s is proportional to the scale height H, we can write $a = (H/r)^2 a'(r)$.

Second, in the limit of negligible viscosity, scaling the aspect ratio H/r proportionally to R_H/r_p, and adopting R_H as basic unit of length, the equation of motion becomes independent of the planet mass (Korycansky and Papaloizou, 1996). Thus, if the disk aspect ratio scales

with the planet Hill radius, the resulting surface density Σ at equilibrium is a function of Δ/R_H only. Consequently $\mathrm{d}\Sigma/(\Sigma \mathrm{d}r)$ is a function of Δ/R_H, divided by R_H. As the gravity torque t_g is proportional to ${R_H}^2 r(\Delta/R_H)^{-4}$ (see Eq. (4.8)), the equilibrium $t_g = t_p$ can hold if and only if $a'(r) = r R_H\ a''(\Delta/R_H)\ r_p {\Omega_p}^2$, where $a''(\Delta/R_H)$ is a dimensionless function and the constant factor $r_p {\Omega_p}^2$ stands for homogeneity reasons.

To evaluate the function a'', we use numerical simulations from which we measure the pressure torque and the relative radial gradient of the surface density. In practice, we consider two simulations: (i) the reference one, with a Jupiter mass planet in a disk with aspect ratio = 0.05 and viscosity = $10^{-5.5}$, which gives information for Δ/R_H in the range 2–7, and (ii) a similar simulation but with viscosity $\nu = 10^{-6.5}$ which, because of its wider gap, allows us to better estimate the asymptotic behavior of a'' at large Δ. We find that $a''(\Delta/R_H)$ can be approximately fitted by the function

$$a''\left(\frac{\Delta}{R_H}\right) = \frac{1}{8}\left|\frac{\Delta}{R_H}\right|^{-1.2} + 200\left|\frac{\Delta}{R_H}\right|^{-10} . \tag{4.10}$$

Equation (4.10) has been determined for the external part of the disk ($\Delta > 0$), outside of the horseshoe region. However, assuming that the streamlines are symmetric relative to the position of the planet, the same expression can be applied in the inner part of the disk, which justifies the absolute value of Δ. In fact, to represent the inner edge of the gap, just rotate figure 4.5 by 180 degrees, and it becomes evident that a negative density gradient leads to a positive torque.

Note that Eq. (4.10) has been determined with reference to the streamlines corresponding to the case with $q = 10^{-3}$, $\nu = 10^{-5.5}$, and $H/r = 5\%$. However, the exact shape of the streamlines depends on q, ν, and H/r, even in rescaled coordinates. We neglect this dependence at this stage.

Thus, we assume that Eq. (4.10) is valid for any value of ν and H/r and a'' depends on q only via R_H. This approximation has the advantage of providing us an analytic expression for the computation of the gap profiles. In fact, the disk equilibrium condition Eq. (4.9) becomes:

$$\left(\frac{R_H}{\Sigma}\frac{\mathrm{d}\Sigma}{\mathrm{d}r}\right) = \frac{t_g - \frac{3}{4}\nu\Omega}{\left(\frac{H}{r}\right)^2 r\, r_p {\Omega_p}^2 a'' + \frac{3}{2}\nu\frac{r}{R_H}\Omega} \tag{4.11}$$

with a'' and t_g given in Eqs. (4.10) and (4.8) respectively.

The right hand side of Eq. (4.11) is independent of Σ and is an explicit function of r. This differential equation can be integrated, once a boundary condition $\Sigma(r_0)$ is given. Unfortunately the integral has no analytic solution, so that it has to be computed numerically.

Figure 4.8 shows comparisons of the gap profiles obtained in numerical simulations with those obtained with the integration of Eq. (4.11), for six different cases with different viscosities or aspect ratios and planetary mass (see figure caption for a list of parameters). The comparisons are done only for the outer part of the disk, because in the inner part, the effect of the boundary condition, not considered in our model, is too prominent in the numerical results. In the integration of Eq. (4.11), Σ has been set equal to the value found in the numerical simulations at a point on the brink of the gap, so as to allow an easier comparison between the numerical and semi-analytic density gradients at the edge of the gap. We remark that in case 1, the semi-analytic gap profile matches almost perfectly the numerical profile. This is not surprising, because this is the reference case for which the streamlines have been computed, so that our expression Eq. (4.10) is virtually exact.

In cases 2 and 3, we change the viscosity and keep the same planet mass and aspect ratio as in case 1. Now, the agreement between the numerical and semi-analytic profiles is less good. In particular, in the high-viscosity case, the real density gradient is shallower than the one we

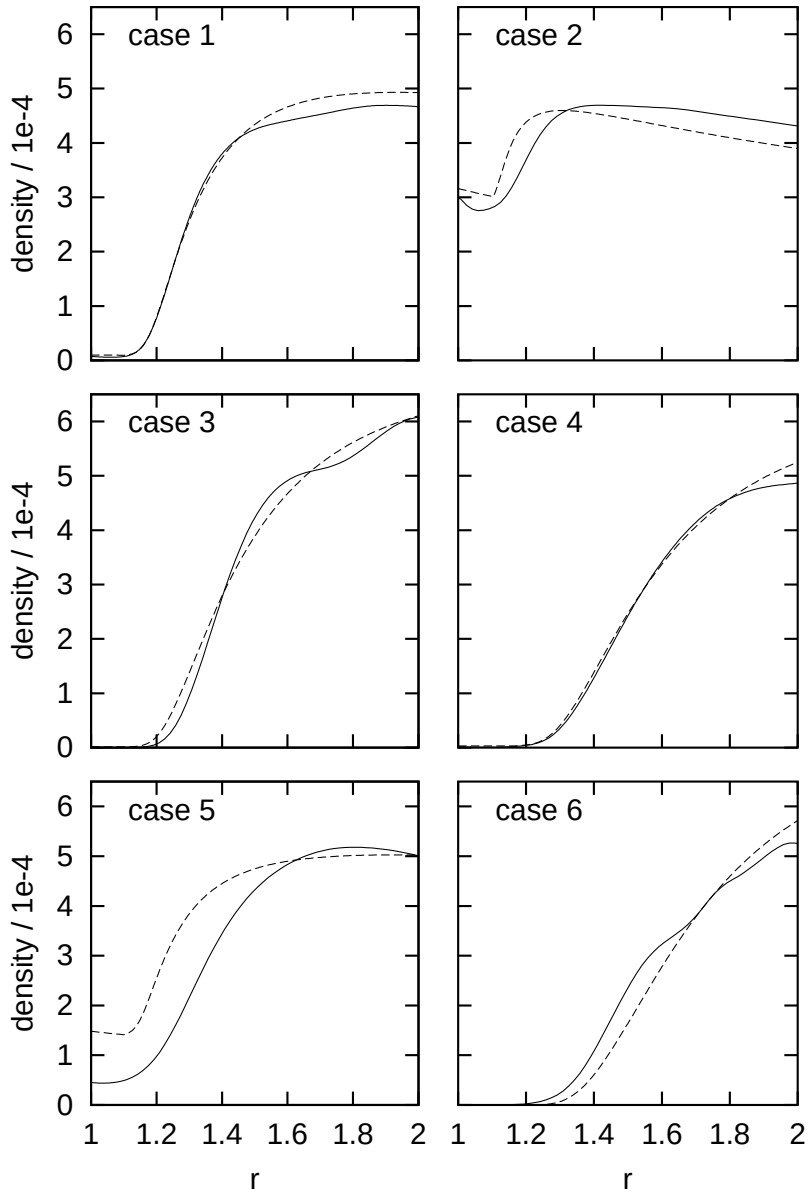

Figure 4.8: Comparison of numerical results (plain lines) and analytic profiles given by Eq. (4.11) (dashed lines).
Case 1: reference case: $q = 10^{-3}$, $H/r = 5\%$, $\nu = 10^{-5.5}$.
Case 2: more viscous case: $q = 10^{-3}$, $H/r = 5\%$, $\nu = 10^{-4}$.
Case 3: less viscous case: $q = 10^{-3}$, $H/r = 5\%$, $\nu = 10^{-6.5}$.
Case 4: scaled case: $q = 3.10^{-3}$, $H/r = 7.2\%$, $\nu = 10^{-5.5}$.
Case 5: thicker disk case: $q = 10^{-3}$, $H/r = 10\%$, $\nu = 10^{-5.5}$.
Case 6: more massive case: $q = 3.10^{-3}$, $H/r = 5\%$, $\nu = 10^{-5.5}$.

compute, while in the low-viscosity case it is steeper. This is because the real streamlines are not identical to those for which Eq. (4.10) has been computed. In the more viscous case, the

equilibrium in the disk is achieved with a weaker pressure torque. The distortion of the streamlines at the wake is dictated by the difference between the local gravity and pressure torques. Thus, a weaker pressure torque gives streamlines that are more distorted at the wake than in our reference case. But, as sketched in figure 4.5, the more a streamline is distorted, the more efficient it is in producing a pressure torque from a radial surface density gradient. Consequently the pressure torque required to set the equilibrium in the disk is achieved with a smaller density gradient than the one needed if the streamlines were as in the reference case. The opposite holds in the less viscous case.

In case 4, we increase the mass of the planet and the disk aspect ratio, in a way such that H/R_H is the same as in case 1. The viscosity is also the same as in case 1, and the agreement between the model and the simulation is equally good.

Finally, in case 5 and 6, we change H/R_H. In case 5, we keep the planet mass and viscosity of case 1 but increase the aspect ratio to 10%; the model gap is quite narrower and shallower than the numerical one. In case 6, we use the same planet as in case 4 but with the aspect ratio and viscosity of case 1, which gives as smaller H/R_H; the gap that our model predicts is now slightly wider than the one obtained in the numerical calculation. The interpretation for the disagreements observed in cases 5 and 6 is the same as that offered for cases 2 and 3.

4.4.2 Note on disk evolution during gap opening

Figure 4.8 shows significant differences in the value of Σ between the numerical simulation and the analytic expression. However, we stress that a large difference in Σ can correspond to almost no difference in the relative slope $(\frac{1}{\Sigma}\frac{\mathrm{d}\Sigma}{\mathrm{d}r})$. For instance, in the case with viscosity equal to 10^{-4} (case 2), the surface density profiles for $r > 1.6$ seem quite different, but in fact, they have the same relative slope.

As we have shown above, it is the relative slope $(\frac{1}{\Sigma}\frac{\mathrm{d}\Sigma}{\mathrm{d}r})$ that sets the equilibrium. This equilibrium must be reached quickly, on a time scale independent of viscosity. In fact, in absence of equilibrium, the fluid elements are displaced radially over a synodic period and the trajectories are not periodic. This corresponds to the opening of the gap. Then, once the equilibrium is almost set, the value of Σ can still significantly evolve on a long (viscous) time scale, but keeping $(\frac{1}{\Sigma}\frac{\mathrm{d}\Sigma}{\mathrm{d}r})$ essentially unchanged. This fact is illustrated on figure 4.9, which compares the evolution of $(\frac{1}{\Sigma}\frac{\mathrm{d}\Sigma}{\mathrm{d}r})$ (top panel) with the evolution of Σ (bottom panel) for a weakly viscous case ($\nu = 10^{-6.5}$). This behavior explains why, when simulating the gap opening in low viscosity disks, the surface density profile seems to have attained a stationary solution within a limited number of planetary orbits, despite that the presence a prominent 'bump' at the outer edge of the gap indicates that there is still room for evolution (see figure 4.1).

In the inner disk, once the gap profile is set in terms of relative slope, we expect that the density Σ decreases on a viscous timescale, because of the accretion on the central star. In the approximation of a fixed planet, this viscous evolution would lead to the formation of an inner hole in the disk, extended up to the planet position.

4.5 Dependence of gap profiles on viscosity and aspect ratio

In the previous section, we have presented a semi-analytic method to compute gap profiles. It gave overall satisfactory results, as shown in figure 4.8. In this section, we use our method to explore the dependence of the gap profile on the two key parameters of the disk: viscosity ν and

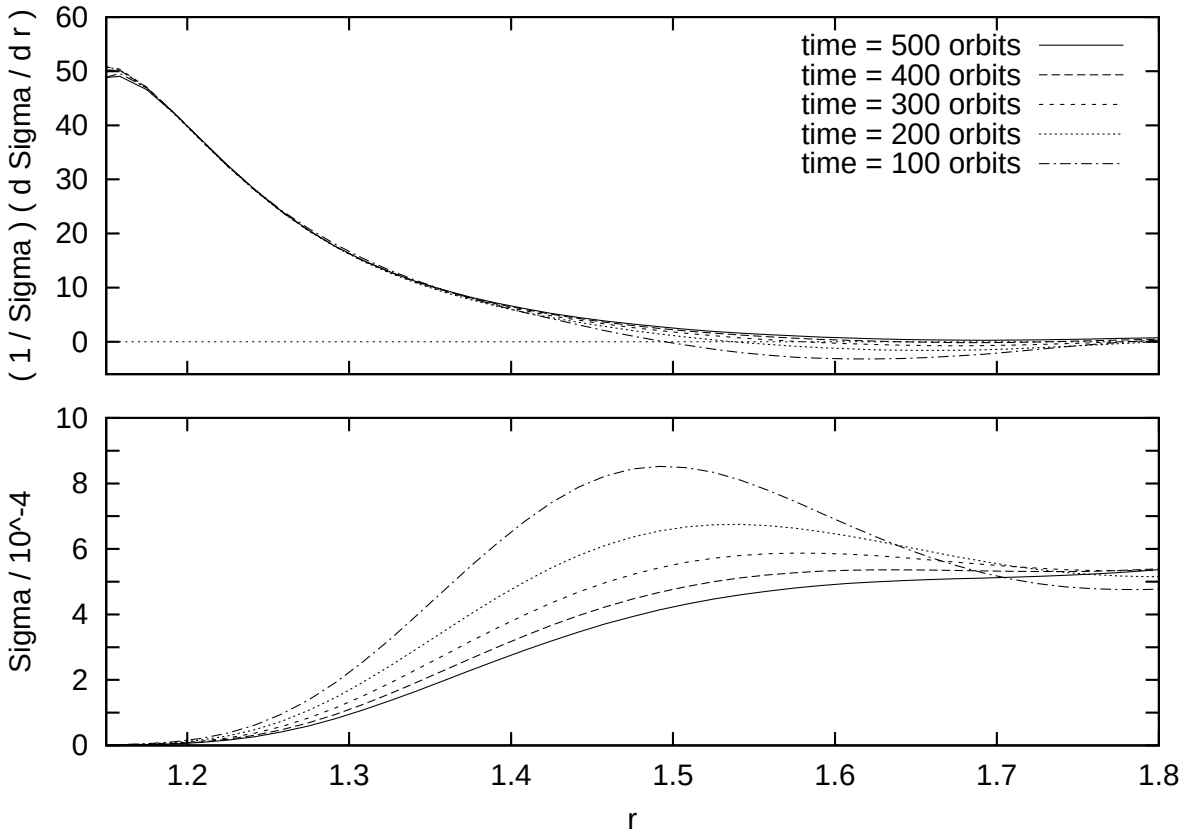

Figure 4.9: Evolution with time of the profile of the external edge of the gap opened by a Jupiter mass planet in a 5% aspect ratio disk, with a $10^{-6.5}$ viscosity. Top panel shows the relative radial gradient of the density ; the fact that the curves overlap argues that the equilibrium function has been rapidly reached. Bottom panel shows the evolution of the surface density at the same times ; a 'bump' appears, which is a consequence of the matter removed from the gap, and it is eroded on a viscous time scale. This happens without modifying substantially the relative slope.

aspect ratio H/r. In particular, we wish to revisit, with a unitary approach, the gap opening criteria mentioned in section 2.5 :
(i) the viscosity needs to be smaller than a threshold value. According to Eq. (2.48), in our case of a Jupiter mass planet this value is $\nu_{\rm crit} \approx 10^{-4}$.
(ii) The disk height at the location of the planet needs to be smaller than $\sim R_H$. For a Jupiter mass planet it corresponds to an aspect ratio $\sim 7\%$.

In the computation of the gap profiles by integration of Eq. (4.11), two problems are encountered.

First, a boundary condition is needed. This choice is arbitrary, but in principle it should be consistent with the steady state of the disk. However, the steady state is an academic concept which exists only if the density is kept fixed somewhere in the disk, otherwise the disk spreads to infinity following Lynden-Bell and Pringle (1974) equations (see section 2.6.2). In our numerical code, the surface density is kept equal to the unperturbed value at the outer boundary of the grid ($r = 3$). Thus, for the solutions of Eq. (4.11) presented in figures 4.10 and 4.11, we impose $\Sigma(r = 3) = 1/\sqrt{3}$. In this way, our solution should correspond to the steady state solution that the code would converge to. Moreover, this choice allows a direct comparison of our profiles with

those obtained with Varnière et al. model, illustrated in the top panel of figure 4.1 using the same boundary condition.

The steady state solution provided by the numerical simulation does not depend on the size of the grid, provided that the boundaries are sufficiently far from the planet (negligible differential planetary and pressure torques, or equivalently, negligible wave carried angular momentum flux, as in our nominal case –see Appendix C). This required size increases with decreasing viscosity because the radial range over which the wave is damped increases.

Thus, in a very low viscosity case, the steady state solution obtained by the numerical simulation over an extended disk would be different from the model profiles given on figure 4.10. However, our model profiles would bound the gap observed in the numerical simulation as long as the normalized surface density at $r = 3$ does not decrease below $1/\sqrt{3}$. In such low viscosity cases, this happens after an exceedingly long time. Thus, we claim that our model profiles are significant for the description of gaps in realistic disks.

The second problem concerns the treatment of the horseshoe region. The gravity and pressure torques, t_g and t_P, are considered null in the horseshoe region $|\Delta| < 2\,R_H$. The depth of the gap is thus set by the value of the density at $r_P + 2\,R_H$. At the edges of the gap, the slope is very steep, so that a little change in the assumed width of the horseshoe region leads to a major change in the gap depth. This is a limitation of our results from a quantitative point of view. Though, it does not change the qualitative evolution of the gap profiles with respect to the disk parameters.

This sensitivity to the width of the horseshoe region is also a problem for the construction of the surface density profile in the inner disk. The integration for the inner disk starts from $r_P - 2\,R_H$ down to $r = 0$, with the density at the bottom of the gap acting as the boundary condition. In principle, if the gap profile is symmetric, the errors at the right hand side and left hand side borders of the gap compensate each other: the value of the surface density at the bottom of the gap is not quantitatively correct, but the density profile in the inner disk is realistic.

Figure 4.10 shows the results of our semi-analytic calculation for a fixed value of the aspect ratio (5%) and different values of the viscosity ν (from 0 to 10^{-3} in normalized units). Figure 4.11 keeps the viscosity $\nu = 10^{-5.5}$ and explores the dependence of the gap profile on the disk aspect ratio (from 0 to 30%). The plotted curves naturally order themselves from bottom to top, from the less viscous case (respectively the smallest aspect ratio) to the most viscous case (respectively the biggest aspect ratio). Notice that this progression does not represent an evolution with time, but different steady state gap profiles, for different parameters.

dependence on viscosity : First of all, we remark on figure 4.10 that the different shapes of the gaps qualitatively agree with those computed with numerical simulations, shown in the bottom panel of figure 4.1. Indeed, not only do we get deeper and wider gaps as viscosity decreases, but we also correctly reproduce the limited gap width achieved in the small viscosity cases. This means we have solved the problem that initially motivated our investigation.
As viscosity increases, the gap is filled with gas, and the profile tends to the unperturbed profile set by the sole viscous effects: $\Sigma \propto 1/\sqrt{r}$ (see section 4.2). Nevertheless, it is hard to determine a precise threshold value for gap opening, for at least two reasons. The first one is that the gap profiles have a smooth dependence on the viscosity. The concept of threshold viscosity for gap opening does not hold. The gap gradually increases in depth over a range of viscosities of about one order of magnitude. The second reason is that the depth of our gaps is very sensitive to the assumed width of the horseshoe region, as discussed above. Thus, there is some uncertainty on

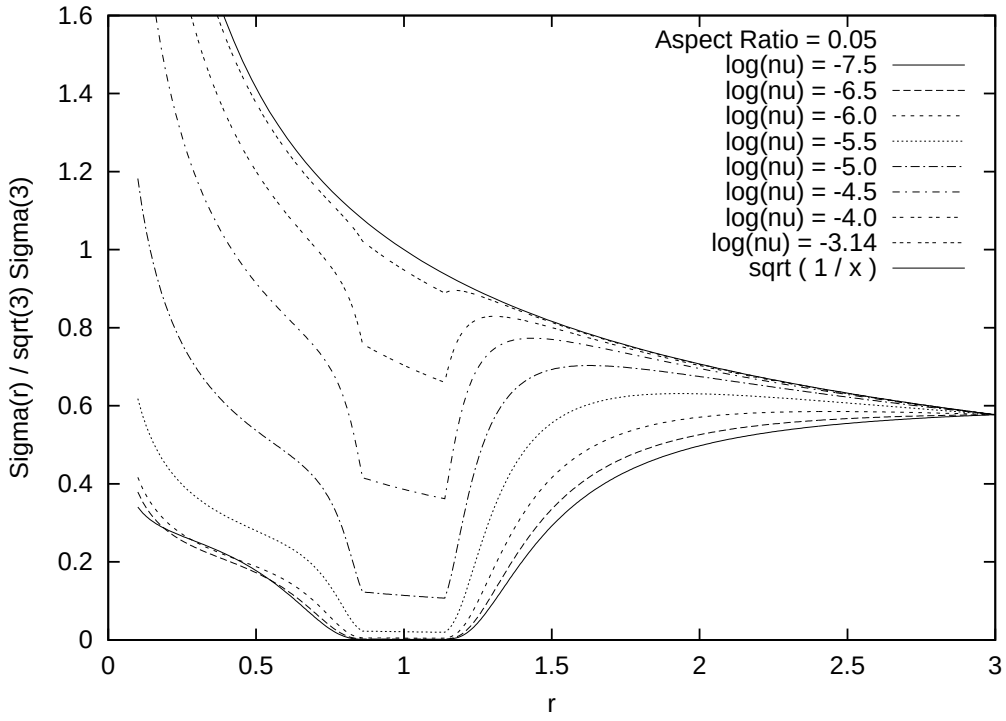

Figure 4.10: Analytical gap profiles given by Eq. (4.11) for different viscosities. The gap deepens as viscosity decreases, but its width remains bounded, even for $\nu = 0$.

the value of the viscosity that makes the gap become only a dip. Assuming that a gap is opened if the surface density falls below 10% of the unperturbed density, we find that $\nu_{\rm crit} \approx 10^{-5}$. We remind that the 'classical' threshold for gap opening is $\nu_{\rm crit} \approx 10^{-4}$. However, the numerical experiments in figure 4.1 (bottom panel) also suggest that $\Sigma \sim 0.1$ at the bottom of the gap is achieved for $\nu \sim 10^{-5}$.

dependence on aspect ratio: Consider now figure 4.11. We see a smooth evolution from deep gaps to shallow or inexistent gaps with increasing aspect ratios. This is easy to understand, because $(H/r)^2$ is a multiplicative coefficient in the expression of the pressure torque (see section 4.4). Therefore, the larger (H/r), the shallower needs to be the relative slope at the edge of the gap to achieve the equilibrium given by Eq. (4.9). As in the previous case, it is not possible to determine a threshold value of (H/r) for gap opening, but we find that the 'classical' value $(H/r)_{\rm crit} \approx 0.07$ corresponds to about 90% depletion in the gap.

More generally, with our approach we find that the viscosity required to fill the gap is a decreasing function of the aspect ratio. If the aspect ratio is too large, the gap cannot be opened whatever the viscosity. To our knowledge, this is the first time that an analytic approach gives the correct description of the evolution of the gap profile with respect to *both* disk viscosity *and* aspect ratio.

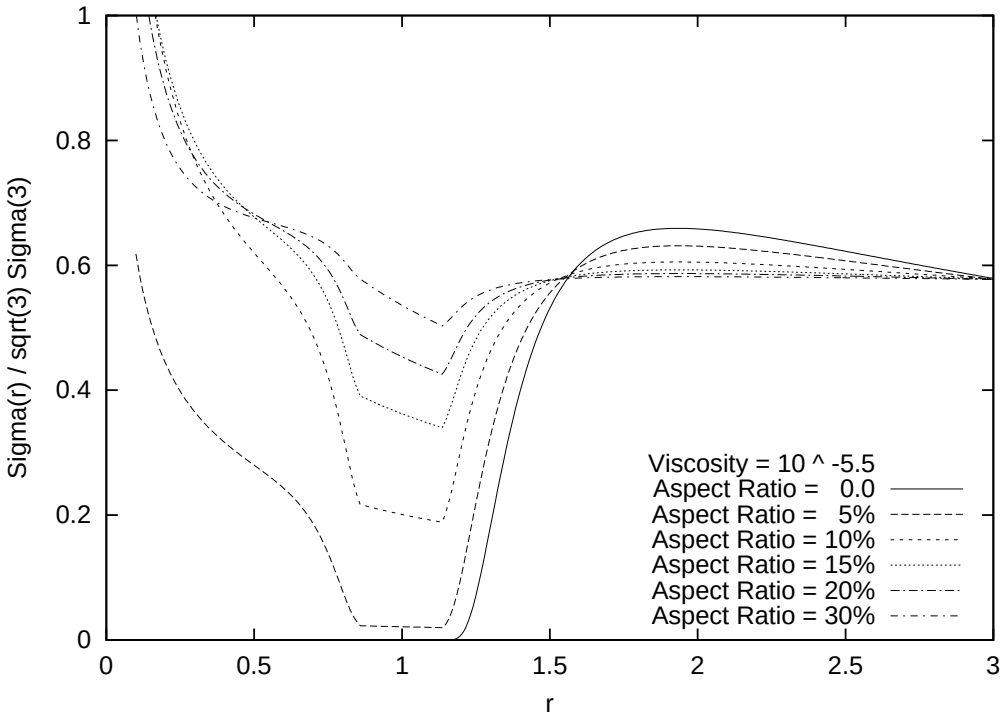

Figure 4.11: Analytical gap profiles given by Eq. (4.11) for different aspect ratios. The gap deepens as the aspect ratio decreases.

4.6 A new generalized criterion for gap opening

To go beyond the qualitative considerations of the previous section, we try to generalize the gap opening criterion with an expression that involves simultaneously the three main parameters of the problem : mass of the planet, scale height of the disk and viscosity.

We start with a few considerations on two limiting cases. In the zero viscosity limit, as we have seen in section 4.4, changing the scale height of the disk in proportion to the Hill radius of the planet preserves the gap profile in scaled units Δ/R_H. This means that, whatever depth threshold is adopted for the definition of 'gap', the threshold value of H for gap opening in the zero viscosity limit, H_0, is proportional to R_H :

$$H_0 \propto R_H \propto q^{\frac{1}{3}} \ .$$

In the infinitely thin disk limit ($H/r \to 0$), the disk equilibrium is set by the equation $t_g = t_\nu$. At the border of the gap where the slope of the surface density is relevant, t_ν is proportional to $\nu \frac{r\,\mathrm{d}\Sigma}{\Sigma\,\mathrm{d}r}$. By changing the mass of the planet, the gravity torque changes proportionally to ${R_H}^2 r(\Delta/R_H)^{-4}$. If the viscosity ν is changed proportionally to ${R_H}^3 \propto q$, then the surface density profile Σ remains an invariant function of Δ/R_H. Thus, independently of the adopted definition of 'gap' as in the previous case, the threshold viscosity for gap opening in the infinitely thin disk limit, ν_0, scales proportionally to q. This is consistent with the gap opening criterion given by Eq. (2.48) :

$$\nu_0 \propto q \ .$$

We now come to the general case where neither H nor ν are null. From the considerations above and Eq. (4.11) it is evident that a change in the planet mass q can give an invariant surface

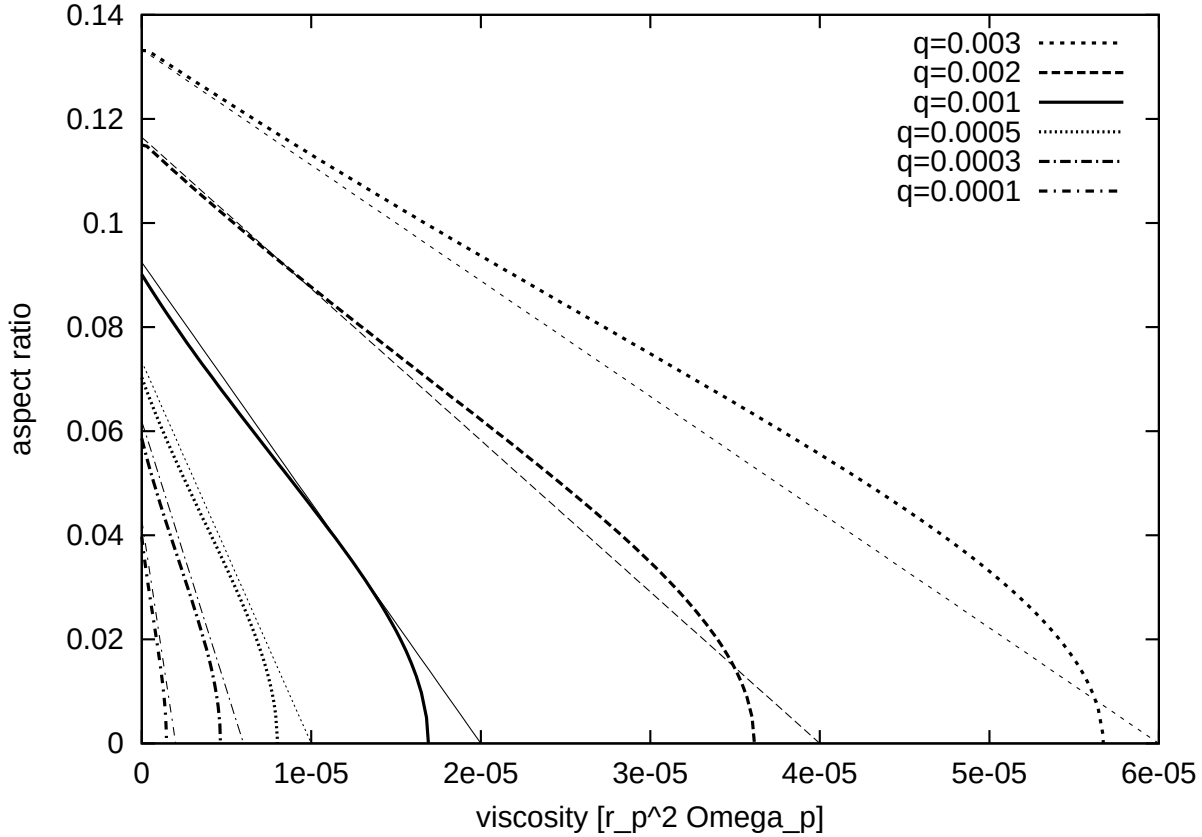

Figure 4.12: The bold curves represent the values of (H/r) that make the gap depth be 10% of the unperturbed density for given values of ν. They have been computed from the solutions of Eq. (4.11). Each curve corresponds to a planet mass. The thin lines represent our linear approximations given by Eq. (4.12) for the corresponding planet mass.

density profile in scaled units Δ/R_H provided that H is changed proportionally to $q^{\frac{1}{3}}$ *and* ν is changed proportionally to q.

The most complicated case that remains to be analyzed is that where q is constant, but H and ν are changed. It is evident from Eq. (4.11) that it is not possible to have an invariant surface density profile by decreasing H and increasing ν or vice-versa. The question is therefore how to keep the central gap depth invariant, despite changes in the gap profile. We answer this question using our semi-analytic calculation of gap profiles, based on the integration of Eq. (4.11). For this, we define – arbitrarily – that the minimal depth that defines a gap is 1/10 of the unperturbed disk density at $r = r_p$. Figure 4.12 shows as bold lines, for six different values of the planet mass, the relationships H vs. ν that preserve such central gap depth.

As one can see, these relationships are almost linear.

We can fit each one with a relation of type $H/H_0 + \nu/\nu_0 = 1$, where H_0 and ν_0 have been defined above. As we have $\nu_0 \propto q$ and $H_0 \propto q^{1/3}$, we can derive a general relation involving H, ν and q that approximately describes all the curves plotted on figure 4.12, and thus a general criterion for gap opening. Denoting by $\mathcal{R}$ the Reynolds number $r_p^2\Omega_p/\nu$, we find that a gap is

opened if q, H and $\mathcal{R}$ satisfy the following inequality :

$$\frac{3}{4}\frac{H}{R_H} + \frac{50}{q\mathcal{R}} \lesssim 1 \ . \tag{4.12}$$

The thin lines on figure 4.12 correspond to the limit case $\frac{3}{4}\frac{H}{R_H} + \frac{50}{q\mathcal{R}} = 1$, for any of the six considered values of q.

4.7 Discussion

In this chapter, we have analyzed in detail the process of gap opening in proto-planetary disks. In this respect, a key problem is to calculate which fraction of the torque exerted by the planet is locally deposited in the disk and which fraction is transported away by pressure supported waves. We have shown that the angular momentum evacuated by the waves can be computed as a pressure torque. We found that the steady state of the disk is set by the equilibrium among the total gravity torque, the viscous torque, and the pressure torque. From this consideration, we have built a semi-analytical algorithm that, given viscosity and aspect ratio, provides the equilibrium profile of the surface density of the disk, enabling us to explore the gap shape for a large range of parameters.

This work has several types of application. It can be used to achieve a first realistic estimate of the width and depth of gaps in various situations, in view of the future high resolution observations of proto-planetary disks (with ALMA or the SKA projects). Notice that, if the inner disk disappears, the gap transforms into a cavity, which is much easier to detect. We will come back to cavity opening in Chapter 6, applying Eq. (4.11) to develop a toy model of the behavior of a giant planet in an evolving protoplanetary disk. Moreover, our equilibrium gap profiles can be used as a starting condition in numerical simulations if one wants to avoid the intermediate, cpu-consuming phase which leads to the steady state.

Our work is not fully analytic. Indeed our final equation, Eq. (4.11), involves a function a'' which we approximated by the ansatz function given by Eq. (4.10), with coefficients determined with respect to a reference numerical simulation. Also the gravity torque has been refined using fits to the reference numerical results (Eq. (4.8)). As a consequence, if our model matches the results of the reference numerical simulation, it still is in satisfactory agreement with the results of other numerical simulations.

Moreover, the equilibrium profile that we obtain corresponds to the equilibrium configuration of the disk at infinite time in presence of a non-migrating planet, which is evidently an ideal case. Our model is two-dimensional, intended to approximate the behavior of a vertically isothermal 3D disk ; in a 3D, thermally stratified disk, the density waves would not propagate exactly the same way (Bate et al., 2003) and consequently the pressure torque is expected to be somewhat different. Finally, we have assumed a constant shear viscosity ν ; in reality, in the regions where the perturbations are nonlinear, the effective viscosity depends on the local planet's gravitational torque (Goodman and Rafikov, 2001), although this dependence may be weak (Papaloizou et al., 2004).

In spite of these limitations, our work clearly demonstrates the fundamental role of the pressure in setting the equilibrium of the disk. Moreover, it gives a correct, nearly quantitative, description of the evolution of the gap profile with respect to the key parameters of the problem : planet mass, viscosity and aspect ratio. From this we derive a new general criterion for gap opening, involving simultaneously these three parameters.

To conclude, this work explains why the width of the gap is bounded even in the case with very small viscosity, which was the open problem that originally motivated our work. It provides a conceptual unification of the two classically, but independently derived, criteria for gap opening, based on threshold viscosity and aspect ratio.

4.8 Appendix

A: trajectories and streamlines computation.

In a steady state, trajectories and streamlines coincide. Computing the streamlines is then equivalent to computing the trajectories. In principle, to compute a trajectory it is enough to integrate the velocity field. The latter is defined on the grid and output by the code, from which the velocity at any point of the disk can be computed by interpolation. However, using this procedure, the resulting trajectories would in general not be periodic, as a consequence of the accumulation of the integration and interpolation errors. This is a serious problem, because the loss of periodicity would introduce a spurious change of angular momentum, namely a spurious torque.

To obtain perfectly periodic streamlines, we used the following algorithm, that for simplicity we detail for the outer part of the disk ($r > r_p$). We first compute a trajectory from ($r = r_0, \theta = \pi$) to $\theta = -\pi$ by simple numerical integration of the velocity field (the integration runs from π to $-\pi$ because $r_0 > r_p$, so that the fluid element rotates clockwise in the corotating frame). This gives a first curve $r^{(1)}(\theta)$, defined on the interval $[-\pi, \pi]$. By definition $r^{(1)}(\pi) = r_0$, but $r^{(1)}(-\pi)$ is in general close but not equal to r_0, because of numerical errors as said above. On this trajectory, we calculate $\frac{v_r}{v_\theta}(r^{(1)}(\theta), \theta) \equiv f^{(1)}(\theta)$. This is a pseudo-derivative of $r^{(1)}$, *i.e.* the slope of the tangent to the curve according to the velocity field. It should be equal to $\mathrm{d}r^{(1)}/\mathrm{d}\theta$, but is not exactly equal because of the numerical errors in the computation of $r^{(1)}$. Then, we compute the Fourier coefficients $f_n^{(1)}$ of $f^{(1)}(\theta)$. The first one $f_0^{(1)}$ is real, and corresponds to the mean of $f^{(1)}$, namely to a radial drift. It is not zero as $r^{(1)}$ is not exactly periodic, and therefore we set it to zero. The pseudo-derivative of $r^{(1)}$ with respect to θ is thus modified. To get back to a trajectory, we integrate this modified pseudo-derivative. We denote the new trajectory by $r^{(2)}(\theta)$. This trajectory is periodic by construction as its zeroth order Fourier coefficient is null. From $r^{(2)}$, we repeat the algorithm to find $r^{(3)}$, and so on, until the algorithm converges to a fixed point. This fixed point $r(\theta)$ is a periodic trajectory by construction. It fits the velocity field, as it verifies $\frac{\mathrm{d}\, r(\theta)}{\mathrm{d}\theta} = \frac{v_r}{v_\theta}(r(\theta), \theta)$, provided that the zeroth order Fourier coefficient of its pseudo-derivative is negligible. If it isn't, it means that the algorithm failed. This happens in particular if the real streamlines are not periodic because a steady state has not been reached yet.

In practice, for the implementation of this algorithm, we used simulations computed over a grid with a larger resolution than that used in section 4.2. More precisely, we have used 512 cells in radius and 1024 in azimuth. The number of points used to compute the Fourier coefficients of the pseudo-derivative was 1024 too. In all cases, the algorithm explained above converged, and the zeroth order Fourier coefficient of the final pseudo-derivative was negligible (less than 10^{-3} in our normalized units, even less than 10^{-4} for all trajectories with $r(\pi) > 1.2$).

B: a semi-numerical algorithm for the calculation of the equilibrium surface density slope.

We present an algorithm that, given the shape of the streamlines, computes the relative surface density radial gradient that ensures the equilibrium condition Eq. (4.9). This is done in two steps. First, we design a procedure that evaluates t_P on each streamline, for any given value of $\frac{1}{\Sigma}\frac{\mathrm{d}\Sigma}{\mathrm{d}r}$. Second, we solve numerically the implicit equation for $\frac{1}{\Sigma}\frac{\mathrm{d}\Sigma}{\mathrm{d}r}$ given by Eq. (4.9).

First step : computation of the torques The streamlines are ordered with respect to increasing distance to the central star, so that $r_i(\theta) < r_{i+1}(\theta)$ for every i, θ. We call the ith *streamtube* the zone around the ith streamline: $\{\,(r_{i-1}+r_i)/2 < r < (r_i+r_{i+1})/2\,\}$. A total mass m_i or mean density Σ_i can be imposed to be carried by a given streamtube i. Because the steady state is reached, the flux of matter in streamtube i is constant with respect to time and azimuth, and is $F_i = m_i/\mathcal{T}_i$, where $\mathcal{T}_i = \mathcal{T}_i(-\pi)$ is the synodic period along the streamline. Thus, the mass has to be distributed in the streamtube in such a way that the flux

$$F(\theta) = \Sigma(r_i(\theta),\theta)v_\theta(r_i(\theta),\theta)[r_{i+1}(\theta) - r_{i-1}(\theta)]/2 \tag{4.13}$$

is equal to F_i for all θ. The azimuthal speed $v_\theta(r_i(\theta),\theta)$ can be obtained by interpolation from the output of the numerical code; the local density $\Sigma(r_i(\theta),\theta)$ is therefore the only unknown in Eq. (4.13), so that one has:

$$\Sigma(r_i(\theta),\theta) = 2F_i/v_\theta(r_i(\theta),\theta)\,[r_{i+1}(\theta) - r_{i-1}(\theta)]\ . \tag{4.14}$$

Any relative radial density gradient $(1/\Sigma)(\mathrm{d}\Sigma/\mathrm{d}r)$ around the ith streamline can be created by imposing appropriate values for Σ_{i+1} and Σ_{i-1}. The masses m_{i+1} and m_{i-1} carried by the streamlines are obtained by multiplying the mean surface densities by the areas of the stream tubes. Then, the local densities are computed using Eq. (4.14).

Once the streamlines and the local densities are known, the numerical computation of the pressure torque can be done using Eq. (4.7). The partial derivative of the density with respect to the azimuth is delicate to compute. Indeed, from Eq. (4.14) we know $\Sigma(r_i(\theta),\theta)$ only on a discrete set of values $r_i(\theta)$. To compute $(\partial\Sigma/\partial\theta)$ at the location $(r_i(\theta),\theta)$ we need to know $\Sigma(r_i(\theta),\theta\pm\delta\theta)$, for some small $\delta\theta$. This is computed by interpolation between $\Sigma(r_j(\theta\pm\delta\theta),\theta\pm\delta\theta)$ and $\Sigma(r_{j+1}(\theta\pm\delta\theta),\theta\pm\delta\theta)$, where the jth streamline is chosen such that $r_j(\theta\pm\delta\theta) < r_i(\theta) < r_{j+1}(\theta\pm\delta\theta)$.

The viscous and gravity torques are given by Eqs. (4.1) and (4.8) respectively, with $r \equiv r(\pi)$. Equation (4.1) is preferred to Eq. (4.6), despite of its limitations in the very vicinity of the planet (see figure 4.6) because it is simple and explicit.

Second step : computation of the gap profile To obtain the density profile we impose that the sum of the three torques vanishes on every streamline. Thus, for each streamline, the goal is to find the value of the relative surface density slope $s = (\frac{1}{\Sigma}\frac{\mathrm{d}\Sigma}{\mathrm{d}r})$ that makes the total torque $t_{\mathrm{total}}(s) = (t_P + t_\nu + t_g)$ equal to zero. As the pressure torque is numerically computed, the solution can be found only numerically. We use a secant method algorithm, described next.

A first value s_0 of s is arbitrarily chosen (typically 0 or the solution found on a neighboring streamline). Then, another value s_1 is taken (for instance $s_0 + 100\,t_{\mathrm{total}}(s_0)$). The secant method algorithm is then used. The value chosen for s_2 is: $s_1 - t_{\mathrm{total}}(s_1).(s_1 - s_0)/\,[t_{\mathrm{total}}(s_1) - t_{\mathrm{total}}(s_0)]$. A sequence $(s_n)_{n=0,1,\ldots}$ is build this way. At each step, the tested value is: $s_n = s_{n-1} -$

$t_{\rm total}(s_{n-1}).(s_{n-1}-s_{n-2})/\left[t_{\rm total}(s_{n-1})-t_{\rm total}(s_{n-2})\right]$. The sequence converges to $s_{\rm equil}$, such that $t_{\rm total}(s_{\rm equil})=0$. We stop when we reach a value for s that makes $|t_{\rm total}(s)|$ smaller than $10^{-4}t_g$, and we take that as our solution for $(\frac{1}{\Sigma}\frac{{\rm d}\Sigma}{{\rm d}r})_{\rm equil}$.

With this procedure, we get $(\frac{1}{\Sigma}\frac{{\rm d}\Sigma}{{\rm d}r})_{\rm equil}$ for each streamline or, equivalently, each $r_i(\pi)$. It represents a data point for the relative radial derivative of the density, shown as a cross on figure 4.7.

C: Flux of angular momentum.

The flux of angular momentum through a circle reads $F_J=\int_0^{2\pi}(\Sigma j)v_r r{\rm d}\theta$. Denoting by a prime the perturbed quantities ($v'_\theta=v_\theta-\bar{v_\theta}$ and $v'_r=v_r-\bar{v_r}$, the barred quantities denoting the averages over the circle of integration) and assuming $\bar{v_r}=0$, one gets:

$$F_J=\int_0^{2\pi}(\Sigma r v'_\theta)v'_r r{\rm d}\theta$$

(see also Eq. (5.7) further).

The flux of angular momentum has to be evaluated in a frame in which angular momentum is conserved. This is not the case for the frame centered on the primary (which is accelerated), whereas it is the case in the non-rotating frame centered on the center of mass of the system (star plus planet plus disk) C, which is inertial. One therefore needs to evaluate the following expression:

$$F_J=\int_0^{2\pi}(\Sigma r v'_\theta)v'_r r{\rm d}\theta, \tag{4.15}$$

where v'_θ and v'_r are the perturbed azimuthal and radial velocities in the C centered frame.

We assume that $q\ll 1$. We remark that the perturbed quantities are proportional to q, and F_J to q^2. Then, to compute Eq. (4.15) from the velocities output by the code, we need a sequence of transformations. Neglecting terms that will give corrections of order q^3 in F_J, this reduces to two transformations on v_r and v_θ:

(i) The velocity of C in the heliocentric frame has to be subtracted. In polar coordinates centered on the star, it is to first order in q: $\vec{v}(C)=qr_p\Omega_p\big(\sin(\theta-\theta_p),\cos(\theta-\theta_p)\big)$, where the subscript p refers to the planet.

(ii) The radial and azimuthal components of a fluid element velocity are different in the heliocentric and barycentric frames. For any vector $\vec{X}=(X_r,X_\theta)$ in the heliocentric frame, the radial component in the barycentric frame is written, to first order in q, as: $X_r-X_\theta q(r_p/r)\sin(\theta-\theta_p)$. Similarly, the azimuthal component of X in the barycentric frame is: $X_\theta+X_r q(r_p/r)\sin(\theta-\theta_p)$. We stress that the radial component of the velocity of a fluid element is proportional to q, so that the above correction on the azimuthal component is second order in q and will be neglected.

The application of (i) and (ii) give the following expression for F_J:

$$F_J=\bar{\Sigma}\int_0^{2\pi}\Big[r\left(v'_\theta-qr_p\Omega_p\cos(\theta-\theta_p)\right)\times$$

$$\left(v'_r-q\frac{r_p}{r}(r\Omega_p+\bar{v_\theta})\sin(\theta-\theta_p)\right)\Big]\,r{\rm d}\theta\ , \tag{4.16}$$

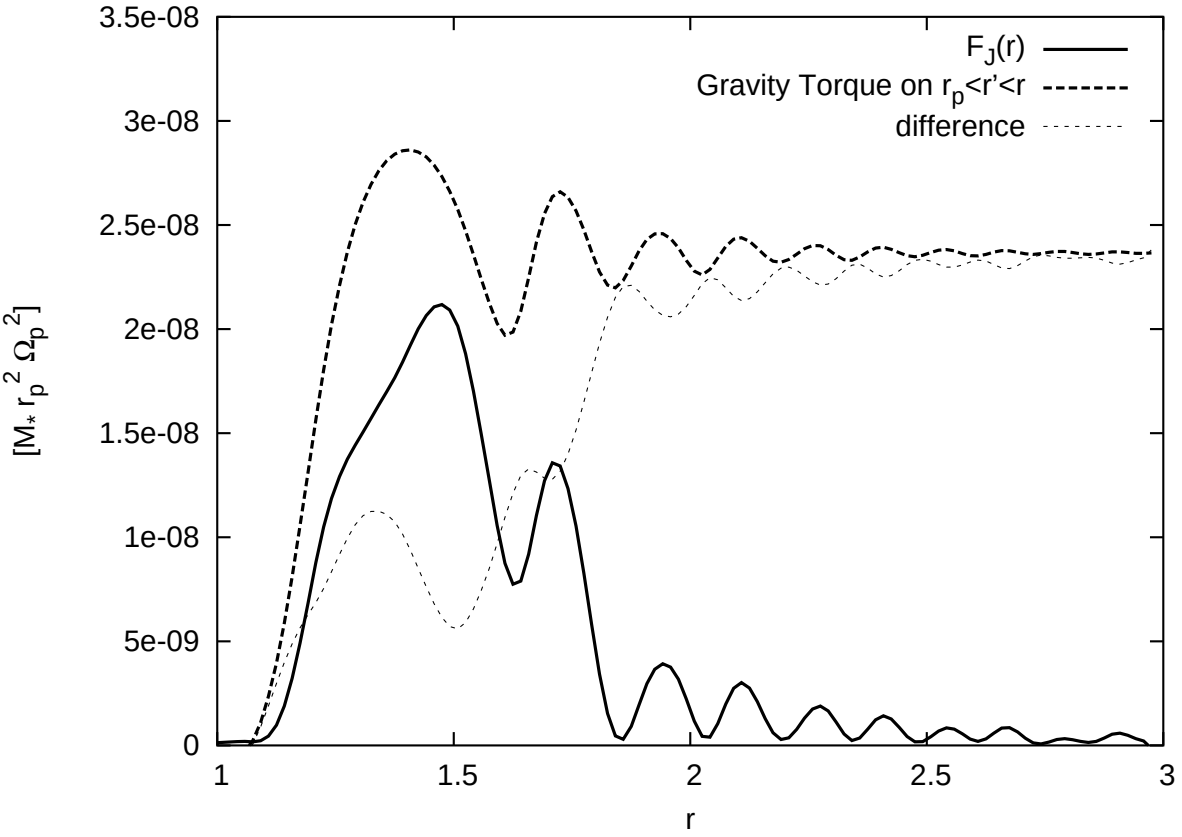

Figure 4.13: Angular momentum flux carried by the wave launched by the planet (bold plain line, corresponding to Eq. (4.16)), compared to the total gravity torque (bold dashed line) as functions of the distance to central star. The difference is plotted as a thin dot-dashed line.

where $\bar{\Sigma}$ is the mean density on the circle and all the quantities are the ones output by the code in the heliocentric frame. This corresponds to the flux of angular momentum through the circle of radius r, due exclusively to the wave launched by the planet.

The assumption $q \ll 1$ has allowed us to neglect the following effects :

(a) The density Σ should be evaluated along the circle, but $\Sigma = \bar{\Sigma} + \Sigma'$, and $\Sigma' \propto q\Sigma \ll \bar{\Sigma}$, so that Σ can be replaced by $\bar{\Sigma}$ in the integral.

(b) The circle of radius r centered on C differs from the circle of radius r centered on the star. As the distance between the two circles is proportional to q, this only introduces negligible modifications in the value of every quantity.

(c) In the previous calculations, C corresponds to the barycenter of the star-planet system, and not of the whole system including the disk. The latter is initially axisymmetric, and the perturbations are proportional to q. As the mass of the disk is also of the order of the mass of the planet, the influence of the disk on the barycenter position is negligible.

We computed the flux F_J on our reference simulation ($q = 10^{-3}$, $\nu = 10^{-5.5}$, $H/r = 0.05$) using Eq. (4.16). In figure 4.13, $F_J(r)$ is plotted as a bold plain line, whereas the total gravity torque T_g computed on the annulus between the planet orbit and the circle of radius r is shown

as a bold dashed line. The gravity torque is computed using the direct terms due to the planet (GM_p/d^2, d being the distance between the planet and the considered point) and to the star (GM_*/r^2), as it is evaluated in an inertial frame. The difference between F_J and T_g is the thin dot-dashed line; it corresponds to the cumulative locally deposited gravity torque (*i.e.* the fraction of the gravity torque that is not evacuated by the pressure supported wave). The wave carries an increasing flux near the planet (in the zone $\{1.15 \lesssim r \lesssim 1.5\}$), and takes away a large fraction of the gravity torque; this corresponds to the radius where the pressure torque t_P appears to be of the same order as the gravity torque t_g (see figure 4.6). This angular momentum is then deposited further from the planet, in particular in the $\{1.5 \lesssim r \lesssim 2\}$ region, where $F_J(r)$ sharply decreases. Beyond $r \sim 2$ the flux vanishes. At the outer boundary of our grid, the flux of angular momentum taken away by the wave is negligible with respect to the total gravity torque.

This shows that the outer boundary of the grid is sufficiently far from the planet so that the angular momentum transfer from the wake to the disk is correctly described, while the angular momentum leakage at the outer boundary is negligible. Thus, we conclude that our simulations are realistic, and our gap profiles correspond to steady states in the non-migrating planet hypothesis.

Chapter 5

Simulating planet migration in globally evolving disks

5.1 Introduction

In Chapter 2, we have seen that a planet massive enough to open a clear gap is locked in the gap, so that its migration has to follow the viscous evolution of the disk (type II migration). Moreover, we have seen in section 2.6.2 that the global disk evolution is not necessarily a constant inward accretion. In addition, the role of the horseshoe region, highlighted in section 2.4 and in Chapter 3, may be non-negligible if the gap is not completely empty. Thus, if we want to investigate mechanisms that may slow down, or prevent, type II migration, we need a tool for numerical simulations that correctly takes into account both the *local* planet-disk interactions and the *global* evolution of the disk. The development of such a code is the goal of this Chapter.

Typical hydro-dynamical codes used for planet disk interactions consider a polar grid composed of N_r rings and N_s sectors, each one $\delta\theta = 2\pi/N_s$ wide. In each cell, the density of gas, and the two components of the velocity are defined. In staggered mesh codes, the density is defined at the center of the cell, while the radial velocity is considered centered in azimuth and half centered in radius (applied at the lower r edge of the cell), and the tangential velocity is centered in radius but half centered in azimuth (applied at the lower θ edge of the cell), as illustrated in figure 5.1. The time step is the same for all cells. During a time-step, all hydrodynamic quantities are updated according to the continuity and momentum equations (Eqs. (2.4) and (2.5)). The momentum equation reads :

$$\frac{\partial \vec{v}}{\partial t} = -\left(\vec{v}.\vec{\nabla}\right)\vec{v} + \underbrace{\vec{F} + \frac{1}{\Sigma}\nabla\bar{\bar{\sigma}}}_{\text{Source terms}} \ .$$

The Source terms include the external forces $\vec{F}$ and the internal stress. The external forces are the gravity of the star and the planet(s). The internal stress is the divergence of the stress tensor. In FARGO, the bulk viscosity ζ is assumed null, so that $\bar{\bar{\sigma}} = 2\Sigma\nu\left(\bar{\bar{D}} - \frac{1}{3}(\nabla\vec{v})\bar{\bar{I}}\right) - P\bar{\bar{I}}$; $\bar{\bar{D}}$ is the strain tensor given by Eq. (2.1) or (2.8) ; P is the pressure, given by the equation of state : $P = {c_s}^2\Sigma$, where c_s is the sound speed defined by $c_s = H\Omega_K$ with H the disk scale height and Ω_K the Keplerian angular velocity given by Eq. (1.1). The aspect ratio H/r (where r is the distance to central star) is assumed to be constant in space and time, hence the disk is locally isothermal and the sound speed is constant in time. The shear viscosity ν is most often assumed constant in space and time. Another well-known prescription for the shear viscosity has been proposed

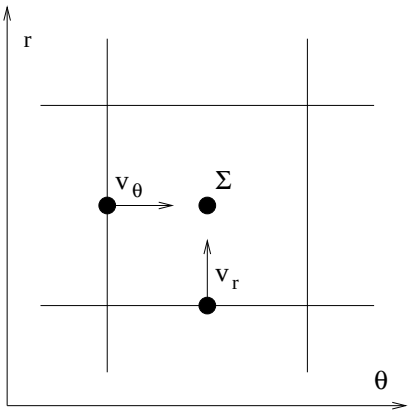

Figure 5.1: A cell of a 2D polar grid in a staggered mesh scheme. The dots correspond to the location in the cell where the corresponding quantities Σ, v_r, and v_θ are defined.

by Shakura and Sunyaev (1973) : $\nu = \alpha c_s H$, where α is a dimensionless coefficient. It is also implemented in FARGO and we sometimes use it.

In hydrocodes, the integration of $\partial_t \vec{v} = -(\vec{v}.\vec{\nabla})\vec{v}$ leads to numerical instabilities if the resolution is not high enough to describe the velocity gradient. The viscosity in the stress tensor (in the source terms) tends to smooth the velocity profile and to limit shocks. However, typical viscosities used in astrophysical disks are too low for a direct numerical integration of this equation. Therefore, the term $(\vec{v}.\vec{\nabla})\vec{v}$, which physically corresponds to the local arrival of material with different velocity, is interpreted and computed as a transport term.

So, a time step decomposes in two main parts (Stone and Norman, 1992) :

Eulerian substep : The velocity is updated according to the Source terms.

Transport substep : Mass and Momentum are conservatively advected through the grid according to the flow given by previous substep.

The time-step length δt is determined by the Courant-Friedrichs-Lewy (CFL) condition (Stone and Norman, 1993, , paragraph 4.6). To avoid numerical instabilities, the time-step length δt is set so that information does not propagate more than one cell over one time-step. Thus, the limit most likely comes from the cells with smallest radii, where the angular velocity is the largest : $\delta t < \delta\theta/\Omega$; consequently, denoting by $R_{\rm min}$ the inner boundary radius of the grid, one has generally $\delta t \propto R_{\rm min}^{3/2}$.

In the FARGO algorithm, the azimuthal transport is decomposed in two parts. The mean angular velocity $\bar{v_\theta}$ on a ring is computed. The classical azimuthal transport step is then computed with the *residual azimuthal velocity*: $v_\theta - \bar{v_\theta}$. Thus, only the residual azimuthal velocity should be considered in the CFL condition, which is much less constraining than the Keplerian velocity. Then, an additional azimuthal transport step is performed, with the mean azimuthal velocity for every cell ; this corresponds to a simple shift of $l = \delta t\, \bar{v_\theta}/r$ cells in azimuth. As l is not necessarily an integer number of cells, a shift of n cells is performed with n the closest integer to l, plus a classical azimuthal transport of amplitude $l - n$ cell (which is smaller than 0.5 in absolute value). This additional azimuthal transport step requires no condition on the time-step length.

This algorithm permits to increase sensibly the time-step length, and thus to improve the speed of the computation, by an order r/H without loss of accuracy. For more details on the

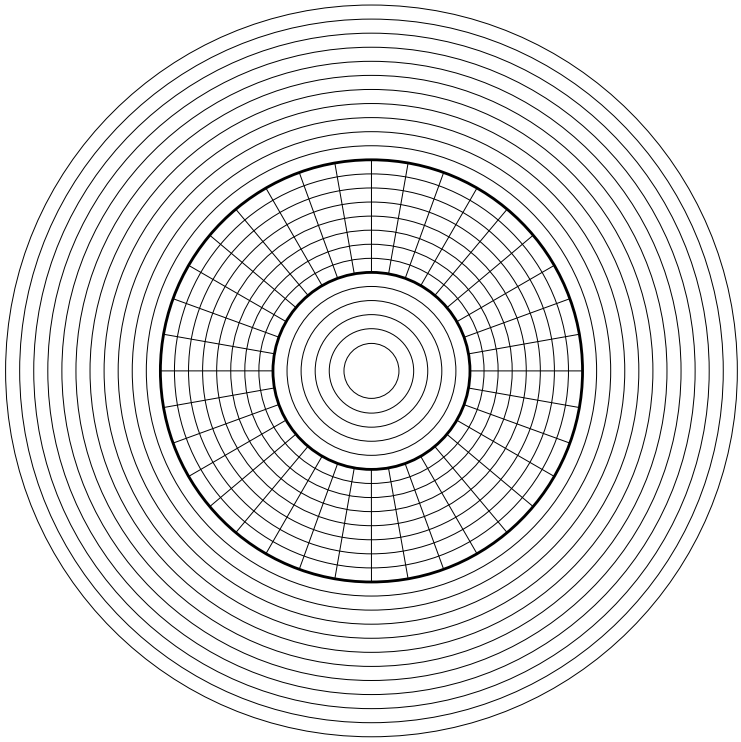

Figure 5.2: Our algorithm scheme. The classical 2D polar grid covers an annulus of disk between the two bold circles. It is surrounded by two 1D grids, made of concentric elementary rings.

FARGO algorithm, one should refer to Masset (2000a,b). Accuracy and speed comparative tests have been performed in Nelson et al. (2000), where the FARGO algorithm appears to be very performing.

Despite the FARGO algorithm is performing, the 2 dimensional polar grid has to be truncated at an inner and an outer radius, for numerical reasons. However, the boundary conditions at the extreme rings of the polar grid cannot take into account what happens in the whole disk, outside of the grid. For instance, the use of *open* boundary conditions allows the gas to leave the region covered by the grid; this makes the studied disk annulus behave as if it were surrounded by vacuum, so that it empties very rapidly, which is not realistic. In the opposite extreme case, boundary conditions that impose that the mean density on the extreme rings remains constant with time disable the accretion and spreading of the gas. Some other prescriptions between these two extremes may be used (for instance allowing inflow, or imposing an outflow given by an analytical model, or setting the flow on the last ring equal to the viscous flow measured in the neighboring rings, etc.). However, it is very difficult to adapt these prescriptions to the changing behavior of the disk with time, in particular when the disk undergoes perturbation from the planets. Also these prescriptions are rather arbitrary and they may introduce artifacts in the disk evolution, so that the accuracy of the resulting planetary migration can be questioned.

Our idea is to surround the 2D polar grid with a 1D radial grid, as shown in figure 5.2. The 1D grid extends from the real inner edge of the gas disk (e.g. the X-wind truncation radius at a few tenths of AU) to the real outer edge (e.g. the photo-dissociation radius at hundreds of AU), with open boundaries. In the 1D grid, the disk evolution is described by numerical integration of the classical equations, assuming axisymmetry (that is the equations studied in section 2.6.2).

This 1D grid exchanges information with the 2D grid to take into account the disk perturbations and to provide the 2D grid realistic, time-dependent boundary conditions. Our algorithm for the interface between the 1D and 2D grids is driven by the requirement that the angular momentum of the global system (the disk in the 2D section, plus the disk in the 1D section plus the planet-star system) is conserved. It will be described in detail in section 5.3. First, however, we revisit the algorithm used to model the gas evolution and planet-disk interactions on the 2D grid, to make sure that it also conserves angular momentum, which is often not the case in standard implementations. This issue is developed in section 5.2. In section 5.4, the results of our new algorithm are discussed, in terms of CPU time and robustness with respect to the positioning of the interfaces between the two grids. This work has been subject of an article (Crida et al., 2007), and this Chapter is based on the paper.

5.2 Angular momentum conservation in 2D hydrodynamical algorithms

Consider a simulation of the planet-disk interactions, with the disk represented on a 2D polar grid with open boundary conditions. A necessary requirement for the simulation to be correct is that the sum of the angular momenta of the disk, of the star-planet(s) system and of the gas outflowing through the boundaries remains constant over time.

We have tested if this is the case, using the code FARGO described above.

Our simulation accounts for a Jupiter mass planet ($M_p = q = 10^{-3}$) on an initially circular orbit at $r = 1$, so that initially $\Omega_p = 1$ and an orbit lasts 2π time units. The grid used to represent the disk extends from $r = 0.25$ to $r = 3$ with open boundaries. It is equally divided in $N_r = 165$ elementary rings, and $N_s = 320$ sectors. The disk aspect ratio (H/r) is set to 5% (uniform in space and time). The gas kinematic viscosity is $\nu = 10^{-5.5}$ in our normalized units (which corresponds to $\alpha = 1.25\,10^{-3}$ at $r = 1$ in a Shakura and Sunyaev (1973) prescription, but ν is assumed independent of radius for simplicity). The initial density profile can be seen in figure 5.7 ; it has been provided by Hueso and Guillot and corresponds to a disk that evolved for some time under the effect of its own viscosity (see Hueso and Guillot, 2005) ; consistently with the results of section 2.6.2, it can be very well approximated by a Gaussian function :

$$\Sigma(r) = 0.000306\ \exp(-r^2/52.8)\ . \tag{5.1}$$

Assuming the length unit is 5 AU, the density there corresponds to the Minimal Mass Solar Nebula (see Chapter 1).

The evolution of the total mass and angular momentum of the whole system (including the outflow, e.g. the cumulated mass and momentum advected outside of the region spanned by the 2D grid by the gas outflowing through the boundaries) is presented in figure 5.3. While the total mass is conserved at the level of numerical errors (top panel), the conservation of the angular momentum is quite poor (middle panel).

The bottom panel shows that the gain of angular momentum of the whole system (plain line), which is the error of the simulation, amounts to 10% of what the planet exchanges with the gas in its migration process (dashed line). Thus we can expect that the migration of the planet measured in the simulation is correct only at the 10% level.

This shows the need to improve the algorithm in order to achieve a much better conservation of angular momentum. We describe a procedure that considerably improves angular momentum conservation below.

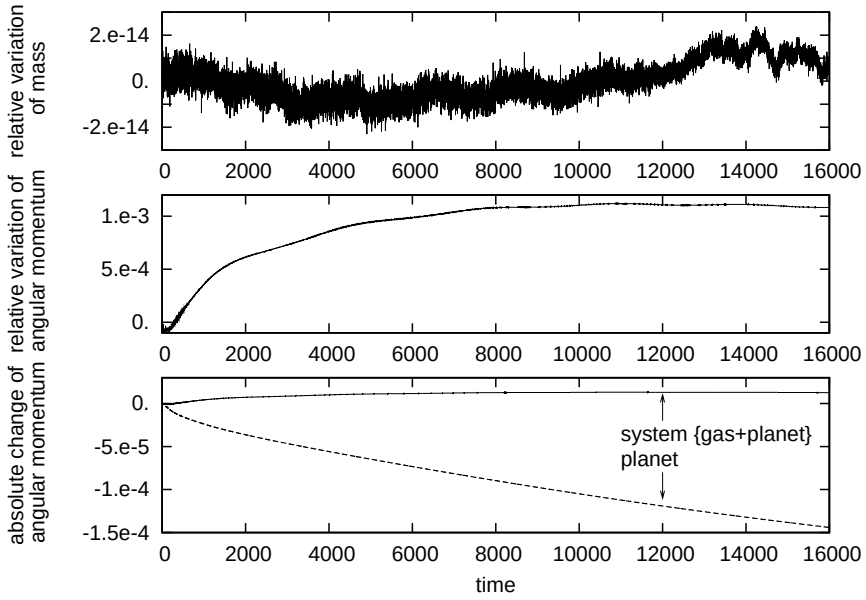

Figure 5.3: Relative variation of mass (top panel) and angular momentum (middle panel) of the system {gas + Jupiter + outflow} with time. The absolute variation of angular momentum of the system is compared to that of the planet on the bottom panel (in our units, in which the initial angular momentum of the planet is 10^{-3}).

5.2.1 Choice of reference frame

Need for a frame centered on the center of mass. Most, if not all, the published numerical simulations of disk-planet interaction that we are aware of use a non-inertial frame centered on the primary (Kley, 1999; Masset, 2002; Masset et al., 2006; Nelson et al., 2000; Nelson and Benz, 2003; Varnière et al., 2004, 2006a, and preceding Chapters). This is done for practical reasons, and because it is thought to be better adapted to describe the motion of the inner part of the disk. This reference frame is not inertial, so that indirect forces are taken into account for the simulation to be realistic. It is well known that the presence of these forces destroys the conservation of the angular momentum measured in the non-inertial frame. In principle however, one can make at any time a change of coordinates to compute position and velocities in the inertial frame (centered on the center of mass), and the angular momentum computed from these coordinates should remain conserved. This is for instance what happens in N-body codes, when the simulation is done in heliocentric coordinates (except for truncation and round-off errors). This is not the case here. The transport substep for the gas – in which mass, angular momentum, and linear momentum advect from a cell to its neighbors (see section 5.1) – imposes the conservation of each of these quantities. This is correct for the mass, but not for the momenta, because they are not supposed to be conserved in the adopted frame. As a consequence of this imposed, unphysical conservation, the conservation of the momenta in the inertial frame is corrupted, as shown below.

Consider the two first cells of two successive elementary rings, and label these cells 1 and 2. Assume for simplicity that the azimuth of the center of mass is also 0 in the heliocentric frame (see figure above). Assume also that the center of mass is fixed in the heliocentric frame, and denote r_c its distance to the star. Let the superscript $*$ (resp. c) denote quantities measured in the heliocentric (resp. inertial) frame. The two assumptions ensure that the tangential velocity in the two cells is the same in the two frames: $v^*_{\theta i} = v^c_{\theta i} = v_{\theta i}$. Denoting δm the quantity of gas that flows from 1 to 2 (which is independent of the frame), and $\delta j^{(*,c)}$ the quantity of angular momentum it carries, one has:

$$\delta j^c = (\delta m) r_1^c \, v_\theta = \delta j^* \frac{r_1^c}{r_1^*} \; .$$

To preserve angular momentum conservation, the angular velocity in the cell 2 is set accordingly to the angular momentum received. Suppose the cell 2 was empty before this transport, then: $v_{\theta 2}^{(*,c)} = \delta j^{(*,c)} / (\delta m \, r_2^{(*,c)})$. So,:

$$v^c_{\theta 2} = v^*_{\theta 2} \frac{r_1^c r_2^*}{r_1^* r_2^c} = v^*_{\theta 2} \left(1 + r_c \frac{r_2^* - r_1^*}{r_1^* r_2^*} \right)$$

Even in this simple case, the prescription for angular momentum conservation is not the same in the two frames. Therefore, ensuring angular momentum conservation in the heliocentric frame corrupts angular momentum conservation in the inertial frame.

The considerations above concern the flux of angular momentum due to the flow of matter. In addition, as mentioned in Appendix C of Chapter 4, the flux of angular momentum through due to the wave –which has to be taken into account in the coupling of the two grids (see section 5.3.3)– should also be evaluated in the inertial frame. If the reference frame is not barycentric, this requires a sequence of cumbersome and approximated transformations, that we want to avoid.

This shows that the computation needs to be done in the frame centered on the center of mass throughout the algorithm.

Implementation. This is not trivial to implement. A first possibility is to suppress all indirect forces in the algorithm and, whenever the position and the velocity of the star are needed, to compute them imposing that the position of the center of mass of the whole system (star, planets and disk) is at (0,0). This is, for instance, what is usually done in N-body barycentric simulations. In this case, however, the situation is more complicated. While in N-body codes all interactions are treated simultaneously, planet-disk interaction simulators divide a time-step in a transport substep and an Eulerian substep (as mentioned in section 5.1). In addition, the Eulerian substep involves a purely gravitational part and a hydrodynamical part, and the planetary system and the disk are treated separately (see subsection 5.2.2 for the detailed sequence of integration substeps). When the disk is advected, the star is moved to assure the position of the center of mass, but not the planet. Thus, at the next step, the planet sees a star in a different location in phase-space with respect to the end of the previous step. This has a dramatic effect on the orbital stability of the planet and the overall conservation properties. A second, more advantageous possibility is to consider the star exactly like a planet during all the stages of the computation. This ensures a symmetry in the treatment of the star and of the planet(s). When the gas is advected, the planetary system (now including the star) is translated in phase-space to ensure that the center of mass of the whole system remains motionless at $r = 0$. This correction does

not perturb the relative planetary motion. In principle, it corrupts the conservation of the total angular momentum, but the errors introduced have negligible consequences, as we will test and discuss below.

Caveats. Because the grid is centered on the center of mass, a good numerical accuracy can be achieved only if the motion of the gas is approximated by a rotation around the center of mass. This is the case as long as the central object is close to the center of mass, namely if the total mass of the planets is negligible with respect to the one of the star (which is the common case) or – in the case of a large stellar companion – if one considers a distant circumbinary disk. The choice of a frame centered on the center of mass is not adapted to study a disk around a star with a massive companion or a circumplanetary disk.

In the case of an axisymmetric problem (accretion disk with no planet), the choice of such a frame may lead to numerical instabilities because small deviations from axial symmetry in the disk due to numerical errors cause a shift of the star relative to the center of mass, which in turn can enhance the disk's asymmetries. Thus, if the planetary system is made of the star alone, we recommend to keep it fixed at the origin of the frame.

In many applications, the equations of motion are implemented in a rotating frame in order to keep the planet at a constant position. This can still be done in a frame centered on the center of mass.

5.2.2 Sub-steps sequence

As we anticipated above, the integration algorithm separately treats the pure gravitational part and the hydrodynamical part inside the Eulerian substep. To ensure a good preservation of the conserved quantities, it is necessary to respect as much as possible the action-reaction principle in the planet-disk interactions. This requires that the sequence of integration sub-steps is taken in a specific order.

Here is the sequence that we adopt:

1. The gravitational potential of the planets and star is computed and stored.

2. The velocities of the planets and the star are updated using the gravitational influence of the disk.

3. The velocities of the gas are changed in each cell according to the non advective part of the Navier-Stokes equations (the external forces dues to the gradients of pressure and gravity field and the viscous stress); the gravitational potential computed at sub-step 1 is used.

4. The planet-star system is advanced under its own gravitational interactions using an N-body algorithm (specifically a 5th order Runge-Kutta integrator).

5. The advective part of the Navier-Stokes equations is performed: using the disk velocities computed at sub-step 3, the mass, angular and radial momentum are advected from each cell to the neighboring cells. The new velocities of the gas are then computed in each cell from the new momenta and masses.

6. The conservation of the center of mass is ensured by translating in space and velocity the center of mass of the planets-star system.

The first four sub-steps correspond to the Eulerian substep of section 5.1 ; the fifth one is the transport substep ; the last one is an additional sub-step necessary in the inertial frame. In the above algorithm, every time that an action is made on the planetary system, the equivalent action is immediately applied on the disk. Moreover, there is no difference in treatment between planets and star, which is essential for the reasons discussed above. However, particular care has to be paid to the implementation of the algorithm to ensure the effective symmetry of these actions ; this is discussed in the next subsection.

5.2.3 Action-reaction symmetry

The action-reaction principle has to be perfectly fulfilled in the computation of sub-steps 2 and 3. It is not the case, for instance, if one computes the action of a planet on the disk from the gradient of its potential on each cell, and the action of the gas on the planet from the sum of the elementary gravitational forces that it feels from each cell. In principle, both calculations should be equivalent, giving total forces of the same strength and opposite directions. However, if the gradient is computed by finite differences (typical in grid calculations), this introduces a difference with respect to the force exerted by the corresponding cell on the planet.

In order to impose action-reaction symmetry, we proceed as follows. After sub-step 1, we measure the total change of angular momentum that the gas will have at sub-step 3 due to the potential of each planet. Then, in sub-step 2, we compute the change of azimuthal velocity of each planet according to the change of angular momentum that it causes to the disk. This ensures angular momentum conservation between sub-step 2 and sub-step 3. Similarly, in sub-step 2 the planet's radial velocity change is computed by measuring the total change of linear momentum in this direction caused to the gas disk by the same planet.

5.2.4 Results and discussion

All these precautions allow us to greatly improve the angular momentum conservation of the whole system. The same simulation as in figure 5.3 is computed with our modified algorithm. We denote by δJ the variation of angular momentum, in the inertial frame centered on the center of mass, of the whole system (the sum of the momenta of the gas in the 2D grid of the planet-star system and of the outflow which is the cumulated momentum carried by the gas that left the grid). It should be zero if the code were perfectly conservative. Thus δJ is a measure of the error of the integration scheme. It is compared with three relevant quantities in figure 5.4. The bottom curve (solid line) corresponds to the logarithm of the relative variation of angular momentum of the system : $\delta J/J_0$, where J_0 is the initial total angular momentum (it corresponds to the middle panel of figure 5.3) ; on a long timescale (16000 time units, $\gtrsim$ 2500 orbits at $r = 1$), this normalized error does not exceed $10^{-5.5}$. The middle curve (long dashed line) corresponds to the logarithm of $\delta J/J_p$, where J_p is the angular momentum of the planet : the error in total angular momentum is about 4.5 orders of magnitude smaller than the angular momentum of the planet. Thus, it should not affect its migration. The top curve (short dashed line) shows the logarithm of the ratio between δJ and δJ_p, where δJ_p is the variation of angular momentum of the planet : this ratio is smaller than 10^{-3}.

Although highly satisfactory for our purposes, the conservation is admittedly not perfect, in particular when compared to the mass conservation (which in the new simulation is as good as in the example of figure 5.3). This is due to two sources of error.

The most obvious one is that the algorithm used for the advancement of the planetary system,

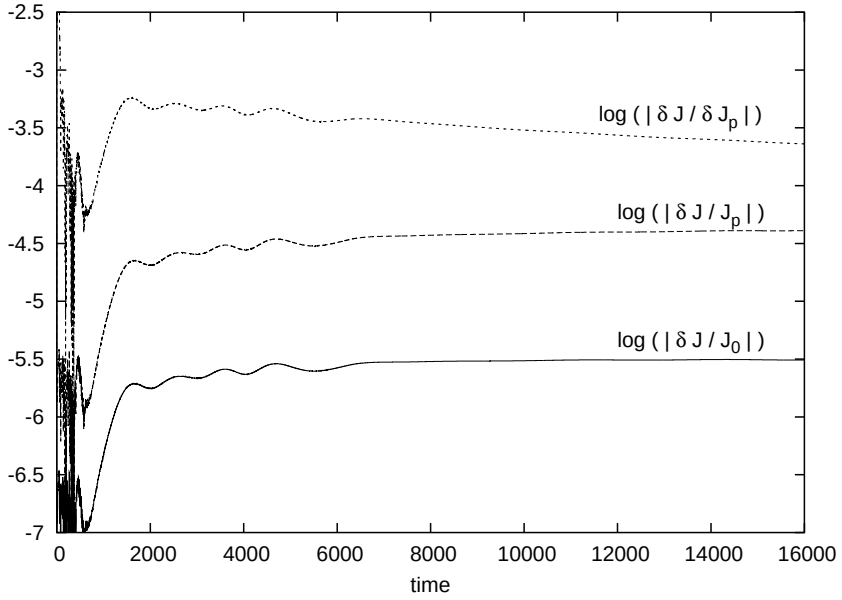

Figure 5.4: Relative angular momentum variation as a function of time. The variation of angular momentum of the system { gas + planet + star + outflow }, δJ, is compared to its initial value J_0 (bottom curve, plain line), to the angular momentum of the planet J_p (middle curve, long-dashed line), and to the variation of the latter δJ_p (top curve, short-dashed line).

which is in our case a Runge-Kutta algorithm, is not symplectic. However, we checked that in our simulation, the amount of angular momentum artificially introduced in the system in this way is 3 orders of magnitude smaller than the total global error.

The second source of error is in sub-step 6, due to the translation of the center of mass of the planet-star system. This translation occurs for two reasons. (i) It is required to compensate the center of mass motion due to errors introduced by the discretization of the grid and to the second order (in time) advection of the disk. Thus, the amplitude of this effect decreases with increasing disk resolution and decreasing time-step. (ii) Gas continuously leaves the grid through its inner or outer boundary. This gas is deleted from the simulation, while its total mass and momentum are recorded as outflow. The problem is that the outflowing gas is in general not axisymmetric. Therefore, its elimination from the simulation causes a shift (in position and velocity) of the center of mass of the whole system. The shift is artificial, in the sense that it would not exist if the gas were modeled with an infinite 2D grid, and it requires, for compensation, the translation of the planetary system. This issue is a conceptual one. Thus this source of error cannot be reduced by tuning the grid resolution or time-step. This seems unavoidable: it is the price to pay to work with 2D grids that are not as extended as the physical disk. However, as we have seen in figure 5.4, this error is so small that for all practical purposes we can safely ignore it.

5.3 Coupling of the 2D grid with a 1D grid

As we discussed in the introduction, for a correct simulation of type II migration the conservation of angular momentum is a necessary, but not sufficient condition. It is also necessary that the global evolution of the disk is correctly reproduced, which is not the case if only a portion of the

disk (the annulus represented by the 2D grid) is considered.

For this reason, we consider the whole disk, from its real inner to outer radius, corresponding respectively to the 'X' radius at the inner edge (Shu, 2002), and to a photo-evaporation radius at the outer edge (see Hollenbach and Adams, 2004a,b). Because the representation of the whole disk with a 2D grid would be computationally prohibitive, outside of the radial distance range covered by the usual 2D grid we study the evolution of the extended disk in one dimension, with the aid of a 1D grid representation. In practise, the 1D grid is made of two parts : one extending from the real inner edge of the disk to the inner edge of the 2D grid, and the other one extending from the outer edge of the 2D grid to the real outer edge of the disk (see figure 5.2.1).

In this section, we first present the equations for the 1D disk. Then we detail how we couple the 1D and 2D portions of the disk in a way that conserves mass and angular momentum, and that ensures a proper simulation of the disk's global evolution.

5.3.1 1D equations

The Navier-Stokes equation and the advection of the gas are computed in the 1D grid exactly as in the 2D grid, but with $N_s = 1$, so that each cell can be considered as an elementary ring. Consequently, there are no azimuthal components for the various gradients, nor an advective transport phase in the azimuthal direction. The gravitational potential due to the planets and the star is computed for the 1D grid as a function of r only : the whole planetary system is considered as a single central mass, the mass of which is the sum of all the bodies inside the considered radius. Denoting by $\mathcal{H}$ the Heaviside function equal to 1 for positive arguments and to 0 for negative ones, the gravitational potential felt by a cell of the 1D grid located at a radius r from the center of mass reads :

$$\Phi^{1\mathrm{D}}(r) = \sum_p -\frac{GM_p}{r}\mathcal{H}(r - r_p)$$

where the index p goes through the whole planetary system (including the star). This means that the potential felt is equal to $-G/r$ multiplied by the mass of all the celestial bodies that lie inside the ring. Thus the position of the star with respect to the center of mass has no influence ; it would be the same if the 1D rings were centered on the star.

We assume that the gas disk in the 1D grid is axisymmetric, so that in principle there is no torque in the interaction between the planets and the 1D grid. For more realism, however, one can assume that each 1D ring feels a gravitational torque due to each planet, using the formula of Goldreich and Tremaine (1980) or Lin and Papaloizou (1979) :

$$\delta T_g(r) \approx 0.4 \left(\frac{M_p}{M_*}\right)^2 {r_p}^3 {\Omega_p}^2 r^{-1} \left(\frac{r_p}{\Delta}\right)^4 (2\pi r \Sigma\, \delta r) \tag{5.2}$$

where $\Delta = r - r_p$, Ω_p is the angular velocity of the planet, and δr is the width of the ring. Of course, for angular momentum conservation, the opposite of this torque exerted on the 1D grid has to be exerted on the planet.

Because of the assumption of axial symmetry, what leaves the 1D grid through its boundaries does not impose any re-adjustment of the star-planet(s) center of mass. Thus, the conceptual problem discussed at the end of subsection 5.2.4 is not relevant here. Consequently, the evolution on the 1D grid always shows a perfect angular momentum conservation, at the level of numerical errors.

Despite this perfect conservation, however, for the results to be correct it is necessary that the assumption of axial symmetry is a good approximation for the real disk. Moreover, because Eq. (5.2) is an approximation, it is necessary that the planetary torque is small for the error to be small in absolute value. Both requirements are fulfilled if the interfaces between the 1D and 2D portions of the disk are placed sufficiently far from the planet(s). We will discuss this issue in section 5.4, with quantitative tests.

Open boundary

The "open" boundary condition that allows outflow from the grid but not inflow is implemented as follows. The description below concerns the inner edge; a symmetrical algorithm is used for the outer edge.

In the innermost ring (number 0), the radial velocity is always 0 and the density is that of the neighboring ring. In the next (ring number 1), the radial velocity is set equal to that of the following ring (number 2) if and only if it corresponds to outflow from the grid (negative radial velocity), and to 0 otherwise to prevent inflow in the grid. This gives:

- $\Sigma(0)$ is set to $\Sigma(1)$.
- Whenever $v_r(2) \geqslant 0$, $v_r(1)$ is set to 0.
- Whenever $v_r(2) < 0$, $v_r(1)$ is set to $v_r(2)$.

So, the first three rings are used for this computation, which explains the artifact observed in figures 5.6, 5.7, 5.9, and 5.10.

5.3.2 Ghost rings

The 1D grid and the 2D grid communicate with each other through a system of *ghost rings*. This technique is derived from that used for the parallelization of a hydro-code on a distributed memory architecture. We describe it here for the inner interface between the 1D grid and the 2D grid, that is the interface at the inner edge of the 2D grid; the 1D grid is inside, extending from the real inner edge of the disk (the truncation radius or the surface of the star) to the 2D grid; the 2D grid lies outside this interface, as sketched in figure 5.5.

Outside the interface, a number N_G of 1D rings are added, which are superimposed on the first N_G rings of the 2D grid; they are the ghosts of the inner 1D grid (see figure 5.5). At the beginning of each time-step, the density and the velocity in the 1D ghost rings are set as follows. The density of gas (Σ), radial momentum (Σv_r), and angular momentum ($\Sigma r v_\theta$) in the ghost ring are set to the azimuthal average of the respective quantities in the corresponding ring of the 2D grid. Denoting with the superscript '1D' the quantities in 1D rings and by j the specific angular momentum ($j = r v_\theta$), this leads to the following equations:

$$\Sigma^{1\mathrm{D}} = \frac{1}{2\pi r}\int_0^{2\pi} \Sigma\, r \mathrm{d}\theta \,, \tag{5.3}$$

$$\Sigma^{1\mathrm{D}} {v_r}^{1\mathrm{D}} = \frac{1}{2\pi r}\int_0^{2\pi} \Sigma v_r\, r \mathrm{d}\theta \,, \tag{5.4}$$

$$\Sigma^{1\mathrm{D}} j^{1\mathrm{D}} = \frac{1}{2\pi r}\int_0^{2\pi} \Sigma j\, r \mathrm{d}\theta \,. \tag{5.5}$$

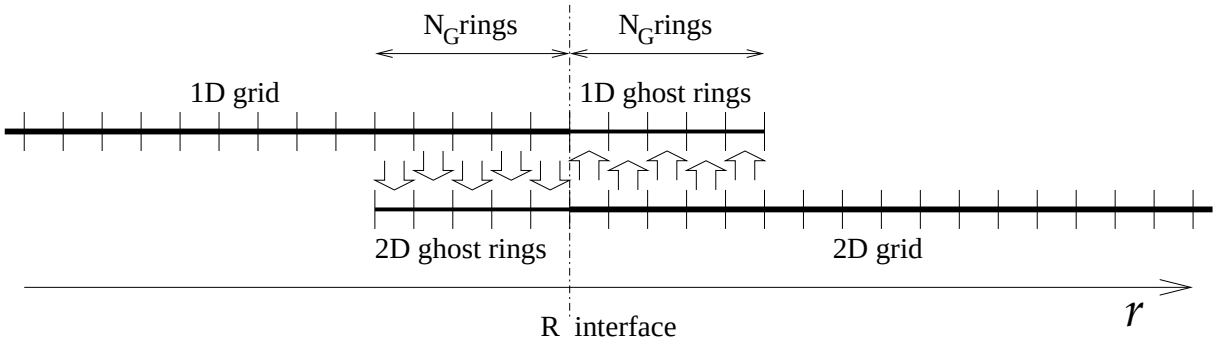

Figure 5.5: Sketch of the coupling via ghost rings at the inner interface between the 1D grid and the 2D grid.

As Σ^{1D} is given by Eq. (5.3), ${v_r}^{1D}$ and ${v_\theta}^{1D}$ are easily computed from Eqs. (5.4) and (5.5).

Then, during the time step, the computation of all stages is performed in the 1D grid as well as in the ghost rings. The 1D grid 'feels' the ghosts via the Navier-Stokes equations. As the 1D ghost rings have been filled with quantities inherited from the 2D grid, the 1D grid behaves as if it felt the 2D grid outside the interface.

Symmetrically, inside the interface, a N_G number of 2D rings are added : the 2D grid ghosts. They are treated as normal 2D rings, except that at the beginning of each time step, the azimuthal means of surface density, of radial momentum and angular momentum density are set equal to the respective values measured in the corresponding 1D rings, as sketched with arrows in figure 5.5. So, the 2D grid effectively 'feels' the 1D grid inside the interface. Filling the 2D ghosts is more elaborate than in the 1D ghost rings case. For a given 2D ghost ring, one has to proceed in four steps : (i) store for each cell the surface density, the radial momentum, and the angular momentum ; (ii) compute the azimuthal means of these quantities ; (iii) subtract in each cell, for each of the three considered quantities, the difference between its azimuthal mean and its value in the corresponding 1D ring ; (iv) find the velocity in each cell by dividing the new momenta by the new surface density.

The minimal number of ghost rings needed, N_G, depends on the numerical scheme : it is the number of rings that causally affects a given ring during a time-step, or equivalently the number of rings in which the information contained in a ring propagates during a time-step ; it is often called the kernel. For instance in FARGO, $N_G = 5$.

This way of coupling the 1D and 2D grids ensures a smooth transition for each of the quantities computed in the code. In particular, if there is no planetary perturbation, the global disk (2D + 1D parts) behaves exactly as predicted by the Lynden-Bell and Pringle (1974) equations (see section 2.6.2). This can be seen in figure 5.6, which corresponds to figure 4 in the aforementioned paper : it shows the evolution of the density distribution at four times, for $\Sigma_{t=0}(r) = \delta(r-1)$, with δ the Dirac distribution. As in Lynden-Bell and Pringle (1974), $T^* = 6\nu t$ in our units (which is different from $T = 12\nu t + 1$ in section 2.6.2). The little discrepancy between the theoretical profile (thin) and the numerical one (bold) at $T^* = 0.004$ most likely comes from the fact that the initial distribution is not exactly a δ function ; this little difference vanishes with time.

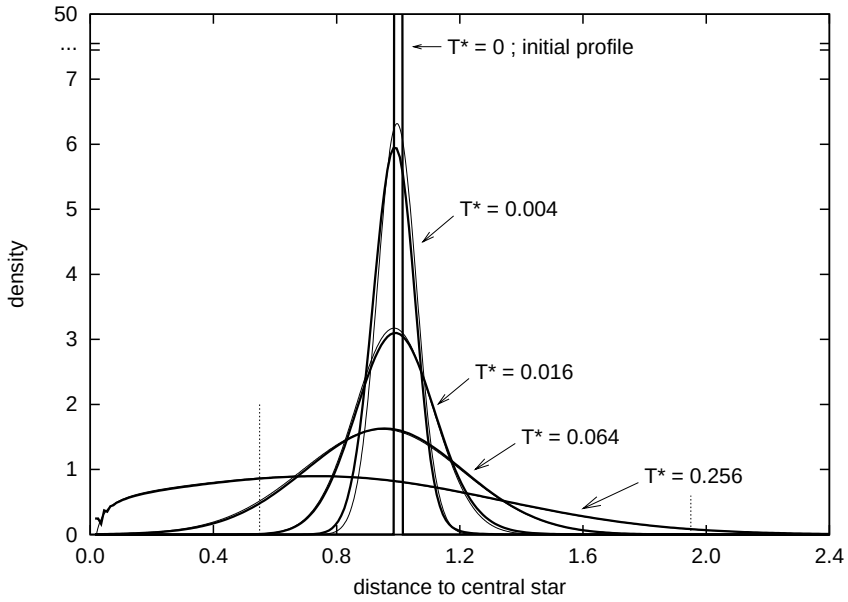

Figure 5.6: Viscous spreading of a ring. The theoretical curves (obtained by numerical solution of Eq. (2.54) with the boundary condition $\Sigma(0.02) = 0$) are thin, while the numerical ones obtained with our code are bold. The vertical dashed lines show the position of the interfaces, where the solution provided by our code remains perfectly smooth.

5.3.3 Fluxes at the interface

The fluxes of mass and angular momentum through the interfaces have to be perfectly conservative. What leaves the 2D grid has to enter the surrounding 1D grid, and vice-versa.

Mass Flux

The definition of ${v_r}^{1\mathrm{D}}$ in Eq. (5.4) makes the mass flux computed in 1D the same as the one computed in 2D. Their theoretical expressions are:

$$\begin{aligned} {F_m}^{2\mathrm{D}} &= \int_0^{2\pi} \Sigma v_r \, r \mathrm{d}\theta \\ {F_m}^{1\mathrm{D}} &= 2\pi r \Sigma^{1\mathrm{D}} {v_r}^{1\mathrm{D}} \ . \end{aligned}$$

Equation (5.4) is equivalent to ${F_m}^{1\mathrm{D}} = {F_m}^{2\mathrm{D}}$. However, in a numerical scheme with finite time steps and discrete grid, the flux is most often not computed so straightforwardly. Care has to be taken that the numerical expressions of the flux coincide at the interface between the 1D and the 2D grid. In staggered mesh codes, the density and the velocity are not defined at the same locations in the cells of the grid; typically, the density is given at the center, while the radial component of the velocity is given on the middle point of the inner edge and the tangential component on the middle point of the left edge (see figure 5.1). Thus, the fluxes are most often computed as:

$$\begin{aligned} {F_m}^{1\mathrm{D}}{}_{\mathrm{computed}} &= 2\pi r \Sigma^{1\mathrm{D}*} {v_r}^{1\mathrm{D}} \\ {F_m}^{2\mathrm{D}}{}_{\mathrm{computed}} &= \sum_k \Sigma^*[k] v_r[k] \, r \delta\theta \end{aligned}$$

where the index k goes through all the cells of the ring, $\delta\theta$ is the angular size of a cell, r is the radius of the interface, and Σ^* and ${\Sigma^{1D}}^*$ are the values of the densities Σ and Σ^{1D} at the interface after half a time-step (Stone and Norman, 1993, paragraph 4.4).

To ensure the mass conservation, we solve the following equation instead of Eq. 5.4 for the ring next to the interface:

$$ {F_m}^{1D}{}_{\text{computed}} = {F_m}^{2D}{}_{\text{computed}} \ . \tag{5.6} $$

This equation is only slightly different from Eq. (5.4). It is an implicit equation in ${v_r}^{1D}$, because ${\Sigma^{1D}}^*$ depends on ${v_r}^{1D}$. Nevertheless, it can be solved by iteration.

Angular momentum Flux

Denoting with a prime sign the non axisymmetric components of the quantities ($j' = j - {j}^{1D}$, $v_r' = v_r - {v_r}^{1D}$), using Eqs. (5.3)-(5.5) the angular momentum fluxes in 1D and in 2D are:

$$ \begin{aligned}
{F_j}^{1D} &= 2\pi r \Sigma^{1D} {j}^{1D} {v_r}^{1D} \\
{F_j}^{2D} &= \int_0^{2\pi} \Sigma j v_r \, r \mathrm{d}\theta \\
&= \int_0^{2\pi} \Sigma {j}^{1D} {v_r}^{1D} \, r\mathrm{d}\theta + \int_0^{2\pi} \Sigma {j}^{1D} {v_r}' \, r\mathrm{d}\theta + \int_0^{2\pi} \Sigma j' {v_r}^{1D} \, r\mathrm{d}\theta + \int_0^{2\pi} \Sigma j' v_r' \, r\mathrm{d}\theta \\
&= \underbrace{{j}^{1D} {v_r}^{1D} \int_0^{2\pi} \Sigma \, r\mathrm{d}\theta}_{{F_j}^{1D}} + {j}^{1D} \underbrace{\int_0^{2\pi} \Sigma {v_r}' \, r\mathrm{d}\theta}_{0} + {v_r}^{1D} \underbrace{\int_0^{2\pi} \Sigma j' \, r\mathrm{d}\theta}_{0} + \underbrace{\int_0^{2\pi} \Sigma j' v_r' \, r\mathrm{d}\theta}_{F_j'} \ ,
\end{aligned} $$

$$ {F_j}^{2D} = {F_j}^{1D} + F_j' \ . \tag{5.7} $$

Independently of the numerical scheme and of the modification of ${v_r}^{1D}$ seen before, it appears that it is impossible for the 1D flux to equal the 2D flux. While ${F_j}^{1D}$ corresponds to the angular momentum carried by the gas flowing through the interface, the term $F_j' = \int_0^{2\pi} \Sigma j' v_r' \, r\mathrm{d}\theta$ corresponds to a flux of angular momentum that is not due to advection by the axisymmetric flow; it comes from the azimuthal perturbations of v_r and v_θ, that represents the angular momentum carried by a wave. The wave-carried propagation of angular momentum is well-known in planet-disk interactions (see for instance Appendix C of Chapter 4, Goldreich and Nicholson, 1989; Takeuchi et al., 1996), but cannot be accounted for by a 1D grid. This is a conceptual problem.

We face a degree of freedom problem. With only 3 free variables (Σ^{1D}, ${v_r}^{1D}$, and ${v_\theta}^{1D}$), 4 quantities have to be set in the 1D ghosts: the mass and the angular momentum that is in each ring, the mass and angular momentum fluxes. The first two are set with the prescriptions Eq. (5.3) and Eq. (5.5), which determine the values of Σ^{1D} and ${v_\theta}^{1D}$. The third variable, ${v_r}^{1D}$ is naturally set by Eq. (5.4)/Eq. (5.6). It appears here that it is impossible to obtain the correct flux of angular momentum in the 1D grid ghosts.

A possible solution is that, during the advection phase in the 1D part of the algorithm, one imposes that the angular momentum flowing through the interface corresponds to the flux computed in the 2D grid, ${F_j}^{2D}{}_{\text{computed}}$. However, as the flux of angular momentum carried by a non axisymmetric wave cannot be represented with 1D Navier-Stokes equations, F_j' would be deposited abruptly in the first ring of the 1D grid. This would lead to the formation of a spurious gap at the interface, and possibly lead to a numerical instability.

It has been shown that pressure-supported waves travel through the disk and deposit their angular momentum smoothly, as they get damped viscously (Takeuchi et al., 1996) or through shocks (Goodman and Rafikov, 2001). Thus, a better solution is to model this wave propagation through the 1D grid. We first perform advection as usual in each grid and evaluate at the interface $F'_j = {F_j}^{\rm 2D} - {F_j}^{\rm 1D}$ (or, better, $\delta F_j \equiv {F_j}^{\rm 2D}{}_{\rm computed} - {F_j}^{\rm 1D}{}_{\rm computed} \approx F'_j$, which might be slightly different to the former according to the numerical scheme). Then, over a time-step δt, we spread in the 1D grid the amount of angular momentum $\delta F_j\, \delta t$. A prescription for the deposition of the flux can be found in Goodman and Rafikov (2001) as a function of the distance from the planet. This could be used when there is only one planet, but not if there are several planets, because it is difficult to know what fraction of δF_j is due to each planet. Thus, we adopt an exponential function, because it is scale free so that, once δF_j is known at the interface, its deposition does not depend on the position of the planet(s) and is a function of the distance from the interface only. In practice, we assume that, over a time-step δt, the angular momentum deposited by the wave in a ring of width dr located at a distance d from the interface between the 1D and 2D grids is :

$$\delta j = \delta F_j\, \delta t\, \lambda \exp(-\frac{d}{\lambda})\, {\rm d}r \ , \tag{5.8}$$

where λ is the damping length-scale of the flux. This assumption will be justified in section 5.4.1, where the evolution of the disk in the 1D grid is found to be insensitive to the position of the interface with respect to the planet.

We assume that $\lambda = 0.5$ in natural units, which is the value obtained by fitting with an exponential the decay of the wave-carried flux in appendix C of Chapter 4. For simplicity, we assume that λ does not depend on the disk's viscosity and scale-height (an assumption partially justified in Goodman and Rafikov, 2001).

The deposit of the quantity δj of angular momentum in a ring is simulated by applying a suitable torque, namely by adding to v_θ^{1D} the quantity $\delta v_\theta^{1D} = \delta j / mr$, where r is the radial distance of the ring from the star and m the mass of gas in the cell.

Notice that the integral of Eq. (5.8) from $d = 0$ to infinity is equal to the total angular momentum $\delta F_j\, \delta t$ carried by the wave at the grid interface. However, the 1D disk is not infinite in radial extent. Thus, a fraction of the angular momentum carried by the wave will *not* be deposited in the disk, but will outflow from the system. This outflowing momentum, as well as the angular momentum and mass advected through the inner and outer radius of the 1D grid, are recorded, in analogy with what was done in section 5.2 for the 2D grid alone.

Mean viscous torque

The coupling of the 1D and the 2D grid described in the two subsections above ensures a smooth, conservative evolution of the disk. The gas is free to accrete and spread from the star to its physical outer edge, through the interfaces between the grids. However, at the interfaces, the shear gives an azimuthal viscous stress. This appears as a torque exerted on a grid by its ghosts (and reciprocally). The torque exerted by the part of the disk inside a given radius r_0 on the part of the disk outside r_0 reads, from the Navier-Stokes equation (Eq. (2.7)) :

$$t_\nu(r_0) = r_0 \int_0^{2\pi} \sigma_{r\theta}\, r_0 {\rm d}\theta \ ,$$

where $\bar{\bar{\sigma}} = \begin{pmatrix} \sigma_{rr} & \sigma_{r\theta} \\ \sigma_{\theta r} & \sigma_{\theta\theta} \end{pmatrix}$ is the viscous stress tensor, $\bar{\bar{\sigma}} = 2\Sigma\nu \left(\bar{\bar{D}} - (\frac{1}{3}\nabla\vec{v})\bar{\bar{I}} \right)$ (see sections 2.1 and 5.1). In a staggered mesh scheme, $\sigma_{r\theta}$ is defined at the inner edge of each cell.

For angular momentum conservation, the torque felt by the 1D grid from its ghosts must equal the one exerted by the 2D grid on its ghosts. This requires $\sigma_{r\theta}^{1D}(r_{\text{interface}}) = \frac{1}{N_s}\sum_k \sigma_{r\theta}[k](r_{\text{interface}})$, where the index k goes through the N_s cells of the 2D ring next to the interface. However, given that the expression of $\sigma_{r\theta}$ implies the product of velocity gradients by the density, its average is not equal to the product of the averages, and the required equality is not necessarily true. Thus, one has to replace the value of $\sigma_{r\theta}^{1D}$ at the interface by the average of $\sigma_{r\theta}$ on the interface in the 2D grid.

5.3.4 Results and discussion

We consider the final state of the simulation of section 5.2 : a Jupiter mass planet initially at $r_p = 1$ evolves in a gas disk represented by a 2D grid extending from $r = 0.25$ to 3 for 16000 time units ($\approx$ 2500 orbits). The final density profile of the gas disk is shown in figure 5.7 as a dashed line. One can see that the planet has opened a gap and migrated inward (the planet is located in the middle of the gap). Moreover, the surface density of the gas over the considered range is strongly reduced relative to its initial value (dot-dashed line in figure 5.7). We then compute another simulation with the same planetary system and the same 2D grid, but introducing a 1D grid extending from 0.117 to 20 length units (approximately from 0.5 to 100 AU, assuming the unit length equal to 5 AU). The final profile of the gas distribution obtained in this new simulation is shown as a solid line in figure 5.7. Its bold part corresponds to the 2D portion of the disk.

We see two important aspects in figure 5.7. First, the radial profile of our new solution is clearly smooth, which indicates that there are no artifacts in the passage of information from the 2D grid to the 1D grid and vice-versa. The small kink visible at the inner boundary of the 1D grid ($r \sim 0.15$) is due to the implementation of the open boundary condition (see section 5.3.1) ; this artifact also appears in figures 5.6, 5.9 and 5.10. The change of sign of the second order derivative of the radial profile near the outer interface ($r \sim 3$) is a real feature at the considered time-step, as we will discuss later (see figure 5.11 and the related discussion). Second, despite that the disk in the new simulation has also significantly evolved relative to the initial profile, the new surface density of the disk is very different from that obtained in the simple 2D simulation (compare the solid and dashed curves). In particular, in the new simulation the outer part of the disk has not significantly evolved, which is due to the long viscous time there, as the latter scales with r^2/ν. Conversely, in the old simulation, because of the open boundary condition, we observed a significant disk erosion. This shows the importance of the boundary conditions for the global evolution of the system. We will return more specifically to this issue in Chapter 6.

The global conservation in the system (namely the evolution of the mass and angular momentum of the planetary system, plus those of the gas in the two grids, plus those advected through the inner and outer radius of the 1D grid and recorded as outflow) is presented in figure 5.8, and compared to the conservation obtained in the code using the 2D grid only. One can see that the use of the extended 1D disk does not change the excellent result obtained in section 5.2. Thus, the coupling between the two grids that we described above is correct in terms of conservation properties. Actually, the error in angular momentum is slightly larger in the case with the 1D grid because the density at the inner interface of the 2D grid does not vanish, as can be seen in figure 5.7; so, the major source of error (the non axisymmetric outflow from the 2D grid, discussed at the end of section 5.2.4) does not disappear, while it does for the simulation using the 2D grid alone.

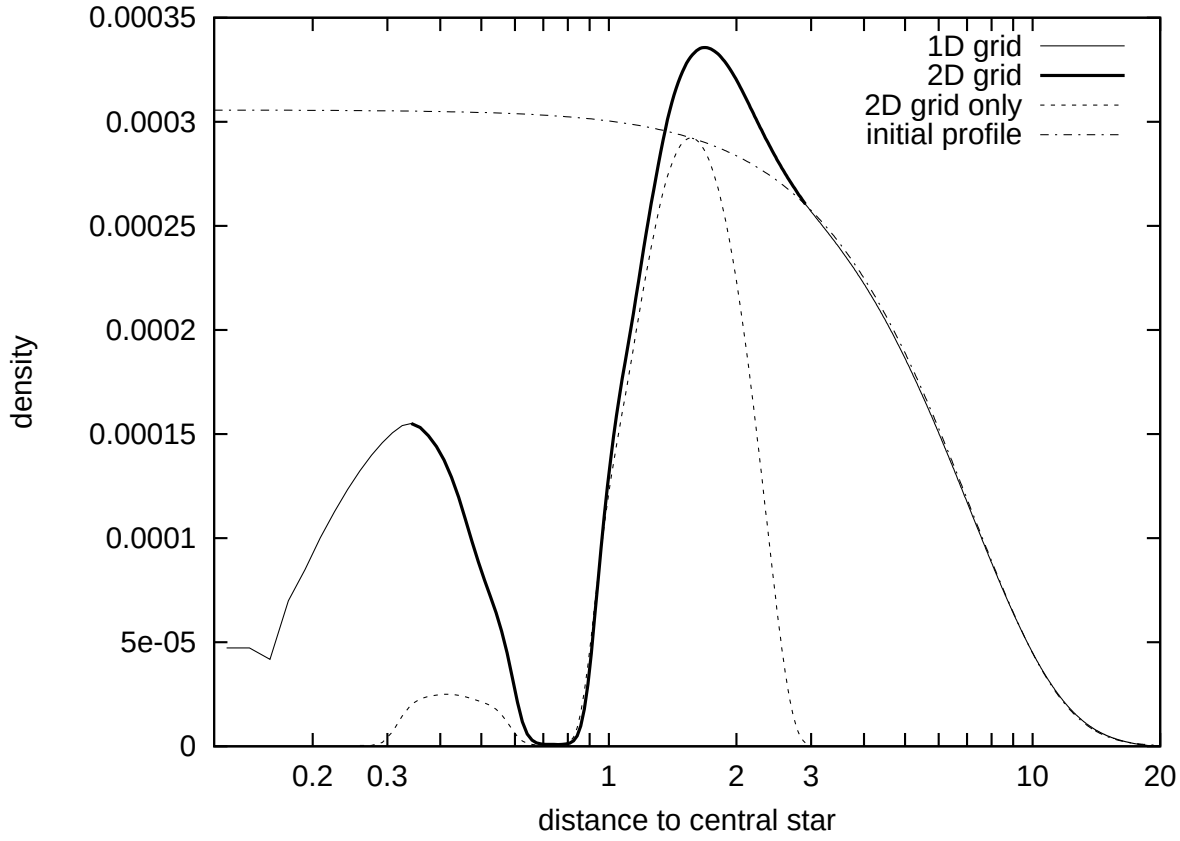

Figure 5.7: Gas surface density profile after 16000 time units $\sim$ 2500 orbits of the Jupiter mass planet initially placed at $r_p = 1$. The solid line corresponds to a 2D (bold) and a 1D (thin) grid coupled, while the dashed line stands for a 2D grid alone. The dot-dashed line shows the initial profile.

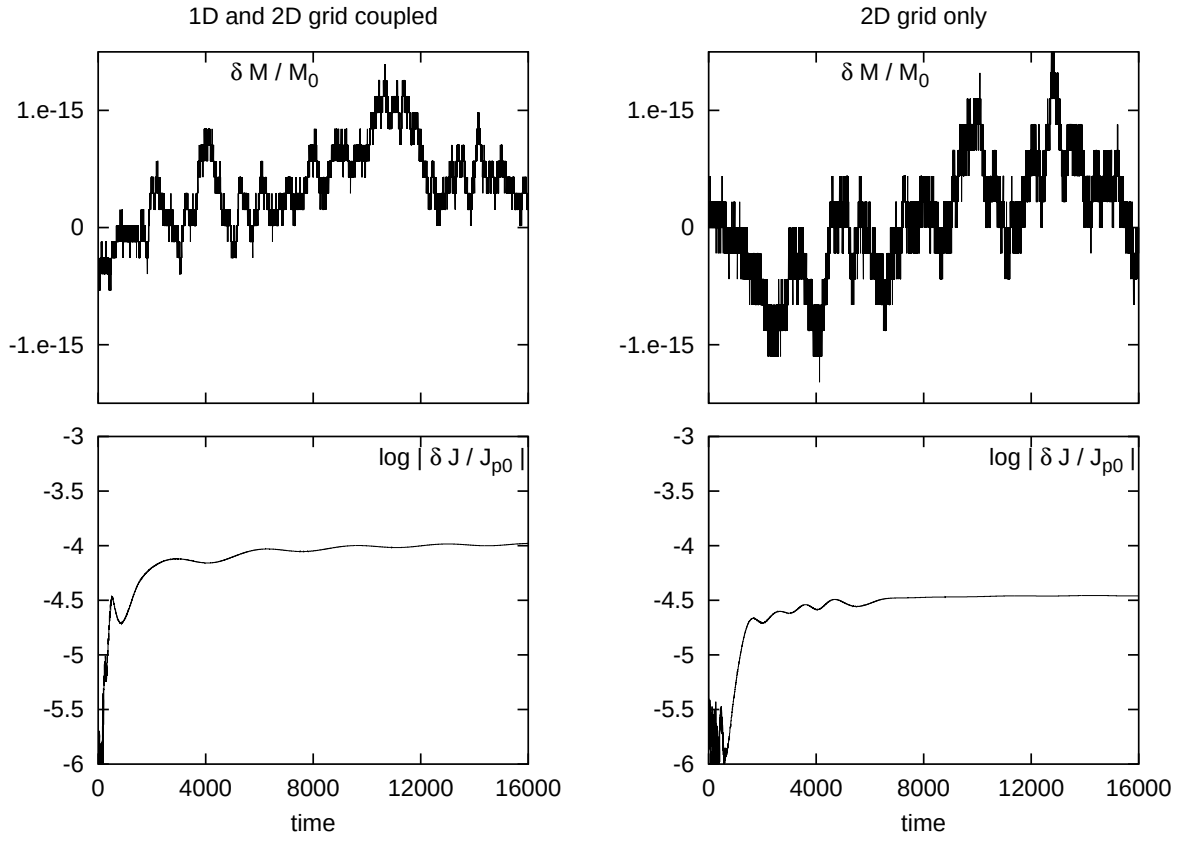

Figure 5.8: Relative variation of mass and angular momentum in the case of a 2D grid with open boundaries and a 2D grid coupled with a 1D grid.

5.4 Performance of the code

In this section, we check the accuracy of the results, as a function of the size of the 2D grid, and we discuss the CPU cost of this hybrid scheme. We show that the coupling of a 1D grid increases by far the realism of the results of the hydro-code, for a low additional computation cost.

5.4.1 Position of the interfaces with respect to the planet.

As already mentioned it in section 5.3.1, the interface between the 2D and the 1D grids has to be sufficiently far from each planet so that the flux of angular momentum carried by the wave at the grid interface and the azimuthal dependence of the disk surface density are both small enough. An obvious test of our code is to check the dependence of the results on the positions of the interfaces between the two grids.

We ran simulations like the one described in subsection 5.3.4, with different inner radii for the 2D grid, but keeping the grid resolutions constant. Figure 5.9 shows the density profiles of the inner disk obtained at the end of the computations (16000 time units $\sim$ 2500 orbits). It appears that the differences among the results are small, even in the cases where the planet is not very far from the interface ($r_p \approx 0.75$). Only the cases with a transition radius greater than 0.5 show not negligible differences with the three other runs, which are remarkably similar to each other, in particular in the density profile of the inner edge of the gap. The case with an interface at 0.5833 is clearly not accurate, but note that it is not unrealistic, while the 1D grid starts only at 4 Hill radii from the planet.

All cases, however, give a quite consistent representation of the surface density profile of the inner disk, which is – on the contrary – very different from that obtained by using the 2D grid alone (compare with the dashed curve in figure 5.7).

This would *not* be the case if we had not implemented in the 1D disk the exponential damping of the angular momentum carried by the density wave launched by the planet. For instance, figure 5.10 shows 3 of the simulations, recomputed by switching off the computation of Eq. (5.8). One sees a kind of discontinuity at the interface, where the angular momentum deposition abruptly stops in the disk. This change implies a modification of the local equilibrium and of the shape of the density profile. Consequently, the results are strongly dependent on $R_{\rm interface}$. This also highlights the importance for the gap structure of the flux of angular momentum carried away by the pressure supported wake. This flux is equivalent to the pressure torque studied in Chapter 4.

The outer interface has a much smaller influence on the disk's profile than the inner one, because it is further from the planet in the studied case. In figure 5.7, it appears that the outer interface corresponds to a change of sign in the second order derivative of the density profile. Figure 5.11 shows that this is a real feature, specific to the chosen output time. Indeed, this figure shows the density profile at different times in the same simulation; its evolution convincingly demonstrates that the second derivative of the density at the interface ($R_{\rm interface} = 2.9167$, right vertical dashed line) varies with time and can be non-zero. We also repeated the same simulation, moving the outer interface to $R_{\rm interface} = 2.3167$ (left vertical dashed line). The obtained surface density profiles overlap exactly with those of figure 5.11 at the corresponding time, so they are not plotted. This test also demonstrates that the position of the outer interface has a negligible influence on the global disk evolution.

The evolution of the disk has a strong influence on the type II migration of the planet. Figure 5.12 shows the different migration rates in the simulations of figure 5.9, and in the simulation

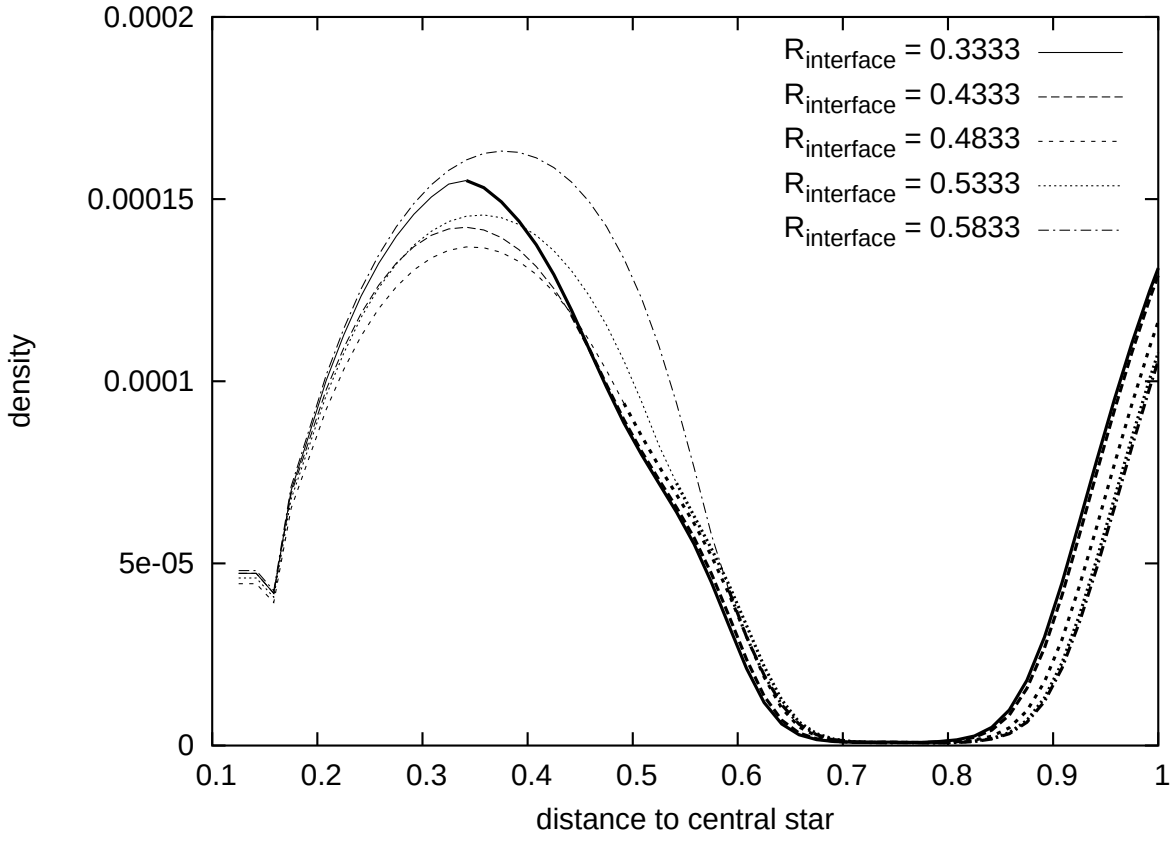

Figure 5.9: Inner disk profiles at the end of simulations with different locations of the inner interface between the 1D and the 2D grid. The bold part of the profiles corresponds to the 2D grid.

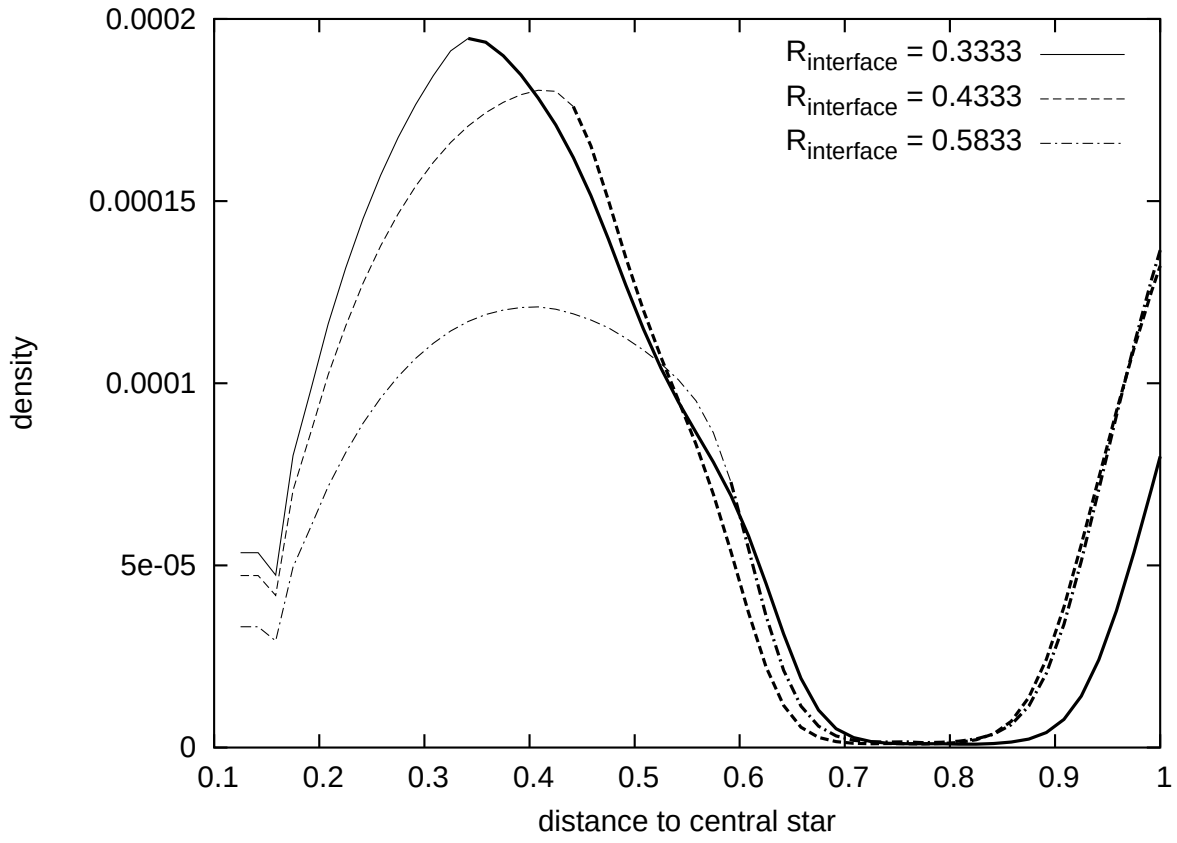

Figure 5.10: Inner disk profiles at the end of simulations similar to those of figure 5.9, but without the implementation of the wave damping algorithm (Eq. (5.8)). A strong sensitivity on $R_{\rm interface}$ appears.

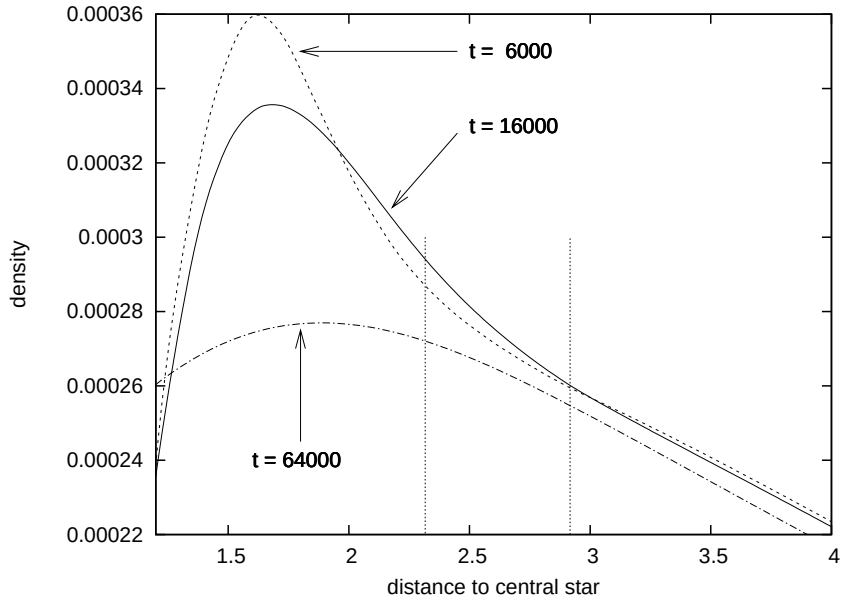

Figure 5.11: Outer disk profile close to the outer interface ($R_{\text{interface}} = 2.9167$, marked by a vertical line) at 3 different times. The vertical line at $r = 2.3167$ marks the outer interface used in a second simulation, whose results are indistinguishable from those plotted in this figure.

obtained with the 2D grid alone. Once again, the two first cases ($R_{\text{interface}} = 0.3333$ and 0.4333) are remarkably similar, while the other ones show a slightly slower inward motion of the planet. However, the simulation done with only a 2D grid gives a migration that is sensibly faster, as expected due to the disappearance of the inner disk.

The results presented in this section show that our method for coupling the 2D and 1D calculations not only ensures the conservation of the angular momentum, but also allows a robust (i.e. weakly dependent on the grid interface position) modeling of the disk's structure and evolution.

5.4.2 Computational cost

In this subsection, we show how the use of a 1D grid allows the study of the whole disk for a negligible extra cost while the use of an extended 2D grid would be prohibitive.

From a theoretical complexity point of view, the number of elementary operations for the computation of a time-step is proportional to the number of cells of the considered grid. Thus, the computation of the disk evolution in the 1D grid is negligible with respect to the computation in the 2D grid. In addition, one has to consider the three operations required to couple the grids, which also need to be done at every time-step. They are the filling of the ghost rings, the computation of δF_j and its spreading, and the change of $\sigma_{r\theta}$ in the 1D grid. They require computation on N_G 2D rings or less. As the size of the ghost area is usually negligible with respect to the size of the 2D grid, the computational cost of the coupling is also negligible with respect to the one of a time-step in the 2D grid.

In the previous paragraph, we studied the number of elementary operations to be computed during a time-step. In most codes, the length of the time-step is adapted to the conditions imposed by the required resolution and the existing perturbation. In general, it is determined by

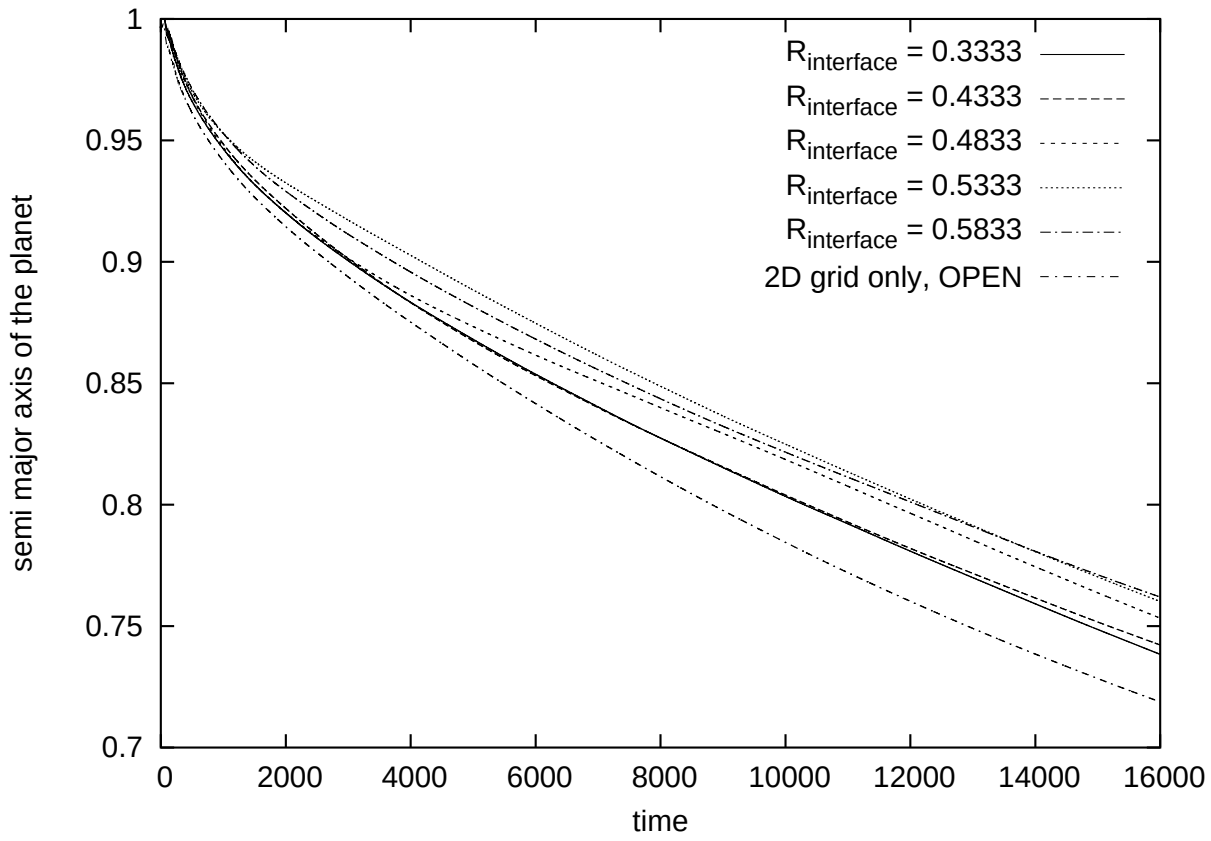

Figure 5.12: Type II migration of the Jupiter mass planet in the disk. The semi-major axis is plotted as a function of time for all the cases already discussed: various positions of the inner interface between the two grids, and no 1D grid.

Table 5.1: Benchmarking results

parameters of the 2D grid			1D grid	CPU time
extension	N_r	N_s	extension	of process
0.35 - 3.0	165	320	none	6167 s.
0.35 - 3.0	165	320	0.1167 - 20	6008 s.
0.1167 - 5.0	294	320	none	99494 s.

the Courant-Friedrichs-Lewy (CFL) condition. In section 5.1, we have shown that denoting by $R_{\rm min}$ the inner boundary radius of the 2D grid, one has $\delta t \propto R_{\rm min}^{3/2}$. This shows that extending the 2D grid toward the star shortens the time-step and slows down the simulation significantly. The use of the FARGO algorithm (Masset, 2000a,b) enables one remove the mean angular velocity and to consider only the perturbed motion and the shear, but this leads to a similar conclusion, although the scaling of δt with $R_{\rm min}$ is generally different.

The CFL condition in a 1D grid is much less constraining. Consequently, the addition of a 1D grid inside the inner edge of the 2D grid has no influence on the time step length, still determined by what happens in the 2D grid. It is thus important to increase $R_{\rm interface}$ as much as possible, to speed up the computation. The accuracy loss of the computation with the increase of $R_{\rm interface}$ has been discussed in subsection 5.4.1, so that an acceptable trade-off can be found.

Some benchmarking confirms this reasoning on computing time. We ran 3 simulations of a Jupiter mass planet initially placed at $r_p = 1$, evolving in a gas disk for 1000 time units on an Intel Xenon 2.66 GHz processor. The results are shown in table 5.1. This confirms that :

- The computation in the 1D grid has a negligible cost : with or without the 1D grid, the computing cost is about the same.

- The computing time is not directly proportional to the number of cells, and is strongly increased by the higher shear in the vicinity of the star, otherwise the third simulation would not have been more that twice as long as the first one.

In addition, the second simulation was slightly shorter than the first one because with the 1D grid, the density at the boundaries of the 2D grid does not tend to zero, the profile is smoother and consequently the CFL condition is less constraining there.

These results show how interesting the coupling of a 1D and a 2D grid is, particularly for the computing of the innermost part of accretion disks.

5.5 An astrophysical application : Outwards type II migration

As discussed in section 2.6, the viscous evolution of the protoplanetary disk is thought to govern type II migration. In particular, we mentioned the possibility of outwards type II migration for planets orbiting in the outermost part of the disk, that spreads outwards. Veras and Armitage (2004) found this possible using a 1D model ; in their model, the disk evolved under its own viscosity, the torque exerted in the planet-disk interaction had the form of Eq. (5.2), and the effect of waves carrying angular momentum flux was neglected.

Using our code, we perform more precise simulations of this process. The interaction between the planet and the disk is simulated in 2D, and the effect of waves is taken into account. This

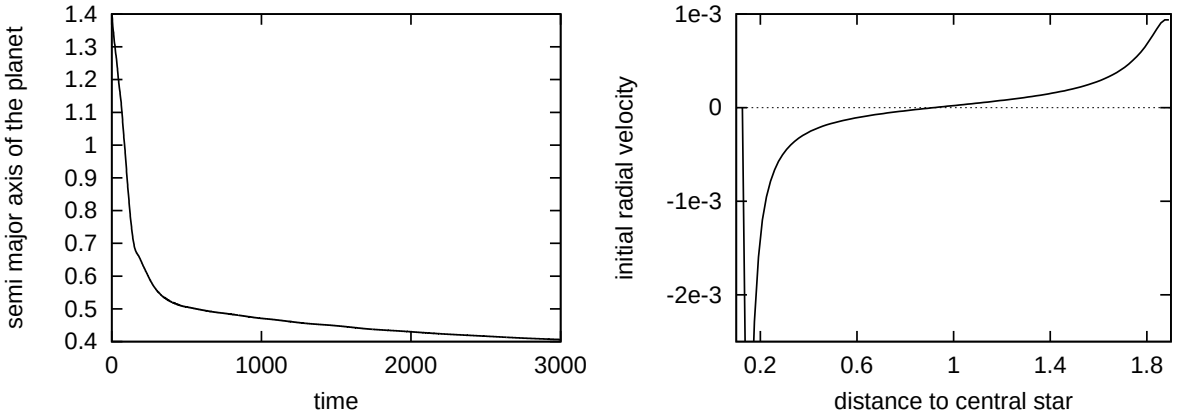

Figure 5.13: Left panel: migration of a Jupiter mass planet initially put on a circular orbit at $r_p = 1.4$. Right panel: Radial velocity in the gas disk when the planet is introduced.

implies that the gap opened by the planet in the disk is less wide and deep than in the Veras and Armitage (2004) representation, as shown in Chapter 4. Moreover, the planet also feels a corotation torque, which is otherwise neglected in the analytic expression of the planetary torque given by Eq. (5.2).

We find that the situation is not as simple as illustrated by Veras and Armitage (2004). For instance, the left panel of figure 5.13 shows the result of a simulation in which the planet is initially put at $r_p = 1.4$, which is deeply in the outward spreading zone as shown by the right panel. Nevertheless, the planet migrates inwards, in what seems to be a runaway type III migration (section 2.4.2 and Masset and Papaloizou, 2003). This is because the spreading disk forces enough gas to pass through the coorbital region of the planet so that the planet feels a strong corotation torque and decouples from the disk evolution.

We do obtain outward planet migrations, but only in specific cases. For instance when we place the planet initially outside of the spreading disk (which is unrealistic), or if we hold it for a sufficiently large number of orbits, so that it can open a deep gap that effectively truncates the disk at its inner edge (which, in practice, again places the planet outside of the spreading disk).

We think this example shows that the evolution of a Jovian mass planet is not an ideal type II migration. Because the gap is not extremely clean, the planet is not fully locked in the disk's evolution. The planet feels the global motion of the disk (accretion or spreading) but at the same time it also feels a non-negligible corotation torque. This idea will be developed in Chapter 6, looking for quasi-stationary solutions for Jovian-like planets. Only a code like the one that we have developed here can simulate the two effects correctly and hence allow a quantitative study of the planet's evolution.

5.6 Discussion and perspectives

It is well known that the migration of giant planets (i.e. planets massive enough to open significant gaps in the disk's density distribution) is governed – or at least strongly affected – by the global evolution of the disk under its own viscosity.

The usual simulation algorithms solve the hydrodynamical equations over a 2 dimensional polar grid that is truncated at an inner and outer radius to keep the computing time within

reasonable limits. Thus, they cannot correctly reproduce the evolution of the disk, nor the planet's migration.

In this Chapter, we have shown how the use of a 1D grid surrounding a classical 2D grid allows us to simulate the global evolution of the disk, while resolving the local planet-disk interactions with the accuracy of the usual algorithms. Coupling the two grids via a system of ghost rings, with special attention paid to the conservation of angular momentum leads to a smooth evolution of the disk from its inner radius (the truncation radius or the surface of the star) to its outer edge, several hundreds of AU away. This increases by far the accuracy of the simulation with essentially no additional CPU cost.

Consequently, this algorithm is the tool of choice to properly simulate type II migration and related problems. It also enables the study of the effect of the presence of planets on the disk's global evolution, which in turn affects the migration of the planets in a feedback effect. We will use this new code in the numerical experiments described in the next two chapters.

In our simulations, we observe that the disks slowly disappear through the open boundaries of the 1D grid. However, disks are believed to disappear rapidly after only a few million years, under the action of photo-evaporation. We plan to introduce this phenomenon in our code in the future, via a simplified prescription consisting of removing a fraction of the gas in each cell, depending on time and location along the lines of Guillot and Hueso (2006). This will open the possibility of simulating the evolution of planets in a globally evolving gas disk, over the disk's lifetime.

Chapter 6

Type II migration and cavity opening

6.1 Introduction

As discussed in Chapters 1, 2 and 4, if a planet is massive enough (compared to a threshold value depending on the viscosity and scale height of the disk), it opens a gap in the disk density profile. Then, it is locked into it because the outer and the inner disk are repellent for the planet. Thus, it is supposed to follow the viscous evolution of the disk ; this is the definition of type II migration (see Chapter 2).

In this and in the following chapter we study mechanisms that can reduce the speed of type II migration and, in some cases, even stop it completely. In this chapter, we consider the case of a single giant planet, on a circular orbit, in a disk of mass equivalent to the planet mass.

The migration of a giant planet is intimately related to the structure of the disk that is sculpted by the planet itself. Quillen et al. (2004) noticed that if the planet is more massive than the inner disk, the outer disk is not able to push the planet inward at the speed of the natural gaseous accretion on the star. Indeed, in that case the planet has more angular momentum to lose than the unperturbed disk would have, so that it migrates more slowly. Meanwhile, nothing prevents the inner disk from accreting onto the star. Even more, Varnière et al. (2006b) suggested that, as the planet exerts a negative torque on the inner disk, it accelerates the accretion of the latter on the primary. Consequently, the inner disk accretes onto the central star faster than it would naturally. This makes the inner disk disappear before the planet migrates inward. The result is the opening of a *cavity* : a great depletion of the disk from the star to the planet orbit.

Once a cavity is opened, the outer disk still tends to accrete onto the central star and to push the planet inward, while the planet can not take angular momentum from the inner disk anymore. A big mass of the planet with respect to the disk may slow down this process, but the final result should ineluctably be the inward type II migration of the planet toward the star. However, in this work we find that the orbit of the planet is not necessarily "gas proof" and viscous accretion can happen without forcing the migration of the planet. This is a new way of preventing type II migration. This mechanism is presented in section 6.5.

The cavity opening process and its feedback on planet migration is not easy to check and quantify with the help of numerical simulations. Indeed, the computation of the inner disk evolution is prohibitive with classical hydro-codes. Thus, Quillen et al. (2004) only made the simulation of a planet orbiting inside a pre-existing cavity – showing that it did not migrate inward very fast – and Varnière et al. (2006b) performed only a few simulations showing the opening of a cavity by a Jupiter-mass planet in a low density disk. The cavity opening appeared

to be more rapid than the viscous time scale, confirming the idea that the planet "helps" the accretion of the inner disk onto the star. However, Varnière et al. (2006b) did not provide an exploration of the parameter space, and could not study the planetary migration because the planet was about 100 times more massive than the disk. With the help of the new simulation hybrid scheme presented in the previous chapter, we can perform such a study for the first time. The use of a grid extended down to the inner physical radius of the disk is particularly important for a proper simulation of the inner disk evolution, as illustrated in the test example of figure 5.7.

This analysis of cavity opening and migration timescale is particularly interesting because observations suggest that some protoplanetary disks most likely host cavities (see section 6.2). Understanding what kind of cavity a planet can open in terms of size, shape, and depth, in which conditions and with which life-time, may provide some keys to interpret these observations, and future data from the ALMA interferometer, that will enable us to image the inner part of protoplanetary disks. After a review of the observations of protoplanetary disks that seem to host cavities in section 6.2, we present the results of our numerical simulations in section 6.3 in terms of cavity opening and migration. These numerical experiments are interpreted in sections 6.4 and 6.5. In particular, we find that in the case where the gap is not very deep, the corotation torque can prevent inward type II migration, consistently with numerical results. We then discuss in section 6.6 the influence of the migration on cavity opening. Finally, we conclude and discuss the implications of this work in section 6.7. In particular we address how the results should be affected by the gas accretion onto the planet and we discuss the differences between gas cavities and dust cavities.

6.2 Evidences for cavities in protoplanetary disks.

Disks of gas and dust around young stars are heated by the star and by internal viscous dissipation. Consequently, the dust becomes an Infra-Red source. In the spectral energy distribution (SED) of the star, an infra-red excess points out the presence of such a disk. The Near-Infra-Red emission corresponds to the hottest part of the disk, which is the closest to the central star, while the Mid-Infra-Red emission is due to colder dust, corresponding to the outer part of the disk. Consequently, a lack of infra red excess in the NIR part of the spectrum can be interpreted as the presence of an inner cavity in the disk (Beckwith, 1999). Such a cavity discovered by SED analysis is sometimes called a *spectral hole*.

One of the most clear example of spectral hole is given in figure 2 in Forrest et al. (2004) for the T-Tauri star CoKu Tau/4 observed with the Spitzer telescope. The size of the spectral hole is such that there seems to be no dust at temperature larger than 123K. The authors convincingly deduce from this SED that dust grains in the disk of CoKu Tau/4 are excluded from the inner most 10 AU ; this makes a remarkable dust cavity. The question whether this cavity could be opened and maintained by a planet has been addressed in Quillen et al. (2004). They suppose that a planet opened a gap in the disk at 10 AU, and that the inner disk then accreted onto the star. Then the age of the system has to be bigger than the viscous timescale of accretion onto the star of the inner disk. This gives a lower limit for the viscosity. Given the viscosity, a minimum planet mass is required to open a gap. For the planet not to migrate immediately after the depletion of the inner disk, the planet has to be more massive than the outer disk, so that the angular momentum taken by the latter from the planet is a negligible fraction of the angular momentum of the planet. From these considerations, they performed a simulation with a planet of mass $3.10^{-4} M_*$ on a circular orbit at 10 AU in a disk with Reynold number 10^5 and density

$\Sigma(r) = 10^{-6}(1.1r_p/r)\, M_*\mathrm{AU}^{-2}$ for $r > 1.1r_p$ and 100 times smaller for smaller radii. The planet efficiently maintains the cavity for 100 orbits and the result is a probable identity picture of the CoKu Tau/4 system. However, they did not make a simulation of the opening of the cavity.

The T-Tauri stars TW Hya, DM Tau and GM Aur also present a spectral hole. To interpret their SEDs, Calvet et al. (2002, 2005) used the following model. They divided the disk into 3 components : an optically thick outer disk, its inner edge (represented as a wall directly exposed to stellar radiations), and an optically thin inner region. Adjusting the free parameters (the wall radius and height, the outer disk scale height, its mass and viscosity) they obtain a satisfactory fit of the SED of these three objects. They concluded that TW Hya and DM Tau present a 3-4 AU wide cavity, while GM Aur should have the truncation radius of the outer disk located at 24 AU from the star. Previous work on GM Aur (Bergin et al., 2004) based on different data had concluded to a 6 AU wide cavity, that could be maintained by a 1.7 Jupiter mass planet on a fixed circular orbit at 2.5 AU (Rice et al., 2003).

Other cavities have been inferred in the system of KH 15D (Herbst et al., 2002), HR4796A (Schneider et al., 1999), HD141569A (Clampin et al., 2003). More recently, interferometric observations at Plateau de Bure Interferometer clearly show a remarkable dust depletion of the inner part of the disk of LkCa15 (Piétu et al., 2006). A cavity has been unambiguously imaged at 1.4 mm. Its radius is about 50 AU.

Thus, cavities are relatively common features in protoplanetary disks. It is not easy to constrain their characteristics, as sometimes different dust distributions can give indiscernible SEDs, but the evidence for cavities existence in protoplanetary disks is quite strong.

6.3 Numerical simulations

As anticipated above, in this study we use the simulation hybrid scheme developed in the previous chapter, because it allows us to describe correctly the global evolution of the disk, from an arbitrary small inner radius to an arbitrary large outer radius.

The initial density profile that we adopt is the same as used in the tests of the previous Chapter, and corresponds to a disk that evolved under the effect of its own viscosity until its density at 5 AU (our unit length hereafter) corresponds to the Minimal Mass Solar Nebula (see section 1.2.3). The default value for of the aspect ratio of the disk is $H/r = 0.05$, unless specifically noted.

The 2D grid extends radially from $R_{\mathrm{in}} = 0.35$ to $R_{\mathrm{out}} = 3.$ and is divided in $N_r = 165$ elementary rings, themselves divided into $N_s = 320$ sectors. The 1D grid extends radially from 0.1133 to 20, over $N_r^{\mathrm{1D}} = 1193$ elementary rings.

We computed a few simulations with a Jupiter mass planet ($q = 10^{-3}$) initially placed on a circular orbit at $r_p = 1$ in a disk with different viscosities. The kinematic viscosity of the gas, ν, is constant in space and time. Its values in the simulations range between 10^{-6} and $10^{-3.8}$. In this chapter, the viscosity is characterized by the Reynolds number at the initial location of the planet : $\mathcal{R} = {r_p}^2\Omega_p/\nu = \nu^{-1}$.

6.3.1 Density profile and cavity opening

Figure 6.1 shows as bold lines the density profiles for four simulations after half a viscous time ($\tau_\nu = \nu/r_p^2$), or only a quarter of viscous time in the least viscous case. The depth of the gap opened by the planet strongly depends on the Reynolds number. This is not surprising, as it is well-known that viscosity plays against gap opening (see Chapter 4 and references therein).

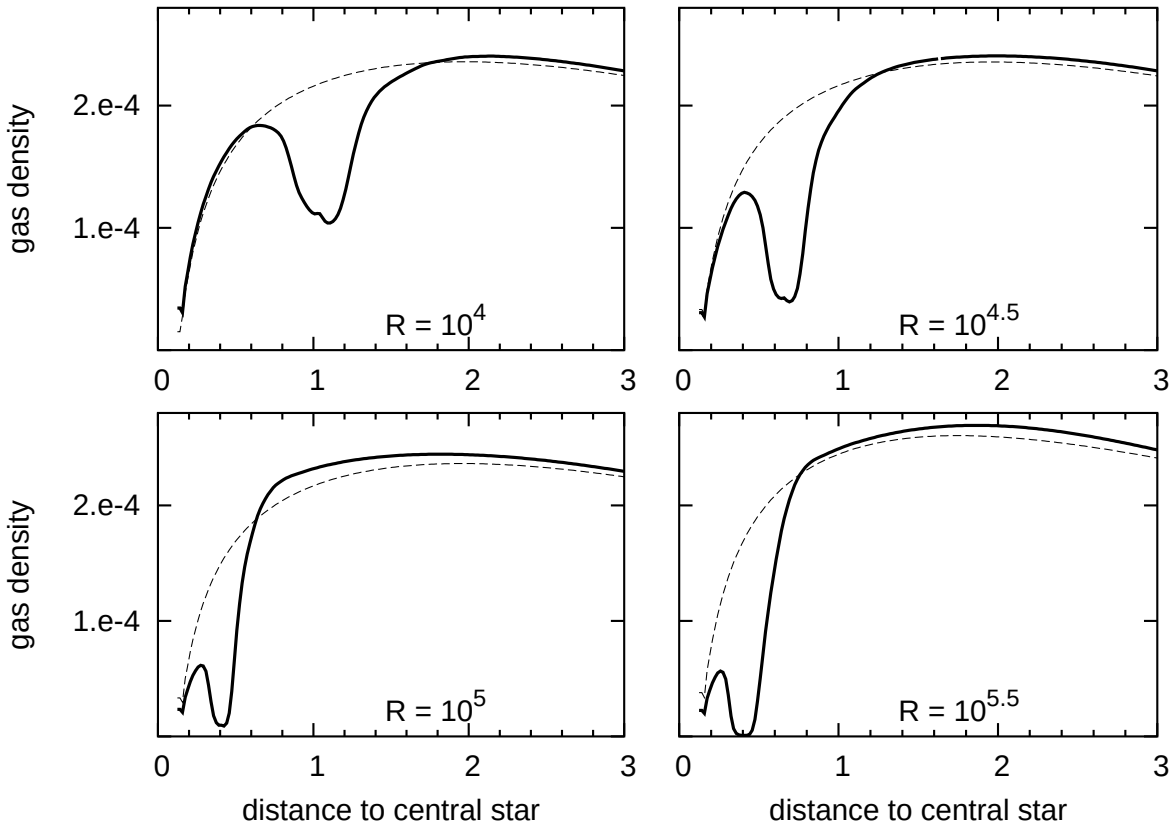

Figure 6.1: Bold lines: Surface density profile at $\tau_\nu/2$, for different Reynolds number, and at $\tau_\nu/4$ for $\mathcal{R} = 10^{5.5}$. Thin dashed lines: surface density profile obtained by natural viscous evolution of the disk with no planet at the same time. The units of mass and length are the ones specified in section 2.6.2, that is respectively the solar mass and the initial semi major axis of the planet.

The gap is centered on the planetary orbit, which is not any more at 1 because the planet has migrated.

Concerning the opening of a cavity, we see that the density in the inner disk is significantly smaller than in the outer disk. In particular the least viscous cases show an inner disk with very low density, so that a sort of cavity is formed: in fact, the density is about 5 times smaller for $r < 0.5$ than for $r > 0.6$. The profile clearly shows a wall at $r \approx 0.5$, beyond which the disk profile is about flat while the density is negligible at the base of the wall.

The thin dotted lines show the density profile obtained in similar simulations, at the same time, in the same conditions, but without the planet. The density also decreases in the innermost region of the disk. So, it seems that the observed depletion of the inner disk is not fully caused by the planet, as will be discussed in section 6.4.

6.3.2 Migration rate

Figure 6.2 shows the evolution of the semi major axis of the planet with time, in units of the viscous time τ_ν. In proper type II migration, the migration rate is proportional to the viscosity and thus, in this unit, it should be independent of $\mathcal{R}$. This is indeed the case for $\mathcal{R} \geqslant 10^5$: the

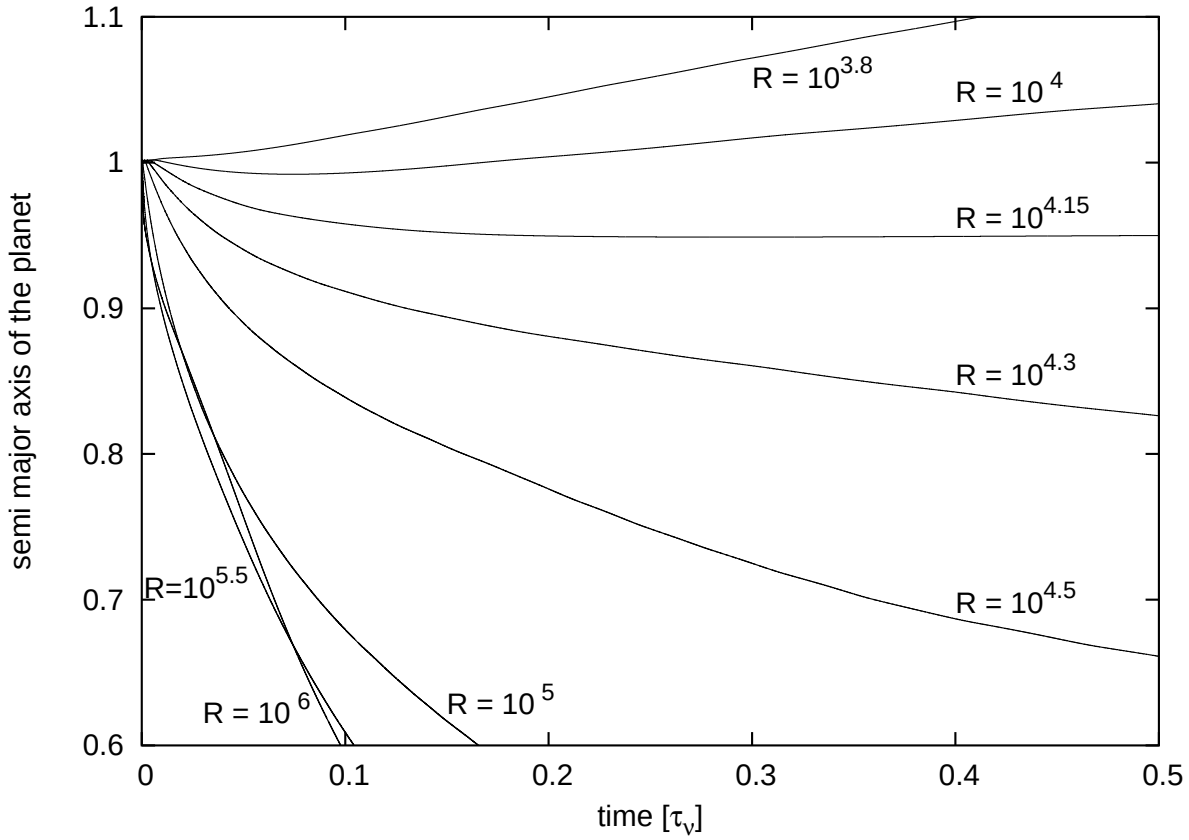

Figure 6.2: Migration of a Jupiter mass planet for different Reynolds numbers in the disk.

three curves are almost linear and overlapped. However, for higher viscosities, a very different behavior is observed. When $\mathcal{R}$ decreases below 10^5, the migration rate becomes slower than expected. As viscosity increases, the planets migrates inward more and more slowly with respect to the viscous time, and the migration is even stopped for $\mathcal{R} = 10^{4.15}$. For larger viscosities, the migration is reversed and the planet moves outward.

This result is particularly surprising and new. It is observed for the first time. This outward migration is not an effect of the resolution of the grid; we have computed the simulation with $\mathcal{R} = 10^4$ with $N_r = 330$, $N_s = 640$: the planet also migrates outward with this increased resolution, at about the same speed (see top panel in figure 6.3). With this high resolution, the size of a cell around the planet is about a tenth of the Hill Radius in radius and a seventh of the Hill radius in azimuth, so that the surface of the Hill sphere of the planet is covered by about 220 cells. This is largely sufficient for no artifact from the resolution to perturb the planet-disk interactions; in particular the corotating zone of the planet, which plays a crucial role as will be shown further, is correctly simulated. We also investigated the effect of the aspect ratio on the migration rate, from the stationary case. It appears that this parameter only plays a marginal role (see bottom panel in figure 6.3).

One may wonder if the stationary migration observed for $\mathcal{R} = 10^{4.15}$ for a Jupiter mass planet is a feature valid for any planet mass. Figure 6.4 shows that it is not the case. The more massive the planet is, the more it tends to migrate inward, like in classical type II regime. For lighter than Jupiter planets, the migration is directed outward. However, we will show in section 6.5.5

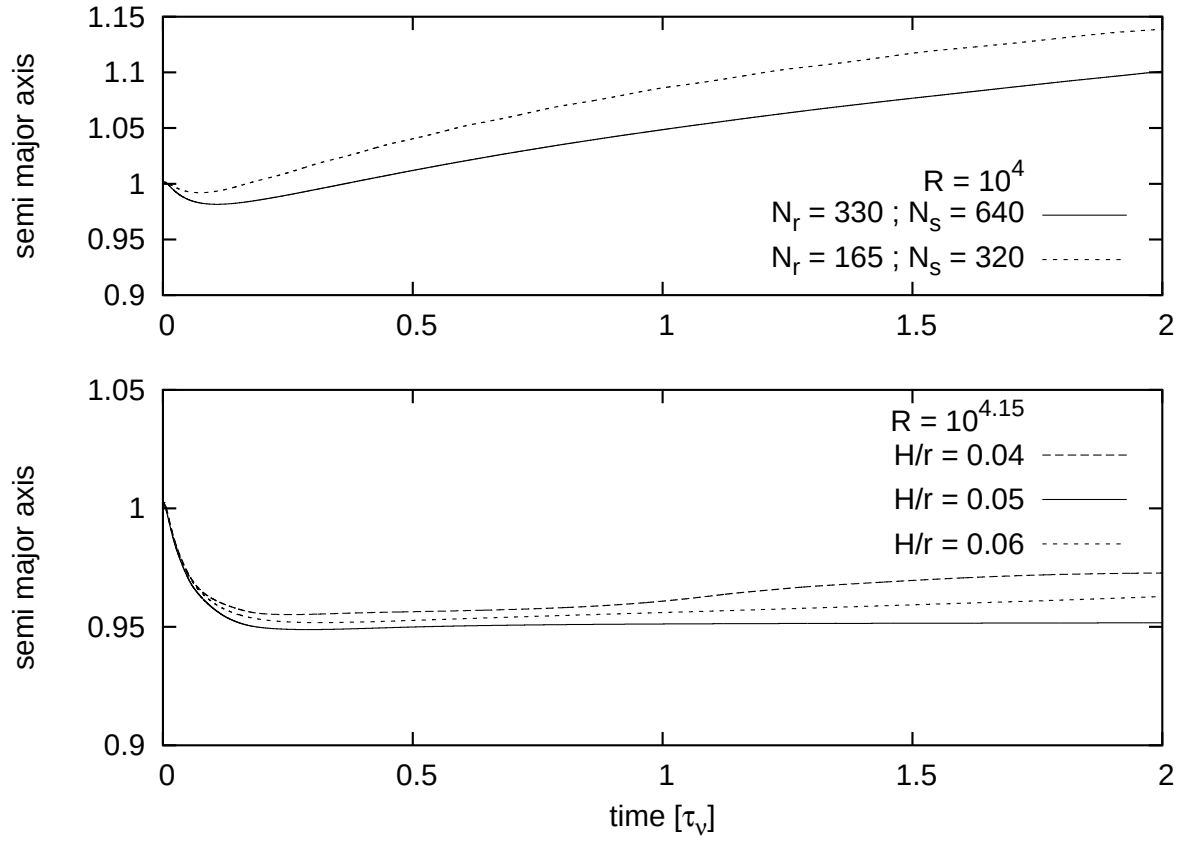

Figure 6.3: Top panel: Outward migration of a Jupiter mass planet for $\mathcal{R} = 10^4$ and two different resolutions. Bottom panel: Quasi stationary migration of a Jupiter mass planet for $\mathcal{R} = 10^{4.15}$ and 3 different aspect ratios.

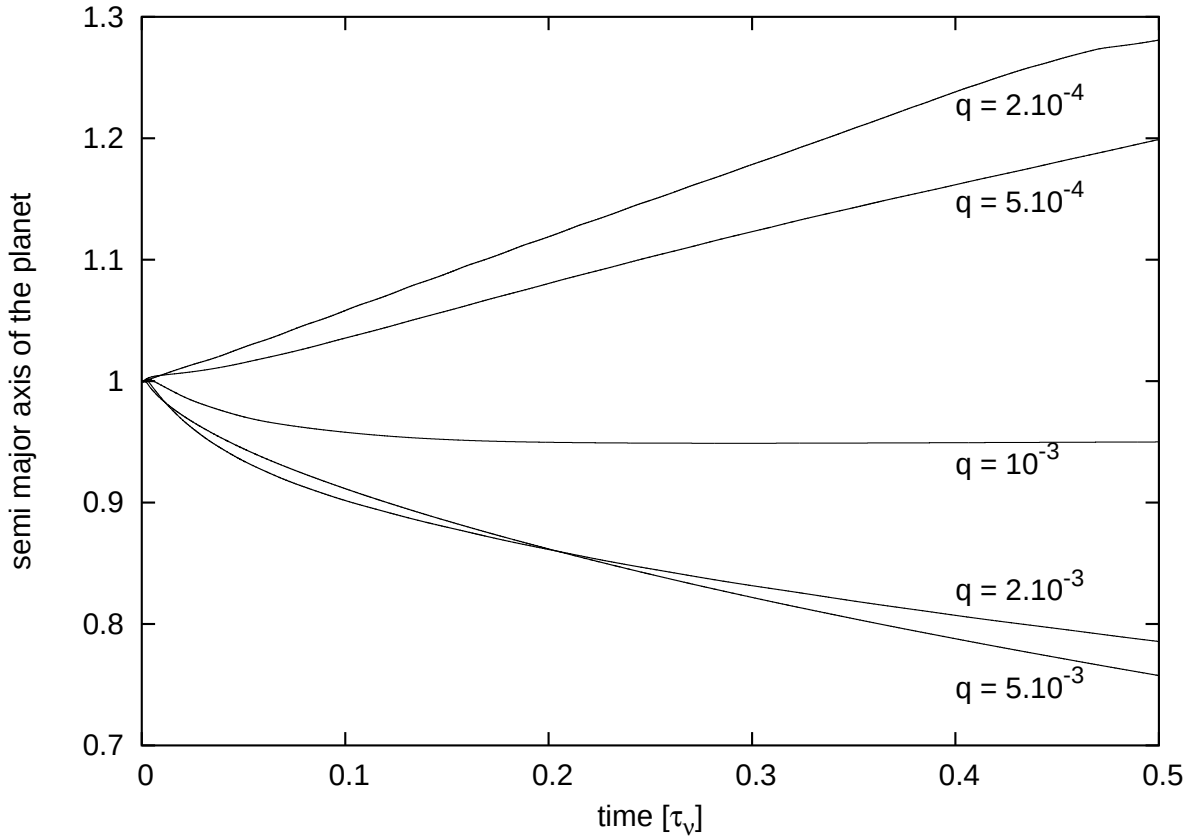

Figure 6.4: Migration of giant planets of different masses in a disk with $\mathcal{R} = 10^{4.15}$ (and $H/r = 0.05$, which is our default value).

that if the viscosity in independent of the radius, there is an equilibrium point further from the star in the disk where these low mass planets also have a stationary migration.

6.4 Interpretation of the density profile

The natural viscous evolution of a gaseous disk is described in Lynden-Bell and Pringle (1974; LP74 hereafter) (see Chapter 2). The theoretical solution for a disk extending between 0 and infinity in radius is given in Eqs. (2.59)-(2.62) and figure 2.5. However, the inner radius of the disk, $R_{\rm inf}$, is never 0; it is at least the radius of the central star, most likely the X-wind truncation radius at a few tenth of AU. It could even be bigger, in the case of Jet Emitting Disk (JED): indeed, at the base of the jet, which is several AUs large, accretion is dominated by the jet torque and is much larger than the standard accretion; so, the outer radius of the JED could be considered as the inner open boundary of the standard disk. The explicit solution of the LP74 equations with a finite inner edge of the disk comes from Eq. (25) of LP74. With our units ($G = M_* = 1$), it gives:

$$\Sigma_{\rm LP74}(r,t) = \Sigma_0 \mathcal{T}^{-5/4} \left(\frac{\sqrt{r} - \sqrt{R_{\rm inf}}}{\sqrt{r}} \right) \exp\left(-\frac{ar^2}{\mathcal{T}} \right) \ , \tag{6.1}$$

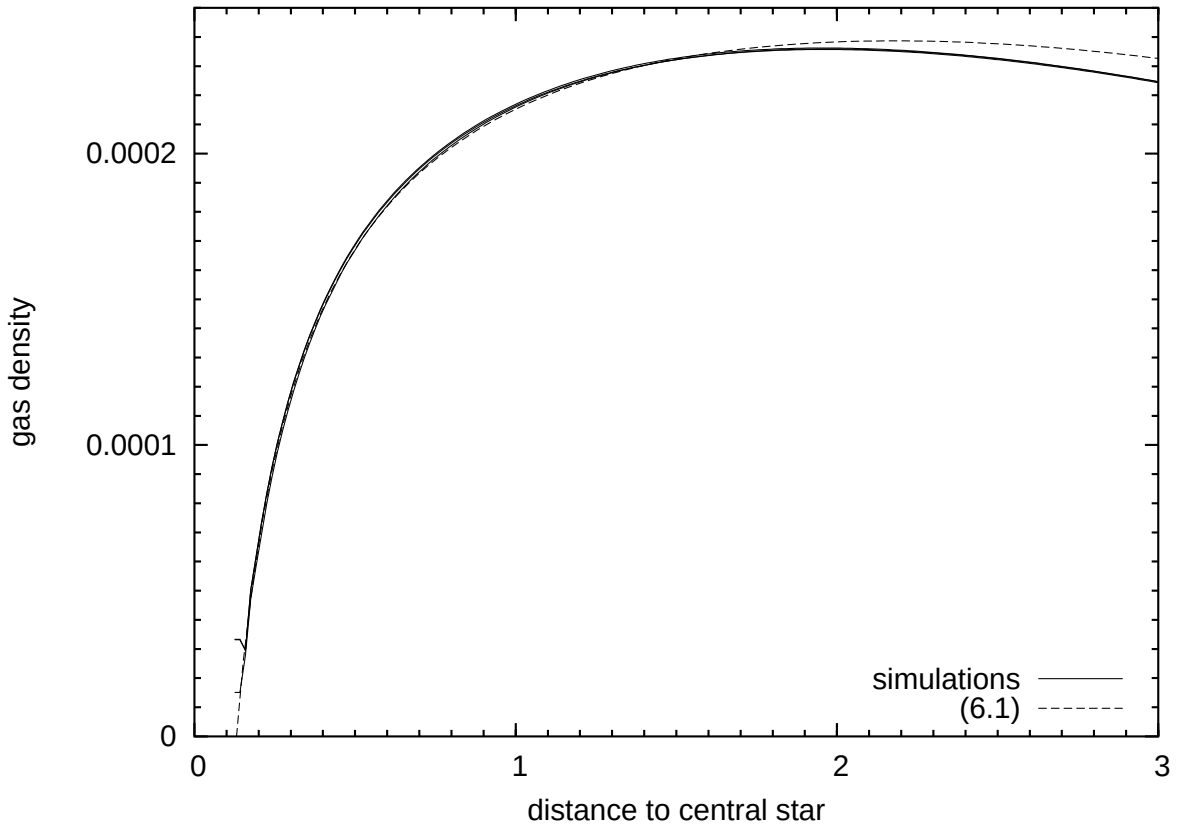

Figure 6.5: Natural viscous evolution of an unperturbed disk at $t = \tau_\nu/2$. Plain lines: profiles from simulations with $\mathcal{R} = 10^4$, $10^{4.5}$, and 10^5. Dashed line: profile from Eq. (6.1).

where $\mathcal{T} = 12a\nu t + 1$. Thus the density starts from 0 at $r = R_{\rm inf}$ and grows with r until $r \gg R_{\rm inf}$, where a classical Gaussian shape is reached. This kind of profile corresponds to the thin dashed lines in figure 6.1, which are very close to what Eq. (6.1) gives. Figure 6.5 shows the agreement between simulations in which the planet has been removed and the theoretical profile given by Eq. (6.1) with $\Sigma_0 = 3.06\ 10^{-4}$ and $a = 1/52.8$ at $\tau_\nu/2$, (*id est* $\mathcal{T} = 1.114$). All profiles overlap with each other. This shows that, once the time is renormalized relative to the viscous time, the evolution of the disk density distribution is independent of the Reynolds number. Also, it shows the excellent agreement between numerics and Eq. (6.1) achieved with our simulation scheme, as already highlighted in figure 5.6. The little discrepancy between the numerical solutions and the analytic profile comes from the fact that the initial condition in the simulations is not given by Eq. (6.1) at $\mathcal{T} = 1$ but by Eq. (5.1).

6.4.1 Gap opening in an evolving disk

Equation (4.11) provides a way of computing semi-analytically the density profile of a gap for any disk and planet parameters. We remind that the equation applies outside the corotation zone of the planet, which approximately extends on each side of the orbit over a width $x_s^+ \approx x_s^- \approx 2R_H$, where R_H is the Hill radius of the planet.

The solutions of Eq. (4.11) correspond to the gap profile $\Sigma(r)$ in an ideal, non evolving disk

in equilibrium with the presence of a non-migrating planet. The unperturbed profile of such a disk is proportional to $r^{-1/2}$ because ν is assumed to be independent of r. Thus, to compute the profile in the inner part of the disk, we start from $\Sigma = \Sigma_0/\sqrt{R_{\rm inf}}$ at $r = R_{\rm inf}$ and we compute the density step by step until $r = r_p - x_s^-$. For the outer disk, we start with $\Sigma = \sigma_0/\sqrt{R_{\rm sup}}$ at $r = R_{\rm sup}$ and follow Eq. (4.11) down to $r = r_p + x_s^+$. As the slope of the density is very steep on the gap edges, the gap depth, given by $\Sigma(r_p \pm x_s^\pm)$, is very sensitive on the assumed width of the corotation zone ($x_s^\pm = 2R_H$), and $\Sigma(r_p + 2R_H)$ is not necessarily equal to $\Sigma(r_p - 2R_H)$. We chose the deepest of the two edges obtained, and start from this point to fill the bottom of the gap until the opposite edge. As shown in Chapter 4, this procedure gives a satisfactory approximation of the gap depth.

The use of Eq. (4.11) with this method provides the gap profile in a disk which unperturbed profile is $\Sigma(r) = \Sigma_0 r^{-1/2}$. Thus, multiplying this gap profile by $\sqrt{r}/\Sigma_0$ gives the gap profile in terms of fraction of the unperturbed profile. Let us denote $\sigma(r)$ this *fractional profile*. We think that it is reasonable to assume that the fractional profile is independent of the unperturbed profile. This is supported in figure 6.1, which shows that the planet apparently opens a gap in the natural profile of the disk without essentially changing it. Consequently, as a simple model of the gap profile in an evolving disk, we suggest that the unperturbed profile given by Eq. (6.1) can be multiplied by the fractional profile, obtaining:

$$\Sigma(r) = \sigma(r)\Sigma_{\rm LP74}(r,t) \ . \tag{6.2}$$

Figure 6.6 displays this model in the $\mathcal{R} = 10^{4.15}$ case at $\tau_\nu/2$. In the secondary panel is drawn the fraction profile $\sigma(r)$. In the major plot, the unperturbed profile $\Sigma_{\rm LP74}(r, \tau_\nu/2)$ appears as a dashed line. The gap profiles from numerical simulation (thin line) and from Eq. (6.2) (bold line) are compared. The agreement is very satisfactory if one keeps in mind we only have a semi-analytic estimation of the gap profile. Indeed, we discussed in Chapter 4 that Eq. (4.11) provides gap profiles a bit too narrow and not enough deep for $\mathcal{R} \leqslant 10^5$ (while it provides slightly too large and deep gaps for $\mathcal{R} > 10^{5.5}$). This is observed here, but the gap edges in the model correspond quite well to the ones from the simulation in terms of position and slope. In addition, the profile in the inner and outer disk nearly matches the simulation.

We present here only this case, corresponding to a non-migrating planet. In the cases with a migrating planet, the situation is essentially the same. This shows that this simple idea of multiplying the unperturbed profile by a schematic gap profile is valid in first approximation. As a matter of fact, a slight depletion of the inner disk with respect to the unperturbed profile is visible for cases with inward migrating planets. We will explain it in section 6.6, after having developed a model that reproduces the migration rates.

6.4.2 Cavity opening

The numerical experiments shown in figure 6.1 as well as the simple model presented in subsection 6.4.1 enlighten that a Jupiter mass planet in a disk of density of the order of the MMSN does not significantly influence its global evolution. The fractional gap profile simply multiplies the natural profile described by Eq. (6.1). This equation describes the density profile of a viscously evolving disk with inner boundary at $R_{\rm inf} > 0$. It gives profiles which are proportional to $\left(1 - (r/R_{\rm inf})^{-1/2}\right) \exp(-ar^2/T)$. The first term is about 1 for $r > 30R_{\rm inf}$, and the profile at large radius is about Gaussian. However, for $r/R_{\rm inf} < 5$, the first term shapes the profile growing from 0 at $r = R_{\rm inf}$ with a slope proportional to $(r/R_{\rm inf})^{-3/2}$. Thus it seems that $R_{\rm inf}$ is a key

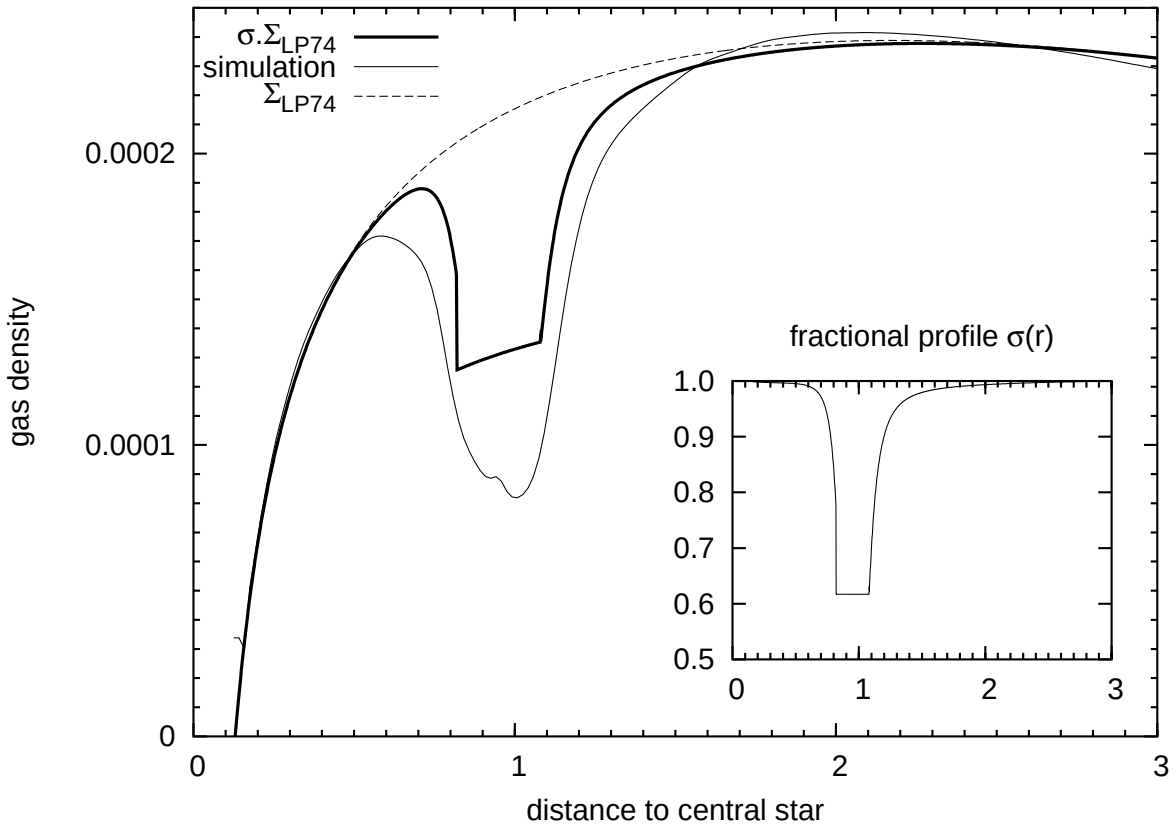

Figure 6.6: Gap profile in an evolving disk with $\mathcal{R} = 10^{4.15}$: the thin line results from numerical simulation while the bold line comes from our simple model. Dashed line : the unperturbed profile $\Sigma_{\rm LP74}(r, \tau_\nu/2)$ from Eq. (6.1). Secondary panel : "fraction profile" $\sigma(r)$ of the gap integrated from Eq. (4.11).

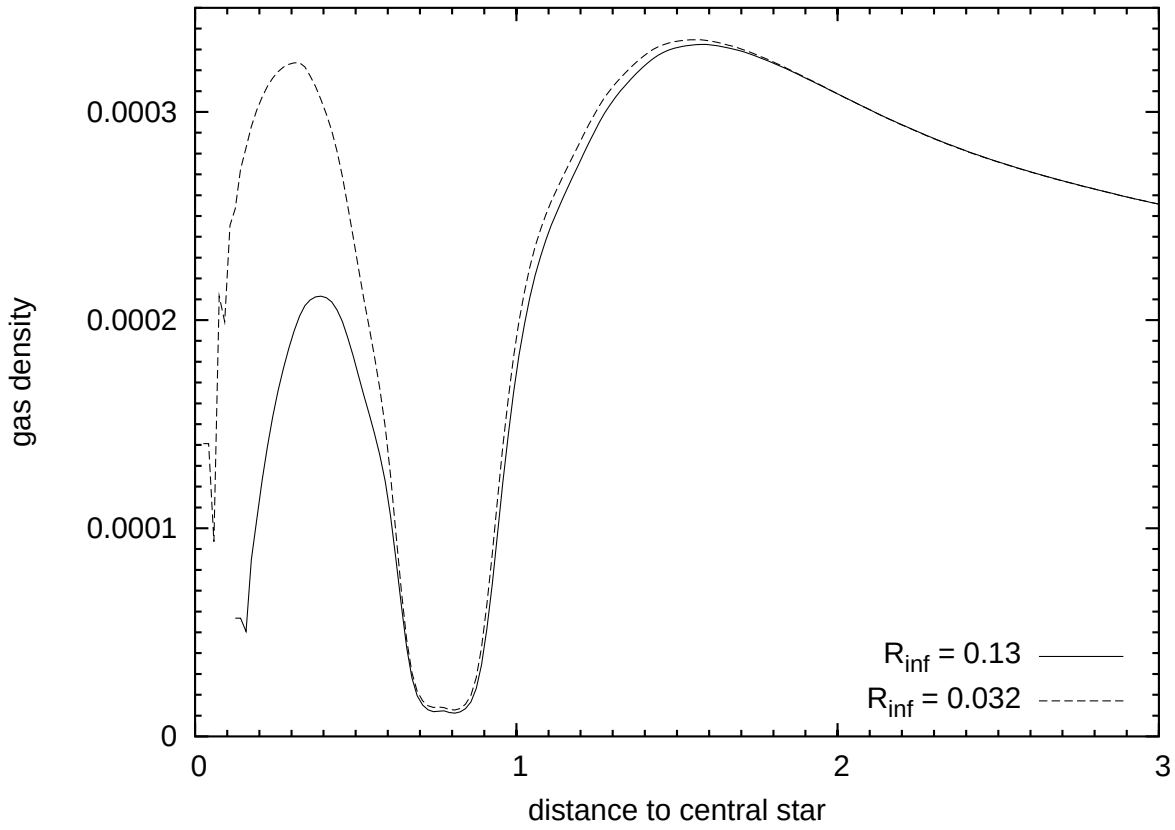

Figure 6.7: Density profile at $t = \tau_\nu/20$ with $\mathcal{R} = 10^5$ for two different values of $R_{\rm inf}$ in numerical simulations.

parameter for the profile of the innermost part of an evolving disk (see also Lubow and D'Angelo, 2006).

Figure 6.7 shows the density profile of the disk at $t = \tau_\nu/20$ in the case $\mathcal{R} = 10^5$ for two different values of $R_{\rm inf}$. The first case (plain line) corresponds to $R_{\rm inf} = 0.13$ as before. In the second case (dashed line), $R_{\rm inf}$ is four times smaller. This is the only difference between the two simulations. In both cases, the Jupiter mass planet has opened a gap in the disk and migrated down to $r_p \approx 0.75$. The outer disk profiles almost overlap. The inner disk profiles, however, present a huge difference: the maximum density is nearly twice as big in the small $R_{\rm inf}$ case as in the classical $R_{\rm inf}$ case. In the classical case, the inner disk is being depleted and a cavity is appearing. In the small $R_{\rm inf}$ case, there is only a gap. The discrepancy between the two cases shows the fundamental role of the parameter $R_{\rm inf}$ on the profile of the innermost part of an evolving disk in numerical simulations.

Eventually, depending on the width and shape of the gap and of the position of the planet r_p with respect to the inner edge of the disk $R_{\rm inf}$, the density profile may show a cavity or not. Indeed, if the inner edge of the gap falls in the flat profile zone ($r \gtrsim 10\,R_{\rm inf}$), a classical gap is shaped (case $\mathcal{R} = 10^4$ in figure 6.1 and case $R_{\rm inf} = 0.032$ in figure 6.7). If it falls between 0 and $\sim 4\,R_{\rm inf}$, the density in the inner disk cannot grow before the inner edge of the gap, and the planet opens a cavity (case $\mathcal{R} = 10^{5.5}$ in figure 6.1). The main parameter to determine whether a planet opens a cavity or not is the ratio between r_p and $R_{\rm inf}$. This is also illustrated on figure 6.8,

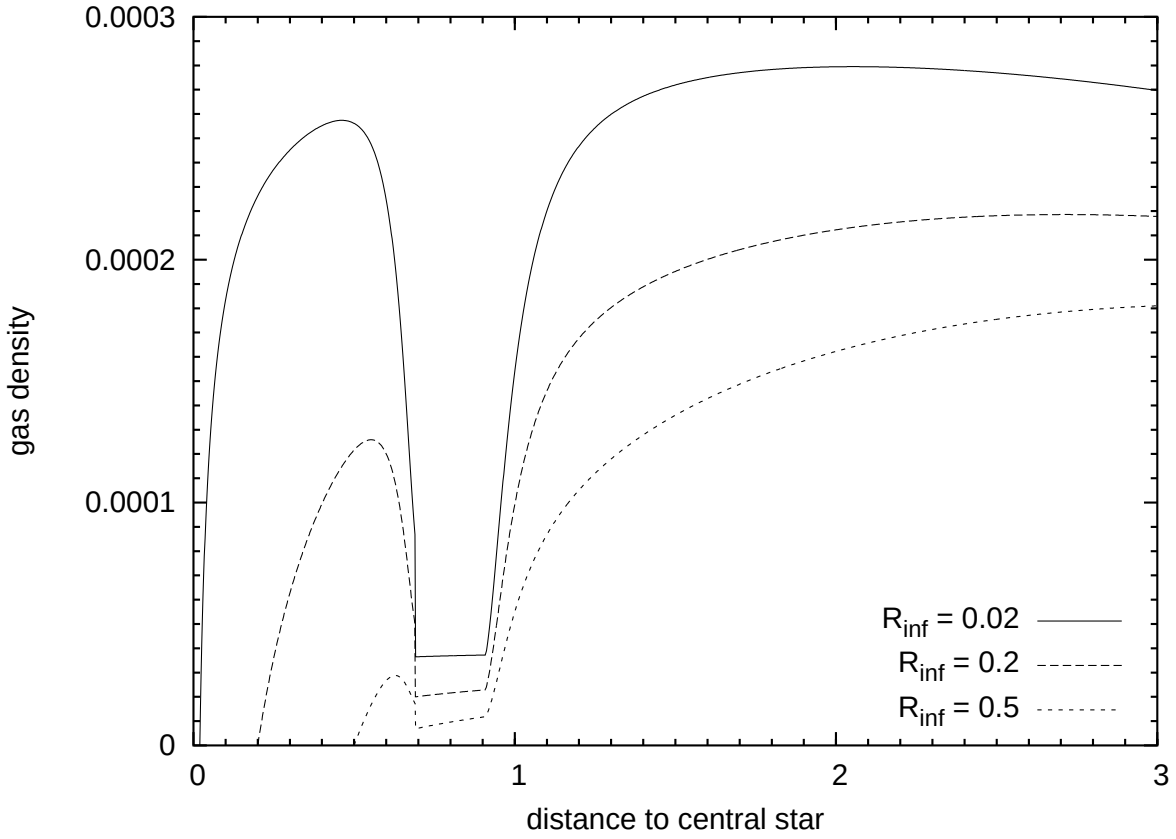

Figure 6.8: Density profile given by Eq. (6.2) of a disk with $\mathcal{R} = 10^5$ at $t = \tau_\nu/2$, for different values of $R_{\rm inf}$. A Jupiter mass planet located at $r_p = 0.8$ shapes a gap in the profile.

which shows the effect of a Jupiter-mass planet located at $r = 0.8$ on the disk profile at $t = \tau_\nu/2$ for $\mathcal{R} = 10^5$, and for different values of $R_{\rm inf}$, as computed using our model of Eq. (6.2).

This result differs from the one by Varnière et al. (2006b). They claimed that the depletion of the inner disk was faster than viscous because of the negative torque exerted on it by the planet. However, a planet in equilibrium in the middle of the gap simply transmits to the inner disk the torque it feels from the outer disk; otherwise, the planet would move with respect to the gap. To be more precise, in type II migration, the planet generally feels a total negative torque, and migrates inward, together with the disk and the gap; thus, the negative torque that the planet exerts on the inner disk is a bit smaller in magnitude than the one it feels from the outer disk. The difference corresponds to the loss of angular momentum of the planet. In the absence of the planet, there would be gas in the gap; this gas would also feel a negative torque from the outer disk, exert a smaller negative torque on the inner disk, and migrate inward losing angular momentum. If the planet has the same mass as the gas that was initially in the gap, it has exactly the same effect on the disk. Consequently, we believe there is no reason for the presence of the planet to modify substantially the evolution of the inner disk – except maybe if the planet is much more massive than the disk, which was indeed the case in Varnière et al.'s analysis. This is confirmed in our simulations.

To conclude on this point, we stress that the simple fact that $R_{\rm inf} > 0$ makes the accretion of the inner disk onto the central star faster than viscous. This should be taken into account in

the interpretation of numerical simulations. In addition, to perform realistic simulations, it is necessary to have a realistic value of $R_{\rm inf} > 0$. Thus, our hybrid scheme using coupled 2D and 1D grids (Chapter 4) seems to be a tool of choice.

6.5 Interpretation of the migration rate: a simple model

It seems quite logical that, when the planet opens a clean gap (least viscous or most massive cases), its migration follows a proper type II regime. Our model of the density profile shows that, outside the gap, the gas disk is nearly not perturbed by the planet while the density is only a fraction of its unperturbed value inside the gap. This fraction, which is the depth of the gap, increases with increasing viscosity. With a Jupiter mass planet and an Aspect Ratio of 5%, this fraction is negligible with respect to unity – in other words, the gap is very deep – for $\mathcal{R} > 10^5$ (see figure 6.1). This corresponds to the cases for which the migration rate is related to the viscous timescale, as expected.

For smaller Reynolds numbers, the gap is not completely gas-proof. The gas in the gap has two major consequences: (i) it partially sustains the outer disk, effectively reducing the torque felt by the planet from the outer disk (ii) it exerts a corotation torque onto the planet. Thus the planet decouples from the gas evolution.

Below we evaluate the torque exerted by the outer disk on the planet in the case of a clean gap and then quantify the effects (i) and (ii) just mentioned. Our analysis is based on previous works on the corotation torque (Masset, 2001), the viscous evolution of accretion disks (LP74), and the results of Chapter 4 on the shape of the gap.

6.5.1 Classical type II torque

As shown in Chapter 2, in a Keplerian, circular disk with ν and Σ independent of the radius, the viscous torque is given by Eq. (2.10): $T_\nu = 3\pi\nu\Sigma r^2\Omega$. It causes a radial drift of the gas at a velocity given by Eq. (2.64): $v_r = -\frac{3}{2}\frac{\nu}{r}$. In the following we will use the inverse relationship, namely:

$$\nu = -2v_r r/3 \ . \tag{6.3}$$

If a planet opens a deep gap in such a disk, no gas flow is permitted across the planetary orbit. The outer disk is maintained outside the gap by the planet, and an equilibrium is reached so that the planetary torque balances T_ν. Consequently, the planet feels from the outer disk the torque T_ν. This torque is proportional to the viscosity and not to the planet mass. This is the case of classic type II migration.

In a more realistic, viscously evolving disk, the scheme for type II migration is the same, but the above formula for T_ν is no longer valid. In that case, the equations of LP74 provide the density, the viscous torque, and the radial velocity as a function of radius and time. In our case of a disk with $R_{\rm inf} > 0$, it gives:

$$T_\nu = 3\pi\nu\Sigma_0\mathcal{T}^{-5/4}\,(j - j_{\rm inf})\exp\left(-\frac{ar^2}{\mathcal{T}}\right) \tag{6.4}$$

$$\Sigma_{\rm LP74} = T_\nu/\left(3\pi\nu\sqrt{r}\right) \tag{6.5}$$

$$F = -\frac{\partial T_\nu}{\partial j} \tag{6.6}$$

$$v_r = F/\left(2\pi r\Sigma_{\rm LP74}\right) \ . \tag{6.7}$$

where $j = r^2\Omega = \sqrt{r}$ is the specific angular momentum. Notice that Eq. (6.4) is exactly Eq. (25) in LP74, while Eq. (6.5) is equivalent to Eq. (6.1).

In our model, we consider that the planet feels from the disk a torque

$$T_{\rm II} = Fj = 2\pi r_e \Sigma_{\rm LP74}(r_e) v_r(r_e) \sqrt{r_e}, \tag{6.8}$$

where $r_e = r_p + x_s$ is the radius of the external edge of the gap, and $\Sigma_{\rm LP74}$ and v_r come from Eqs. (6.5) and (6.7) respectively. This torque corresponds to a classical type II migration in a realistic viscously evolving disk.

6.5.2 Torque exerted on the outer disk by the gas in the gap

The gas in the gap, the density of which is denoted $\Sigma_{\rm gap}$, exerts on the outer disk a positive viscous torque $T_{(i)}$ that is given by Eq. (6.8), with $\Sigma_{\rm gap}$ instead of $\Sigma_{\rm LP74}$ and the opposite sign. This torque partially sustains the outer disk, and therefore needs to be subtracted from the torque that the planet would suffer from the outer disk if the gap were clean (given by Eq. (6.8)).

To estimate $\Sigma_{\rm gap}$, we could follow the recipe presented in section 6.4. However, making a step by step integration until the bottom of the gap is not very convenient. Consequently, we looked for a simple formula for the gap depth as a function of the viscosity, the aspect ratio of the disk and the planet mass. In Chapter 4 we showed that the density inside the gap is less than 10% of the unperturbed value if and only if:

$$\mathcal{P} = \frac{3}{4}\frac{H}{R_H} + \frac{50}{q\mathcal{R}} \lesssim 1 \ . \tag{6.9}$$

We have computed semi-analytically the depth of the gap for various values of the parameter $\mathcal{P}$. For each value of $\mathcal{P}$, we impose $q = 10^{-3}$ and $H/r = 0.05$, and find the corresponding viscosity. Then, we use these parameters in Eq. (4.11); the obtained gap depth is shown as big dots in figure 6.9. We repeat the same operation for q ranging from 5.10^{-4} to 2.10^{-3}; the results are reported as crosses in figure 6.9. Furthermore, we impose $q = 10^{-3}$ and $\nu = 0$, and find the corresponding H/r and the resulting gap depth. We repeat the operation for ν ranging up to its maximum possible value compatible with $\mathcal{P}$; the results are shown as dots in figure 6.9. In conclusion, for a given value of $\mathcal{P}$, different depths are observed because the shape of the gap is not the same whether the viscosity or the pressure dominates, but there is a very clear tendency for deeper gaps with decreasing $\mathcal{P}$, as could be expected. The bold line in figure 6.9 shows the arbitrary fit that we adopt:

$$f(\mathcal{P}) = \begin{cases} (\mathcal{P} - 0.541)/4 & \text{if } \mathcal{P} < 2.4646 \\ 1 - \exp(-\frac{\mathcal{P}^{0.75}}{3}) & \text{if } \mathcal{P} \geqslant 2.4646 \end{cases} \tag{6.10}$$

where $f(\mathcal{P})$ stands for $\Sigma_{\rm gap}/\Sigma_{\rm LP74}$.

As the gap depth given by Eq. (4.11) is not very precise and shows variations at fixed $\mathcal{P}$, this fit is clearly an approximation of the real depth. However, the evolution of the gap depth as a function of the parameters is correctly described by $f(\mathcal{P})$, in particular if one imposes $q = 10^{-3}$ and $H/r = 0.05$, which is the most common case in our simulations. As we are looking for a simple model, this approximation is sufficient for our purpose.

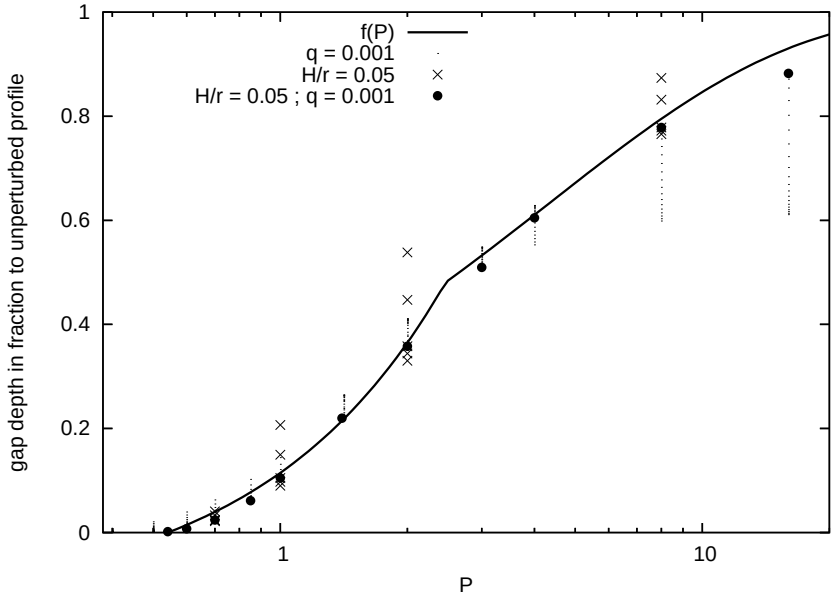

Figure 6.9: Gap depth as a function of $\mathcal{P}$ in terms of fraction to unperturbed profile at $r = r_p + 2R_H$. The bold line is an approximate fit of the data set, defined by Eq. (6.10). The datapoints for each value of $\mathcal{P}$ are obtained assuming different values of ν and H/r with $q = 10^{-3}$ (points) or different values of ν and q with $H/r = 0.05$ (crosses); the big dots correspond to the gap depths obtained with $H/r = 0.05$ and $q = 10^{-3}$.

6.5.3 Corotation torque

The corotation torque is given by Eq. (2.38):

$$T_C = \frac{3}{4}{\Omega_p}^2 {x_s}^4 \Sigma \frac{\mathrm{d}\log(\Sigma/B)}{\mathrm{d}\log r} \mathcal{F}\left(\frac{1}{(x_s/r_p)^3\mathcal{R}}\right) .$$

If we consider $x_s = 2R_H$, then $(x_s/r_p)^{-3} \approx 3/8q$. For $q = 10^{-3}$ and $\mathcal{R} > 10^{3.6}$, we have $\mathcal{R}^{-1}(x_s/r_p)^{-3} < 0.1$. In figure 2 in Masset (2001), it appears that for $z < 0.1$, $\mathcal{F}(z) \approx 20z$. Thus, in the cases we consider here, we may write:

$$T_C = \frac{3}{4}\, 20 x_s \Omega_p r_p \Sigma \nu \frac{\mathrm{d}\log(\Sigma/B)}{\mathrm{d}\log r}$$

Using Eq. (6.3), we rewrite this equation as:

$$T_C = -10\, x_s \Omega_p {r_p}^2 \Sigma v_r \frac{\mathrm{d}\log(\Sigma/B)}{\mathrm{d}\log r} \tag{6.11}$$

Here, Σ is the density inside the gap, which is equal to $\Sigma_{\mathrm{gap}} = \Sigma_{\mathrm{LP74}}(r_e) f(\mathcal{P})$, and v_r is the radial velocity at $r = r_p$, which can be derived from Eq. (6.7). The term $\frac{\mathrm{d}\log(\Sigma/B)}{\mathrm{d}\log r}$ is computed from the unperturbed density $\Sigma_{\mathrm{LP74}}(r)$, assuming a Keplerian rotation of the disk that gives $B \propto \Omega \propto r^{-3/2}$.

6.5.4 Total torque exerted on the planet

As we said above, the total torque felt by the planet is

$$T_p = T_{\rm II} + T_{(i)} + T_C \ .$$

Using the expressions computed above for these three torques, we obtain:

$$\begin{aligned} T_p &= 2\pi r_e \Sigma_{\rm LP74}(r_e) v_r(r_e) \sqrt{r_e} \times \\ &\quad \left[1 - f(\mathcal{P}) - \tfrac{5}{\pi} \tfrac{x_s}{r_e} \tfrac{\Omega_p {r_p}^2}{\sqrt{r_e}} \tfrac{v_r(r_p)}{v_r(r_e)} \tfrac{{\rm d}\log(\Sigma/B)}{{\rm d}\log r} f(\mathcal{P})\right] \ . \end{aligned} \tag{6.12}$$

With $\mathcal{P}$ and f defined respectively in Eqs. (6.9) and (6.10), while $r_e = r_p + x_s$, $x_s = 2R_H$, and $\Sigma_{\rm LP74}$ and v_r come from Eqs. (6.4)-(6.7), this gives an analytical expression for the torque felt by the planet in an evolving disk. This expression involves (directly or via v_r or $\Sigma_{\rm LP74}$) the viscosity of the disk ν, its aspect ratio H/r, the planet to primary mass ratio q, the radius of the planetary orbit r_p, and the radius of the inner edge of the disk $R_{\rm inf}$. It can be tested against numerical simulations for a wide range of these parameters and provides an overview of the resulting behavior of the planet. In figure 6.10 we plot the total torque felt by a Jupiter mass planet located at $r_p \approx 1$ in a disk with 5% aspect ratio and $R_{\rm inf} = 0.13$ as a function of $\mathcal{R}$, according to Eq. (6.12) as a bold line. The crosses with the error bars represent the torque felt by the planet in the numerical simulation, measured at $t = \tau_\nu/100$ (so that the planet is still at about $r_p = 1$). The error bars correspond to the maximum and minimum migration rates measured between $\tau_\nu/200$ and $\tau_\nu/50$. The torque $T_{\rm II}$, corresponding to classical type II migration, is drawn as a thin line; it is proportional to $\nu \propto \mathcal{R}^{-1}$. The bottom panel shows the corresponding evolution of $f(\mathcal{P})$.

As one can see in figure 6.10, the model reproduces very correctly the general tendency. For $\mathcal{R} > 10^5$, $f(\mathcal{P}) < 0.125$ and T_p is close to $T_{\rm II}$, negative and proportional to the viscosity, as expected in proper type II migration; in other words, $T_{\rm II}$ dominates $T_{(i)}$ and T_C in the calculation of T_p. For lower Reynold numbers, the effects of the gas in the gap counterbalance the classical $T_{\rm II}$. For $\mathcal{R} < 10^4$, $f(\mathcal{P}) > 0.7$ and the total torque is positive. The agreement with the numerical result is satisfactory, which validates our simple model. For very low Reynolds number (high viscosity) however, the match is not good. This corresponds to the validity limits of the model: the gap depth $f(\mathcal{P})$ is more than 80%, so that there is almost no gap.

In figure 6.11, the torque exerted on a planet placed at $r_p = 1$ in a disk with $\mathcal{R} = 10^{4.15}$, $H/r = 5\%$ and $R_{\rm inf} = 0.13$ is plotted as a function of the planet mass. The bold line corresponds to our model, and the crosses with the error bars correspond to numerical experiments (with the same prescription as before). Once again, we recover the observed trend. The explanation for this behavior is quite easy to understand: the lighter is the planet, the shallower is the gap, and the more important are the effects of the material in the gap for the total planet torque. Symmetrically, the more massive is the planet, the deeper is the gap it opens, and thus the closer to type II migration is its migration regime, which corresponds to a negative torque on the planet, proportional to the viscosity.

6.5.5 Dependence of the migration rate on inner disk radii

One may wonder about the dependence of the migration rate on the planet's location in the disk. This is governed by the radial dependence of viscosity and aspect ratio.

If the viscosity is constant, the Reynolds number $\mathcal{R}$ increases as $\sqrt{r}$. Thus, the depth of the gap opened by the planet *increases* with the planet's location r_p. As a consequence a planet

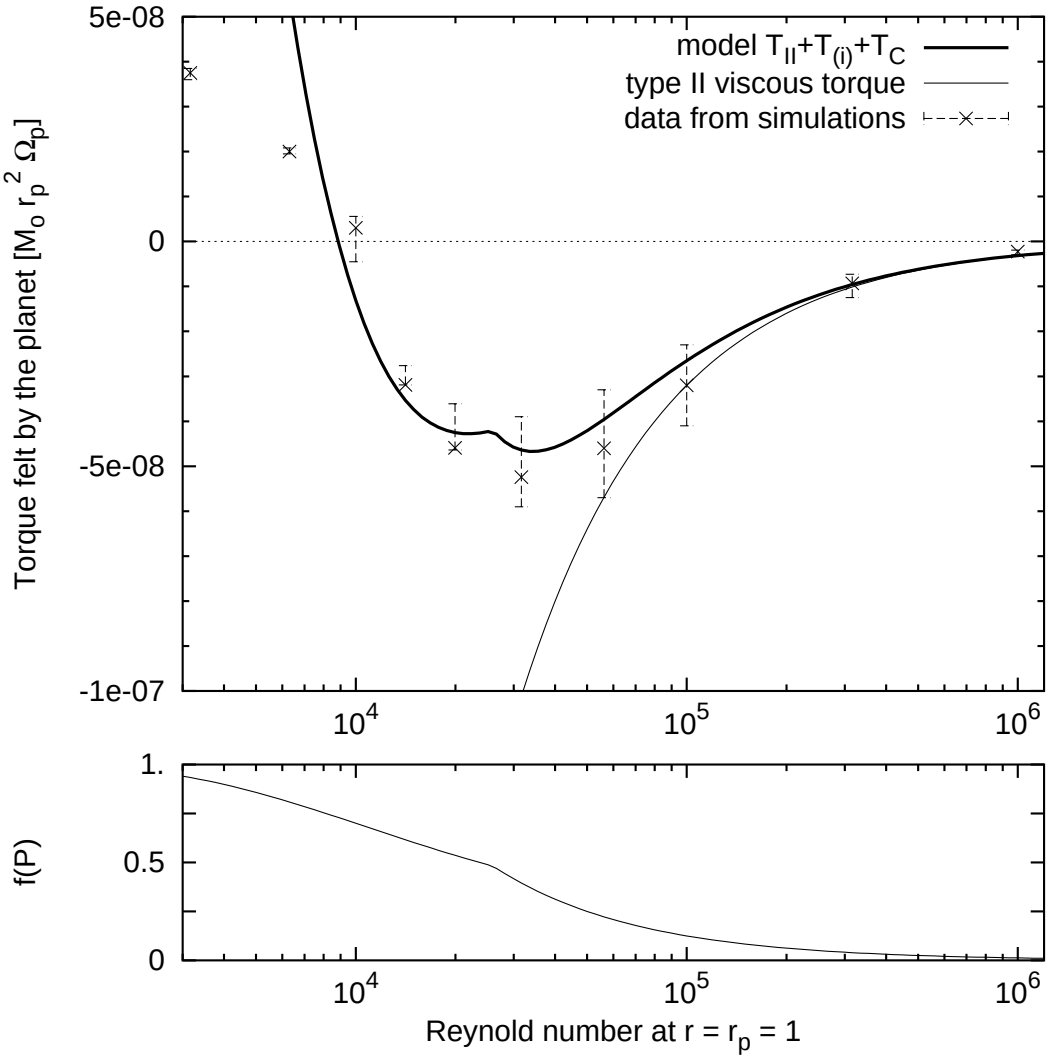

Figure 6.10: Top panel: torque felt by the planet, expressed in the units defined in section 2.6.2, as a function of the Reynolds number. Bottom panel: corresponding evolution of $f(\mathcal{P})$.

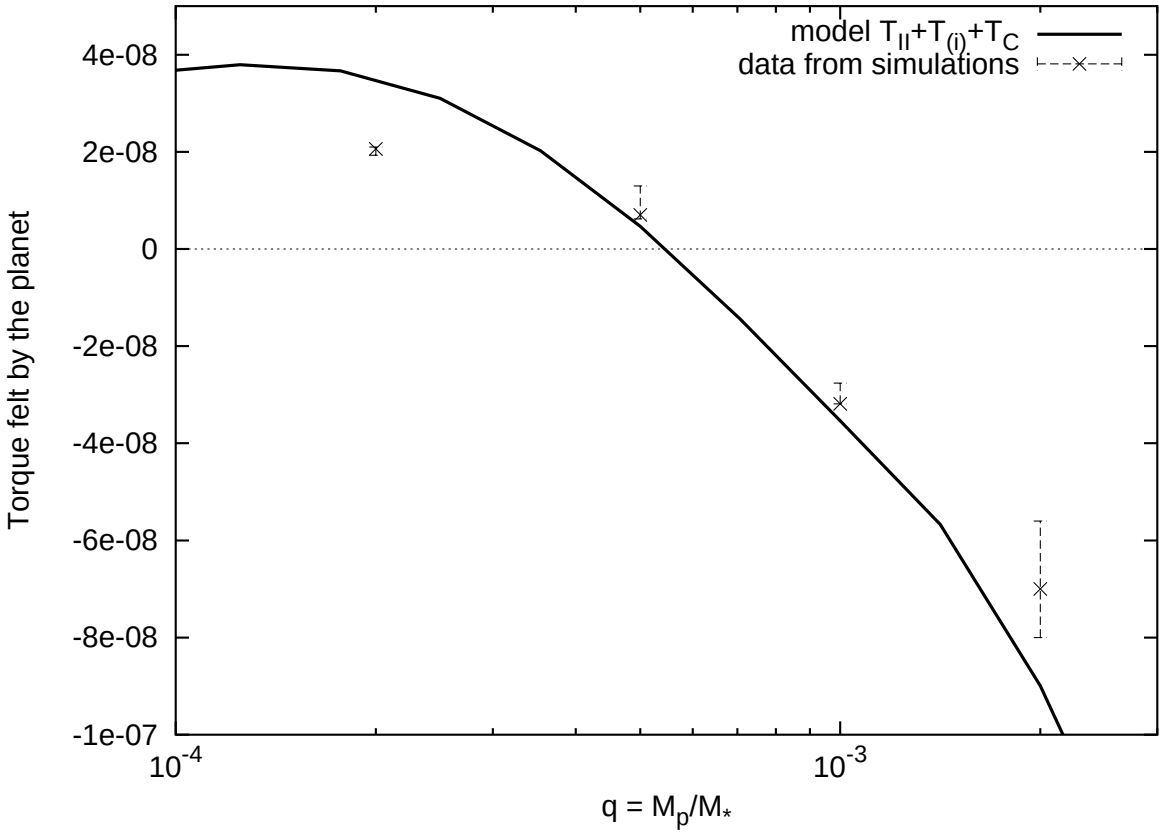

Figure 6.11: Torque felt by a planet as a function of its mass.

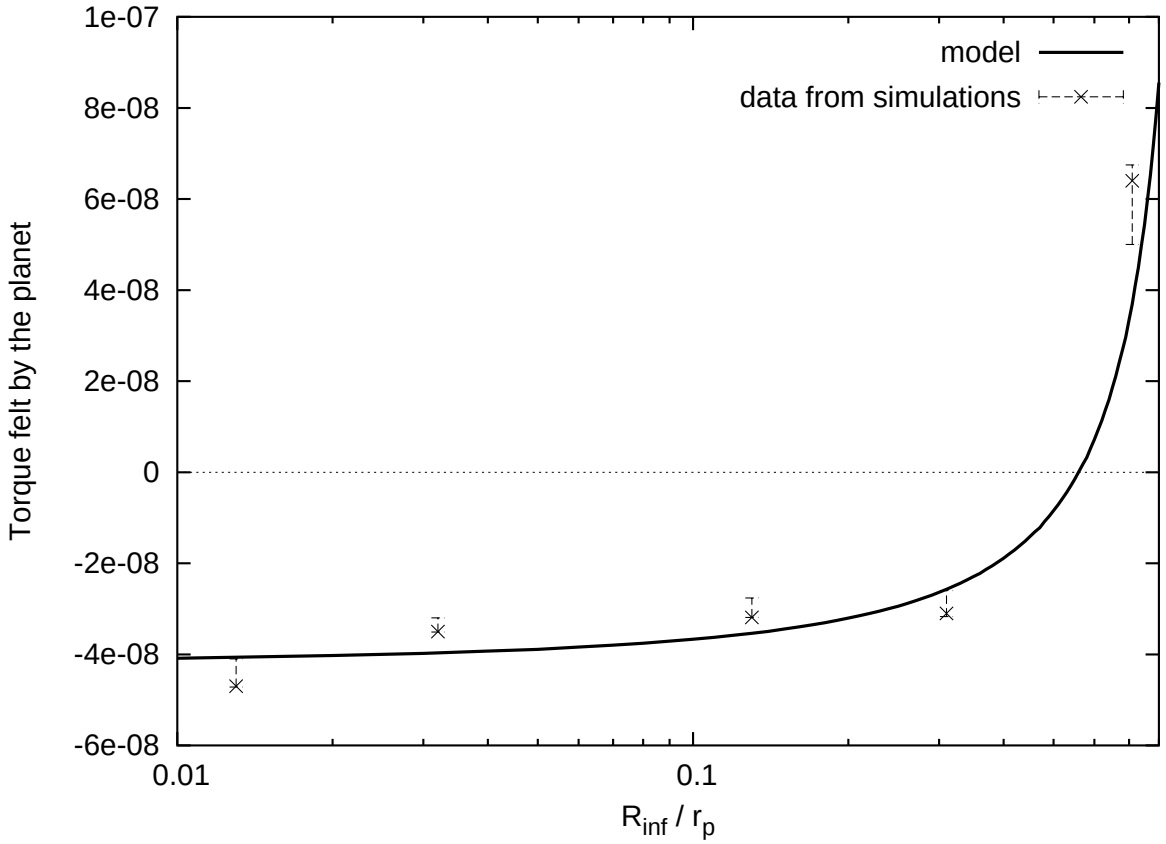

Figure 6.12: Torque felt by a Jupiter mass planet at $r_p = 1$ as a function of the radius of the inner edge of the disk $R_{\rm inf}$.

should migrate inward if it is sufficiently far from the star, and outward if it is sufficiently close. The migration paths therefore converge towards the stationary solution, at some specific radius, dependent on viscosity and planet mass.

However, if the viscosity of the disk depends on radius as described in an α model (Shakura and Sunyaev, 1973), the Reynolds number is independent of radius. If the disk is flared, H/r increases with r and therefore the depth of a gap opened by the planet *decreases* with r_p. Consequently the planet tends to move outward if it is far from the star and inward if it is close. Any stationary solution would therefore be unstable.

If the disk is not flared and the Reynolds number does not depend on r, then the behavior of the planet depends on the ratio $r_p/R_{\rm inf}$. This effect is subtle. If the ratio $r_p/R_{\rm inf}$ is smaller, the planet is in a location of the disk where Σ and v_r have a steeper positive slope, and v_r is also larger in absolute value, following Eq. (2.62). In our model, the gas radial velocity multiplies all the torques that appear in Eq. (6.12). Therefore, the only dependence on $r_p/R_{\rm inf}$ is through the gradient of the gas radial velocity $v_r(r_p)/v_r(r_e)$ and the gradient of the logarithm of the density that appear in Eq. (6.12) for the corotation torque. Figure 6.12 shows as a bold line the expected torque felt by a Jupiter mass planet in our model with $\mathcal{R} = 10^{4.15}$, at $t = \tau_\nu/100$. The gradient effect becomes important when $R_{\rm inf}/r_p \geqslant 1/2$. The crosses with the error bars correspond to measures from numerical simulations. Once again, our model reproduces very well the observed trend.

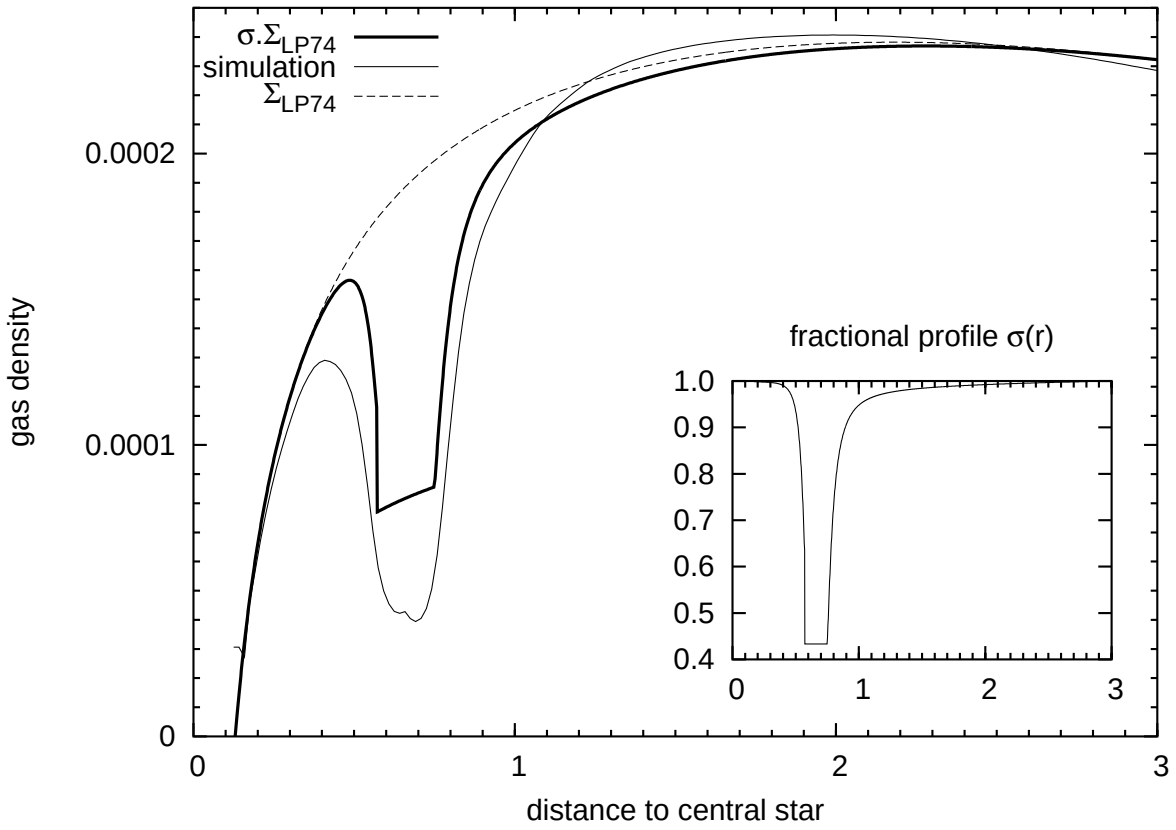

Figure 6.13: Gap profile in an evolving disk with $\mathcal{R} = 10^{4.5}$: the thin line results from numerical simulation while the bold line comes from our simple model. Dashed line : the unperturbed profile $\Sigma_{\rm LP74}(r, \tau_\nu/2)$ from Eq. (6.1). Secondary panel : "fraction profile" $\sigma(r)$ of the gap integrated from Eq. (4.11).

6.6 Effect of planet migration on the inner disk depletion

In figure 6.6 we have shown that in the case of a non-migrating planet, the density profile in the inner part of the disk coincides with the unperturbed profile given by LP74 equations. This showed that the overall mass flow through the disk was unperturbed by the presence of the planet.

Figure 6.13 is the same as figure 6.6 but for a case where the planet moves inward at slow rate. In this case there appears to be a deficit in the inner part of the disk, while the outer part shows a little over-density, relative to the unperturbed case. This reveals that only a fraction of the unperturbed mass flow effectively passes from the outer to the inner disk.

Based on the model developed above, we can illustrate this fact and develop an algorithm for the *a priori* computation of the inner disk mass deficit.

Due to the migration of the planet, the surface of the inner disk shrinks at a speed :

$$\dot{A}_p = 2\pi r_p \dot{r_p} \ .$$

In the unperturbed case, if we draw a fictitious boundary between the inner and the outer disk moving at the radial velocity of the gas, the surface of the inner disk shrinks at a speed :

$$\dot{A}_{\rm unp} = 2\pi r_p v_r \ .$$

Thus, for the inner mass of the disk to remain the same as in the unperturbed case, the mass flow into the inner disk through a planet's gap must be equal to:

$$\dot{M}_0 = -(\dot{A}_{\rm unp} - \dot{A}_p)\Sigma = 2\pi r_p(\dot{r_p} - v_r)\Sigma$$

where Σ is the unperturbed gas density, to be identified with $\Sigma_{\rm LP74}$ above.

The mass flow into the inner disk through the planet's gap corresponds to the angular momentum loss of the outer disk. It can be expressed as:

$$\dot{M}' = -\dot{J}_{\rm o}/j$$

where $J_{\rm o}$ is the total angular momentum of the outer disk and j is the specific angular momentum as usual. Obviously, $\dot{J}_{\rm o} = \dot{J}_{\rm o,unp} - \dot{J}_p$, where $\dot{J}_{\rm o,unp}$ is the change of angular momentum of the outer disk in the unperturbed case and $\dot{J}_p$ is the change of angular momentum of the planet.

Thus, the mass flow deficit into the inner disk is:

$$\delta\dot{M} = \dot{M}_0 - \dot{M}' = 2\pi r_p(\dot{r_p} - v_r)\Sigma + (\dot{J}_{\rm o,unp} - \dot{J}_p)/j \ .$$

Now, remembering that $\dot{J}_p = r_p\dot{r_p}M_p/2$ and that $\dot{J}_{\rm o,unp} = 2\pi r_p v_r \Sigma j$, the expression above becomes:

$$\delta\dot{M} = \frac{\dot{J}_p}{j}\left(4\frac{\mu}{q} - 1\right) \ , \tag{6.13}$$

where $\mu = \pi r^2\Sigma/M_*$ and $q = M_p/M_*$ as in Chapter 2.

Some remarks on Eq. (6.13) are in order. If the planet does not migrate, $\dot{J}_p = 0$ and thus there is no mass flow deficit into the inner disk, in agreement with figure 6.6. If $q = 4\mu$ there is also no mass deficit in the inner disk. This case corresponds to $\dot{r_p} = v_r$, that is to a planet that migrates inward at the same speed of the unperturbed gas. We recall that this is the maximal migration speed of a planet in type II migration. So, if $q < 4\mu$, Eq. (6.13) does not apply.

Note that in Chapter 2, we found that the threshold mass of the planet under which the migration occurs on a viscous timescale was not 4μ but 6μ (Eq. (2.50)). The discrepancy comes from the use in Chapter 2 of the viscous time $\tau_\nu = r^2/\nu$, whereas more precisely τ_ν should be defined as $|r/v_r|$ with v_r given by Eq. (2.64) ; this gives $\tau_\nu = \frac{2}{3}r^2/\nu$. Using this definition of τ_ν in Chapter 2 would also lead to the criterion $q < 4\mu$.

Finally, to compute the mass of the inner part of the disk (and therefore the cavity depth) one can follow the approach illustrated in section 6.4 and multiply the result by the relative mass flow deficit:

$$\delta\dot{M}/\dot{M}_0 = \frac{q/4\mu - 1}{1 - \dfrac{q}{4\mu}\dfrac{\dot{J}_{\rm o,unp}}{\dot{J}_p}} \ . \tag{6.14}$$

From Eq. (6.14), it also appears that if the planet mass is large with respect to the disk mass, then the mass flow deficit tends to $\dot{J}_p/j$. If this planet opens a clean gap, $\dot{J}_p \approx \dot{J}_{\rm o,unp}$ and $\dot{r_p}/v_r \ll 1$ so that $\delta\dot{M} \approx \dot{M}_0$. In summary, the two conditions $q/\mu \gg 1$ and formation of a clean gap are required to deplete strongly the inner disk and form a deep cavity.

6.7 Discussion

In this Chapter, we have computed numerical simulations of the evolution of giant planets embedded in a gas disk of equivalent mass. We used the new algorithm described in Chapter 5,

which allowed us to take into account the global evolution of the disk. This is a key point both for the opening of a cavity by a planet and for its migration, as we already discussed. To our knowledge, this is the first time such a study is performed.

We found that the planet does not modify substantially the profile of the disk with respect to its free viscous evolution; it simply opens a more or less deep gap in it. Consequently, the opening of a cavity mainly depends on the position of the planetary orbit with respect to the inner edge of the disk $R_{\rm inf}$. Indeed, the density grows from 0 at $R_{\rm inf}$ until the inner edge of the gap; thus, if the gap is too close to the inner edge of the disk, the density in the inner disk does not reach high values and a cavity appears. This seems to be the only way to open a cavity in a disk with mass of the order of the planet mass.

The presence of a migrating planet, admittedly, causes some depletion of the inner disk with respect to the unperturbed situation. However, this depletion, expressed in Eq. (6.14), is generally small. Only if the planet is much more massive than the disk and opens a clean gap, the depletion of the inner disk can be substantial. In this case a proper cavity opens on the timescale of the viscous accretion of the inner disk onto the central star.

In any case, it is much easier to open cavities in disks with large $R_{\rm inf}$ than in disks with small $R_{\rm inf}$. The size of this inner radius may vary in astrophysical disks, depending on the process that governs the fall of the gas onto the central star.

This global result on the difficulty of opening a cavity in a gas disk may appear at first sight in contradiction with observations that show that cavities are quite common. However, observations track dust, and we studied gas. In first approximation, it is considered that the dust density is a uniform fraction of the gas density, but this may not be true in the presence of the planet. If the gas can flow through the gap and refill the inner disk, the dust has a different behavior. In fact, at a positive gas density gradient in the disk, the pressure gradient is negative, which forces the gas to a super-Keplerian rotation. Dust particles are accelerated by friction with the gas, but they are not sensitive to pressure. Thus, they tend to spiral outward towards the gas density maximum. Consequently, the dust drifting inwards in the outer disk stops at the edge of the planet's gap, due to the local positive gradient of the gas density (Rice et al., 2006). Only small enough dust particles, sufficiently coupled to the gas, can flow through the gap into the inner disk. From a prescription for the gaseous friction and the gas density profile, it is in principle possible to estimate the size of the dust particles that pass through the planet's orbit.

In conclusion, substantial dust cavities could be produced by a planet even in absence of gas cavities. This can explain the simultaneous observation in some systems of a spectral hole in the SED and a high accretion rate onto the central star.

Concerning planetary migration, we found that when the planet opens a non gas-proof gap, its migration may be stopped or reversed. In particular, type II migration may be avoided for a Jupiter mass planet at several AUs in a realistic disk. This may explain why the giant planets in the Solar System and some of those in extra-solar systems are not hot Jupiters. In fact, the gas in the gap helps the planet to sustain the outer disk, so that the negative torque felt by the planet is reduced with respect to the classical type II migration case in which the gap is clean. In addition, the corotation torque is proportional to the density in the gap and is positive. These two effects may cancel the total torque felt by the planet, or even make it positive, if the gap is only barely depleted. We built a model based on this simple idea, that leads to an easy expression of the total torque felt by a planet in an evolving disk (Eq. (6.12)). This qualitative model enables us to study the influence of the various physical quantities (viscosity, planet mass, aspect ratio, $R_{\rm inf}$) on the planetary migration. The trends are in excellent agreement with the

numerical simulations.

A limitation to this model is that it does not take into account planetary accretion. The accretion had been disabled in the numerical simulations as well. However, it may have some influence on the planet behavior. Gas accreted onto the planet, supposing that it comes mostly from the outer disk, exerts a positive torque on the planet. However, this torque is approximately half of the one that it would have exerted if it had passed through the gap into the inner disk, via a horseshoe U-turn (see Chapter 2). Consequently, accretion reduces the corotation torque. Therefore, stopping the inward migration of an accreting planet requires somewhat more favorable conditions than for a non-accreting planet, for instance a shallower gap or a smaller $r_p/R_{\rm inf}$ ratio. In addition, the gas accreted on the planet does not refill the inner disk (Lubow and D'Angelo, 2006). This increases the mass flow deficit and the depletion of the inner disk. In the limit where the planet accretes all the gas that passes through its orbit, $\dot{M}$ vanishes. This leads to the opening of a cavity, if the planet migrates more slowly than the gas would do in an unperturbed disk. The efficiency of the accretion is still a parameter hard to constrain. In particular, new results (Klahr and Kley, 2006) suggest that the accretion rate might be slower than previously expected.

Chapter 7

Dynamics of Jupiter and Saturn in the protoplanetary disk

7.1 Introduction

In the end of Chapter 1, the constraints on planetary migration in the Solar System have been highlighted. The need for an almost stationary evolution of the four giant planets in the protoplanetary disk have been stressed. In Chapter 6, the evolution of a single giant planet has been shown possibly stationary in some disk conditions. However, the conditions found for preventing the migration of the planet depend on the planet mass. Therefore, this mechanism cannot be relevant for the four giants of the Solar System at the same time. In this Chapter, we consider two planets with the masses of Jupiter and Saturn, and investigate how they interact and perturb each other's migration.

A pioneer work in this direction has been done by Masset and Snellgrove (2001 ; MS01 hereafter). In that letter the authors presented the first numerical simulation of the evolution of Jupiter and Saturn in a gas disk. Saturn initially started at twice the heliocentric distance of Jupiter. After a phase of inward runaway migration, Saturn was captured into the 2:3 Mean Motion Resonance (MMR) with Jupiter. At that point, the planets reversed their migration, moving outward in parallel, while preserving their resonant relationship. This result is interesting for our purposes in two respects. First, it shows that a two-planet system in some configurations can avoid migration toward the central star. Second, the relative configuration achieved by Saturn and Jupiter is characterized by a ratio of orbital periods smaller than 2, as required by the Nice model discussed in section 1.4.2.

Therefore, we think that it is timely to investigate more in detail the mechanism unveiled by MS01, in particular exploring a wider range of parameters. In fact, there are a few open issues on the validity of the mechanism and its consistency with the Solar System structure that we need to address :

i) The evolution of Jupiter presented in MS01 is not stationary. More precisely, it is probably inconsistent with the Solar System architecture : in fact, after Jupiter and Saturn lock in their mutual 2:3 resonance, their outward migration is rather fast. Jupiter increases its orbital radius by $\sim 40\%$ in 1 000 orbits. If this really occurred in the Solar System, Jupiter would have been at some time in the middle of the asteroid belt, which is excluded as discussed in section 1.4.2. Thus, we need to find orbital evolutions that are much more stationary than the one presented in MS01.

ii) MS01 claim that the trapping of Jupiter and Saturn into the 2:3 resonance is the most likely outcome of their evolution in the gas disk. This might be problematic in the context of the Nice model. This model argues that the ratio of Saturn's and Jupiter's orbital periods was smaller than 2, but requires that it was not too much smaller than this value. Otherwise, the mass of the planetesimal disk remaining after the disappearance of the gas outside the orbit of the outermost giant planet would not have been sufficient to drive Saturn across the 1:2 resonance with Jupiter. Thus, it is important to investigate if other resonances between Jupiter and Saturn are possible in the context of the mechanism of MS01, or if there are possibilities to leave the resonance towards the end of the gas disk lifetime.

iii) It is unclear how the mechanism depends on the adopted initial conditions. If the initial, inward runaway migration of Saturn is a crucial aspect, then the overall result might depend on the numerical resolution of the disk and on its initial state (namely, whether the planets are dropped into a virgin disk, or they are allowed to sculpt the disk for some time before they are let free to migrate). In fact, some researchers could not successfully reproduce the MS01 simulation (Kley, private communication), possibly because of these issues. Moreover, a wide range inward migration of Saturn might be inconsistent with the compact orbital architecture of the giant planets invoked by the Nice model.

iv) Last, MS01 used the standard version of FARGO (Masset, 2000a,b), which only considers an annulus of disk, so that the global evolution of the disk could not properly be taken into account. However, this has a crucial role on the migration of giant planets, as discussed in section 2.6 and shown in previous Chapter. It is true that – as argued in MS01 – once the planets are in the 2:3 resonance, they are no longer locked in the evolution of the disk (the reason for which they can move outward, despite the disk has a global motion towards the Sun, like in previous Chapter). Nevertheless, the torque unbalance that MS01 measured depends critically on the mass of the disk inside the orbit of Jupiter. In particular, if Jupiter opened a deep cavity, Jupiter and Saturn could not migrate outward. In Chapter 6, we showed that the opening of a clean cavity is not likely, but that the inner disk may nevertheless be somewhat depleted due to the presence of the planets. Thus, we think that it is important to re-simulate the dynamics of Jupiter and Saturn using our new, reliable algorithm described in Chapter 5.

With these goals in mind, this chapter is structured as follows. In section 7.2 we briefly review MS01 result using a very similar simulation (and the same numerical code), and then we discuss the dependence of the results on the initial location of Saturn. In section 7.3 we use the algorithm of Chapter 5 to investigate how the dynamics of the Jupiter-Saturn couple depends on the disk aspect ratio and viscosity, and also on numerical parameters such as resolution and smoothing length. In section 7.4 we briefly address the effect of the accretion of mass onto the planets, already partially discussed in MS01. In section 7.5 we explore the dynamics for different values of the planet masses, to understand how generic the MS01 mechanism can be for extra-solar planet cases. In section 7.6 we discuss possible ways to reconcile the MS01 mechanism with the Nice model. Our conclusions are then recollected in the summary section.

7.2 The Masset–Snellgrove mechanism

Figure 7.1 is a quite close reproduction of figure 1 in MS01. It has been obtained using the same code as used in MS01, FARGO (see section 5.1 and Masset, 2000a,b), with similar parameters.

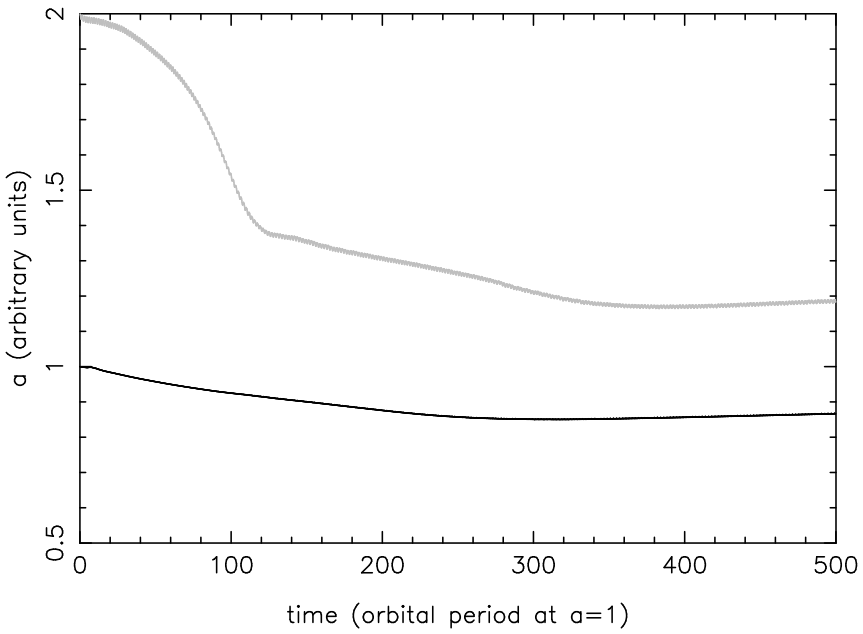

Figure 7.1: An illustration of the dynamical evolution described in MS01. The black and grey curves show the evolutions of the semi major axes of Jupiter and Saturn respectively. When capture in the 2:3 MMR occurs, the migration of Saturn is reversed.

Specifically, Jupiter is initially on a circular orbit at $r = 1$, while Saturn is at $r = 2$. The disk extends from $r = 0.3$ to 5. The polar grid has a resolution 282 in radius and 325 in azimuth. The initial surface density is uniform and is equal to $6.\ 10^{-4}$ in our units (the mass of the Sun is 1), which corresponds to the surface density of the Minimal Mass Solar Nebula (see subsection 1.2.3) if the unit of length corresponds to 5 AU. The boundary conditions allow outflow, but not inflow. An α prescription for the viscosity is adopted ($\nu = \alpha c_s H$, with c_s the sound speed, and H the disk scale height, Shakura and Sunyaev, 1973), with $\alpha = 6.\ 10^{-3}$. The disk aspect ratio H/r is set to 4% and assumed constant in space and time.

Both Jupiter and Saturn initially migrate inward, as expected. The migration of Saturn accelerates exponentially, in a runaway type III regime (see section 2.4.2, and Masset and Papaloizou, 2003). After a time of about 100 Jovian initial orbital periods, Saturn crosses the 1:2 MMR with Jupiter. Because its migration is fast, and its orbital eccentricity is small (less than 0.01), it is not captured in the resonance. As a result of the resonance crossing, Saturn's eccentricity increases to 0.02. The abrupt enhancement of the eccentricity breaks down the runaway migration. Consequently Saturn's inward motion continues at a slower, approximately constant rate, during which the eccentricity damps down. After 280 initial orbital period, the migration of Jupiter stops and then it reverses, which can be interpreted as the disappearance of the outer disk for Jupiter because of the arrival of Saturn's gap inner edge at Jupiter's gap outer edge. As they move in opposite directions, Jupiter and Saturn are eventually captured in their mutual 2:3 MMR, at $t = 350$. After this event, the two planets migrate outward in parallel. The eccentricity of Saturn stabilizes around 0.012 and that of Jupiter around 0.003. It is worth noticing that the ratio of semi major axes of the two planets does not correspond to a 2:3 ratio of the Keplerian orbital periods. It rather corresponds to a 5:8 ratio. However, by looking at the behavior of the resonant angles, we have checked that the planets are really captured in the 2:3 MMR. The

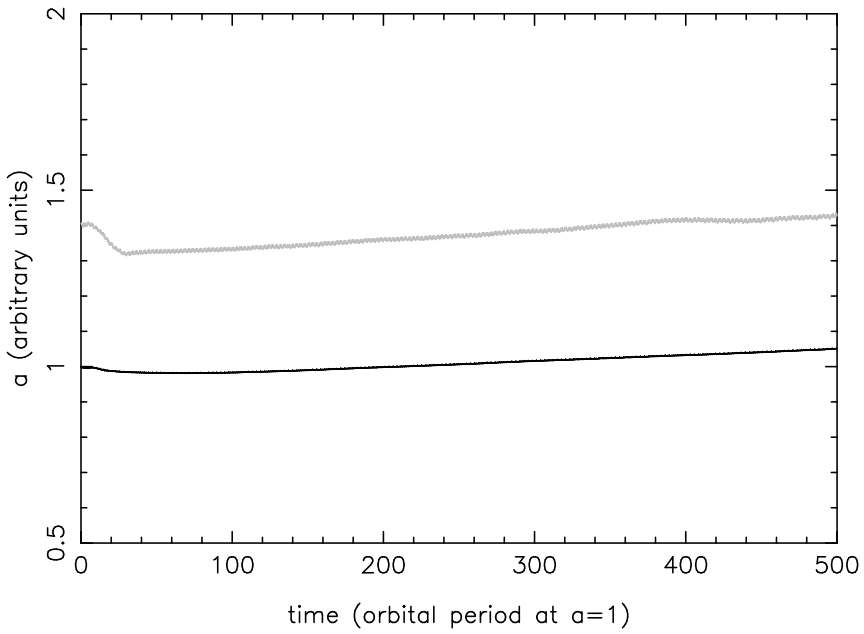

Figure 7.2: The same as figure 7.1, but for an initial location of Saturn close to (but not into) the 2:3 MMR with Jupiter.

gravity of the disk displaces the mean motion resonances relative to the unperturbed Keplerian location.

As we said in the introduction, it is an unsolved issue whether the initial evolution of Saturn, with its runaway migration and fast passage across the 1:2 MMR, plays a role in the subsequent dynamics. For instance, MS01 argue that the capture in the 2:3 MMR is favored by Saturn's eccentricity being enhanced during the previous 1:2 MMR crossing. Our understanding of planet formation is too limited to assess with confidence where Saturn formed. However, there is an emerging view that Saturn might have accreted its atmosphere (and therefore acquired the bulk of its mass) when it was already quite close to Jupiter. In fact, the immediate neighborhood of Jupiter's gap, being a local maximum of the disk surface density, acts as an accumulation point of dust and small planetesimals (Haghighipour and Boss, 2003b), and thus appears as a sweet spot for the growth of Saturn's core (Haghighipour and Boss, 2003c,a). Moreover, Saturn's core, independently of its formation location, should have suffered type I migration until it was halted at the edge of Jupiter's gap, which acts as a planet trap (Chapter 3), or in a Mean Motion Resonance with Jupiter (Thommes, 2005). Thus, we believe that it is important to verify whether the MS01 mechanism can still work if Saturn is released in the proximity of Jupiter.

Figure 7.2 shows the result of a simulation that differs from the previous one only for the initial location of Saturn (now at $r = 1.4$). As one sees, after a short range migration, the planet is trapped into the 2:3 MMR, and then the evolution is the same as in the previous simulation. Thus, the migration reversal found in MS01 does not depend on the history of the previous migration. For this reason, and because of the arguments developed above in favor of a close formation of Saturn, in the following simulations we will always release Saturn at a distance of 1.4 (which corresponds to the typical position of the edge of Jupiter's gap).

7.3 Influence of the disk properties and simulation parameters

To explore how the dynamics of Jupiter and Saturn is affected by the main parameters of the problem, we use, from now on, the numerical scheme described in Chapter 5. In all simulations presented below, the 2D grid is as before (from 0.3 to 5, with 282×325 resolution). The inner 1D grid starts at $r = 0.016$ and the outer 1D grid ends at $r = 40$ (the length unit being the initial radius of the orbit of Jupiter). The radial resolution is the same in the 1D grids as in the 2D grid. The initial surface density profile of the disk is the same as in previous Chapter : proportional to $\exp(-ar^2)$ (as illustrated with a dash-dotted line in figure 7.4) and is derived from the analysis of Hueso and Guillot (2005) for a disk evolving under the collapse of new matter onto the plane from the proto-stellar cloud, viscous evolution and photo-evaporation. The viscosity is assumed constant, for simplicity. We have verified, as MS01, that an α prescription for the viscosity would not change the results significantly, as the planets are very close to each other, although it can affect the global evolution of the disk.

Conversely to what we did in the previous section, we first let the planets evolve in the disk for 8 000 Jupiter orbits without feeling the disk perturbations, assuming a Reynolds number at Jupiter $\mathcal{R} = 1/\nu = 10^{5.5}$ and an aspect ratio $H/r = 3\%$. This allows the planets to sculpt the disk, opening gaps around their orbits, and it sets a new surface density profile of the disk. When we do simulations with different disk parameters, we start from this profile, and let the planets evolve for additional 400 Jovian orbits still without feeling the disk perturbations, so that the disk profile adapts to the new situation. Only at this point we release the planets, letting them evolve under the effects of the disk and of their mutual perturbations. This procedure allows us to avoid possible spurious initial migrations, that might occur if the initial gas distribution is inconsistent with the presence of the planets.

7.3.1 Dependence on the disk aspect ratio

In a first series of runs, we have fixed the value of the viscosity ($\nu = 10^{-5.5}$, in our units), and we have studied the evolution of Jupiter and Saturn as a function of the disk aspect ratio H/r. MS01 found that the aspect ratio simply changes the outward migration speed, by a quantity proportional to $(H/r)^{-3}$. We find that the value of the aspect ratio can have a much more important impact on the dynamical evolution.

As figure 7.3 shows, if the aspect ratio is small ($3 - 4\%$), the evolution is similar to that previously considered. When released, Jupiter starts to migrate outward, while Saturn moves inward. After locking in the mutual 2:3 MMR, both planets move outward. In these cases, the migration is indeed faster if the disk is thinner, as found in MS01. However, for thicker disks, the evolution changes qualitatively. If the aspect ratio is 5%, we find a quasi-stationary solution. After locking in the 2:3 MMR, both Jupiter and Saturn essentially do not migrate any more. To our knowledge, this is the first stationary solution ever found for a system of giant planets in a fully evolving disk. If the disk thickness is increased to 6%, both planets migrate inward, even after being captured into the 2:3 MMR. This migration is very slow, compared to that of an isolated Jupiter in the same disk. This sequence of behaviors relative to aspect ratio also suggests that, in a flaring disk, the planets might migrate until they find a position in the disk with the 'good' local aspect ratio that allows them not to migrate any more.

The reason of this parametric dependence of the evolution on H/r is quite clear if one looks at the gas density profile at the moment when the planets are released (figure 7.4). As explained in Chapter 4, the disk aspect ratio has an important role in determining the width and the depth

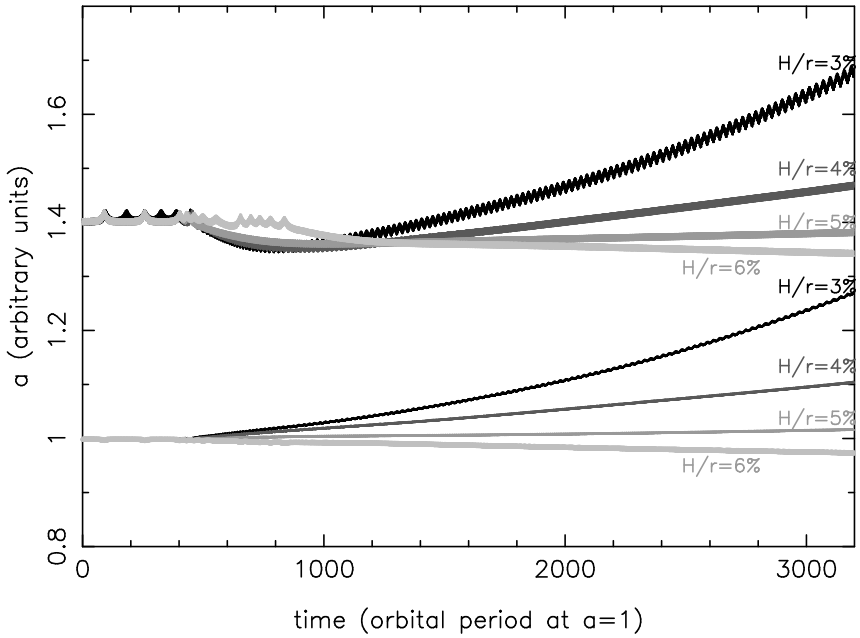

Figure 7.3: The evolution of Jupiter (lower set of curves starting at $r = 1$) and Saturn (upper set of curves, starting at $r = 1.4$). Different grey levels refer to different aspect ratios, as labeled. The viscosity is independent of radius and equal to $10^{-5.5}$ in all cases. The planets are released after 400 orbits.

of the gaps opened by the planets. Therefore, if H/r is large, there is more gas at the location of Saturn (*i.e.* just outside Jupiter's orbit) than in the case where H/r is small. Consistently, there is slightly less gas inside of Jupiter's orbit (for $r < 0.7$), because less material has been removed from the common gap formed by the two planets. As MS01 correctly pointed out, the direction of migration of Jupiter depends on the balance of the torques that the planet receives respectively from the disk inside its orbit (which pushes the planet outward) and from the disk outside its orbit (which pushes the planet inward). In the case of an isolated planet, the torque from the outer disk is typically stronger, so that the planet migrates toward the Sun. But in this case, because the presence of Saturn depletes partially the outer disk, this torque is weakened. Obviously, it is weakened more if the gap at Saturn's position is deeper, namely if the disk aspect ratio is smaller, as visible in figure 7.4. Thus, if the aspect ratio is small enough, the torque received by Jupiter from the inner disk dominates that from the outer disk, and the planet migrates outward, feeling a net positive torque. Indeed, this is what we see happening in figure 7.3.

The direction of migration of Jupiter determines the subsequent evolution of both planets, once they are locked in resonance. The planets have to move in parallel to preserve the resonant configuration. Therefore there is a competition between the net positive torque received by Jupiter and the net negative torque received by Saturn from the disk. Because these torques are monotonic functions of the planets masses, and Jupiter is 3 times heavier than Saturn, in general the positive torque received by Jupiter dominates and the two planets move outward. In the case with $H/r = 5\%$, however, the net torque felt by Jupiter is sufficiently small, due to the specific density profile of the disk, that it can be effectively canceled out by Saturn's torque. Thus, a non-migrating evolution is achieved after the planets lock in resonance.

One may wonder why the pair of planets does not behave like a single planet, locked in the

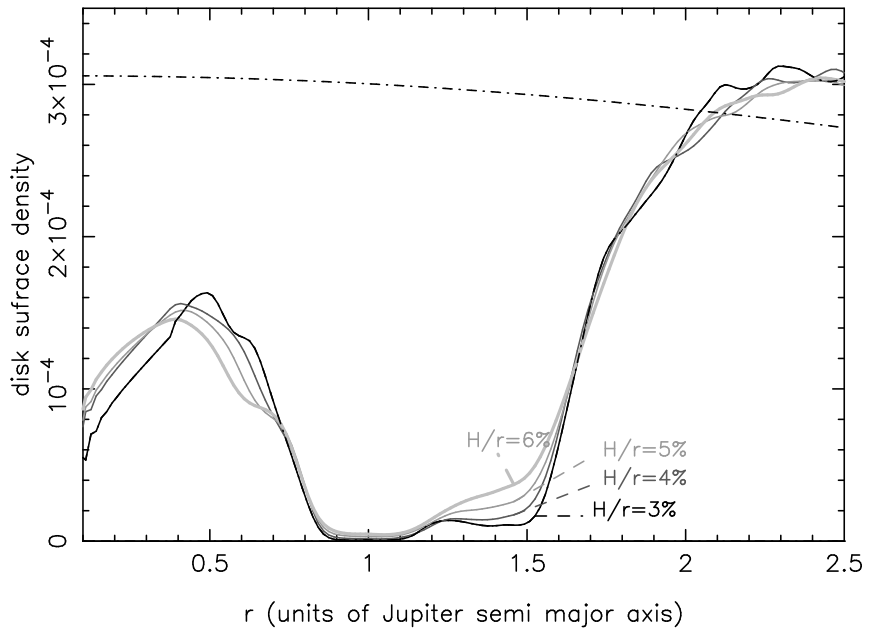

Figure 7.4: The dash-dotted curve shows the initial density profile of the disk, adopted in all simulations. The solid curves show the density profile corresponding to the moment when the planets are released, at 1 and 1.4 respectively for Jupiter and Saturn. Different grey levels refer to different aspect ratios, as labeled. The viscosity is independent of radius and equal to $10^{-5.5}$ in all cases.

common gap, in type II migration. The outer migration of the pair of planets should approach Saturn to the outer edge of its gap, until Saturn feels a stronger torque that counterbalances the one received by Jupiter. In this situation the outward migration should stop, and the two planets should start to evolve towards the Sun, together with the disk. This, apparently, does not happen. Saturn is not massive enough to open a clean gap (see figure 7.4). Thus, if its radial migration is not the same as the natural radial motion of the gas, new material flows into its gap. However, the gaps of Jupiter and Saturn overlap, so that material flowing from the outer disk into the coorbital region of Saturn, after experiencing half of a horseshoe trajectory relative to Saturn and performing a U-turn inward, can also perform half of a horseshoe trajectory relative to Jupiter, experience a U-turn inward, and be left in the inner disk. The net result is a flow of matter from the outer part of the disk, through the Jupiter-Saturn common gap, into the inner part of the disk. Thus, like in Chapter 6, the planets decouple from the gas disk evolution. To illustrate this process, figure 7.5 shows the surface density profile of the disk in the simulation with $H/r = 3\%$, at various times. Notice how, in first approximation, the Jupiter-Saturn gap simply 'shifts' through the disk. As the planets move outward, the disk is rebuilt inside the orbit of Jupiter and the surface density at the bottom of the gap increases as well. Both features are diagnostic of a mass flow through the planets system. In fact, in our code, the boundary conditions cannot act as a source of mass (see section 5.3.1). Thus, an increase of the surface density in the inner part of the disk is possible only if there is an influx of mass from the outer disk.

The flow of gas has several effects. First, it unlocks the planets from the disk, allowing them to move against the gas stream. Second, it has positive feedbacks on the outer migration

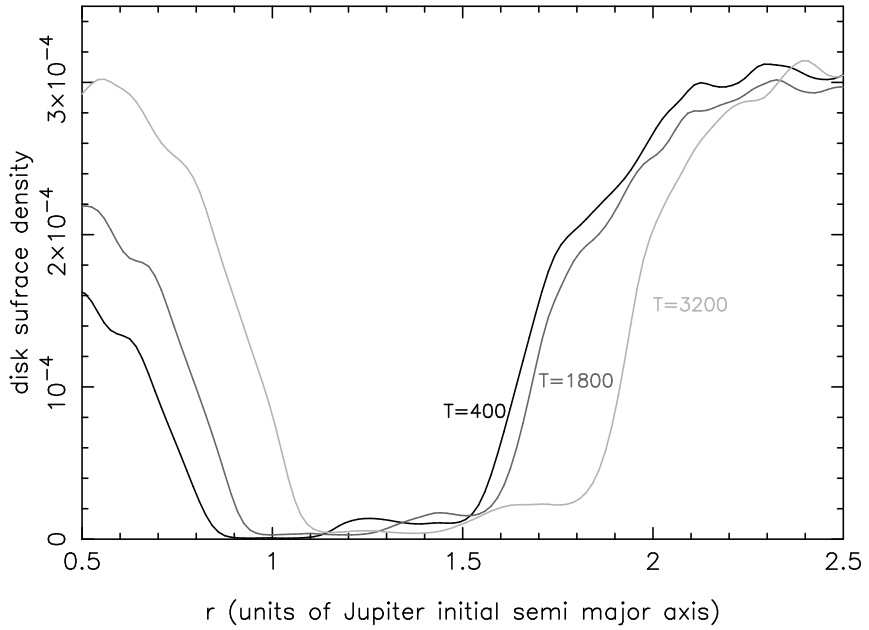

Figure 7.5: The surface density of the disk in the simulation with $H/r = 3\%$. Different grey levels refer to different times, labeled in unit of initial Jupiter's orbital period. The planets are released at time $t = 400$.

of the planets by (i) exerting a corotation torque on them, as it passes through their horseshoe regions and (ii) refurbishing the inner part of the disk, which exerts the positive torque on Jupiter discussed above. The signature of this feedback is well visible in the simulation with $H/r = 3\%$ in figure 7.3 : the outward migration rate accelerates exponentially, which implies that there is a positive net torque that increases with the migration speed.

At this point, one might wonder whether the motion of the planets is dominated by the torque felt by Jupiter from the inner disk, or by the corotation torque exerted by the gas flowing through the planets orbits. The flow of gas through the orbits of Saturn and Jupiter is the same ; the size of the horseshoe regions of the two planets (and hence the magnitude of the corotation torque felt by each planet) is proportional to $M_p^{1/3}$; thus, the effect on the migration rate $\dot{r}_p$ of the planet is proportional to $1/M_p^{2/3}$, namely it is larger for a lighter planet. So, if the corotation torque dominated the evolution of the planets, Saturn would be extracted from the resonance and would migrate away from Jupiter. As long as this does not happen (as in figure 7.3), the corotation torque cannot be the dominant force driving the planets migration. If a simulation like that with $H/r = 3\%$ (showing an exponential acceleration of the migration rate) is carried forward for a sufficiently long time, eventually the corotation torque becomes predominant, and a runaway migration of Saturn away from Jupiter is observed (Masset, private communication ; see figure 26 of Masset, 2006).

This reasoning shows that the mechanism observed here differs from the one studied in previous Chapter. Indeed, in previous Chapter, to prevent the inward migration of the planet, the corotation region of the planet had to be quite dense. In that case, the corotation torque played a crucial role to counterbalance the negative torque felt by the planet from the outer disk (even if this torque was partially supported by the gas in the gap). On the contrary here, the corotation torque plays a marginal role, but the torque felt by Jupiter from the disk is globally positive, as

well as the total torque felt by the Jupiter-Saturn pair.

7.3.2 Dependence on the technical parameters of the simulations

Before proceeding further with our exploration of the dynamical evolution of Jupiter and Saturn, it is wise to check the impact of some technical parameters used in the simulation: specifically the smoothing length for the gravitational potential and the grid resolution for the disk.

As usual in 2 dimensional hydrodynamical simulations, the equations of motions are regularized in the vicinity of the planet by modifying the gravitational potential energy $E_p(d) = -(M_p m)/d$ into $U_\epsilon(d) = -(M_p m)/\sqrt{d^2+\epsilon^2}$, where d is the distance between the planet of mass M_p and a fluid element of mass m, and ϵ is called the *smoothing length*. The choice of an appropriate value for the smoothing length is the subject of a vast debate. Essentially, two recipes are used: either ϵ is chosen proportionally to the Hill radius of the planet, or proportionally to the local thickness of the disk. The first choice aims at preventing the formation of a massive, circumplanetary disk which would cause problems in the simulation. The second choice is more physically motivated: in 3 dimensions, the fluid elements that seem to collide with the planet when projected onto the disk plane pass in most cases at a distance from the planet of the order of the disk thickness (Kley et al., 2001; Bate et al., 2003). The appropriate choice of the smoothing length can be calibrated in specific cases, for instance by requiring that the type I migration rate of an isolated small planet matches the analytic expectations. However, a general prescription, valid for all cases, does not exist.

In the simulations presented above, our choice of ϵ was equal to 60% of the planet Hill radius $R_H = r_p(q/3)^{1/3}$ (where again r_p is the semi major axis of the planet and q is the planet to central star mass ratio). We have re-computed the simulation with $H/r = 3\%$, adopting $\epsilon = 0.7H$, where H is the thickness of the disk at the distance of the planet (namely 0.03 r_p). In this case, the new value of ϵ for Saturn and Jupiter is, respectively, 73% and 50% of those previously adopted. The new simulation is compared with the previous one in figure 7.6. Because the simulations do not start exactly in the same way, for a more meaningful comparison we have plotted the evolution of the planets only from the time at which Saturn starts its outward migration (this time is slightly different in the two simulations) and we have renormalized the semi major axes of the planets by the semi major axis of Jupiter at this time. As one sees, the difference is not very big. Using the new value of ϵ leads to a slightly faster migration. The reason is that Saturn opens a wider and deeper gap in the new simulation, because the smaller value of the smoothing length is equivalent to an enhancement of its gravitational potential. As we have seen before, a deeper gap at Saturn's location increases the unbalance of the torques exerted on Jupiter from the inner and the outer parts of the disk, and hence leads to a faster outward migration speed. We have performed all the simulations of figure 7.3 with the new prescription of the smoothing length. None of the simulations changes significantly. In particular we still find a stationary, non-migrating evolution in the case with $H/r = 5\%$, and an inward migration in the case of $H/r = 6\%$. Because the choice of ϵ based from the local thickness of the disk seems more physically motivated, we will adopt this prescription in all the simulations presented further in this chapter.

The resolution of the grid used to represent the disk can also have, in principle, an important impact on the evolution of the system. In particular it can affect the corotation torque that, as we have seen, plays a role in the outward migration of the planets. To test the effects of the grid resolution, we have repeated the simulation with $H/r = 3\%$ and $\epsilon = 0.7H$, increasing by a factor of two both the radial and azimuthal resolutions of the 2D grid, and the radial resolution of the 1D grids. The new simulation is also plotted in figure 7.6. As one sees, the difference with

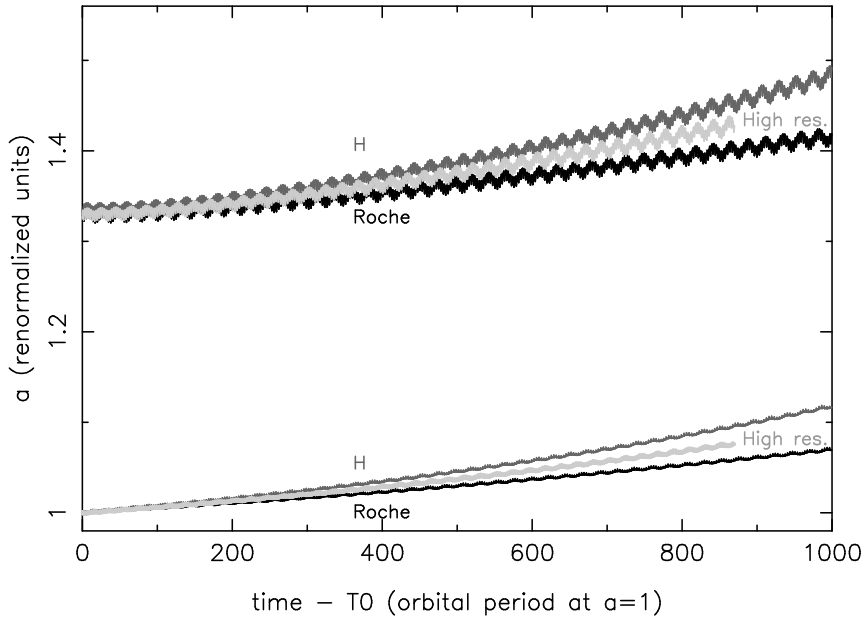

Figure 7.6: Evolution of Jupiter and Saturn in three simulations, with $H/r = 3\%$ and $\nu = 10^{-5.5}$. The simulation plotted in black and labeled 'Roche' is the one already shown in figure 7.3. The simulation reported in grey and labeled 'H' adopts a different prescription for the smoothing length, which is now imposed equal to 70% of the local thickness of the disk. The simulation plotted in light grey and labeled 'High res.' is the same as the latter simulation, but with azimuthal and radial grid resolutions increased by a factor of 2. Time is measured relative to the instant t_0 when Saturn starts to migrate outward. The semi major axes of the planets are normalized relative to the semi major axis of Jupiter at t_0.

respect to the simulation with our nominal resolution is negligible. Given the computational cost of the high resolution simulation, we will continue to use 282×325 cells in the 2D grid in the subsequent experiments.

7.3.3 Dependence on the disk viscosity

We have done a series of simulations, changing the value of the viscosity, from $\nu = 10^{-6}$ to 2×10^{-5} in our units. The disk aspect ratio is 4% in all simulations. As usual, Saturn starts at $r = 1.4$ and Jupiter at $r = 1$. The results are illustrated in figure 7.7.

Given that the viscosity, like the aspect ratio, governs the width and the depth of the gaps (see Chapter 4), we could expect that the dependence of the dynamics on the considered parameter is analog to the one that we have illustrated in section 7.3.1 : a fast outward migration for low viscosity (*i.e.* deep and large overlapping gaps), a stationary solution for some intermediate value, and an inward migration for large viscosity (*i.e.* shallow and narrow, non-overlapping gaps). The reality, however, is not that simple.

For a viscosity $\nu = 10^{-6}$ Jupiter migrates outward after it has been released. Saturn initially migrates inward and, after being locked in the 2:3 MMR with Jupiter, the two planets migrate outward in parallel. For a viscosity $\nu = 5 \times 10^{-6}$ the evolution is qualitatively similar. The outward migration speed, however, is faster than in the previous case, in contrast with what we would expect from the analogy with section 7.3.1. The reason is that, while the inner edge

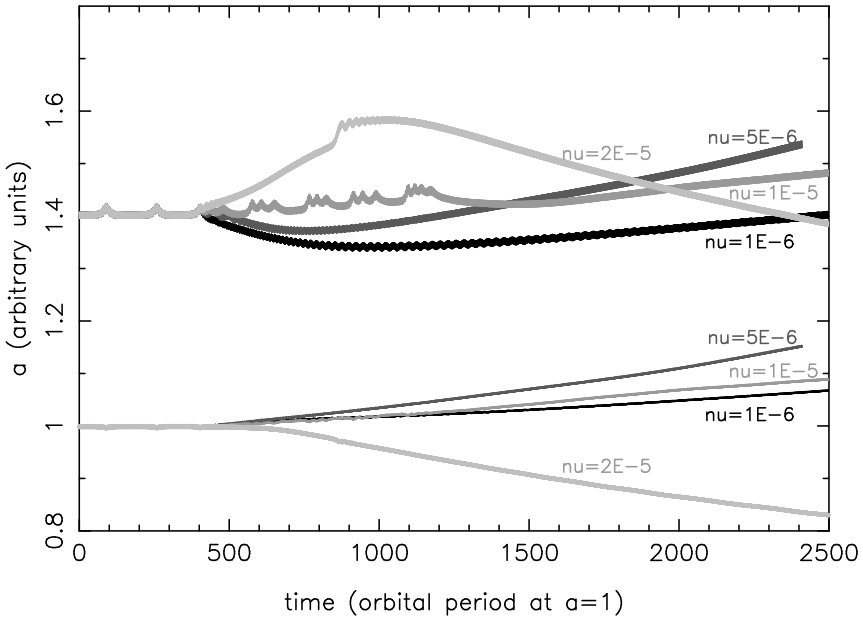

Figure 7.7: The evolution of Jupiter (lower set of curves starting at $r = 1$) and Saturn (upper set of curves, starting at $r = 1.4$). Different grey levels refer to different viscosities, as labeled. The aspect ratio H/r is equal to 4% in all cases. The planets are released after 400 initial Jovian orbits.

of Jupiter's gap is essentially in the same position in the $H/r = 3\%$ and 4% cases, the gap is significantly wider in the $\nu = 10^{-6}$ case than in the $\nu = 5 \times 10^{-6}$ case (compare figure 7.4 with figure 7.8).

For a viscosity $\nu = 10^{-5}$, Saturn, when released, has some erratic motion, which is slightly outward, on average, until $t = 1200$. During this time-span, Jupiter, which is also migrating outward, approaches Saturn. Eventually Saturn has a short inward migration and is captured in the 2:3 MMR with Jupiter, and the two planets migrate outward together. Their common outward migration is slower than in the previous cases. If the viscosity is increased to 2×10^{-5}, as soon as released Saturn migrates outward. Jupiter in the meantime migrates inward. The mutual 1:2 MMR is crossed at $t = 880$. The eccentricity enhancement that results from this resonance crossing breaks Saturn's outward migration. The planet starts a 'normal' inward migration, at a rate comparable to that of Jupiter. The two planets are close to the 1:2 MMR, but not locked in it; the resonant angles are in fact in circulation. The reason for the initial behavior of Saturn in these two simulations is most likely the mechanism explained in Chapter 6. As figure 7.8 illustrates, for these values of the viscosity there is quite a large amount of gas at Saturn's location. In addition, Jupiter's gap becomes shallower, which reveals that, even before that the planets are released, there is a net flow of gas from the outer part of the disk, through the planetary orbits, towards the inner part of the disk. Thus, the planets are decoupled from the gas global evolution and feel a corotation torque, like in previous Chapter.

Putting together these results with those of section 7.3.1, we conclude that the mechanism of MS01 works for a large range of values of aspect ratio and viscosity of the disk. Whenever the disk is enough thin and low viscous, Jupiter and Saturn can have a common outward migration, once locked in the 2:3 MMR. Finding a quasi-stationary solution, however, is more delicate. If

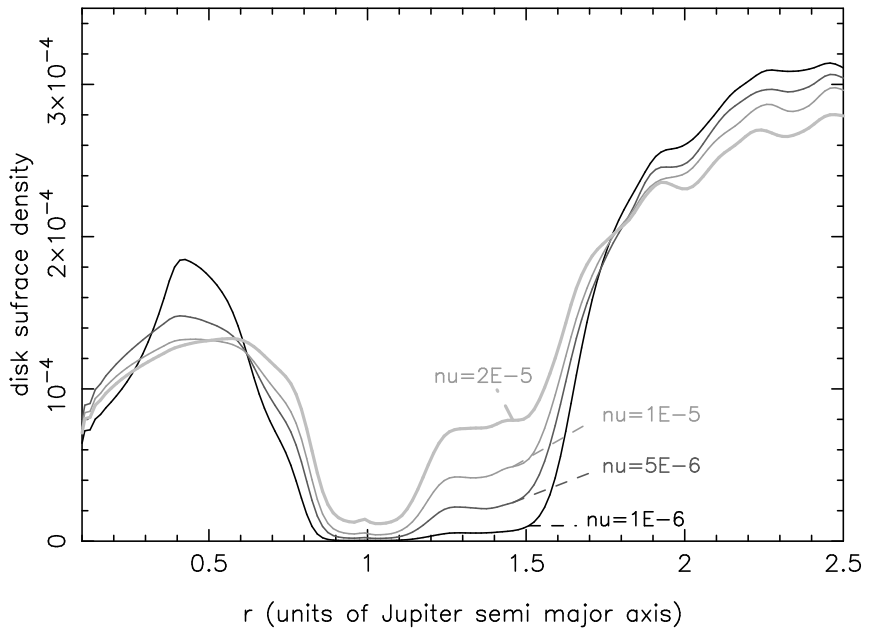

Figure 7.8: The density profiles of the disk at the moment when the planets are released. Different grey levels refer to different viscosities, as labeled. The aspect ratio is 4% in all simulations.

the disk is relatively thick (5% and, presumably, more), a quasi-stationary solution can be found for some value of the viscosity. Conversely, if the disk is thin (4% or less), a quasi-stationary solution may not be found. The reason is that, if the disk aspect ratio is decreased, in principle the viscosity needs to be increased in order to maintain a density at Saturn's location that is sufficiently large to exert on Jupiter a torque that counterbalances the one received by the planet from the inner disk. This larger viscosity, however, tends to destabilize Saturn, because the corotation torque on the planet is less saturated (see Eq. (2.38)).

7.4 The effect of mass accretion onto the planets

In all previous simulations, the mass of the planets was kept constant with time. The investigation of the effects of mass accretion onto the planets is also interesting. Mass accretion exerts additional torques onto the planets and breaks the flow of the gas across the planetary orbits. So, in principle it could modify the dynamics significantly.

MS01 already explored the effect of mass accretion onto Jupiter, and found that it is negligible even from the quantitative point of view. Here we consider also the effect of mass accretion onto Saturn, which might have a larger impact on the dynamics. Our understanding on how planet accretion proceeds, and how it stops, is still too vague to be able to assert a priori which planet should have had a more important mass growth rate.

As MS01, we have implemented mass accretion onto the planets following the recipe of Kley (1999). It consists in removing a fraction of the material in the Hill sphere of the planet and adding it to the mass of the planet. The removal rate (expressed as fraction of mass removed in the unit of time) is imposed as an input parameter. More precisely, we apply the input removal rate in the inner Hill sphere (extended up to 45% of the Hill radius R_H), we apply 2/3 of the removal rate in the region from 0.45 to 0.75 R_H, and no removal rate in the region beyond

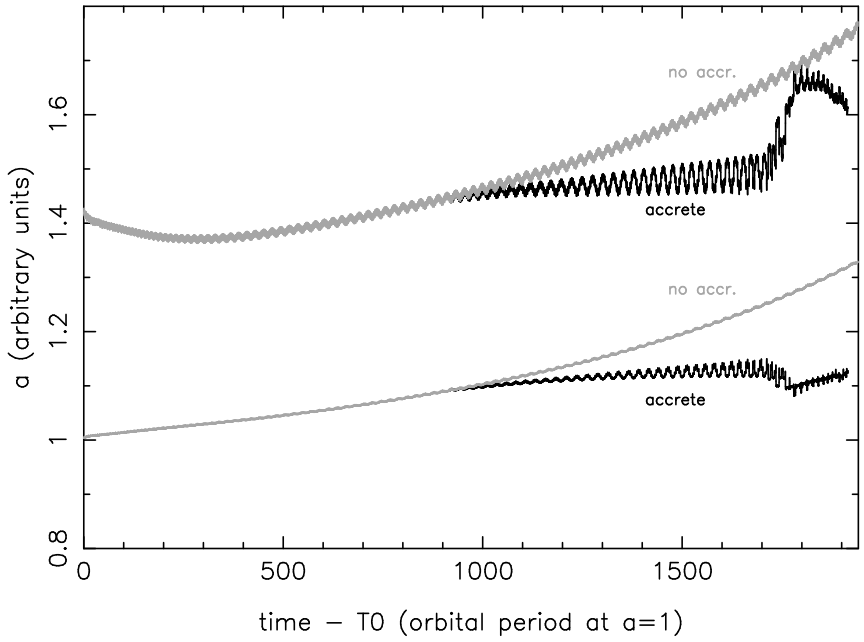

Figure 7.9: The grey curves show the evolutions of Saturn (starting at 1.4) and Jupiter (starting at 1) in the simulation with $H/r = 3\%$, $\nu = 10^{-5.5}$ and $\epsilon = 0.7H$. Time is counted in initial Jovian orbital periods, from the instant when the planets are released. The black curves show how the evolutions of Saturn and Jupiter change, starting from $t = 900$, in the case where Saturn (but not Jupiter) is allowed to accrete mass with a removal rate of 1.

0.75 R_H. We have done 6 simulations, with three removal rates applied to Saturn only or both Jupiter and Saturn. The removal rates are 0.1, 1 and 5, as in Kley (1999). All the simulations started from an intermediate state achieved in the simulation with $H/r = 3\%$, $\nu = 10^{-5.5}$ and $\epsilon = 0.7H$ (already presented in figure 7.6), precisely after a time corresponding to 900 initial Jovian orbital periods after the release of the planets.

Figure 7.9 shows the result in the case of an accretion rate of 1 applied on Saturn only and compares it with the nominal simulation that we started from, where no accretion was allowed. We notice that the outward migration rate of Saturn and Jupiter (up to 1700 orbital periods) is significantly smaller. During this time, the eccentricity of Saturn is larger than in the case without accretion (~ 0.05 instead of ~ 0.02), which means that Saturn is offering a stronger resistance to the outward push exerted by Jupiter through the 2:3 MMR. This is most likely due to the fact that Saturn is growing in mass, so that the negative torque that it receives from the outer part of the disk increases. In fact, from $t = 900$ to $t = 1700$, Saturn doubles it mass, in an essentially linear mode.

At $t = 1700$ the dynamical evolution changes abruptly. The mass of Saturn starts to grow exponentially, reaching one Jupiter mass at $t = 1800$. This abrupt flow of mass onto the planet, essentially from the outer disk, exerts a strong positive torque. Therefore Saturn is extracted from the 2:3 MMR with Jupiter and runs away from it.

The simulation where the mass of Jupiter is also allowed to grow, is essentially identical to the one presented in figure 7.9. During the linear growth regime, while the mass of Saturn doubles, the mass of Jupiter increases by only 15%. This shows that neglecting the growth of Saturn while allowing the growth of Jupiter is not justified. We also remark that the growth of the planets does

not stall until they reach a mass of several Jupiter masses. This stresses the unsolved problem of explaining the final masses of the giant planets of the Solar System (and of extra-solar systems in general).

The simulations with a smaller (0.1) or larger (5) removal rate parameter behave essentially like that presented in figure 7.9. Obviously, during the linear mass growth regime, the deviation with respect to the nominal simulation without mass accretion is smaller in the first case and larger in the second case. Even in the case with a removal rate of 5, though, we observe an outer migration of Jupiter and Saturn. This implies that this kind of dynamical evolution is robust with respect to the accretion rate, until the runaway growth regime is triggered.

7.5 Generic two-planet dynamics: dependence on the masses and mass ratio

Although this Chapter is devoted to the evolution of Jupiter and Saturn, it is interesting to do a quick exploration of how the dynamics changes with the masses of the planets (assumed constant). We have done three simulations, all with $H/r = 5\%$, $\nu = 10^{-5.5}$ and $\epsilon = 0.7H$ (these parameters corresponds to the quasi-stationary solution for the Jupiter-Saturn system) : the first one assumes that the inner planet has the mass of Saturn and the outer one has the mass of Jupiter; the second one assumes both masses are equal to one Jupiter mass; the third simulation multiplies the masses of the real planets by a factor of three.

The first two simulations give no surprise. As we explained in section 7.3.1, the outward migration is possible only if the inner planet is more massive than the outer one. Otherwise the balance between the positive torque felt by the inner planet and the negative torque felt by the outer planet is in favor of the latter one. In fact, in both the first and the second simulation the planets migrate inward. Initially, the outer planet migrates faster than the inner one, so that the two planets get captured in the 2:3 MMR after some time.

The third simulation is the most interesting. In this case the mass ratio is the same as in the Jupiter-Saturn case, favoring an outward migration. However, because the outer planet is more massive than Saturn, it may be more difficult to unlock the evolution of the planetary system from the evolution of the gas, which favors an inward migration. So, the result of this experiment is not evident a priori. Figure 7.10 shows the outcome. When the planets are released (as usual after 400 orbital periods of the inner planet), the inner planet starts to move outward as expected. The outer planet remains essentially on the spot. Before that a resonant configuration is achieved, the planets destabilize each other, because their separation corresponds to less than 3 mutual Hill radii (a mutual Hill radius is defined as $[(a_1 + a_2)/2][(M_1 + M_2)/3]^{1/3}$, where a_1, a_2 are the semi major axes and M_1, M_2 the masses). As a result of this instability, at $t = 600$ the outer planet is propelled outward on an orbit with eccentricity equal to 0.25, and the inner planet is kicked inward, onto an orbit with eccentricity equal to 0.1. Because of the large masses of the planets, the two gaps still partially overlap. Therefore, the inner planet feels a net positive torque, and the outer planet a net inward torque and, at $t = 700 - 800$, they start to migrate in converging directions. During this time, their orbital eccentricities are damped down to less than 0.05. At $t = 1000$ the planets are captured in their mutual 1:2 MMR. For a while after the resonant capture, the two planets move outward, but then eventually they stop, in a sort of quasi-stationary configuration. Our interpretation is that the gap of the outer planet is much more impermeable to the gas flow than in Saturn's case. Consequently, under the push felt from the inner planet, the outer planet simply approaches the edge of its gap until the torque that it

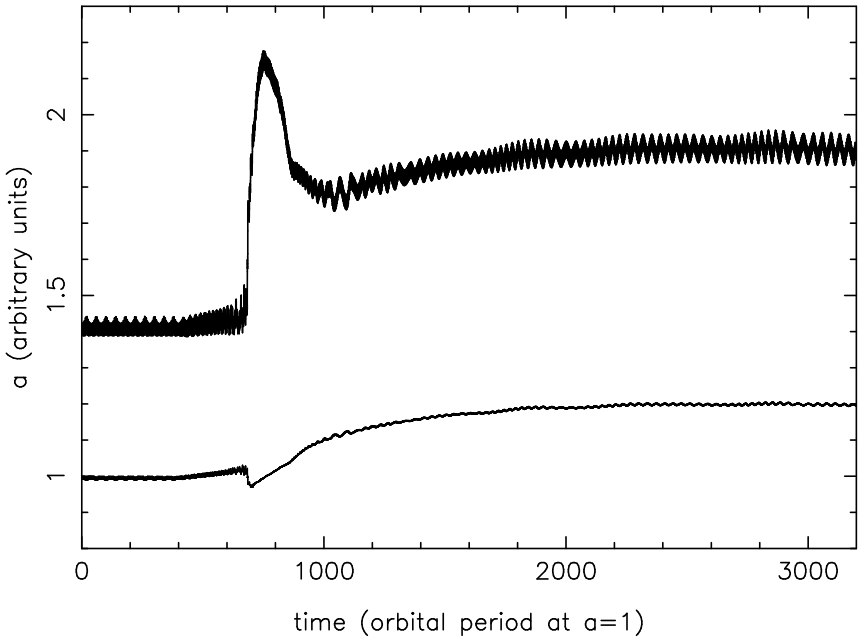

Figure 7.10: The evolution of two planets with 3 Jupiter masses (starting at $r = 1$) and 1 Jupiter mass (starting at $r = 1.4$). The disk aspect ratio is 3% and the viscosity is $10^{-5.5}$, independent of radius. A smoothing length equal to 70% of the local disk height is used.

receives from the outer disk can counterbalance the torque from the inner planet. This stops the migration.

In conclusion, the mechanism proposed in MS01 is not necessarily specific to the Solar System. It can apply to extra-solar planetary systems but only at given, stringent conditions: (i) the outer planet has to be significantly less massive than the inner one and (ii) the planets have to be locked in a resonance characterized by an orbital separation that is sufficiently small to allow the overlapping of the respective gaps. All of the 20 multi-planets extra-solar systems discovered so far should have suffered a wide range migration, as suggested by the close proximity of the planets to the central star (typically, the inner planet is within $1.5 - 2$ AU and the outer planet within 4 AU). So, we should expect that the mechanism of MS01 did not work in these systems. In fact, in 13 cases criterion (i) is not fulfilled. In the remaining cases the planets are too separated, with ratios of orbital periods larger than 3, so that it is unlikely that they have ever been locked in resonances with small orbital separation in the past. We predict that extra-solar systems satisfying both conditions (i) and (ii) will be discovered in the future, when the observation time-span will become long enough to allow the detection of distant planets that did not migrate significantly.

7.6 Possible ratios of orbital periods of Jupiter and Saturn

In all the simulations reported above, as well as in those of MS01, whenever Jupiter and Saturn are in a configuration that prevents their migration towards the Sun, they are locked in the 2:3 MMR. This supports the idea, proposed in the Nice model (see Chapter 1), that the system of the giant planets in the Solar System was very compact (*i.e.* characterized by small separations

between the planets orbits) at the end of the gas disk phase. However, from the quantitative point of view, our results do not support directly the initial conditions adopted in the Nice model. The initial ratio between the orbital periods of Saturn and Jupiter in that model was $\sim 1.8-1.9$. The exact value is not important, but it is required that it is close to 2, so that Saturn can cross the 1:2 MMR with Jupiter in ~ 650 My (the time of the Late Heavy Bombardment) due to its interaction with the remaining planetesimal disk. If, at the end of the gas disk phase, the ratio of orbital periods had been close to 1.5 (*i.e.* 2:3 MMR), it is unlikely that this would have happened (unless a very massive planetesimal disk is assumed, but this would lead to other problems concerning the evolution of Uranus and Neptune). Therefore, in this section we explore different ways to reconcile the MS01 mechanism with the initial conditions of the LHB model.

In principle, it is not necessary that Saturn and Jupiter are locked in the 2:3 MMR in order to prevent their inward migration. Other resonances, characterized by a larger ratio of orbital periods, may work, provided that the gaps formed in the disk by the two planets are wide enough to overlap. This would give a constraint on the maximal viscosity and scale height of the disk for each chosen resonant configuration. Reality, however, is not that simple, because the resonances located between the 2:3 and 1:2 MMR are Mean Motion Resonances of order more than one: the 3:5 for instance, or the 4:7. Thus, they are much thinner than first order resonances and they may be characterized by unstable motion. So, the possibility of capture and permanence of the planets in these resonances is not guaranteed, a priori.

We have done a series of 5 simulations, starting Saturn at a distance of 1.5 (Jupiter being initially at 1, as usual, so that the initial ratio of the orbital periods is 1.84), in disks with aspect ratio of 3.5% and viscosities in the range $1-3.\ 10^{-6}$. In all simulations we have observed only captures in the 3:5 MMR, which led to a quasi-stationary evolution or a slow outward migration of the giant planets. However, in all cases, once captured in the resonance, the eccentricity of Saturn grew above 0.1 in about 150 initial Jovian orbital periods. This led to an instability of the planetary motion, which eventually led to a phase of violent scattering among the planets. Thus, we conclude that resonances of order larger than 1, located in between the 2:3 and 1:2 MMR are not viable for a long phase of quiescent, non-migrating evolution. They either don't capture the planets, or lead to an unstable motion after a short timescale.

We have also done two simulations with Saturn initially at a distance of ~ 1.65 (initial ratio with Jupiter's orbital period of ~ 2.1), in a disk with $H/r = 3\%$ and viscosity of $5.\ 10^{-6}$. In both cases we have obtained capture in the 1:2 MMR, and a subsequent quasi-stationary evolution of the semi major axes of the two planets. This shows that the passage across the resonance without capture observed in MS01 (and in figure 7.1 above) was due to the fact that Saturn was migrating very fast. Our initial conditions and the low viscosity of the disk allow a slower migration and a more gradual growth of the eccentricity, which favor capture. Once captured in the resonance, despite the eccentricities of the planets are not negligible, the orbital evolution of the planets looks stable. We have not found any obvious way of extracting the planets from the resonance after some time, and delivering them onto orbits with orbital period ratio smaller than 2. So, we doubt that a capture in the 1:2 MMR during the gas disk phase may be compatible with the initial conditions of the LHB model.

Finally, we have studied the possibility that Saturn is extracted from the 2:3 MMR with Jupiter, after a long phase of stationary evolution, and is transported to larger semi major axis, approaching the 1:2 MMR.

A first idea is that, as the surface density of the disk decreases during the disk dissipation phase, the planetary motion might become unstable so that the planets push each other onto more widely separated orbits. We have rapidly discarded this possibility, by continuing with an

N-body symplectic integrator (Duncan et al., 1998) some of the simulations in which Jupiter and Saturn are in the 2:3 MMR, after suppression of the disk. These 3 body simulations are much faster than the hydrodynamical ones, and thus can easily cover a time-span of 10^9 years (we assume here that the orbital period at $r = 1$ is 12 years). In no case, we have seen signs of instability. In fact, a 'stability map' shows that the Jupiter-Saturn system at low eccentricity is stable if the ratio of the orbital periods is larger than 1.45 (Gayon, private communication).

A second idea is suggested by the simulation presented in figure 7.9. The simulation should be considered only at a qualitative level for several reasons: accretion was started when Saturn already had one Saturn's mass, so that the final mass of the planet is larger than the real one; the prescription used for mass accretion was ad-hoc and idealized. Nevertheless, the simulation shows that runaway accretion of mass onto a planet exerts a negative torque that can extract the planet from the resonance. For instance, in figure 7.9 the ratio of orbital periods of Saturn and Jupiter at $t - t_0 = 1800$ is 1.85, consistent with the initial conditions of the LHB model. Of course, once the planets are extracted from the resonance, their orbital evolution is no longer at equilibrium, and migration is resumed. Thus, to advocate a final position of the planets close to the 1:2 MMR, one has to assume that the disk disappeared 'at the right time'. Our understanding of planetary growth is still too poor to draw definite conclusions. However, the moderate mass of Saturn may be an indication that its runaway growth was indeed aborted by the disappearance of the disk (Pollack et al., 1996).

A further, possibly more promising idea, concerns the evolution of the viscosity of the disk. As we have seen in section 7.3.3, the MS01 mechanism works only if the viscosity is sufficiently small. If the viscosity exceeds some value, Saturn can be extracted from the resonance in a runaway migration mode (see figure 7.7). Thus, it is interesting to explore the dynamics of Jupiter and Saturn in the case of a disk whose viscosity increases with time. In principle, there are a few reasons to believe that the disk viscosity might grow towards the end of the disk lifetime. If the origin of viscosity is MHD turbulence (Balbus and Hawley, 1991), the viscosity depends on the ionization of the disk. A sufficiently massive disk is optically thick, so that the radiation from the star cannot penetrate in the disk and the gas is not ionized. Thus, a *dead zone* can exist inside the disk, at a typical distance from a few to a few tens of AU, where MRI turbulence is not sustained and therefore the viscosity is very small (Gammie, 1996). The giant planets might very well have formed in such a dead zone. When the disk starts to disappear, the radiation of the star can penetrate deeper into the disk, ionizing the disk on the mid-plane at larger heliocentric distance. The dead zone is re-activated, which causes an important enhancement of the local viscosity. Moreover, dust tends to have chemical bonds with the ions, subtracting them from the gas. Thus, even if undergoing the ionizing effect of the stellar radiation, a disk might not exhibit MHD turbulence if a sufficient amount of dust is present (Ilgner and Nelson, 2006). As time passes, most of the dust is accreted in planetesimals, and therefore cannot subtract ions as efficiently as before. Therefore, a late disk should be increasingly coupled to the magnetic field and be characterized by a more violent turbulence and stronger viscosity.

Motivated by these considerations, we have designed the following experiment. We considered the simulation with Jupiter initially at $r = 1$, Saturn at $r = 1.4$ and a disk with $H/r = 5\%$ and $\nu = 10^{-5.5}$, performed assuming a smoothing length $\epsilon = 0.7H$. In this simulation, after capture in the mutual 2:3 MMR, Jupiter and Saturn exhibit a remarkable stationary solution (see figure 7.11 up to $t = 3200$). At $t = 3200$ we started to increase the viscosity of the disk, at the rate of 10^{-9} per unit of time (we remind that in our units the orbital period at $r = 1$ is 2π). This rate is totally arbitrary, and not justified by any astrophysical considerations. As a consequence of the increase in viscosity, the gaps formed by the planets become narrower and overlap more

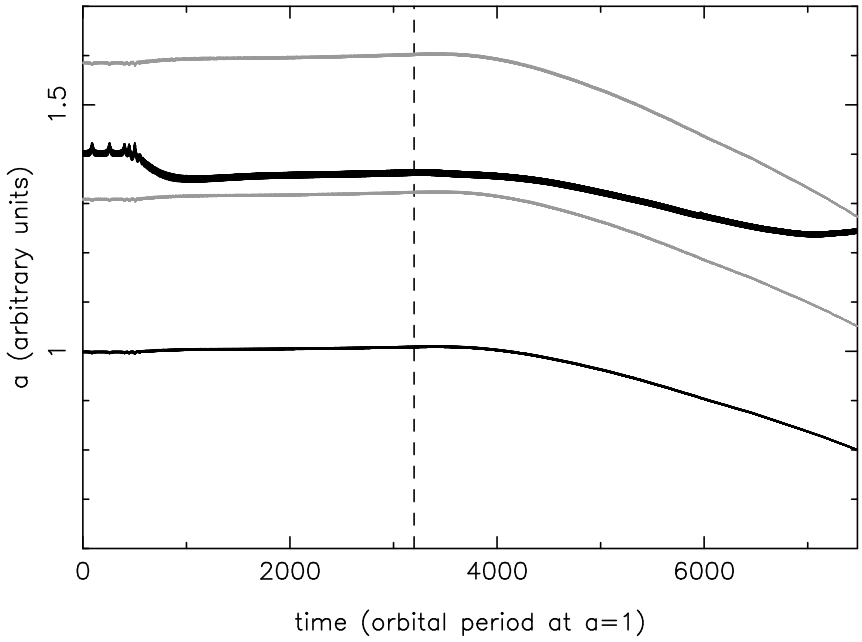

Figure 7.11: The black solid curves show the evolution of Jupiter and Saturn. As usual, the planets start at $r = 1$ and 1.4 respectively, and are released after 400 initial Jovian orbital periods. The disk scale height is 5% and the viscosity is $10^{-5.5}$. After that the planets lock in the 2:3 MMR (at $t \sim 900$) the planets semi major axes remain substantially constant. The grey curves show the location of the 2:3 and 1:2 MMR with Jupiter, according to Kepler law. Notice that the semi major axis of Saturn is slightly larger than that corresponding to the 2:3 MMR in the Kepler approximation, due to the effects of the disk gravity. At $t = 3200$ (marked by a vertical dashed line), the viscosity of the disk is increased at a rate of 6.28×10^{-9} per orbital period. This eventually forces Jupiter to migrate inward and extracts Saturn from the 2:3 MMR. The simulation is stopped when Saturn reaches the vicinity of the 1:2 MMR with Jupiter.

marginally. Thus, the shape of the gap formed by Jupiter becomes more symmetric with respect to the position of the planet, so that the torque received by Jupiter from the outer part of the disk starts to dominate over that from the inner part of the disk. Consequently Jupiter starts to migrate towards the Sun. The migration rate increases with increasing viscosity. As the resonance with Jupiter moves inward, Saturn also migrates towards the Sun, but at a smaller rate. In fact, the flow of gas from the outer disk towards Jupiter exerts a corotation torque on Saturn, slowing down its inward migration. This extracts Saturn from the 2:3 MMR. As the viscosity increases, the corotation torque becomes stronger, and eventually Saturn starts an outward runaway migration. At $t = 7200$ Saturn is very close to the 1:2 MMR with Jupiter, as required in the initial conditions of the LHB model. The eccentricities of Jupiter and Saturn are very low, less than 0.005 and 0.01 respectively, which is also consistent with the LHB model. At that time, the viscosity of the disk is $\nu = 3.1 \times 10^{-5}$. Given that the aspect ratio is 5%, this viscosity would correspond to a value of $\alpha \sim 10^{-2}$, which is still reasonable. Obviously, to support the initial conditions of the LHB model, one has to assume that the disk disappears at that time. If this were not the case, and the viscosity kept growing, Saturn would cross the 1:2 MMR with Jupiter. Notice that, overall, Jupiter has an inward migration that covers only 20% of its initial heliocentric distance. Thus, in this scenario, to justify its current position, Jupiter

should have formed at about 6.5 AU (and Saturn at about 8.5 AU, to end up, more or less, at the same position). These ranges of migration are moderate, and do not violate, a priori, any of the constraints imposed by the current Solar System architecture.

Again, we think that this simulation should be considered only at a qualitative level. Our knowledge of the evolution of the disk close to its disappearance is too approximated to be able to build a realistic simulation. Figure 7.11 is presented simply to show that it is possible, in principle, to release the planets on non-resonant orbits after that they have spent most of the disk lifetime on resonant, non-migrating ones. Obviously, making the bridge between the formation of the planets, their dynamics in the gas disk, and their subsequent evolution in the planetesimal disk remains an open, crucial problem that goes beyond the scopes of this work.

7.7 Summary

In this Chapter we have analyzed in detail, by performing many numerical simulations, the mechanism proposed by Masset and Snellgrove (2001) to explain why Jupiter and Saturn did not migrate towards the Sun. The simulations have been done with the new code presented in Chapter 5, that is particularly suitable to study the migration of the giant planets. We confirmed that, if Jupiter and Saturn are locked into their mutual 2:3 MMR and the disk viscosity and aspect ratio are sufficiently small, the planets do not migrate toward the Sun. The mechanism is robust with respect to grid resolution used for the disk, the smoothing length used for the regularization of the gravitational potential, and the accretion of mass onto the planets. In most cases, the planets migrate outward, which is not a viable evolution in the Solar System, because it would imply that Jupiter was in the asteroid belt in the past. However, there is a range of values of viscosity and disk scale height such that, once in resonance, the planets have a quasi-stationary evolution during which their semi major axes remain practically constant. We argue that Jupiter and Saturn actually followed this kind of evolution.

In general terms for a pair of planets, a quasi-stationary solution can be found only if the outer planet is significantly less massive than the inner one, and if the planets are locked in a resonance characterized by a small orbital separation, so that the gaps opened by the planets in the disk can overlap. We find that these conditions are not satisfied by any known extra-solar system of multiple planets. This is consistent with these planets having suffered a significant migration, that brought them close to the parent star where they could be discovered. We predict that systems similar to the Jupiter-Saturn case in terms of mass ratio and separation will be discovered only when it will be possible to detect distant planets that did not migrate substantially.

The results of this chapter support the view, proposed in the Nice model (Tsiganis et al., 2005; Gomes et al., 2005; Morbidelli et al., 2005), that the giant planets of the Solar System, at the end of the protoplanetary gas disk phase, were on orbits with small mutual separation. However, from the quantitative point of view, supporting the initial conditions adopted in the Nice model is problematic. We suggest that the late runaway growth of Saturn's mass or, more likely, a late enhancement of the viscosity towards the end of the disk lifetime, could have extracted Saturn from the 2:3 resonance with Jupiter and driven it close to the 1:2 resonance. We supported this scenario with simulations, but which are nevertheless qualitative, given our limited knowledge of process of planet growth and of disk disappearance.

This results opens the possibility to elaborate on a consistent scenario of the growth and migration of the giant planets of the Solar System, which is the ultimate goal of this thesis. This

consistent scenario is finally discussed in next Chapter.

Chapter 8

Conclusion

In the previous Chapters, several planet-disk interactions have been studied. If not exhaustive, this gives an overview of planet migration and of its consequences, and gives hints on how migration could be prevented in some specific cases.

In Chapter 2, former works on planet migration, and the classical equations that rule type I, type II and type III migrations have been reviewed. In particular, it has been shown why the type I migration, due to the differential Lindblad Torque, causes the planet to drift at a speed proportional to its own mass. Two conditions for gap opening have been presented, showing that a giant planet generally opens a gap in a protoplanetary gas disk. The viscous evolution of a gaseous accretion disk has been studied, and we have shown that type II migration happens on a viscous time-scale (or longer, if the planet is significantly more massive than the disk). The corotation torque and the effects of the dynamics in the horseshoe region have also been discussed and the conditions for type III, runaway migration have been derived. In Chapter 4, we have presented a new detailed study of the mechanism of gap opening by a giant planet. We derived a unified criterion for gap opening, that involves simultaneously planet mass, disk viscosity, and aspect ratio. In the other chapters, we have presented new mechanisms that can prevent planet migration. We review them briefly in next section.

8.1 Preventing planetary migration

In Chapter 3, we have shown that a density 'jump' in the disk acts as a planet trap, because the corotation torque at the jump is positive and exceeds in absolute value the differential Lindblad torque if the 'jump' is steep enough. Thus, any embryo subject to type I inwards migration is stopped at the location of the jump. We suggested that this planet trap could be a sweet spot for accreting the massive solid core of a giant planet, although our preliminary numerical simulations show that this might be more problematic than we originally envisioned.

In Chapter 5, an improvement to the classical hydro-codes has been presented. By surrounding the classical 2D grid with a radial 1D grid – that extends over the full physical disk – we showed that it is possible to take into account the global viscous evolution of the disk in the simulations, for a negligible additional computing cost. In coupling the two grids, special attention has been paid to the conservation of angular momentum. Because type II migration is governed by the global evolution of the disk, this new code allows us to study this type of migration more accurately and realistically than previously done. We have applied this code in Chapters 6 and 7.

The migration of a giant planet in a gaseous disk of various viscosities has been explored in

Chapter 6. It appeared that proper type II migration occurs only if the planet opens a very clean gap ; otherwise, the planet may decouple from the disk evolution. In fact, the gas in the gap exerts a positive corotation torque on the planet, and helps the planet to sustain the outer disk that pushes the planet inward. If the total torque felt by the planet is null, the planet does not migrate, and the gas flow through its orbit is the same as if the planet were not there. In that case, the presence of the planet has no influence on the density in the inner or outer disk. In particular the planet simply opens a gap in the unperturbed profile ; an inner disk cavity opens only if the inner edge of the disk is close to the planetary orbit. Conversely, if the planet migrates inwards,it perturbs the disk density and slightly depletes the inner disk. We have estimated the depletion of the inner disk relative to the unperturbed density, as a function of the planet mass, the disk mass and the migration speed of the planet relative to its maximal type II speed.

Finally in Chapter 7, the case of two giant planets (typically Jupiter and Saturn) has been addressed. Following the idea of Masset and Snellgrove (2001), we have shown that a pair of planets does not behave like two individual, non-interacting planets, if they lock in Mean Motion Resonance and open a common gap. In that case, the pair of planet decouples from the gas disk evolution. We have studied a wide range of disk parameters and found a non-migrating solution for the Jupiter and Saturn couple : in this configuration, the planets are locked in the 2:3 MMR, in a disk with 5% aspect ratio and Reynolds number at the location of Jupiter $\mathcal{R} = 10^{5.5}$. Jupiter and Saturn are not in the 2:3 MMR nowadays (they are close to the 2:5 resonance), but the 'Nice model' of the late evolution of the outer Solar System argues that the ratio of their orbital periods was less than 2 after the disappearance of the gas disk, and that the planets reached their current orbit only at the time of the Late Heavy Bombardment (approximately 650 million years after planet formation). So the idea of having Jupiter and Saturn much closer to each other at the time of the disk is not absurd.

8.2 Placing our work in the general context

Other ideas to form giant planets in the core-accretion model despite of type I migration have been proposed by other authors and should be mentioned for completeness.

Thommes and Murray (2006) suggested that a giant planet core could survive in the disk at the end of the disk lifetime, when the gas density has decreased enough for the migration timescale to be comparable to the formation timescale of the core ; if the gas density is still high enough for the core to accrete a gaseous atmosphere, a giant planet can be formed. Chambers (2006) suggested that the accretion of a giant planet core can be faster than the type I migration timescale, if most of the mass is accreted from small, sub-kilometer planetesimals, rather than from larger bodies.

These works, however, did not propose a mechanism to change the type I migration regime. They simply suggested ways to speed up the core accretion process relative to the theoretical type I migration timescale.

There are only a few works concerning the modification of the type I migration rate that we are aware of. Menou and Goodman (2004) have found that the opacity transitions may induce a significant reduction of the differential Lindblad torque. More recently, Paardekooper and Mellema (2006) found that in non-isothermal disks, type I migration could be halted or reversed because of the shock heating of the gas behind the planet, that creates a strong positive corotation torque.

More promising, the stochastic migration mentioned in section 1.3 can prevent many embryos

from accreting onto the central star, for masses up to 10 Earth masses (Nelson, 2005) ; however, if turbulence is strong enough to prevent inward migration, it forces the relative velocities of the planetesimals to be too high for constructive collisions to occur, which might prevent the runaway accretion of the embryos themselves.

Thus, preventing type I migration of embryos or solid cores of giant planets is a very prominent topic at the moment. Up to date, no general solution has been found to solve this issue. Our contribution is the proposition of a local solution, the planet trap, which could be present, even quite generically, in astrophysical disks. Once a core is trapped, it can complete its accretion of solids without migrating any further, until its mass becomes large enough for the onset of the runaway accretion of a gaseous atmosphere, in agreement with the Pollack et al. (1996) model.

Concerning type II migration, there has been few studies so far on how giant planets might avoid to drift towards the central star and become 'hot Jupiters'. Most works simply invoke the disappearance of the disk, or a low viscosity in order to extend the type II migration timescale. Veras and Armitage (2004) proposed that some planets might form in the outer part of the disk, where the viscous evolution of the gas is outwards. This mechanism should be relevant in disks truncated at a small radius by external agents (photo-evaporation, stellar encounters), and prevent the inward migration of the planets. However, we have shown in section 5.5 and in Chapter 6 that the real evolution of giant planets in expanding disks is not as simple as envisioned in Veras and Armitage's one-dimensional model. Finally, as we said above, Masset and Snellgrove (2001) pointed out that a pair of planets like Jupiter and Saturn might have migrated outward, and we have explored more in detail their mechanism in this work.

Our contribution in this thesis has been to show that type II migration is quite an idealized concept. In most cases of interest, the gaps are not totally clean and therefore there is a complex interplay between the viscous accretion of the disk onto the star (which pushes the planet inward) and the corotation torque exerted on the planet by the gas in the gap or flowing through it (which pushes the planet outward). We have found non-migrating solutions for both a single planet in a disk with large viscosity and in the Jupiter-Saturn case. These solutions open the way for a better understanding of the structure of our Solar System, and of extra-solar systems with distant giant planets, which will be presumably more and more frequently discovered in the future. Moreover, we have studied the sculpting of the disk by a giant planet, for what concerns the opening of gaps and cavities ; this will be interesting for the detection of the signatures of protoplanets in disks with the new generation of interferometers, particularly ALMA.

8.3 Outlining a scheme of Solar System formation

Putting together the various results of our work, we can elaborate a possible scenario of formation of the Solar System from the protoplanetary disk, that is consistent and coherent from the point of view of dynamics. It is illustrated in figure 8.1 and described below.

First, assume that the disk presented a density jump at about 5.5 AU from the Sun, due to a viscosity transition or the base of a jet (first step in figure 8.1). At this planet trap, the core of Jupiter can be formed, and stored for a sufficiently long time for it to accrete its gaseous atmosphere and becomes a giant planet (second step in figure 8.1). Then, the new-born Jupiter opens a gap (third step). Consequently, it starts to migrate inwards, under a type II regime. Actually, given that the original density profile of the disk has a steep gradient at the planet location, the conditions might be favorable to reduce type II migration speed, similarly to the

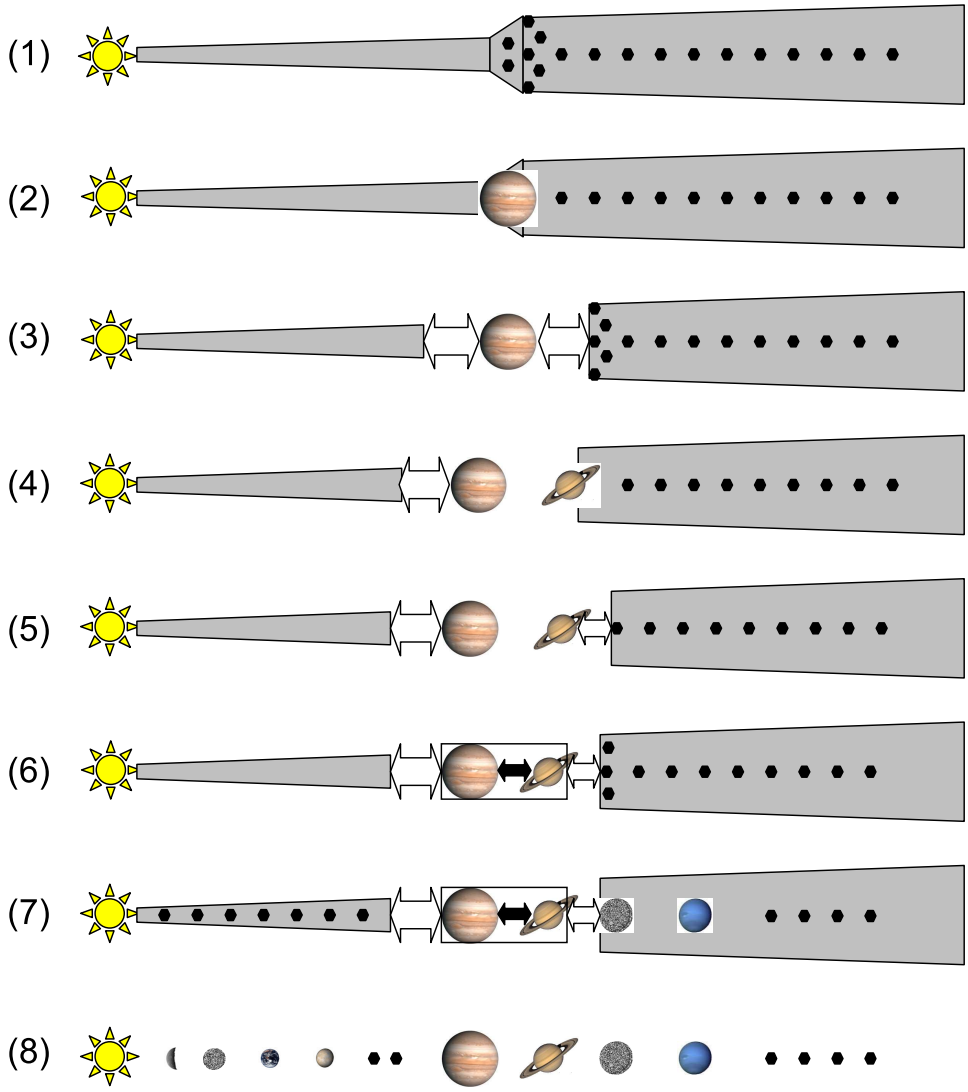

Figure 8.1: Scheme of a dynamically consistent scenario of the formation of the Solar System.

case illustrated in Chapter 6 for planets close to the inner edge of the disk. Anyway, even if type II migration is not significantly slowed down, the giant planet migrates more slowly than any embryo forming in the outer disk and subject to type I migration. Thus, embryos catch up with Jupiter. However, the outer edge of Jupiter's gap, with its steep density gradient, represents a planet trap for the migrating embryos. In addition, the embryos may be captured in one of the external Mean Motion Resonances with Jupiter. Consequently, embryos accumulate outside the orbit of Jupiter (as illustrated in third step in figure 8.1), and the formation of a new solid core is enhanced there. This core eventually accretes a gaseous atmosphere, and gives birth to Saturn (fourth step). Saturn opens a gap, that overlaps with Jupiter's one, given the small orbital separation between the planets (fifth step). The two planets in the gap are pushed by the disk and lock in the 2:3 Mean Motion Resonance, which stops their migration (see Chapter 7 and sixth step in figure 8.1) – provided that the disk parameters are favorable. Meanwhile, the inner terrestrial planets may form in the inner disk without being disturbed by the migration of the two giants. At the outer edge of the common gap of Jupiter and Saturn, the formation of Uranus is likely to occur, in analogy with the formation of Saturn described before. Then the formation of Neptune follows (seventh step). The disk may dissipate before that Uranus and Neptune become giant, gaseous planets, and before that new big objects form beyond Neptune's orbit, so that only a disk of planetesimals remains there.

Once the disk dissipates, one is left with a Solar System in which the four giant planets are in a compact configuration, and surrounded by a disk of planetesimals (last step in figure 8.1). This is not the present Solar System, admittedly, but such a configuration is similar to that required by the 'Nice model' of the late evolution of the Solar System. As discussed in Chapter 7, the configuration that we obtain does not correspond exactly to the one required by the Nice model. However, we presented a mechanism that could extract Jupiter and Saturn from their 2:3 MMR during the disk dissipation. It might also be possible to modify the initial orbits of the giant planets in the Nice model, so to have Saturn in the 2:3 MMR with Jupiter in agreement with Chapter 7 (and maybe Uranus in the 3:4 MMR with Saturn and Neptune in the 3:4 MMR with Uranus), and still achieve a late instability of the planetary system under planetesimal-driven migration. Thus, although this has not been proved yet, we are confident that it will soon be possible to 'bridge the gap' between the disk phase evolution and the late evolution of the Solar System. This opens the possibility to construct a scenario of the formation and evolution of the Solar System that covers the period ranging from the era of the protoplanetary disk up to the present time, and which is consistent and coherent from a dynamical point of view.

Discussion

This scheme, however, does not consider the problem of the final masses of the giant planets and of the influence of planetary accretion on dynamics. Mass accretion by giant planets is still not well understood and the masses of Jupiter and Saturn are not explained currently by the classical accretion schemes. A way of limiting accretion has to be found to prevent the planets from reaching several Jupiter masses. For this reason, we assumed implicitly in this work that the planets acquire their current mass almost instantaneously and then did not accrete anymore. Nevertheless, we have briefly addressed in Chapters 6 and 7, the influence of accretion on the dynamics and found that it should not change the picture qualitatively, although this might depend on the accretion rate.

Another issue that is not taken into account in our proposed scheme of formation and evolution of the Solar System concerns the chemical composition of the planets, and their enrichment with

respect to the Solar composition. There are a few models on this, from the capture of elements by clathration to the enrichment of the outer nebula by evaporation and ejection of grains by the Sun from the inner nebula. As far as we understand it, this issue should not lead to strong constraints on the location of the formation of the giant planets and their forthcoming evolution. More precisely, Alibert et al. (2005) consider that the differences of composition between Jupiter and Saturn could be explained by a local formation of Jupiter while Saturn would have formed further out in the nebula, more or less in agreement with our model.

From the masses and the chemical composition of the giant planets, Guillot and Hueso (2006) argue for a slow growth of the solid core and a late capture of the gaseous envelope of Jupiter and Saturn, when the gas density is already low in the disk. So, the metallicity of the disk is enhanced and the accretion is slowed down. In this case, the type II migration problem would be a alleviated because the disk would dissipate relatively rapidly after the planets formation.

8.4 Perspectives

In this work, we studied the dynamics of planets embedded in gas disks. The global viscous evolution of the disk has been taken into account, thanks to the coupling of a 1D grid to the classical 2D grid of hydro-codes. However, the final evolution of the disk is not governed by the viscous accretion. Disks are thought to disappear on a short time-scale after a few millions of years, due to photo-evaporation by their central star or by neighboring, UV-emitting young stars (Alexander et al., 2006). The addition of a photo-evaporation module in our hydro-code would enable us to study the phase of disk dissipation. The disk disappearance is not uniform in radius, and thus it may have important consequences on planet migration, both of type I and type II. Consequently, we think that including photo-evaporation and, more in general, the thermo-dynamics of the disk, with temperature evolving in radius and time, is an important perspective of evolution of our work that would allow us to achieve a more realistic description of planet formation and evolution. The one-dimensional disk evolution model elaborated by Hueso and Guillot (2005) should be implemented in the one-dimensional grid that we use in our hydro-code in the future.

The implementation of a realistic disk evolution would also be useful for the study of cavity opening, maybe enhanced by photo-evaporation from the central star. In addition, as stated in Chapter 6, the study of the cavities in terms of dust cavities should be more precisely performed in order to determine whether the cavities obtained in our numerical simulations are detectable as spectral holes. This is work in progress at the moment and should be submitted to peer review within the end of 2006.

As we said above, in our work we have basically neglected mass accretion onto the planets and its effects. The planetary accretion could not be resolved by our numerical code, and we used the prescription by Kley (1999) (see section 7.4). This prescription is judicious but does not take into account the detailed physics of the growing planet and of its accretion disk.

During my post-doc at Universität Tübingen, I plan to work with W. Kley on the circum-planetary disk. Most likely, some outcomes of this work will concern planetary accretion. It would then be possible to use these future results to provide a more accurate prescription for planetary accretion in our numerical simulations. In this way, the question of the final masses of Jupiter, Saturn, and the exoplanets could be addressed, especially if the disk disappearance is correctly simulated by taking into account photo-evaporation and thermodynamical evolution,

as discussed above.

8.5 Summary

To summarize, we have studied a very timely problem in present planetary science: planet migration. It consists in angular momentum loss by a protoplanet due to interactions with the gaseous protoplanetary disk around the central star. The outcome of this process is the rapid decline of the semi-major axis of the planet or the planetary core. In this frame, the existence of giant planets far from their central star (like Jupiter and Saturn) is hard to explain. Therefore, we looked for mechanisms that could prevent migration, first of the solid core precursor to a giant planet, then of a giant planet itself, or of two giant planets. Our work is based on numerical simulations; to study type II migration more reliably, we built an improvement to classical hydrocodes, by adding a 1D grid to compute the global evolution of the disk over its full physical extent. We proposed a possible solution to save planetary cores from type I migration (the planet trap), and therefore allow the formation of a gas giant by the core accretion model. Then, we provided a generalized gap opening criterion for giant planets, and we developed a model to determine to what extent a giant planet can open a cavity in a gaseous protoplanetary disk; both issues are of great importance for type II migration. We eventually presented possibilities for giant planets to avoid type II migration, in particular for what concerns the Jupiter-Saturn pair. This enabled us to draw a possible dynamical scenario of the formation of the Solar System (section 8.3).

Appendix A

Papers from the thesis at day of thesis defense

1. Crida, A., Morbidelli, A., Masset, F. , 2006.
On the width and shape of gaps in protoplanetary disks.
Icarus 181, 587-604.

2. Crida, A., Morbidelli, A., Masset, F. , 2007.
Simulating planets in globally evolving disks.
A&A, in press.
(published in january 2007. Ref.: A&A, 461, 1173-1183)

3. Crida, A., Morbidelli, A. , 2007.
Cavity opening by a giant planet in a protoplanetary disc, and effects on planetary migration.
in preparation.
(submitted to M.N.R.A.S. on January the 24^{th}, 2007, accepted on March the 6^{th}.
Ref.: MNRAS, 377, 1324-1336).

4. Masset, F., Morbidelli, A., Crida, A., Ferreira, J. , 2006.
Disk Surface Density Transitions as Protoplanet Traps.
ApJ 642, 478-487.

5. Morbidelli, A., Crida, A. , 2007.
The dynamics of Jupiter and Saturn in the gaseous protoplanetary disk.
Icarus, submitted on 28/11/2006.
(accepted on April the 9^{th}, 2007. Ref.: Icarus 191, 158-171)

Appendix B

Notations index – Index des notations

B.1 Notations index (in english)

r	distance to central star
r_p	radius of the planet orbit
θ	azimuth in polar coordinates
d	distance to the planet
ϵ	smoothing length
H	disk scale height
H/r	disk aspect ratio
c_s	sound speed ($c_s = H\Omega$)
$M_\odot$	solar mass (mass unit)
$M_\oplus$	Earth mass
M_p	planet mass
M_*	mass of the central star
q	planet to primary mass ratio
Σ	disk surface density
$\mu(r)$	$\pi r^2 \Sigma / M_*$
$\vec{F}$	force per unit volume
R_H	Hill radius of the planet
Ω_m	Ω at the m^{th} Lindblad Resonance
D	distance to the resonance
T_{LR}^m	torque from the m^{th} L. R.
T_{Lo}	outer Lindblad torque
T_g	gravitational torque ($= T_{Lo,i}$)
T_C	corotation torque
Φ	gravitational potential
$\Re$	real part
J	angular momentum
j	specific angular momentum ($j = r^2\Omega$)
Ω	angular velocity
κ	epicyclic frequency
b	impact parameter
Δ	distance to the planet orbit ($r - r_p$)
x_s	half-width of the horseshoe region
B	second Oort constant ($B = \Omega + \frac{r}{2}\frac{\mathrm{d}\Omega}{\mathrm{d}r}$)
G	gravitational constant (unity)
$\bar{\bar{d}}$	viscous stress tensor
$\bar{\bar{D}}$	strain tensor
$\bar{\bar{\sigma}}$	stress tensor
$\vec{v}$	velocity
ν	shear or kinematic viscosity
τ_ν	viscous time ($\tau_\nu = r^2/\nu$)
F_{x}	flux of x
$\mathcal{R}$	Reynolds number $\mathcal{R} = r^2\Omega/\nu$
r_m	effective location of the m^{th} L. R.
$\mathcal{D}$	$\mathrm{d}D/\mathrm{d}r$
T_{dLR}	differential Lindblad torque
T_{Li}	inner Lindblad torque
T_ν	viscous torque
T_{HS}	torque due to horseshoe effects
$\hat{X}^m$	mth Fourier component of X
$\Im$	imaginary part

B.2 Index des notations (en français)

r	distance à l'étoile centrale
r_p	rayon de l'orbite de la planète
θ	azimuth en coordonnées polaires
d	distance à la planète
ϵ	longueur de "smoothing"
H	échelle de hauteur du disque
H/r	rapport d'aspect du disque
c_s	vitesse du son ($c_s = H\Omega$)
$M_\odot$	masse solaire (unité de masse)
$M_\oplus$	masse terrestre
M_p	masse de la planète
M_*	masse de l'étoile centrale
q	M_p/M_*
Σ	densité surfacique du disque
$\mu(r)$	$\pi r^2 \Sigma / M_*$
$\vec{F}$	force par unité de volume
R_H	rayon de Hill de la planète
Ω_m	Ω à la Résonance de Lindblad m
D	distance à la résonance
T_{LR}^m	couple dû à la R. L. m
T_{Lo}	couple de Lindblad externe
T_g	couple gravitationnel ($= T_{Lo,i}$)
T_C	couple de corotation
Φ	potentiel gravitationnel
$\Re$	partie réelle
J	moment cinétique
j	moment cinétique spécifique ($j = r^2\Omega$)
Ω	vitesse angulaire
κ	fréquence épicyclique
b	paramètre d'impact
Δ	distance à l'orbite planétaire ($r - r_p$)
x_s	demi largeur de la région des orbites fer à cheval
B	$2^{\text{ème}}$ constante de Oort ($B = \Omega + \frac{r}{2}\frac{\mathrm{d}\Omega}{\mathrm{d}r}$)
G	constante de gravité (unité)
$\bar{\bar{d}}$	tenseur des contraintes visqueux
$\bar{\bar{D}}$	tenseur des taux de déformation
$\bar{\bar{\sigma}}$	tenseur des contraintes
$\vec{v}$	vitesse
ν	viscosité cinématique
τ_ν	temps visqueux ($\tau_\nu = r^2/\nu$)
F_{x}	flux de x
$\mathcal{R}$	nombre de Reynolds $\mathcal{R} = r^2\Omega/\nu$
r_m	position effective de la R. L. m
$\mathcal{D}$	$\mathrm{d}D/\mathrm{d}r$
T_{dLR}	couple différentiel de Lindblad
T_{Li}	couple de Lindblad interne
T_ν	couple visqueux
T_{HS}	couple dû aux effets "horseshoe"
$\hat{X}^m$	$m^{\text{ème}}$ composante de Fourier de X
$\Im$	partie imaginaire

Appendix C

Ackowledgments – Remerciements

I wish to thank particularly my PhD advisor, **Alessandro Morbidelli**, with whom it was a pleasure and an honnor to work. He really took care of me, and he gave precious advises in science. His flair, his efficiency, and his well-known competence have enabled him to drive this thesis to particularly interesting topics. He was never reluctant to explain a specific point that may be intriguing to me, and not only he understands things very well but he can also explain them very clearly. Collaborating with him to solve a problem or to understand a phenomenon is always efficient, instructive, and pleasant. Consequently, during these three years, I learnt a lot in planetary science from him. But he also put me in excellent conditions to learn a lot from other people. Indeed, he has a lot of collaborators world-wide, and it was a chance for me to meet them ; in addition, he co-organised or allowed me to go to several schools or international meetings. Thanks to him, I got in contact to the captivating problem of the formation of the Solar System, and to the impassionned people who work on it.

I hope that seeing him at work also teached me a lot on the methodology of work, the way to produce a paper, to present results, in a word how to be a good scientist. Tristan Guillot once told me that everybody would agree that I have been lucky to have Morby as my PhD advisor, but that from now on I should try to make people think that Morby was lucky to have had me as a student. Well, there is still a lot of work ...

And not only we worked together to make good science (at least, we hope so), but we also colaborated in climbing the roof of Europe, the Mont-Blanc, which was a great success of our cooperation. We lived great experiences together, including for instance swimming with marine turtles in Hawai'i or seeing a solar eclipse in the middle of the Sahara. Weekly jogging around the observatory was also pleasant. Definitely, I think I could not find a better PhD advisor in the Solar System.

I also thank specially **Frédéric Masset**, who was almost a co-advisor for me. He first provided us with his powerfull hydrocode FARGO, and helped us to get familiar with it, which saved a lot of our time. Then, he gave us precious informations and advices concerning planet-disk interaction, which helped us to enter this topic. In particular, his teaching at the Aussois 2004 winter school on the Solar System formation was very clear and very complete. It represented a solid basis for this thesis.

During these three years, his suggestions were always pertinent and his advices precious. When he came to Nice, this always led to several days of very efficient work, and major steps forward in our understanding of planet-disk interactions. Brillant at computer programming, he was often availible to help me when I encountered an apparently unsolvable problem ; thanks to

his advices, I acquired a lot of experience in this field, which will be usefull in the future.

For these reasons, I thank him and I hope that we will have other opportunities to work together in the future.

In addition, I wish to thank the members of the commitee, particularly Prs. **Kley** and **Nelson** who refereed this work, and came in Nice from Germany and England, respectively. Pr. **Faurobert** simply came from the university of Nice, but she accepted to be the president of the commitee, which I thank her for. It was also a pleasure to have in this commitee Prs **Huré** and **Sicardy**, who I thank for coming from Bordeaux and Paris and for showing interest in my work.

The working conditions provided in the Observatoire de la Côte d'Azur in Nice are particularly good. The site is calm and beautiful, with pine trees, fig trees, orchids, boars, and see view, with a rich history and the impressive greatest refractor still in use in the world. The people are efficient, and I wish to thank those who provide the researchers good working conditions : the director Jacques Colin, the director of the Cassiopée laboratory Albert Bijaoui, all the administration team, particularly Rose and Sébastien, all the members of the "services techniques" who take care of the buildings and the park, the restaurant team who provides excellent meals in a friendly athmosphere, and all the people who take care of the computers and the network.

During my three years in the Observatoire de la Côte d'Azur in Nice, I met a lot of very nice people there, without whom this thesis would not have happened in so pleasant conditions. It was every day a pleasure to go to work, and for this I thank all my collegues there. As they are (almost) all french, below I thank particularly some of them in Molière's language.

Je remercie tout d'abord :

Khaled pour son tajine de viande hachée irrésistible, sa tartiflette aussi bonne que celle de ma mère, ses cuisses de canard confites aux pommes campagnardes, ses gambas, ses fondants au chocolat, son lapin façon Morby, sa sauce au roquefort, sa sauce poivronade ... mais surtout pour sa gentillesse et sa faconde méditerranéenne. Et je ne dois pas oublier son aide précieuse pour l'organisation du buffet et de la soirée qui ont suivi la soutenance.

Je remercie aussi :

Alejandra pour ses cours de spagnol, quelques courses à pied autour de l'obs, son faible appétit, sa gentillesse, son rire et son sourire,

Patrick pour ses leçons de squash, sa grande motivation rugbystique, son sens de l'hospitalité généreux, son don à mettre une bonne ambiance et son accent sètois,

Fabrice pour son noble esprit rugby, son attention pour les autres et sa gentillesse, quelques matches de ping-pong et plusieurs bonnes soirées ; je remercie également sa copine **Chloé** pour avoir corrigé l'anglais de mon introduction, et tous les deux pour leur soutien pendant la rédaction de cette thèse,

Éric, très joueur avec un ballon, une guitare, ou les mots, pour la grosse ambiance qu'il mettait à l'obs et tous les matches de foot disputés ou vus ensemble,

Sébastien P. qui nous a aussi manqué après son exil en post-doc, pour son humour, sa sensibilité, et tous les matches de foot (ou de rugby) vus ou joués ensemble ; je tiens à l'écrire ici : vive la pizza, et Issa Nissa !

Guilherme pour m'avoir fait découvrir la caïpirinha, quelques mots de portugais, et le talent Brésilien au foutchebol,

Julien pour nos nombreuses discussions au bureau sur l'actualité, le ski ou le poker, mais aussi sur la turbulence et la MHD, pour sa générosité, les soirées lessives chez lui, les parties de ping-pong, les sorties en montagne, à la mer, et le sympathique week-end à Florence entre co-bureaux,

Jean-Luc pour son bon goût et ses idées saines et pondérées, pour m'avoir fait découvrir pas moins de trois journaux très intéressants, et pour nos week-ends entre co-bureaux à Venise et Florence,

François, mon co-bureau le plus fidèle, pour avoir raccroché le téléphone de temps en temps, pour s'être toujours montré ouvert et sincère, pour nos week-ends co-bureaux à Venise et Florence, et notre voyage en Libye,

Nicolas N. pour son fidèle esprit d'équipe au foot comme au rugby, et nos expéditions ensemble en Libye et à la Tournette, avec sa copine **Magali** ; bis bald in Deutschland,

Caroline pour le bon temps passé ensemble, dont d'agréables week-ends à Gênes et Rome,

Nicolas B. pour son enthousiasme à défendre nos couleurs au foot comme au rugby, son sens de l'humour, et pour raccompagner Dominique tous les midis avec une voiture au toit transparent,

Dominique S. pour m'avoir offert un café du CION, pour ses élégantes casquettes, son soutien à l'équipe de rugby, et pour avoir guidé une visite de l'Observatoire à mes proches venus à ma soutenance,

Menios for his efforts to speak french, our intersting discussions and his hospitality in Thessaloniki after this thesis,

Charline pour avoir introduit un peu de hauteur, de finesse, et de charme dans la "Pacheco team",

Julie pour sa serviabilité, l'organisation d'une sortie aux îles de Lérins et d'une journée via ferrata qui avait l'air super, conclue par une bonne soirée chez **Étienne**, que je remercie aussi pour les sorties escalades et sa participation méritante à notre équipe de rugby,

Bénédicte pour avoir créé ma culture cinématographique (via son ciné-club qui contribuait à la bonne ambiance de l'observatoire) et enrichi ma culture en bandes-dessinées grâce à des échanges fructueux, pour s'être battue avec énergie et panache contre les projets "disciplinaires", et pour de nombreuses discussions intéressantes,

Fabien, autre joueur de foot sympathique, qui soutenait quand j'écrivais ces lignes : bon courage !

Gilbert pour nos discussions sur d'amusants problèmes de physique, à base de skis paraboliques et de pentes enneigées principalement,

Matias pour sa simplicité et son intérêt pour mes travaux,

Izan pour son goût de la fête,

Matthieu pour m'avoir permis de bonnes soirées d'observation à la Schaumasse et en Libye,

Claire pour sa bonne humeur et son "manuel de la thèse en LaTeX" sans lequel ce manuscrit ne ressemblerait pas à ça,

Stéphane pour son humour joyeux et son soutien sans faille à notre équipe de rugby,

Karima, **Nora**, et **Michel,** l'équipe cuisine qui nous accueille au restaurant dans la bonne humeur et nous sert gentiment les plats qu'elle aide Khaled à préparer ; remerciements particuliers à Nora pour l'extraordinaire spectacle qu'elle nous a offert après cette soutenance,

Marc et **Gilles** qui revenaient régulièrement à l'obs., donnant lieu à des soirées pâtes dans une très bonne ambiance,

Chiara la bella pour son tiramisu et son agréable compagnie, à la SF2A de Strasbourg notamment,

Hervé pour son accueil à Rome, et les sorties escalade ou rando quand il revient à Nice,

Gérald pour quelques bonnes sorties en falaise ou à la neige,

Gary pour ne pas m'avoir tapé,

et **les autres membres des services techniques**, très ouverts et disponibles, toujours accueillants à leur table,

Sébastien F. pour sa bonne humeur permanente et communicative,

Jean-Michel pour ses précieuses compétences informatiques, sa motivation militante, sa disponibilité et son humour,

Serge pour son aide en informatique également, et le coaching d'une équipe de foot à 7 de l'O.C.A. lors d'un tournoi annuel,

Daniel, Pierre, Alain M. et Marie-Laure qui eux aussi font marcher toute l'informatique de l'observatoire, avec dévouement, efficacité et bonne humeur, de sorte qu'on ne peut que se féliciter de leur présence,

Jacques P. (dit **Shibani**), pour être parti à la retraite avant d'avoir transformé le restaurant en self, et pour nous avoir gratifiés de sa présence en Libye,

Rose et **Sébastien** pour leur accueil toujours aimable quand on vient les embêter avec des paperasses urgentes, qu'ils traitent avec efficacité et bonne humeur,

Djamel pour ses conseils et encouragements en semi-marathon ; bon courage au Dôme C !

Alain N. pour sa participation enthousiaste aux jeux de Sophia d'hiver, sa cordialité, son humour belge, et sa compagnie dans le désert,

Sophie pour sa participation brillante aux jeux de Sophia d'hiver, et à d'autres sorties ski (de rando),

Yannick pour sa participation professionnelle aux jeux de Sophia d'hiver, et ses avis critiques sur nos modèles de disques turbulents,

Mickaël L. et D. pour me distraire par e-mail,

Christian notre cher gardien, pour m'avoir délivré du C.I.O.N un soir,

Georges pour m'avoir laissé gagner au ping-pong et avoir failli faire planter mon PC au moment d'imprimer ma thèse avec **Raphaël**, ainsi que pour la visite guidée et l'accueil à Athènes après cette thèse, avec les découvertes inoubliables du Parthénon, du backgammon et des souvlakis,

Fathi, Tristan, Patrick M., Paolo, Marco, et toute l'équipe planétologie pour leur gentillesse et tout ce que j'ai appris avec eux.

Mais je voudrais aussi citer des copains astronomes non niçois, qu'il est toujours agréable de revoir lors de congrès ou d'écoles : **Sandrine** VINATIER, **Lydie** BONAL, **Jérémie** BOISSIER, **Clément** BARUTEAU, **Anne-Sophie** LIBERT, **Éric** TATULLI, **Olivier** MOUSIS, **Sébastien** CHARNOZ (encore un Libyen), **Shan** MIGNOT, **Vincent** PIÉTU, **Anne** DUTREY, **Stéphane** GUILLOTEAU, **Franck** SELSIS, **Jean-François** GONZALEZ...

Et aussi des copains niçois non astronomes, qui ont rendu mon séjour dans les Alpes-Maritimes plus agréable : **Olivier** et **Fanny**, **Elsa** et **Olivier**, les partenaires du foot du dimanche (**Seb**, **Greg**, **Vinci**, **RV**, **Guiguinho**...), les fondateurs de **BD-Fugue Nice**...

et bien sûr les tatas flingueuses **Martine** et **Brigitte**, ainsi que **Bénédict**, avec lesquels il est toujours agréable de randonner ou discuter. Merci Martine, toi qui m'as initié à l'astronomie (et à la physique en général d'ailleurs) quand j'avais 6 ans, et avec qui j'ai vu pour la première fois les anneaux de Saturne, de m'avoir régulièrement invité à de bonnes bouffes et de bonnes discussions au cours de cette thèse.

Je n'oublie pas non plus les copains non niçois non astronomes : **Maddy**, qui m'a appris les nombres complexes en randonnée dans la Chartreuse, l'intégration de fonctions au ski...
Et les copains du **C**lub de **T**ennis de **T**able de **P**oisy, qui m'ont toujours accueilli à bras ouverts quand je rentrais au pays pour (tenter de) leur donner un coup de main lors des matches du samedi après-midi. Il y a eu pas mal de bons moments ces trois dernières années avec **Manu**, **Bébert**, **Denis**, **Christophe**, **Helder**, **Lucile**...

La thèse étant un diplôme sanctionnant la fin des études, je voudrais aussi profiter de l'occasion pour remercier mes anciens professeurs, sans qui je n'en serais pas là, en particulier tous ceux du D.E.A. de l'Observatoire de Paris : citons Messieurs **Brahic**, **Laskar**, **Robutel**, **Sicardy**, **Exertier**, **Mamon**, et surtout Mme **Gomez**. Et je voudrais aussi remercier pour leur enseignement Messieurs **Leccia**, **Sauvadet**, **Ganaye**, **Lerasles**, et Mesdames **Ory**, **Perrin**, **Lenzi**.

Comme j'ai eu la chance au cours de cette thèse de passer de l'autre côté de la barrière en donnant des colles au lycée Massenna (merci à **Marc Becker** de me l'avoir permis) puis dans le cadre d'un monitorat à l'Université de Nice Sophia Antipolis (merci à **Marc-Antoine Coppo** avec qui il était simple de travailler), je voudrais aussi remercier **tous mes élèves** avec qui j'ai pris beaucoup de plaisir.

Enfin, je voudrais remercier ma famille et mes amis (les autres), d'abord pour leur compagnie tout au long de ma vie, et aussi pour leur enthousiasme à suivre mes travaux et à venir assister à ma soutenance. C'était un moment important pour moi, la réalisation d'un rêve d'enfance et la fin de mes longues études, et ça m'a touché que vous soyiez présents. **Stéphane**, **Delphine**, **Julien L.**, **Julien D.**, **Olivia**, **Benoît**, **Myriam**, j'ai regretté votre absence mais pensé à vous.

Francesco, bonne chance pour la fin de ta thèse à toi, et à bientôt sur des skis ou devant un abalone,

Charlène, j'espère t'avoir montré que faire une thèse en astro, c'est possible et c'est chouette, et je te souhaite une belle carrière de physicienne,

Guillaume, tu en es convaincu, je te souhaite bonne chance pour la fin de ta propre thèse (et pour la suite), et à bientôt en montagne, ou en conférence,

Marion, Viva Barcelona, et bonne continuation également dans tes études, et dans ta vie,

Nicolle, Roger, merci pour votre toujours bon accueil à la Couloutte, et ça m'a fait plaisir d'avoir un ancien de l'Aspique dans l'assistance,

Joëlle, c'est super que tu ais pu venir représenter la famille **Ferney**, grande amatrice de ski et de toc, de Jeanlain et de saucisson,

ma Mémé Éliane, concurrente de Khaled, qui n'avait pas prévenu qu'elle viendrait voir son petit-fils, puis faire la bringue avec nous,

ma sœur Ameline, qui depuis qu'on est petits a tendance à faire les mêmes études que moi, deux ans après, en mieux ; maintenant que nos chemins vont diverger, je te souhaite au plus vite un chouette poste près de nos montagnes (les plus belles),

mes parents Alain et Annie, pour avoir toujours encouragé et stimulé ma curiosité et ma soif d'apprendre enfantines, puis m'avoir offert ma lunette astronomique et avoir supporté de m'emmener observer dans les froides nuits d'hiver au sommet de montagnes enneigées, et m'avoir offert des conditions d'études et d'épanouissement optimales,

ma chère Lauriane, qui subissait la prépa pendant que je me faisais plaisir sur la Côte, pour tout : ta bonne humeur, tes multiples talents sportifs (foot, ping, ski, tennis), les vacances à Barcelone, l'Ancilevienne... À ton tour de t'éclater en étudiant !

Appendix D

Introduction en français

D.1 Le Système Solaire

D.1.1 Antiquité

Les 5 planètes du Système Solaire visibles à l'œil nu (Mercure, Vénus, Mars, Jupiter et Saturne) ont été identifiées très tôt dans l'histoire de l'humanité. Le nom "planète" vient du grec ancien pour "astre errant". Les grecs ont étudié leur mouvement dans le ciel et ont remarqué qu'elles se déplacent approximativement dans un plan contenant la Terre et le Soleil : l'écliptique. C'est la première notion du Système Solaire.

Aristarque de Samos (~ -310, figure D.1), avait trouvé que les planètes, Terre comprise, orbitent dans ce plan autour du Soleil grâce à un raisonnement astucieux. Il avait remarqué que la Lune se déplace par rapport au fond du ciel d'un diamètre de Lune en une heure. Comme les éclipses de Lune durent au plus trois heures, il conclut que le cylindre d'ombre de la Terre était trois fois plus large que la Lune et donc que la Lune était 3 fois plus petite que la Terre (en fait, la Lune est 4 fois plus petite que la Terre car l'ombre de la Terre n'est pas un cylindre mais un cône). À partir de considérations géométriques sur les phases de la Lune, il trouva que le Soleil était environ 20 fois plus loin de la Terre que la Lune (la valeur exacte est 390 fois plus loin). Comme le Soleil et la Lune ont le même diamètre apparent, le Soleil devait être 20 fois plus gros que la Lune, et donc bien plus gros que la Terre. Aristarque trouvait plus logique que les petits objets bougent autour du plus gros. Cependant, aucune parallaxe n'est observée parmi les étoiles, ce qui devrait être le cas si la Terre se déplace. Aristarque supposa que les étoiles étaient infiniment loin. C'est à peu près vrai : les étoiles ont un mouvement apparent dû à la parallaxe, mais elles sont trop loin pour que ce mouvement soit discernable à l'œil nu ; l'étoile la plus proche est environ 250 000 fois plus loin du Soleil que la Terre, de sorte que son déplacement apparent par rapport aux autres étoiles est inférieur à une seconde d'arc en un an.

Toutefois, l'explication la plus intuitive à l'absence de parallaxe était que la Terre est immobile. Le modèle géocentrique de Ptolémée (deuxième siècle de notre ère, voir figure D.1) était constitué d'orbites circulaires coplanaires centrées sur la Terre pour les 5 planètes, la Lune, et le Soleil. Cependant, le mouvement des planètes dans le ciel ne peut s'expliquer ainsi : elles ont périodiquement un mouvement apparent rétrograde. Ptolémée l'expliqua au moyen d'épicycles : dans son modèle, une planète décrit un cercle autour d'un point qui décrit lui-même un cercle autour de la Terre. Le premier cercle est appelé un *épicycle*, et le second un *déférent*. L'utilisation d'épicycles permet de raffiner le mouvement des planètes, et le système de Ptolémée fournissait des éphémérides fiables. De plus, ce modèle recevait des appuis théologiques. Dans la conception

Figure D.1: À gauche : Aristarque de Samos ; Statue à l'Université Aristoteles à Thessalonique. Panneau de droite : Le système de Ptolémée ; la Terre est au centre de l'univers.

Aristotélicienne du monde, tout est parfait dans les cieux, de sorte que seuls des cercles peuvent être employés pour décrire le mouvement des astres. Dans la religion chrétienne, Dieu créa la Terre et l'Homme sur la Terre, donc ils devaient se trouver au centre de l'Univers. Pour ces raisons, le système de Ptolémée devint la théorie officielle dans les civilisations occidentale et arabe pour plus de 13 siècles.

D.1.2 Les temps modernes

Copernic a été le premier en Europe à suggérer que la Terre n'était pas le centre de l'univers et que les planètes (Terre comprise) orbitaient autour du Soleil (*De Revolutionibus Orbium Cœlestium*, 1543). Ceci s'imposa finalement comme une évidence (du moins, pour les scientifiques) dans les décennies suivantes ; en particulier, les observations remarquablement précises de Tycho Brahe (mort en 1601) montraient sans discussion possible que Mars suivait une ellipse (et non un cercle) dont le Soleil (et non la Terre) occupe l'un des foyers. Toutefois, l'astronome danois restait convaincu que la Terre était immobile car on n'observait pas de parallaxe parmi les étoiles[1]. Il a imaginé un modèle dans lequel les planètes tournent autour du Soleil, et le Soleil tourne autour de la Terre. En étudiant les observations de Tycho Brahe, Kepler (portrait de gauche dans la figure D.3) fut finalement convaincu par l'héliocentrisme. Il synthétisa son travail en ses fameuses trois lois en 1609 et 1618 :

Loi des orbites : L'orbite d'une planète est une ellipse dont le Soleil occupe un des foyers,

[1] La parallaxe des étoiles a enfin été observée en 1838 par Friedrich Wilhelm Bessel. Il fut le premier à utiliser cette technique pour déterminer la distance de l'étoile double 61 Cygni. La position de cette étoile dans le ciel varie de $0''31$ au cours d'une année, ce qui donne une distance de 10,5 années-lumières. Cela confirme définitivement que la Terre tourne autour du Soleil.

Figure D.2: *Copernic, Conversation avec Dieu.* Peinture de Jan Matejko, le plus grand peintre historique de Pologne (1872). On aperçoit le système héliocentrique derrière l'astronome.

Loi des aires : Une ligne joignant une planète et le Soleil balaye des aires égales au cours d'intervalles de temps égaux,

Troisième loi de Kepler : Le carré des périodes orbitales des planètes est proportionnel au cube du demi-grand axe de leurs orbites.

La théorie de l'héliocentrisme a montré que des faits scientifiques pouvaient contredire la Bible et les dogmes religieux, et qu'un raisonnement intelligent valait mieux que des intuitions et des *a priori*. Cela change la conception du monde. C'est la révolution Copernicienne, qui mène aux idées des Lumières. La science moderne se développa, avec pour but de trouver des lois universelles pour modéliser le fonctionnement du monde, telle la loi de la Gravitation exprimée par Newton en 1687. La structure du Système Solaire étant comprise, la question de son origine devint pertinente. Cette question fondamentale s'est posée d'un point de vue philosophique et scientifique et non plus religieux. Parmi de nombreuses théories proposées au cours du XVIII° siècle, le philosophe Kant en 1755 et le scientifique Laplace en 1796 suggérèrent indépendamment que le Système Solaire se serait formé à partir d'un disque froid de gaz et de poussière en rotation autour du Soleil dans le plan de l'écliptique. Cette hypothèse expliquait bien pourquoi toutes les planètes ont des orbites coplanaires et progrades. Les découvertes d'Uranus par Herschel en 1781, et de Neptune par Le Verrier, Adams, et Galle en 1846 sont cohérentes avec cette théorie puisqu'elles orbitent également quasiment dans le plan de l'écliptique et dans le sens prograde. Pluton, avec son inclinaison orbitale de 17° ferait dans ce cadre une planète étrange ; toutefois, ce n'est qu'un parmi les centaines d'objets connus de la ceinture de Kuiper, et il n'est pas une planète mais appartient à la catégorie des "planètes naines" depuis le congrès de l'U.A.I. à Prague en Août 2006.

L'hypothèse de Kant et Laplace pour la formation du Système Solaire est toujours le scénario le plus populaire chez les astronomes. Ce modèle a été confirmé par des observations et raffiné depuis plus de deux cent ans. Dans la section suivante, nous détaillons la formation des étoiles et des disques, et nous montrons comment les planètes se forment dans ces disques.

Figure D.3: Kepler, Kant, et Laplace.

D.2 Formation planétaire

D.2.1 Formation des étoiles

La formation stellaire se déroule dans des nébuleuses de gaz dans le milieu interstellaire. Un nuage de gaz de masse supérieure à une masse critique (la masse de Jeans, égale à quelques masses solaires ($M_\odot$) dans une nébuleuse) s'effondre sous l'effet de sa propre gravité. La nébuleuse initiale se fragmente ainsi en systèmes isolés. L'effondrement dure environ un million d'années. Au cœur du nuage, la pression et la température augmentent considérablement, de sorte que les premières réactions de fusion nucléaire s'allument. Cela donne une proto-étoile, qui émet principalement du rayonnement Infra-Rouge, appelée un objet de *classe 0*. Durant l'effondrement du nuage, la conservation du moment cinétique freine la contraction dans le plan perpendiculaire à l'axe de rotation du nuage, tandis que rien ne l'empêche dans la direction "verticale". Le résultat est la formation autour de la proto-étoile d'un tore en environ dix mille ans. Ces jeunes objets, sources de rayonnement Infra-Rouge, sont appelés des objets de *classe I*. En une centaine de milliers d'années, le tore s'aplatit pour former un disque : son épaisseur H est de quelques pourcents de la distance à l'étoile centrale r. Le *rapport d'aspect* H/r est entre $0,03$ et $0,1$.

Environ un million d'années après sa naissance, la jeune étoile, désormais appelée une étoile T-Tauri Classique (CTTS), est entourée par le disque. Ce dernier émet en Infra-Rouge. La Densité Spectrale d'Énergie[2] (SED) d'un tel objet est celle d'une étoile classique avec un fort excès Infra-Rouge. On le dénomme objet de *classe II*.

En une dizaine de millions d'années, le disque se dissipe. Des objets avec un faible excès Infra-Rouge sont appelés objet de *classe III*, ou étoiles T-Tauri Évoluées ou Faibles (WTTS).

Cette chronologie provient d'observations des densités spectrales d'énergie de très jeunes étoiles. Elles ont été classées en fonction de l'excès Infra-Rouge. Récemment, des disques ont été observés par le télescope spatial (voir figure D.4). Ces observations confirment que les systèmes planétaires se forment dans des disques. Cela impose une contrainte forte sur le processus de formation stellaire : il doit se dérouler en moins de dix millions d'années, avant que le disque ne disparaisse. Ces disques de gaz et de poussière autour de jeunes étoiles, dans lesquels a lieu la formation planétaire, sont appelés *disques protoplanétaires*.

[2]La Densité Spectrale d'Energie est la répartition du flux rayonné par l'étoile en fonction de la longueur d'onde du rayonnement ; par exemple, celle du Soleil présente un maximum dans le jaune.

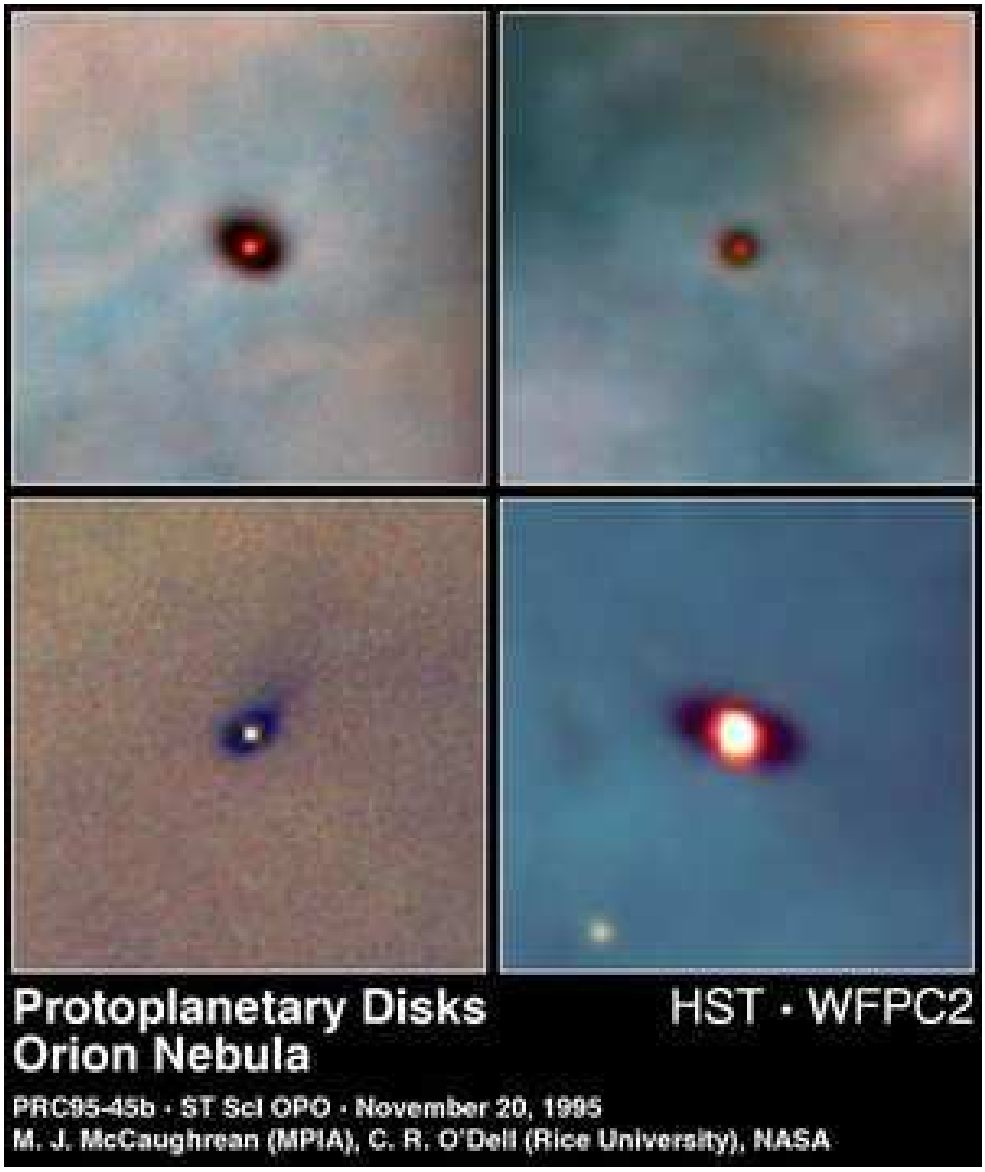

Figure D.4: Disques protoplanétaires dans la nébuleuse d'Orion, imagés par le télescope spatial Hubble de la NASA. La jeune étoile brille au centre, tandis que le disque apparaît sombre en lumière visible.

D.2.2 Formation des planètes

Focalisons-nous sur le disque protoplanétaire. Si la masse du disque M_{disque} est du même ordre que la masse de l'étoile centrale (notée M_*) ou plus grande, des instabilités se développent, qui conduisent à une rapide accrétion du disque sur l'étoile centrale. Le critère de stabilité de Toomre s'écrit $Q = \Omega c_s/\pi G\Sigma > 1$, où c_s est la vitesse du son, Ω la vitesse angulaire, G la constante de gravité, et Σ la densité surfacique du disque. Avec les trois hypothèses $c_s = H\Omega$ (structure de disque classique), Σ constante, et Ω défini par Eq. (D.1) ci-dessous, le paramètre de Toomre se simplifie en $Q = (H/r)(M_*/M_{\text{disque}})$. La condition de stabilité est alors $M_{\text{disque}}/M_* < (H/r)$. Comme H/r est typiquement quelques pourcents, un disque massif est instable et s'effondre rapidement, jusqu'à ce que sa masse soit petite par rapport à celle de l'étoile centrale. Par conséquent, nous ne considérons que des disques de masse inférieure à un dixième de M_*. Dans ces disques, la dynamique du gaz est dominée par la gravité de l'étoile et est à peu près Keplerienne, avec une vitesse angulaire donnée par la troisième loi de Kepler :

$$\Omega = \sqrt{\frac{GM_*}{r^3}} \,. \tag{D.1}$$

À partir de la masse totale du disque et de sa loi de rotation, son moment cinétique total peut être calculé :

$$J = \int_0^{R_{\text{disque}}} \Sigma r^2 \Omega \, 2\pi r \mathrm{d}r = 3 M_{\text{disque}} R_{\text{disque}}^2 \sqrt{GM_*} \,.$$

Comme le nuage est un système isolé, son moment cinétique se conserve au cours de l'effondrement. Une estimation du moment cinétique typique d'un nuage et de la masse d'un disque permet donc d'estimer que la taille du disque R_{disque} est d'environ 500 Unités Astronomiques (UA). Rappelons que l'Unité Astronomique est le rayon de l'orbite de la Terre autour du Soleil, soit 150 000 000 kilomètres.

Ce disque est composé essentiellement d'Hydrogène et d'Hélium, mais aussi d'éléments lourds (carbone, azote, oxygène, néon, magnésium, silicium, souffre, fer ...), qui représentent environ un pourcent de la masse totale pour des étoiles de composition solaire. La formation des planètes à partir de ces éléments lourds se décompose en 5 phases, illustrées par la figure D.5 :

(a) Formation du disque.

(b) Sédimentation : les grains s'accumulent dans le plan équatorial du disque..

(c) Coagulation des premiers solides : croissance de *planétésimaux* (corps kilométriques).

(d) Formation d'embryons (corps de la taille de la Lune) par un processus appelé *runaway growth* : croissance exponentielle emballée.

(e) Formation du système planétaire, et disparition du gaz.

Le passage des grains moléculaires aux planétésimaux n'est pas complètement compris et nous ne détaillerons pas ce point. Après leur formation par croissance exponentielle, les embryons se rencontrent et fusionnent. Ils forment des cœurs planétaires et des planètes telluriques sur des orbites suffisamment séparées pour que le système soit stable (Kokubo and Ida, 2000).

Certains de ces cœurs planétaires peuvent être suffisamment massifs (environ 10 masses terrestres ($M_\oplus$)) pour accreter une atmosphère gazeuse, et devenir une planète géante gazeuse comme Jupiter et Saturne. Le modèle de Pollack et al. (1996) pour la formation des planètes

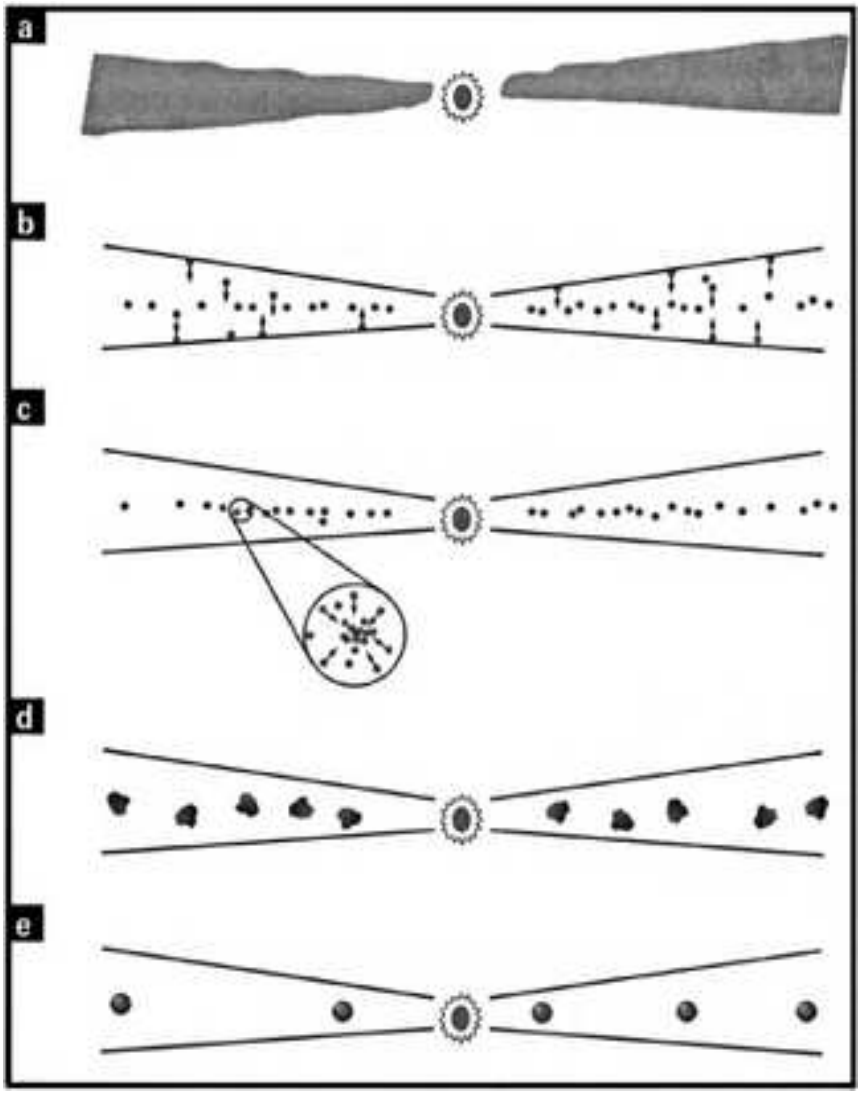

Figure D.5: Schéma des cinq étapes de la formation planétaire dans un disque protoplanétaire. Dessin de Sébastien Charnoz.

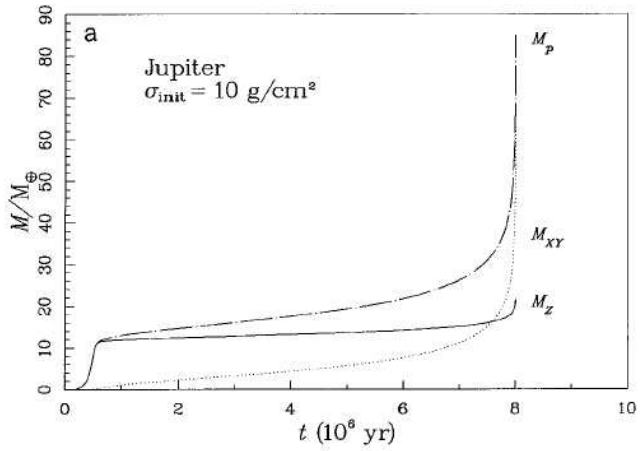

Figure D.6: Formation d'une planète géante gazeuse selon le modèle d'accrétion de cœur (figure issue de Pollack et al., 1996). La masse de la planète est tracée en fonction du temps (en millions d'années) en la ligne pointillée supérieure marquée M_p ; la ligne continue M_Z correspond à la masse de solides, tandis que la ligne pointillée M_{XY} représente la masse de gaz. Après la rapide formation d'un cœur solide de $12 M_\oplus$ (phase (i)), la lente accrétion de gaz commence (phase (ii)). Finalement, quand la planète atteint $20 - 30\, M_\oplus$, une accrétion emballée a lieu (phase (iii)).

géantes se déroule en trois phases : (i) formation d'un cœur massif (environ cent mille ans), (ii) lente accrétion de gaz par le cœur (plusieurs millions d'années), (iii) accrétion exponentielle et effondrement (environ cent mille ans) (voir figure D.6). Un autre modèle par Boss (1997, 2000) propose que les planètes géantes se forment par instabilité gravitationnelle dans le disque proto-planétaire, ce qui a l'avantage de former une planète sur un temps très court, sans la (trop) lente deuxième phase du modèle d'accrétion de cœur ; cependant, ce modèle explique difficilement les masses, obliquités, et compositions des planètes géantes. Au contraire, le modèle d'accrétion de cœur est renforcé par la présence d'un cœur dense de 10 à 25 $M_\oplus$ dans Saturne et d'un cœur solide de 10 à $15\, M_\oplus$ dans Uranus et Neptune. Le cas de Jupiter est plus complexe, car il pourrait avoir un petit cœur de moins de $10\, M_\oplus$, ou pas, mais son cœur pourrait avoir été érodé par l'enveloppe (Guillot, 2005). En parallèle, Alibert et al. (2005, deux articles) proposent un modèle d'accrétion dans lequel le temps de formation est réduit (ce qui le rend en accord avec les durées de vie typiques de disques observés) et la composition chimique globale de Jupiter et Saturne est reproduite aux incertitudes près.

La formation d'un cœur massif nécessite une grande quantité de solides. Elle est donc favorisée si l'eau, qui est une molécule abondante, se trouve sous la forme de glace plutôt que de vapeur. Or, la température dans le disque est une fonction décroissante de la distance à l'étoile centrale, de sorte qu'il existe un rayon au delà duquel l'eau condense et devant lequel elle se sublime. Cette limite est appelée la *ligne des glaces* (*snowline* en anglais). Autour d'une étoile comme le Soleil, cette ligne des glaces se situe à environ 3–5 UA. Ceci implique qu'il est plus facile de former une planète géante juste derrière la ligne des glaces que près de l'étoile centrale. Cela est en accord avec la structure du système solaire. Une autre conséquence est que les planétésimaux formés au delà de la ligne des glaces sont riches en glace, tandis que ceux formés plus près du Soleil sont pauvres en glace. Cela correspond à la différence entre une comète et un astéroïde, là encore en accord avec la structure du système solaire.

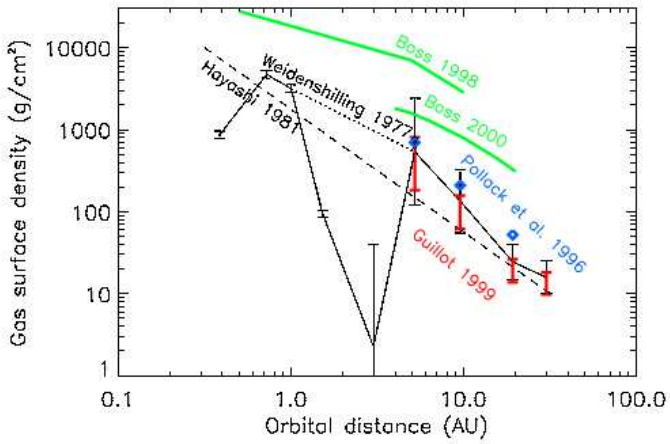

Figure D.7: Le profil de densité de la Nébuleuse Solaire de Masse Minimale (ligne tiretée légendée "Hayashi 1981"), en échelle logarithmique. Les points représentent les contraintes données par les masses des planètes. Pour comparaison, la densité requise pour la formation des planètes par instabilité gravitationnelle est représentée par les deux courbes légendées "Boss".

D.2.3 Formation du système solaire

À partir des masses et des positions des planètes, Hayashi (1981) a proposé le concept d'une Nébuleuse Solaire de Masse Minimale (MMSN en anglais). La matière constitutive des planètes est étalée sur un anneau entre les orbites des deux planètes adjacentes, et complétée d'autres éléments pour reproduire la composition solaire. Cela donne un disque protoplanétaire, dont la densité est proportionnelle à $r^{-3/2}$ et qui a la même composition que le Soleil. La figure D.7 montre le profil de densité de la MMSN (ligne pointillée). Les points avec les barres d'erreurs correspondent aux densités requises pour former chaque planète du système solaire (estimées par différents auteurs). Notons que dans la MMSN, on suppose que les planètes se sont formées là où elles orbitent actuellement.

Cette théorie était très satisfaisante. Elle est résumée symboliquement par le petit strip de la figure D.8. Tous les mécanismes invoqués sont assez généraux pour que l'on s'attende à découvrir d'autres systèmes planétaires semblables au nôtre autour d'autres étoiles.

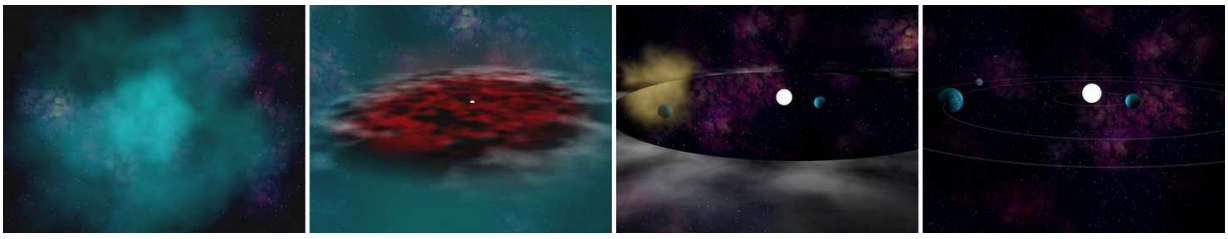

Figure D.8: Résumé graphique de la formation planétaire. De gauche à droite : un nuage moléculaire, qui s'effondre en une proto-étoile entourée d'un disque, dans lequel se forment des planètes, avant que le disque ne se dissipe.

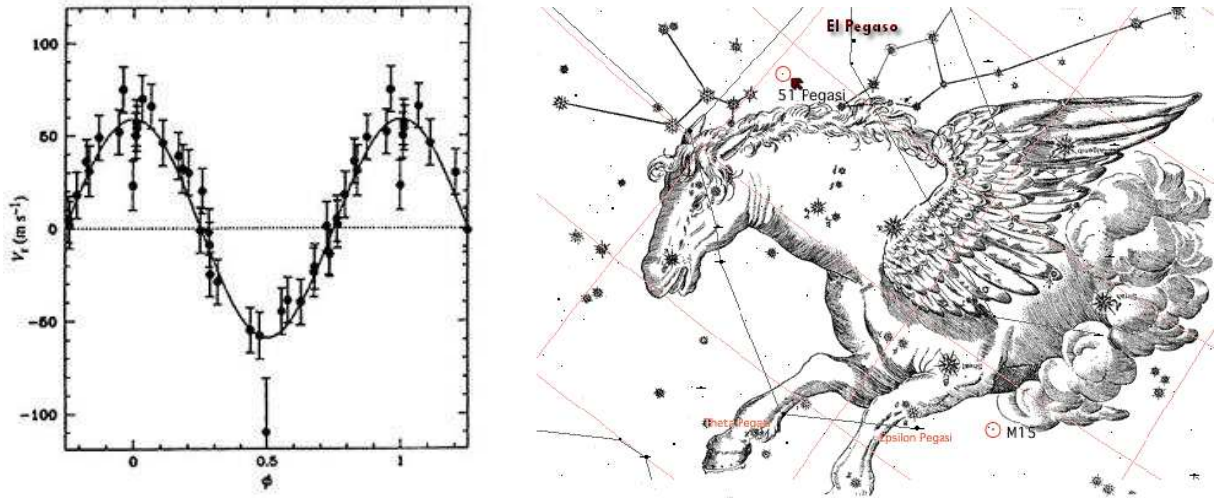

Figure D.9: Panneau de gauche : Les variations de vitesse radiale de l'étoile 51 Pegasi en mètres par seconde, en fonction du temps en orbites planétaires.
Panneau de droite : Position de 51 Pegasi dans le ciel, dans la constellation de Pégase.

D.2.4 Surprenantes exoplanètes

En 1995, la première planète située autour d'une autre étoile que le Soleil (*exoplanète*) a été détectée par Michel Mayor et Didier Queloz à l'Observatoire de Haute-Provence autour de l'étoile 51 Pegasi. Cette détection a été réalisée en utilisant la technique des vitesses radiales. Cela consiste en l'étude des variations de la vitesse de l'étoile projetée sur la ligne de visée (vitesse radiale, qui peut être déterminée par effet Doppler). Si l'étoile a un compagnon planétaire, la planète et l'étoile tournent autour du centre de gravité du système. Ainsi, la planète fait se rapprocher et s'éloigner l'étoile de l'observateur. Les variations de la vitesse radiale de 51 Pegasi sont montrées sur la figure D.9 en fonction du temps en unité normalisée ; il y a indéniablement une oscillation de période 1 dans ce diagramme, trahissant la présence d'une planète en orbite autour de l'étoile avec la même période. Étant données la masse de l'étoile (estimée à partir de sa luminosité et couleur), la période orbitale donne le rayon de l'orbite (troisième loi de Kepler). L'amplitude du mouvement de l'étoile donne la masse de la planète – ou plus exactement, sa masse multipliée par le sinus de l'inclinaison du plan orbital par rapport à la ligne de visée.

La première planète découverte en dehors du système solaire a une masse d'environ la moitié de Jupiter (à peu près 5/3 de Saturne) : c'est une planète géante (gazeuse?). Sa période orbitale est de 4,23 jours, donc le rayon de son orbite est de seulement 0,056 UA, sept fois plus petit que celui de l'orbite de Mercure ! Cette découverte extrêmement surprenante a été comme un coup de tonnerre pour la plupart des astronomes. Depuis cette date, plus de 200 exoplanètes ont été découvertes. La plupart d'entre elles sont des *Jupiters chauds* : des planètes géantes orbitant très près de leur étoile. Quand une exoplanète transite devant son étoile (comme Vénus devant le Soleil le 8 juin 2004), la diminution de luminosité de l'étoile peut être détectée et quantifiée. C'est un autre moyen de détecter des exoplanètes, et cela donne le rayon de la planète qui transite. De plus, dans le cas d'une planète en transit, le plan de l'orbite contient la ligne de visée, de sorte que la masse exacte peut être mesurée avec la technique de la vitesse radiale. À partir de la masse et du rayon, la densité est aisément déterminée. Les treize exoplanètes en transit connues ont des densités faibles : inférieures à 1 pour neuf d'entre elles, moins de 1,5 pour les

quatre autres[3]. Ce sont donc des planètes géantes gazeuses ; on peut soupçonner que les autres ne sont pas différentes.

Finalement, le système solaire semble être une exception. Toutefois, il faut être bien conscient que les Jupiters chauds sont les planètes les plus faciles à détecter. En fait, les observations actuelles ne permettent pas la détection de planètes terrestres, ni celle de géantes à longue période. Il y a peut-être des analogues au système solaire autour d'autres étoiles qui n'ont pas encore été détectés. Quoiqu'il en soit, le système solaire n'est pas le modèle général des systèmes planétaires.

D'après la théorie présentée précédemment, les Jupiters chauds ne peuvent pas se former où ils orbitent actuellement. Il faut ajouter quelque chose. En fait, la théorie était prête bien avant la découverte de la première exoplanète (Lin and Papaloizou, 1979, 1986b; Goldreich and Tremaine, 1980). Les planètes se forment dans des disques protoplanétaires gazeux. Elles acquièrent leur masse finale alors qu'elles sont incluses dans ce disque. Du coup, lors de la formation planétaire, il y a des interactions planète-disque. Via ces interactions, les planètes typiquement perdent du moment cinétique et migrent vers l'intérieur. Bien que des modèles pour la formation locale des Jupiters chauds ont été développés (Bodenheimer et al., 2000), la migration radiale est généralement l'explication de leur existence la plus acceptée : ils se sont formés au delà de la ligne des glaces dans le disque, puis ont migré vers leur orbite actuelle. Dans la prochaine section, nous présentons les différents mécanismes de migration.

D.3 Interactions planète-disque.

Dans cette section, la nature des interactions planète-disque et la théorie de la migration planétaire sont présentées à un niveau purement descriptif. Plus de détails sont fournis dans le Chapitre 2.

Dans le référentiel centré sur l'étoile centrale, avec les axes pointant sur des étoiles distantes fixes, la planète et les éléments du disque tournent autour de l'étoile, avec une vitesse angulaire Ω définie par la troisième loi de Kepler (Eq. (D.1)). Ce référentiel est appelé le *référentiel héliocentrique*. Considérons un repère direct orthonormé centré sur l'étoile, avec l'axe des x toujours pointé sur la planète et l'axe des z dans la direction du vecteur moment cinétique de la planète. Ce repère tourne autour de l'étoile à la même vitesse que la planète dans le référentiel héliocentrique. Il est appelé le *repère tournant*. Dans le repère tournant, la planète est immobile ; la vitesse angulaire d'un élément du disque devient : $\Omega - \Omega_p$, où l'indice p rapporte à la planète. Dans ce repère, une période correspond au laps de temps entre deux conjonctions avec la planète : cela s'appelle une période *synodique*. Une période synodique est égale à $2\pi/|\Omega - \Omega_p|$. Remarquons que les éléments du disque sur des orbites plus grandes que celle de la planète ont une vitesse angulaire dans le repère héliocentrique Ω plus petite que celle de la planète Ω_p ; par conséquent, ils ont une vitesse angulaire négative dans le repère tournant : ils semblent orbiter à l'envers. C'est la raison pour laquelle on a employé le symbole de valeur absolue dans l'expression de la période synodique.

Échanges de moment cinétique

La planète perturbe le mouvement des éléments de fluide. À la conjonction, un élément de fluide est dévié par la gravité de la planète. Cela le fait osciller autour de son orbite circulaire non-perturbée. Les interférences de ces oscillations forment un sillage spirale à un bras, apparent sur

[3]Pour comparaison, la densité de Jupiter est 1,4 , celle de Saturne 0,7 , et celle de la Terre est 5,5 .

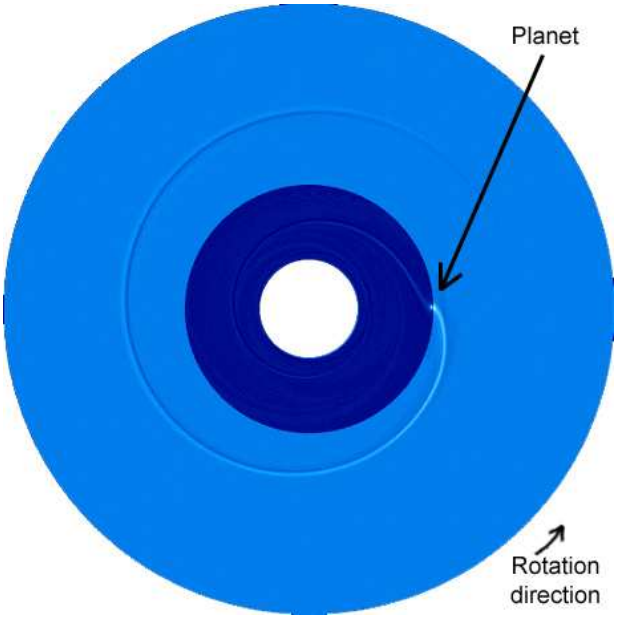

Figure D.10: Une planète sur une orbite circulaire lance un sillage dans le disque de gaz. Le bleu clair correspond aux surdensités. Le disque interne a été artificiellement assombri pour distinction avec le disque externe.

la figure D.10. Ce sillage est fixe dans le repère tournant. Il est dirigé vers l'arrière dans le disque externe, et vers l'avant dans le disque interne. La surdensité du sillage et la planète s'attirent gravitationnellement. Ainsi, la planète exerce une force sur le disque externe dans la direction de la rotation, ce qui donne un couple positif. Cela tend à accélérer le disque externe dans le repère héliocentrique et à le repousser loin de l'étoile ; réciproquement, cela ralentit la planète dans le repère héliocentrique, et la repousse vers l'étoile. Symétriquement, la planète exerce un couple négatif sur le disque interne qui tend à le ralentir et le pousser vers l'étoile ; et réciproquement, le disque interne exerce un couple positif sur la planète et la repousse loin de l'étoile. Tous ces échanges de moment cinétique sont symbolisés ci-dessous :

$$\text{Disque interne} \xrightarrow[\text{m.c.}]{} \text{Planète} \xrightarrow[\text{m.c.}]{} \text{Disque externe} .$$

Les couples sont proportionnels à la masse de la planète et à l'amplitude du sillage car ils proviennent de leur attraction gravitationnelle mutuelle. L'amplitude du sillage est proportionnelle à la masse de la planète car il est créé par le champ de gravité de la planète. Finalement, les couples sont donc proportionnels au carré de la masse de la planète.

Migration de type I

L'effet du disque externe sur la planète est toujours plus fort que celui du disque interne, par un facteur indépendant de la masse de la planète, pour des raisons développées en section 2.3. Par conséquent, le résultat pour la planète est un couple total négatif, proportionnel à sa masse au carré. Cela cause une baisse de son moment cinétique spécifique à une vitesse proportionnelle à sa masse M_p. Le moment cinétique spécifique est $j = r^2\Omega = \sqrt{GM_*/r}$. La dérivée de j par

rapport au temps est donc $(\mathrm{d}j/\mathrm{d}t) = \frac{1}{2}\sqrt{GM_*/r}(\mathrm{d}r/\mathrm{d}t) = \frac{1}{2}r\Omega(\mathrm{d}r/\mathrm{d}t)$. Comme j décroît à un taux proportionnel à M_p, il en est de même pour r_p. Ce régime est la *migration de type I.*

Ouverture d'un sillon

Les couples planétaires repoussent le disque externe vers l'extérieur, et le disque interne vers l'intérieur, c'est-à-dire loin de l'orbite de la planète. Cela tend à séparer les parties interne et externe du disque. Cependant, le gaz à tendance à s'étaler dans les régions vides, et les contraintes internes au disque tendent à aplatir le profil de densité. Ces deux effets s'opposent. Comme les couples planétaires sont proportionnels au carré de la masse de cette dernière, il semble logique que si la planète est assez massive, elle parvient effectivement à repousser le disque et ouvrir un sillon autour de son orbite. Dans les disques protoplanétaires, c'est le cas pour les planètes géantes. Les conditions d'ouverture d'un sillon seront étudiées dans la section 2.5 et le chapitre 4.

Migration de type II

Une planète qui orbite dans un sillon vide est coincée dedans. En effet, si la planète s'approche du disque externe, elle ressent un couple négatif plus fort de sa part, ce qui la repousse vers l'intérieur. Symétriquement, si la planète se déplace vers l'intérieur par rapport au sillon, elle ressent un couple positif plus fort de la part du disque interne, ce qui la repousse vers l'extérieur. Contrairement à la migration de type I, la planète ne peut donc pas bouger par rapport au disque. Nonobstant, un disque d'accrétion évolue sous l'effet de sa propre viscosité. Typiquement, le disque est accrèté par l'étoile centrale tandis que sa partie la plus externe s'étale vers l'extérieur, par conservation du moment cinétique (voir section 2.6.2). Verrouillée dans son sillon, la planète doit suivre cette évolution. Le plus souvent, la zone des planètes se trouve dans la partie du disque qui accrète vers l'étoile centrale (Lin and Papaloizou, 1986b). Cela conduit à une migration de la planète vers l'intérieur. Ici, la migration est contrôlée par l'évolution visqueuse du disque ; la vitesse de migration est donc proportionnelle à la viscosité (Ward, 1997). Ce régime est la *migration de type II.*

Migration de type III

Si la planète n'ouvre qu'un sillon partiel, le disque interne et le disque externe sont séparés par une ornière, un creux, qui n'est pas vide de gaz. Dans ce cas, la planète peut se déplacer par rapport au disque : si la planète migre vers l'intérieur par rapport à l'ornière, elle pénètre dans une région qui n'est pas dépletée. Pour maintenir le creux de densité, elle prend du gaz dans le disque interne et l'envoie vers l'extérieur à travers le sillon qui n'est pas étanche. Ce faisant, la planète donne du moment cinétique au gaz. Cela accélère sa perte de moment cinétique, c'est-à-dire sa migration vers l'intérieur. Sous certaines conditions, le processus s'emballe et mène à une accélération exponentielle de la migration (Masset and Papaloizou, 2003, et section 2.4.2). Ce régime emballé est appelé *migration de type III.*

La migration de type III peut être dirigée aussi bien vers l'intérieur que vers l'extérieur, selon les conditions initiales. La migration ne peut toutefois pas être infiniment rapide et cela s'arrête à un certain point. Toutefois, ce type de migration peut complètement changer le rayon de l'orbite d'une planète en quelques orbites.

Migration stochastique

Enfin, dans les disques turbulents où la densité a de grandes fluctuations, le couple senti par la planète fluctue aussi. Le résultat pour les planètes de faible masse qui n'ouvrent pas de sillon est une migration stochastique, en marche aléatoire. On pourrait penser que le couple stochastique ne fait que se superposer au couple classique. Dans ce cas, la marche aléatoire ne serait que du bruit sur la migration de type I classique. Pourtant, cela ne semble pas être le cas dans les simulations numériques (Nelson, 2005) bien que la raison n'en soit pas très bien comprise. La migration de type I est-elle détruite et remplacée par la migration stochastique dans les disques turbulents ? Cela reste une question ouverte. Toutefois, dans ce travail, nous ne considérons que des disques laminaires dans lesquels le flot n'est pas turbulent. C'est pourquoi nous ne nous intéresserons pas ici à ce régime.

D.4 Problématique et plan de la thèse

Les interactions planète-disque mentionnées ci-dessus montrent que les planètes ne se forment pas nécessairement sur leur orbite finale. En fait, elles migrent très probablement durant leur croissance jusqu'à ce que le disque se dissipe. Dans cette section, nous traitons de l'influence de la théorie de la migration planétaire sur la formation des planètes, et du système solaire en particulier.

D.4.1 Migration et formation planétaire, problèmes généraux

En migration de type I, plus la planète est massive, plus elle migre vite. L'échelle de temps pour la migration jusqu'à l'étoile centrale est plus courte que le temps de vie du disque pour des planètes plus massives que Mars (voir chapitre 2 pour les calculs détaillés). C'est un gros problème pour la théorie de formation planétaire. S'il est possible que les planètes telluriques se forment après la dissipation du gaz, les cœurs de planètes géantes doivent être apparus en présence d'un disque massif, puisqu'ils ont accrété une massive atmosphère d'hydrogène. La phase (ii) du modèle d'accrétion de cœur est particulièrement critique : dans cette phase, l'embryon de planète géante a une masse d'environ $20\,M_\oplus$ et accrète doucement une atmosphère gazeuse sur plusieurs millions d'années. Le cœur n'est pas assez massif pour ouvrir un sillon, mais suffisamment pour que la migration de type I le précipite sur l'étoile centrale en environ cent mille ans, donc bien avant qu'il n'accrète son atmosphère (figure D.6).

Cette théorie ne peut donc pas expliquer l'existence des planètes géantes gazeuses. Une solution possible à ce problème est discutée dans le chapitre 3, où nous présentons l'idée d'un *piège à planète* dans le disque. Nous montrons qu'un saut de densité sur une petite distance constitue une barrière efficace pour des embryons migrants. Capturés là, les embryons pourraient fusionner et accréter une atmosphère gazeuse sans souffrir de migration de type I.

Une fois son atmosphère massive accrétée, la planète ouvre un sillon dans le disque (ce qui détruit le piège). Le processus d'ouverture du sillon n'était pas très bien décrit dans la littérature, et la théorie communément admise (voir section 2.5) n'était pas cohérente avec les simulations numériques. Avec une nouvelle approche, nous avons trouvé un critère d'ouverture de sillon qui implique en même temps les trois paramètres du problème : la masse de la planète, le rapport d'aspect du disque, et la viscosité du gaz. Ce travail est l'objet du chapitre 4.

Si pour quelque raison (l'existence d'un piège à planète, ou un autre mécanisme présenté dans la littérature, ou encore à découvrir) un cœur massif évite la migration de type I jusqu'à ce

qu'il accrète une atmosphère massive et ouvre un sillon, il devrait être sujet à de la migration de type II. Ceci conduit la planète vers l'étoile en un temps de l'ordre de l'évolution du disque. Cela explique de manière assez satisfaisante la présence des Jupiter chauds. Mais c'est un nouveau gros problème pour la formation des planètes géantes 'normales', dont Jupiter, Saturne, et quelques exoplanètes récemment découvertes à des distances de l'ordre de 3-5 UAs de leur étoile. Comment ces planètes peuvent-elles éviter la migration de type II ? Cette question est l'objet des chapitres 6 et 7. Nous montrons que sous certaines conditions, les planètes géantes peuvent se découpler de l'évolution du disque. L'accrétion du gaz sur l'étoile centrale peut avoir lieu à travers l'orbite de la planète sans pour autant pousser sensiblement cette dernière vers l'intérieur.

Toutefois, avant que de chercher un moyen d'arrêter la migration de type II, il nous faut élaborer un outil performant pour des simulations numériques fiables de ce type de migration. Dans les codes hydrodynamiques classiques, seule une partie limitée du disque est considérée, pour d'évidentes raisons de temps de calcul. Ainsi, l'évolution globale du disque, qui détermine la migration de type II, ne peut pas être prise en compte. Pour résoudre ce problème, nous avons amélioré le schéma classique en entourant l'anneau étudié d'une grille simplifiée dans laquelle l'évolution du disque peut être calculée sur toute l'étendue du disque, pour un coût en temps de calcul négligeable. Cet algorithme est présenté dans le chapitre 5.

D.4.2 Structure du système solaire et contraintes

La structure complexe du système solaire impose de fortes contraintes sur l'éventuelle migration de Jupiter et Saturne. Les propriétés de la ceinture d'astéroïdes entre Mars et Jupiter, en particulier son partage assez fin en types taxonomiques montre que Jupiter n'a jamais orbité dans cette région. Sinon, la planète géante aurait dépleté la ceinture et mélangé les astéroïdes survivants beaucoup plus que ce que l'on observe. Une autre ceinture dans le système solaire, appelée la ceinture de Kuiper, se trouve autour de 40 UA du Soleil, au delà de l'orbite de Neptune. La ceinture de Kuiper a une structure encore plus riche que la ceinture principale d'astéroïdes ; en particulier, l'existence d'une population 'froide' exclut le passage d'une planète géante dans cette zone. Ainsi, les 4 planètes géantes, actuellement en orbite à 5,2 , 9,6 , 19 , et 30 UA, ont dû se former entre 4 et 35 UA. Il n'y a quasiment pas de marge pour de la migration de type II dans le système solaire.

Plus précisément, un récent modèle élaboré à Nice en 2004 et publié en 3 articles dans Nature (Tsiganis et al., 2005; Gomes et al., 2005; Morbidelli et al., 2005) impose des contraintes encore plus fortes. Ce modèle suppose une configuration initiale compacte du système solaire externe. Après la disparition du disque de gaz, les 4 géantes devraient s'être trouvées sur des orbites circulaires coplanaires de rayon approximativement 5,45 , 8,2 , 11-13, et 14-17 UAs. En particulier, Saturne devrait se trouver plus proche de Jupiter que leur résonance de moyen mouvement 2:1 mutuelle (où la période orbitale de Saturne est exactement le double de celle de Jupiter, et donc le rayon de son orbite est 1,6 fois celui de Jupiter). Un disque de planétésimaux devrait entourer ce système compact, à partir d'environ 1,5 UA de la planète la plus externe, jusqu'à ~ 35 UAs, pour une masse totale de $\sim 35 M_{\oplus}$. Dans ces conditions, les planétésimaux au bord interne de ce disque sont perturbés par Neptune et ont des rencontres proches avec les planètes qui les éjectent. En moyenne, cela fait migrer Neptune, Uranus et Saturne vers l'extérieur, et Jupiter vers l'intérieur. Ce processus est très lent, dominé par le taux d'échappement des planétésimaux du disque. Cette lente migration se déroule sur plusieurs centaines de millions d'années, jusqu'à ce que Jupiter et Saturne croisent leur résonance de moyen mouvement 2:1. Cette résonance excite l'excentricité des planètes, ce qui déstabilise tout le système des quatre planètes. Les

orbites deviennent chaotiques et commencent à s'approcher mutuellement. Uranus et Neptune sont éjectées vers l'extérieur sur des orbites très excentriques (e ∼0,3–0,4) qui pénètrent profondément dans le disque. Cela déstabilise tout le disque de planétésimaux et entraîne le Grand Bombardement Tardif (LHB en anglais). Il s'agit d'un événement cataclysmique caractérisé par un fort taux d'impact sur toutes les planètes, qui explique la formation des bassins lunaires ; il a eu lieu entre il y a 4 et 3,8 milliards d'années (soit à peu près 600 millions d'années après la formation des planètes). Les interactions avec les planétésimaux amortissent les excentricités des planètes, ce qui restabilise le système planétaire, tout en forçant une dernière migration. Les planètes rejoignent finalement leurs orbites actuelles quand l'essentiel du disque a été éliminé. Les simulations montrent que ce modèle explique, outre le LHB, l'architecture orbitale des planètes géantes du système solaire, en particulier leurs excentricités et espacement.

Si ce modèle est vrai, il est clair que lors de leur formation à l'intérieur du disque, Jupiter, Saturne, Uranus, et Neptune ont à peine migré. De plus, Jupiter et Saturne orbitaient probablement à l'intérieur de leur résonance 2:1 sur des orbites circulaires après la disparition du disque. Dans le chapitre 7, nous étudions en détail un mécanisme, présenté pour la première fois par Masset & Snellgrove (2001), qui permet d'arrêter ou renverser la migration de type II de deux planètes pourvu qu'elles soient assez proches et que la plus externe soit la plus légère. En particulier dans le cas de Jupiter et Saturne, nous obtenons une solution stationnaire pour des paramètres raisonnables du disque, avec Saturne à l'intérieur de la résonance de moyen mouvement 2:1 avec Jupiter.

Enfin, en conclusion de cette thèse, nous discutons un scénario de formation du système solaire externe qui semble cohérent du point de vue de la dynamique, à la lumière de ce que nous avons vu.

Bibliography

Alexander, R. D., Clarke, C. J., Pringle, J. E., 2006. *Photoevaporation of protoplanetary discs - II. Evolutionary models and observable properties.* MNRAS 369, 229–239.

Alibert, Y., Mordasini, C., Benz, W., Winisdoerffer, C., 2005. *Models of giant planet formation with migration and disc evolution.* A&A 434, 343–353.

Alibert, Y., Mordasini, C., Mousis, O., Benz, W., 2005. *Formation of Giant Planets An Attempt in Matching Observational Constraints.* Space Science Reviews 116, 77–95.

Balbus, S. A., Hawley, J. F., 1991. *A powerful local shear instability in weakly magnetized disks. I - Linear analysis. II - Nonlinear evolution.* ApJ 376, 214–233.

Bate, M. R., Lubow, S. H., Ogilvie, G. I., Miller, K. A., 2003. *Three-dimensional calculations of high- and low-mass planets embedded in protoplanetary discs.* MNRAS 341, 213–229.

Beckwith, S. V. W., 1999. *Circumstellar Disks.* In: Lada, C. J., Kylafis, N. D. (Eds.), NATO ASIC Proc. 540: The Origin of Stars and Planetary Systems, pp. 579—+.

Bergin, E., Calvet, N., Sitko, M. L., Abgrall, H., D'Alessio, P., Herczeg, G. J., Roueff, E., Qi, C., Lynch, D. K., Russell, R. W., Brafford, S. M., Perry, R. B., 2004. *A New Probe of the Planet-forming Region in T Tauri Disks.* ApJ 614, L133–L136.

Bodenheimer, P., Hubickyj, O., Lissauer, J. J., 2000. *Models of the in Situ Formation of Detected Extrasolar Giant Planets.* Icarus 143, 2–14.

Boss, A. P., 1997. *Giant planet formation by gravitational instability.* Science 276, 1836–1839.

Boss, A. P., 2000. *Possible Rapid Gas Giant Planet Formation in the Solar Nebula and Other Protoplanetary Disks.* ApJ 536, L101–L104.

Bryden, G., Chen, X., Lin, D. N. C., Nelson, R. P., Papaloizou, J. C. B., 1999. *Tidally Induced Gap Formation in Protostellar Disks: Gap Clearing and Suppression of Protoplanetary Growth.* ApJ 514, 344–367.

Calvet, N., D'Alessio, P., Hartmann, L., Wilner, D., Walsh, A., Sitko, M., 2002. *Evidence for a Developing Gap in a 10 Myr Old Protoplanetary Disk.* ApJ 568, 1008–1016.

Calvet, N., D'Alessio, P., Watson, D. M., Franco-Hernández, R., Furlan, E., Green, J., Sutter, P. M., Forrest, W. J., Hartmann, L., Uchida, K. I., Keller, L. D., Sargent, B., Najita, J., Herter, T. L., Barry, D. J., Hall, P., 2005. *Disks in Transition in the Taurus Population: Spitzer IRS Spectra of GM Aurigae and DM Tauri.* ApJ 630, L185–L188.

Chambers, J., 2006. *A semi-analytic model for oligarchic growth.* Icarus 180, 496–513.

Clampin, M., Krist, J. E., Ardila, D. R., Golimowski, D. A., Hartig, G. F., Ford, H. C., Illingworth, G. D., Bartko, F., Benítez, N., Blakeslee, J. P., Bouwens, R. J., Broadhurst, T. J., Brown, R. A., Burrows, C. J., Cheng, E. S., Cross, N. J. G., Feldman, P. D., Franx, M., Gronwall, C., Infante, L., Kimble, R. A., Lesser, M. P., Martel, A. R., Menanteau, F., Meurer, G. R., Miley, G. K., Postman, M., Rosati, P., Sirianni, M., Sparks, W. B., Tran, H. D., Tsvetanov, Z. I., White, R. L., Zheng, W., 2003. *Hubble Space Telescope ACS Coronagraphic Imaging of the Circumstellar Disk around HD 141569A.* AJ 126, 385–392.

Coffey, D., Bacciotti, F., Woitas, J., Ray, T. P., Eislöffel, J., 2004. *Rotation of Jets from Young Stars: New Clues from the Hubble Space Telescope Imaging Spectrograph.* ApJ 604, 758–765.

Crida, A., Morbidelli, A., Masset, F., 2006. *On the width and shape of gaps in protoplanetary disks.* Icarus 181, 587–604.

Crida, A., Morbidelli, A., Masset, F., 2007. *Simulating planets in globally evolving disks.* A&A 461, 1173–1183.

D'Angelo, G., Bate, M. R., Lubow, S. H., 2005. *The dependence of protoplanet migration rates on co-orbital torques.* MNRAS 358, 316–332.

Duncan, M. J., Levison, H. F., Lee, M. H., 1998. *A Multiple Time Step Symplectic Algorithm for Integrating Close Encounters.* AJ 116, 2067–2077.

Ferreira, J., 1997. *Magnetically-driven jets from Keplerian accretion discs.* A&A 319, 340–359.

Ferreira, J., Pelletier, G., 1995. *Magnetized accretion-ejection structures. III. Stellar and extragalactic jets as weakly dissipative disk outflows.* A&A 295, 807–832.

Forrest, W. J., Sargent, B., Furlan, E., D'Alessio, P., Calvet, N., Hartmann, L., Uchida, K. I., Green, J. D., Watson, D. M., Chen, C. H., Kemper, F., Keller, L. D., Sloan, G. C., Herter, T. L., Brandl, B. R., Houck, J. R., Barry, D. J., Hall, P., Morris, P. W., Najita, J., Myers, P. C., 2004. *Mid-infrared Spectroscopy of Disks around Classical T Tauri Stars.* ApJS 154, 443–447.

Fromang, S., Terquem, C., Balbus, S. A., 2002. *The ionization fraction in α models of protoplanetary discs.* MNRAS 329, 18–28.

Gammie, C. F., 1996. *Layered Accretion in T Tauri Disks.* ApJ 457, 355–362.

Goldreich, P., Nicholson, P. D., 1989. *Tides in rotating fluids.* ApJ 342, 1075–1078.

Goldreich, P., Tremaine, S., 1979. *The excitation of density waves at the Lindblad and corotation resonances by an external potential.* ApJ 233, 857–871.

Goldreich, P., Tremaine, S., 1980. *Disk-satellite interactions.* ApJ 241, 425–441.

Gomes, R., Levison, H. F., Tsiganis, K., Morbidelli, A., 2005. *Origin of the cataclysmic Late Heavy Bombardment period of the terrestrial planets.* Nature 435, 466–469.

Goodman, J., Rafikov, R. R., 2001. *Planetary Torques as the Viscosity of Protoplanetary Disks.* ApJ 552, 793–802.

Guillot, T., 2005. *THE INTERIORS OF GIANT PLANETS: Models and Outstanding Questions.* Annual Review of Earth and Planetary Sciences 33, 493–530.

Guillot, T., Hueso, R., 2006. *The composition of Jupiter: sign of a (relatively) late formation in a chemically evolved protosolar disc.* MNRAS 367, L47–L51.

Haghighipour, N., Boss, A. P., 2003a. *Erratum: "On Pressure Gradients and Rapid Migration of Solids in a Nonuniform Solar Nebula".* ApJ 586, 1442–1442.

Haghighipour, N., Boss, A. P., 2003b. *On Gas Drag-Induced Rapid Migration of Solids in a Nonuniform Solar Nebula.* ApJ 598, 1301–1311.

Haghighipour, N., Boss, A. P., 2003c. *On Pressure Gradients and Rapid Migration of Solids in a Nonuniform Solar Nebula.* ApJ 583, 996–1003.

Hahn, J. M., Ward, W. R., 1996. *Resonance Trapping due to Nebula Disk Torques.* In: Lunar and Planetary Institute Conference Abstracts, pp. 479–480.

Hartigan, P., Edwards, S., Ghandour, L., 1995. *Disk Accretion and Mass Loss from Young Stars.* ApJ 452, 736–768.

Hartmann, L., 2001. *Accretion Processes in Star Formation.* Cambridge University Press, January 2001.

Hayashi, C., 1981. *Structure of the solar nebula, growth and decay of magnetic fields and effects of magnetic and turbulent viscosities on the nebula.* Progress of Theoretical Physics Supplement 70, 35–53.

Herbst, W., Hamilton, C. M., Vrba, F. J., Ibrahimov, M. A., Bailer-Jones, C. A. L., Mundt, R., Lamm, M., Mazeh, T., Webster, Z. T., Haisch, K. E., Williams, E. C., Rhodes, A. H., Balonek, T. J., Scholz, A., Riffeser, A., 2002. *Fine Structure in the Circumstellar Environment of a Young, Solar-like Star: The Unique Eclipses of KH 15D.* PASP 114, 1167–1172.

Hollenbach, D., Adams, F. C., 2004a. *Dispersal of Disks Around Young Stars: Constraints on Kuiper Belt Formation.* In: Caroff, L., Moon, L. J., Backman, D., Praton, E. (Eds.), ASP Conf. Ser. 324: Debris Disks and the Formation of Planets, pp. 168–+.

Hollenbach, D., Adams, F. C., 2004b. *The Disruption of Planet-Forming Disks.* In: Johnstone, D., Adams, F. C., Lin, D. N. C., Neufeeld, D. A., Ostriker, E. C. (Eds.), ASP Conf. Ser. 323: Star Formation in the Interstellar Medium: In Honor of David Hollenbach, pp. 3–+.

Hueso, R., Guillot, T., 2005. *Evolution of protoplanetary disks: constraints from DM Tauri and GM Aurigae.* A&A 442, 703–725.

Ilgner, M., Nelson, R. P., 2006. *On the ionisation fraction in protoplanetary disks. I. Comparing different reaction networks.* A&A 445, 205–222.

Isella, A., Natta, A., 2005. *The shape of the inner rim in proto-planetary disks.* A&A 438, 899–907.

Klahr, H., 2004. *The Global Baroclinic Instability in Accretion Disks. II. Local Linear Analysis.* ApJ 606, 1070–1082.

Klahr, H., Kley, W., 2006. *3D-radiation hydro simulations of disk-planet interactions. I. Numerical algorithm and test cases.* A&A 445, 747–758.

Kley, W., 1999. *Mass flow and accretion through gaps in accretion discs.* MNRAS 303, 696–710.

Kley, W., D'Angelo, G., Henning, T., 2001. *Three-dimensional Simulations of a Planet Embedded in a Protoplanetary Disk.* ApJ 547, 457–464.

Kokubo, E., Ida, S., 2000. *Formation of Protoplanets from Planetesimals in the Solar Nebula.* Icarus 143, 15–27.

Korycansky, D. G., Papaloizou, J. C. B., 1996. *A Method for Calculations of Nonlinear Shear Flow: Application to Formation of Giant Planets in the Solar Nebula.* ApJS 105, 181–190.

Korycansky, D. G., Pollack, J. B., 1993. *Numerical calculations of the linear response of a gaseous disk to a protoplanet.* Icarus 102, 150–165.

Kuchner, M. J., Lecar, M., 2002. *Halting Planet Migration in the Evacuated Centers of Protoplanetary Disks.* ApJ 574, L87–L89.

Li, H., Colgate, S. A., Wendroff, B., Liska, R., 2001. *Rossby Wave Instability of Thin Accretion Disks. III. Nonlinear Simulations.* ApJ 551, 874–896.

Li, H., Finn, J. M., Lovelace, R. V. E., Colgate, S. A., 2000. *Rossby Wave Instability of Thin Accretion Disks. II. Detailed Linear Theory.* ApJ 533, 1023–1034.

Lin, D. N. C., Papaloizou, J., 1979. *Tidal torques on accretion discs in binary systems with extreme mass ratios.* MNRAS 186, 799–812.

Lin, D. N. C., Papaloizou, J., 1986a. *On the tidal interaction between protoplanets and the primordial solar nebula. II - Self-consistent nonlinear interaction.* ApJ 307, 395–409.

Lin, D. N. C., Papaloizou, J., 1986b. *On the tidal interaction between protoplanets and the protoplanetary disk. III - Orbital migration of protoplanets.* ApJ 309, 846–857.

Lin, D. N. C., Papaloizou, J. C. B., 1993. *On the tidal interaction between protostellar disks and companions.* In: Levy, E. H., Lunine, J. I. (Eds.), Protostars and Planets III, pp. 749–835.

Lubow, S. H., D'Angelo, G., 2006. *Gas Flow across Gaps in Protoplanetary Disks.* ApJ 641, 526–533.

Lynden-Bell, D., Pringle, J. E., 1974. *The evolution of viscous discs and the origin of the nebular variables.* MNRAS 168, 603–637.

Masset, F., 2000a. *FARGO: A fast eulerian transport algorithm for differentially rotating disks.* A&AS 141, 165–173.

Masset, F., 2000b. *FARGO: A Fast Eulerian Transport Algorithm for Differentially Rotating Disks.* In: Garzón, G., Eiroa, C., de Winter, D., Mahoney, T. J. (Eds.), ASP Conf. Ser. 219: Disks, Planetesimals, and Planets, pp. 75–80.

Masset, F., 2006. *Planet-Disk Interactions.* In: Goupil, M.-J., Zahn, J.-P. (Eds.), Tidal interactions in composite systems.

Masset, F., Snellgrove, M., 2001. *Reversing type II migration: resonance trapping of a lighter giant protoplanet.* MNRAS 320, L55–L59.

Masset, F. S., 2001. *On the Co-orbital Corotation Torque in a Viscous Disk and Its Impact on Planetary Migration.* ApJ 558, 453–462.

Masset, F. S., 2002. *The co-orbital corotation torque in a viscous disk: Numerical simulations.* A&A 387, 605–623.

Masset, F. S., D'Angelo, G., Kley, W., 2006. *On the migration of protogiant solid cores.* ApJ in press, astro–ph/0607155.

Masset, F. S., Morbidelli, A., Crida, A., Ferreira, J., 2006. *Disk Surface Density Transitions as Protoplanet Traps.* ApJ 642, 478–487.

Masset, F. S., Papaloizou, J. C. B., 2003. *Runaway Migration and the Formation of Hot Jupiters.* ApJ 588, 494–508.

Mayor, M., Queloz, D., 1995. *A Jupiter-Mass Companion to a Solar-Type Star.* Nature 378, 355–+.

Menou, K., Goodman, J., 2004. *Low-Mass Protoplanet Migration in T Tauri α-Disks.* ApJ 606, 520–531.

Meyer-Vernet, N., Sicardy, B., 1987. *On the physics of resonant disk-satellite interaction.* Icarus 69, 157–175.

Morbidelli, A., Levison, H. F., Tsiganis, K., Gomes, R., 2005. *Chaotic capture of Jupiter's Trojan asteroids in the early Solar System.* Nature 435, 462–465.

Nelson, A. F., Benz, W., 2003. *On the Early Evolution of Forming Jovian Planets. I. Initial Conditions, Systematics, and Qualitative Comparisons to Theory.* ApJ 589, 556–577.

Nelson, R. P., 2005. *On the orbital evolution of low mass protoplanets in turbulent, magnetised disks.* A&A 443, 1067–1085.

Nelson, R. P., Papaloizou, J. C. B., 2004. *The interaction of giant planets with a disc with MHD turbulence - IV. Migration rates of embedded protoplanets.* MNRAS 350, 849–864.

Nelson, R. P., Papaloizou, J. C. B., Masset, F., Kley, W., 2000. *The migration and growth of protoplanets in protostellar discs.* MNRAS 318, 18–36.

Ogilvie, G. I., Lubow, S. H., 2002. *On the wake generated by a planet in a disc.* MNRAS 330, 950–954.

Paardekooper, S.-J., Mellema, G., 2006. *Halting Type I planet migration in non-isothermal disks.* A&A 459, L17–L20.

Papaloizou, J., Lin, D. N. C., 1984. *On the tidal interaction between protoplanets and the primordial solar nebula. I - Linear calculation of the role of angular momentum exchange.* ApJ 285, 818–834.

Papaloizou, J. C. B., Nelson, R. P., Snellgrove, M. D., 2004. *The interaction of giant planets with a disc with MHD turbulence - III. Flow morphology and conditions for gap formation in local and global simulations.* MNRAS 350, 829–848.

Pesenti, N., Dougados, C., Cabrit, S., Ferreira, J., Casse, F., Garcia, P., O'Brien, D., 2004. *Predicted rotation signatures in MHD disc winds and comparison to DG Tau observations.* A&A 416, L9–L12.

Piétu, V., Dutrey, A., Guilloteau, S., Chapillon, E., Pety, J., 2006. *Resolving the inner dust disks surrounding LkCa 15 and MWC 480 at mm wavelengths.* A&A 460, L43–L47.

Pollack, J. B., Hubickyj, O., Bodenheimer, P., Lissauer, J. J., Podolak, M., Greenzweig, Y., 1996. *Formation of the Giant Planets by Concurrent Accretion of Solids and Gas.* Icarus 124, 62–85.

Quillen, A. C., Blackman, E. G., Frank, A., Varnière, P., 2004. *On the Planet and the Disk of COKU TAURI/4.* ApJ 612, L137–L140.

Rafikov, R. R., 2002. *Planet Migration and Gap Formation by Tidally Induced Shocks.* ApJ 572, 566–579.

Rice, W. K. M., Armitage, P. J., Wood, K., G., L., 2006. *Dust filtration at gap edges: Implications for the spectral energy distributions of discs with embedded planets.* MNRAS 373, 1619–1626.

Rice, W. K. M., Wood, K., Armitage, P. J., Whitney, B. A., Bjorkman, J. E., 2003. *Constraints on a planetary origin for the gap in the protoplanetary disc of GM Aurigae.* MNRAS 342, 79–85.

Schneider, G., Smith, B. A., Becklin, E. E., Koerner, D. W., Meier, R., Hines, D. C., Lowrance, P. J., Terrile, R. J., Thompson, R. I., Rieke, M., 1999. *NICMOS Imaging of the HR 4796A Circumstellar Disk.* ApJ 513, L127–L130.

Shakura, N. I., Sunyaev, R. A., 1973. *Black holes in binary systems. Observational appearance.* A&A 24, 337–355.

Shu, F. H., 2002. *Star-Disk Coupling Mechanisms.* Bulletin of the American Astronomical Society 34, 731–+.

Stone, J. M., Norman, M. L., 1992. *ZEUS-2D: A radiation magnetohydrodynamics code for astrophysical flows in two space dimensions. I - The hydrodynamic algorithms and tests.* ApJS 80, 753–790.

Stone, J. M., Norman, M. L., 1993. *Numerical simulations of protostellar jets with nonequilibrium cooling. I - Method and two-dimensional results. II - Models of pulsed jets.* ApJ 413, 198–220.

Takeuchi, T., Miyama, S. M., Lin, D. N. C., 1996. *Gap Formation in Protoplanetary Disks.* ApJ 460, 832–847.

Tanaka, H., Takeuchi, T., Ward, W. R., 2002. *Three-Dimensional Interaction between a Planet and an Isothermal Gaseous Disk. I. Corotation and Lindblad Torques and Planet Migration.* ApJ 565, 1257–1274.

Thommes, E. W., 2005. *A Safety Net for Fast Migrators: Interactions between Gap-opening and Sub-Gap-opening Bodies in a Protoplanetary Disk.* ApJ 626, 1033–1044.

Thommes, E. W., Murray, N., 2006. *Giant Planet Accretion and Migration: Surviving the Type I Regime.* ApJ 644, 1214–1222.

Tsiganis, K., Gomes, R., Morbidelli, A., Levison, H. F., 2005. *Origin of the orbital architecture of the giant planets of the Solar System.* Nature 435, 459–461.

Varnière, P., Blackman, E. G., Frank, A., Quillen, A. C., 2006a. *Planets Rapidly Create Holes in Young Circumstellar Disks.* ApJ 640, 1110–1114.

Varnière, P., Blackman, E. G., Frank, A., Quillen, A. C., 2006b. *Planets Rapidly Create Holes in Young Circumstellar Disks.* ApJ 640, 1110–1114.

Varnière, P., Quillen, A. C., Frank, A., 2004. *The Evolution of Protoplanetary Disk Edges.* ApJ 612, 1152–1162.

Veras, D., Armitage, P. J., 2004. *Outward migration of extrasolar planets to large orbital radii.* MNRAS 347, 613–624.

Ward, W. R., 1986. *Density waves in the solar nebula - Differential Lindblad torque.* Icarus 67, 164–180.

Ward, W. R., 1991. *Horsehoe Orbit Drag.* In: Lunar and Planetary Institute Conference Abstracts, pp. 1463–1464.

Ward, W. R., 1992. *Coorbital Corotation Torque.* In: Lunar and Planetary Institute Conference Abstracts, pp. 1491–1492.

Ward, W. R., 1997. *Protoplanet Migration by Nebula Tides.* Icarus 126, 261–281.

Ward, W. R., 2003. *Type II Migration and Giant Planet Survival.* In: Mackwell, S., Stansbery, E. (Eds.), Lunar and Planetary Institute Conference Abstracts, pp. 1736–1737.

MIGRATION PLANÉTAIRE AU COURS DE LA FORMATION DU SYSTÈME SOLAIRE

PLANETARY MIGRATION IN SOLAR SYSTEM FORMATION

Aurélien CRIDA

Résumé

La migration planétaire est un phénomène apparemment inévitable lors de la formation des planètes dans les disques protoplanétaires. Les interactions gravitationnelles entre les embryons de planète et le disque de gaz font décroître le moment cinétique de l'embryon, qui spirale vers l'étoile centrale. Le temps de migration étant plus court que la durée de vie du disque, aucune planète ne devrait survivre (chapitres 1 et 2). Dans cette thèse, nous essayons de trouver des mécanismes qui empêchent ou ralentissent la migration.

Dans le chapitre 3, nous montrons qu'un saut dans le profil de densité du disque de gaz bloque la migration et agit comme un piège à planète. Ainsi bloqué, un coeur solide massif peut accrèter une atmosphère gazeuse et devenir une planète géante. La planète est alors assez massive pour repousser le gaz et ouvrir un sillon autour de son orbite. En analysant des simulations numériques, nous mettons en évidence le rôle des effets de pression dans ce processus dans le chapitre 4 ; un nouveau critère unifié d'ouverture du sillon en découle. Après la présentation dans le chapitre 5 d'un nouvel algorithme fiable et performant pour réaliser des simulations numériques, nous l'utilisons dans le chapitre 6 pour étudier la migration d'une planète géante et son impact sur l'évolution du disque. La formation d'une cavité s'avère moins facile que prévu, mais une possibilité d'arrêter la migration apparaît. Enfin, dans le chapitre 7, nous étudions le cas de Jupiter et Saturne, et trouvons dans quelles conditions les interactions entre les deux planètes en empêchent la migration.

Abstract

Planetary migration seems to be unavoidable during planet formation in protoplanetary disks. Gravitational interactions between the planet embryos and the gas disk make the angular momentum of the embryo decrease, so that it spirals towards the central star. As the migration timescale is shorter than the disk life time, no planet should survive (chapters 1 and 2). In this thesis, we try to find mechanisms that prevent or slow down migration.

In chapter 3, we show that a jump in the gas disk density stops migration and acts like a planet trap. Trapped there, a massive solid core may accrete a gaseous atmosphere and give birth to a giant planet. The planet is then massive enough to repel the gas and open a gap around its orbit. Through analysis of computer simulations, we enlighten the role of pressure effects in this process in chapter 4 ; a new generalized gap opening criterion is derived. After the presentation of a new, reliable and performing algorithm for numerical simulations in chapter 5, we use it in chapter 6 to study the migration of a giant planet and its influence on the disk evolution. The formation of a cavity appears to be less easy than previously expected, but we find a way of preventing migration. Last, in chapter 7, we focus on the case of Jupiter and Saturn, and we find in which conditions the interactions between both planets prevent their migration.